Metal Organic Frameworks based materials for long term solar energy storage application

Anastasia Permyakova

To cite this version:

Anastasia Permyakova. Metal Organic Frameworks based materials for long term solar energy storage application. Material chemistry. Université Paris Saclay (COmUE); Université de Mons, 2016. English. NNT : 2016SACLV031 . tel-01806324

HAL Id: tel-01806324
https://theses.hal.science/tel-01806324

Submitted on 2 Jun 2018

NNT : 2016SACLV031

THESE DE DOCTORAT
DE
L'UNIVERSITE DE MONS
ET DE
L'UNIVERSITE PARIS-SACLAY
PREPAREE A L'UNIVERSITE VERSAILLES SAINT-QUENTIN EN YVELINES et A L'UNIVERSITE DE MONS

ÉCOLE DOCTORALE N°571
Sciences chimiques : molécules, matériaux, instrumentation et biosystèmes

Spécialité de doctorat : Chimie

Par

Mme Anastasia Permyakova

Metal Organic Frameworks based materials for long term solar energy storage application.

Thèse présentée et soutenue à Versailles, le 2 Mai 2016 :

Composition du Jury :

M. G. De Weireld, Professeur, Université de Mons, Président du Jury
M. J. Denayer, Professeur, Vrije Universiteit Brussel, Rapporteur
M. P.L. Llewellyn, Directeur de Recherche, CNRS, Université Aix-Marseille, Rapporteur
M. F. Kapteijn, Professeur, Delft University of Technology, Examinateur
M. P. D'Ans, Docteur, Université Libre de Bruxelles, Examinateur
M. C. Serre, Directeur de Recherche CNRS, Université de Versailles Saint-Quentin, Directeur de thèse
M. M. Frère, Professeur, Université de Mons, Directeur de thèse
Mme N. Steunou, Professeur, Université de Versailles Saint-Quentin, Co-Directeur de thèse

Titre : Matériaux à base de solides hybrides poreux de type MOFs pour le stockage intersaisonnier d'énergie solaire.

Mots clés : Solides hybrides poreux, composites, stockage d'énergie

Résumé : L'évolution rapide des technologies de stockage d'énergie requiert la mise en point de nouveaux matériaux plus performants afin d'utiliser l'énergie relative à l'adsorption d'un fluide (eau) pour restituer l'énergie solaire préalablement stockée sur une période courte (heures) ou prolongée (inter saisonnière). Ces matériaux sont des sels inorganiques (chimisorption de l'eau), des adsorbants physiques ou des composites (sel inorganique dans une matrice poreuse).

Les polymères de coordination poreux (PCPs) ou 'Metal-Organic Frameworks' (MOFs) sont des solides poreux hybrides dont la structure cristalline résulte de l'association de ligands organiques polycomplexants et de briques inorganiques interagissant par liaisons fortes. Les MOFs présentent une plus grande diversité chimique et structurale par rapport aux solides poreux inorganiques, ce qui permet de varier 'à la carte' leur caractère amphiphile, leur volume poreux, la taille et la forme des pores.

Dans le cadre de cette thèse, nous avons étudié en premier lieu une série de MOFs poreux et stables dans l'eau, construits à partir des cations métalliques à haut degré d'oxydation (Fe^{3+}, Al^{3+}, Cr^{3+}, Ti^{4+}, Zr^{4+}) et de ligands polycarboxylates. Nous avons choisi cette série de MOFs en tant qu'adsorbants physiques tout en évaluant dans un second temps leur capacité en tant que matrices d'immobilisation de sels inorganiques.

L'étude des propriétés d'adsorption d'eau des MOFs seuls a démontré leurs grandes capacités d'adsorption conduisant ainsi à des densités énergétiques relativement élevées pour des systèmes en physisorption pure. La synthèse du MOF le plus performant de cette série (MIL-160(Al)) a été mise à l'échelle. Ce matériau a ensuite été mis en forme et ses propriétés de stockage de chaleur ont été évaluées dans un prototype de laboratoire (réacteur ouvert).

Les applications de stockage inter saisonnier requièrent des matériaux avec une densité énergétique plus élevée par rapport à celle des adsorbants physiques et à ce titre, les composites qui résultent de l'encapsulation de sels inorganiques au sein de matrices poreuses sont intéressants en termes de densité énergétique et de stabilité chimique. De ce fait, le deuxième chapitre porte sur l'exploration d'une série de MOFs en tant que matrices d'encapsulation de sels afin de préparer des composites pour le stockage de l'énergie.

Les MOFs sélectionnés permettent d'étudier l'influence de certains paramètres de la matrice (balance amphiphile, volume/taille des pores) sur les propriétés d'adsorption d'eau des composites. Les capacités de stockage énergétique des composites ont été évaluées dans les conditions d'utilisation d'un système de stockage d'énergie. Finalement la capacité de stockage élevée et la bonne stabilité de cyclage (adsorption-désorption) des deux meilleurs composites à base de matrices mésoporeuses (MIL-100(Fe) et MIL-101(Cr)) confirment l'intérêt de ces solides pour ce type d'application.

Université Paris-Saclay
Espace Technologique / Immeuble Discovery
Route de l’Orme aux Merisiers RD 128 / 91190 Saint-Aubin, France

Title : Metal Organic Frameworks based materials for long term solar energy storage application

Keywords : Metal-Organic Frameworks, composites, heat storage

Abstract : Nowadays the forceful development of the energy storage technologies requires the design of novel adsorbents. Energy reallocation concept allows storing renewable solar energies at short (hours) and long term (inter seasonal) using adsorption method. Energy storage materials can be divided in chemical storage materials, physical storage materials and composite materials (inorganic salt in porous matrix).

Metal-Organic Frameworks (MOFs) are a new class of porous crystalline materials that are built from an inorganic subunits and organic ligands defining an ordered structure with regular accessible porosity. In comparison with other classes of porous solids, MOFs display a higher degree of versatility (chemical composition, topology) and tunable amphiphilic character, pore volume, pore size, shape, etc.

In this work, we have studied a series of water stable porous metal carboxylates made from cheap metal cations (Fe^{3+}, Al^{3+}, Cr^{3+}, Ti^{4+}, Zr^{4+}) and polycarboxylate linkers as pure physical adsorbents and as host matrices of salts for the design of composite adsorbents. The study of the adsorption properties of pure MOFs in conditions of thermal energy storage system has shown high water adsorption capacity and high energy storage densities.

The most promising MOF from this series namely MIL-160(Al) has been prepared at large scale, processed as pellets and then evaluated in open-reactor prototype.

The second chapter has been focused on the first exploitation of a series of Metal Organic Framework (MOFs) as host matrices of salts for the preparation of composite sorbents for heat storage application. Indeed, inter seasonal energy storage requires materials with higher energy densities (composite and chemical storage materials), than physical sorption materials can offer. We have selected a series of MOFs differing by their amphiphilic balance and pore volume in order to investigate the impact of such physico-chemical properties on the water sorption properties of composites. The energy storage capacity of salt-MOFs composites has been evaluated in representative conditions of thermal storage devices. The high energy storage capacity and good stability under numerous adsorption-desorption cycles for two composites based on mesoporous MIL-100(Fe) and MIL-101(Cr) confirm the potentiality of such composites for this application.

Université Paris-Saclay
Espace Technologique / Immeuble Discovery
Route de l'Orme aux Merisiers RD 128 / 91190 Saint-Aubin, France

Acknowledgements

First of all I would like to sincerely thank my supervisor Dr. Christian Serre who gave me the opportunity to work on such fascinating project involving simultaneously a foremost material chemistry, fundamental thermodynamics and very specified and relevant applications. I appreciate your guidance, all scientific discussions and your indispensable academic support during my thesis as well as your help on editing of this manuscript. Thank you for the possibility to work on different topics such as synthesis of new MOFs and nanoscale synthesis that helped me gain most valuable experience and in combination with the main direction of my research led to enhanced knowledge and results. I would also like to thank you for allowing me to be part of training schools (formation d'adsorption CNRS) and numerous conferences (AFA-2015 and 2016, SCF-2015 etc.).

I would like to express my sincere gratitude to my supervisor Professor Marc Frère who guided my work in University of Mons. Thank you for involving me in state of the art of energy storage applications, for your advices, helpful remarks and for the time you invested in our scientific discussions and in editing of this manuscript and corresponding articles. I am very grateful for the opportunity to navigate all the way from the development of material to evaluating its capacity in real scale prototype reactor (UMons) and even see an industrial scale production in Hosokawa factory.

I am especially indebted to my co-supervisor Professor Nathalie Steunou who was directly involved in all particularities of my everyday research work. I am infinitely grateful for your immense help and support, your patience, your scientific suggestions and all your time you devoted to discussions and analysis of experimental results and editing this manuscript and corresponding articles. I appreciate your strong support in my first experience of article writing and presentation speech. I would like also to thank you for your initiative in finding necessary collaborators that allowed completing this experimental study.

I wish to express my appreciation to all the members of the thesis Committee, Professor Guy De Weireld, Professor Joeri Denayer, Dr. Philip L. Llewellyn, Professor Freek Kapteijn and Dr. Pierre D'Ans for their acceptance to participate in the evaluation of this thesis. I would like to thank once again my reviewers Professor Joeri Denayer and Dr. Philip L. Llewellyn, and the chairman of my Committee Professor Guy De Weireld.

I wish to express my gratitude to all the members of 'Comité d'Accompagnement' Professor Diane Thomas, Professor Guy De Weireld and Dr. Pierre d'Ans for evaluation of my work and your helpful advices.

I am grateful dearly to all of those with whom I have had pleasure to work during this and other related projects.

I deeply appreciate all the help from Dr. Suging Wang, Emilie Courbon, Dr. Nicolas Heymans, Prof. Wolfgang Hohenauer, Dr. Daniel Lager and Dr. Nicolas Barrier who contributed in the project concerning salt-MOF composites. My very special thanks goes to Sujing - my workmate, who has been developing with me new salt-MOF composite materials. Your hard-work and strong motivation allowed studying a large family of MOFs and obtaining better understanding of MOFs potential in this project. I am very thankful to Emilie, from whom I have learnt thermogravimetric techniques (TG-DSC, BelSorp). Thank you very much for your continuous help, your readiness for discussions and very useful advices. I would like to thank Daniel Lager, Wolfgang Hohenauer and Nicolas Heymans for providing help with calorimetric and adsorption measurements and Nicolas Barrier for X-ray measurements.

My special gratitude goes to Dr. Farid Nouar from whom I have learnt a lot of important things from laboratory techniques to organization of team work. Thank you a lot for your continuous support, your kindness, your patience (especially during my first year of thesis), your helpful advices and scientific discussions. In addition thank you for perfect and numerous SEM-EDX measurements.

I would like to thank Maame Affram, Dr. Georges Mouchaham and Dr. Thomas Devic for our collaborative work concerning optimization of MIL-160(Al) synthesis. I am indebted to Thomas and Georges for their professionalism and important scientific advices and Maame for her diligence and purposefulness. I am indebted to Prof. Jong-San Chang and his students U-Hwang Lee and Anil H. Valekar who performed the shaping procedure of MIL-160(Al). I wish to thank Dr. Alexandre Skrylnyk who was guiding me during experiments in prototype. Thank you for your help in study of prototype equipment and for useful scientific discussions (furthermore, in Russian). I am grateful to Dr. Sandrine Bourrelly who performed calorimetric measurements on MOFs.

I wish to express my gratitude to Dr. Patricia Horcajada who proposed me to work on the project concerning MOFs in nanotechnology fiend. Thank you for your guidance and your advices during this time. It was very enriching experience for me.

I am indebted to Prof. Guy De Weireld for his time and his support invested in the project concerning methanol adsorption on MOFs and composites showing very promising perspectives. My special gratitude goes to Dr. Pierre Billemont and Périne Normand who worked with me on this project. It was my pleasure to collaborate with you.

I am very grateful to Dr. Nathalie Guillou who worked on structural resolution of new crystalline hybrid material that I synthesized during my first year of thesis. Thank you very much for your patience and tremendous amount of time invested in this complicated resolution.

I wish to express my gratitude to all SoTherCo partners and project coordinators Gilbert Descy and Michel Beeckmans. It was amazing experience to work in such a multidisciplinary team, be able to use expanded approach and broader knowledge for this project. I also gained a very important experience of public speaking and public performance in addition to the conference presentations.

I would like to warmly thank all my past and present colleagues from University of Mons, Claudine, Emilie, Renato, Nathalie, Nicolas H., Alexandre, Tangi, Christiana, Nicolas M., Périne, Pierre, Clément, Mathieu and Rémi and UVSQ, Clémence, Carine, Antoine, Jérôme, Paul R., Paul F., Hala, Lucy, Monica, Mazheeva, Teresa, Farid, Georges, Marvin, Fay, Florent, Saad, Tania, Cihang, Elena, Alfonso, Khalil, Tanay, Laurianne, Kevin, Rhizlaine and the numerous students who have come through the lab for short stage projects. The both teams have been a source of friendships as well as good advice and collaboration. I am very grateful to Périne for my speedy adaptation in Belgium from the lab scale to a whole city scale (or even country scale). Thank you for your friendship and all that unforgettable time in our trips etc. I appreciate Lucy, Paul and Elsa (being PhD students in the immediate past and now Dr. Cooper, Dr. Rouschmeyer and Dr. Alvarez) whom we have shared a lot – the office, the lab and several Parisian theatre performances. I am especially grateful for Amandine and Hala who strongly supported me in all my administrative troubles. My special thanks go to Spanish scientists Elena, Teresa, Monica and Tania for their

positive mood and support. I wish to thank my immediate office neighbours Fey, Marvin and Kevin for friendly environment (all three), readiness to help (all three) and calm conditions allowed me to write this manuscript (especially Kevin). It is very important for me to thank all the people I had conversation in French with. It was life changing to learn French in your company!

I appreciate all the people in the both Universities that any time offered their help.

I would like to sincerely thank my nearest and dearest adorable persons who always believe in me and support me in all of my projects: my parents, my husband, my grandparents, my uncle, my cousins and my friends.

Table of content:

List of Abbreviations

AHP	adsorption heat pump
AHT	adsorption heat transformation
ALPO	aluminophosphate
BPDC	4,4’-biphenyldicarboxylate
BTC	benzene-1,3,5 tricarboxylate
CAU	materials from Christian-Albrecht-University
CFSE	crystal field stabilization effect
DLS	dynamic light scattering
DMF	dimethylformamide
EDX	Energy dispersive X-ray
EDXRD	Energy dispersive X-ray diffration
FDCA	2,5-furandicarboxylic acid
IR	Infrared Spectroscopy
ITW	Institute of Thermodynamics and Thermal Engineering
KSK	silica gel (150-200 mesh)
L	ligand
LHS	latent heat storage
M	metal
MIL	materials from Institute Lavoisier
MOF	Metal Organic Framework
MTB	4,4’,4’’,4’’’-methanetetrayltetrabenzoic acid
NDC	naphthalene-2,6 dicarboxylate
NP	nano particles
Prop	i-Propanol
PV	photovoltaic
PXRD	powder X-ray diffraction
RH	Relative humidity
SAPO	silica-aluminophosphate
SBA	Santa Barbara Amorphous mesoporous silica
SBU	Secondary Building Units
SEM	Scanning electron microscopy
SHS	sensible heat storage
SoTherCo	Solar Thermochemical Compact Storage System
STY	Space-Time-Yield
SWS-1L	composite SBA/ $CaCl_2$ (33.7 % wt.)
SXRD	single crystal X-ray diffraction
TCES	Thermochemical energy storage
TCM	Thermochemical storage material
TES	Thermal energy storage
TGA	Thermogravimetric analysis
TXRPD	Thermal X-ray powder diffraction
UiO	materials from University of Oslo
XRPD	X-ray powder diffraction

General introduction

Nowadays, the increasingly austere problems of excessive fossil fuels consumption and greenhouse gas emissions derived from combustion processes are pushing research scientists for the development of more efficient and affordable alternative energy solutions. Different renewable energy sources such as solar energy, wind, water and geothermal technologies shall be used in order to minimize global environmental pollution and reduce energy consumption. There are numerous applications that require advanced storage technologies in order to efficiently use energy. One of them is space heating using thermal solar collectors.

Thermochemical energy storage (TCES) is a very promising way to store produced alternative energy with extremely low losses. This technology is based on the reversible reaction A (solid or liquid) + B (vapor) ↔ C (solid or liquid) + heat and generally uses energy from solar source. Water vapor (B) is the most widespread working fluid for this application. At the present time the research in this field is focused on studying properties of inorganic and hybrid porous solids (zeolite, silica gel, aluminophosphates (ALPOs), metal–organic frameworks) as physical sorption materials, inorganic salts as chemical sorption materials and composites combining inorganic porous matrices and inorganic salts. Composites are novel and very promising materials due to the synergy between the physic-chemical properties of the confined salt and the host matrix, and as result, exhibit a good energy density and stability as well as an improved thermal and mass transfer.

Metal–organic frameworks (MOFs) are a recent class of porous ordered materials with tunable features in terms of internal surface area and pore volume as well as structural properties and chemical functionality. As reported previously, MOFs are very promising water adsorbents since their water uptake easily outperforms that of any conventional material such as silica gel, zeolites or metal phosphates (ALPOs…). Their surface area typically ranges from 500 to 6000 m^2/g, exceeding often those of traditional porous materials. Thus, they tend to adsorb a larger amount of water and/or might encapsulate larger amounts of salts than other porous matrices. In addition, the surface functionalization of MOFs by using hydrophilic or hydrophobic organic linkers makes it possible to tune their amphiphilic character (hydrophilic-hydrophobic balance) and thus tune the water pressure range of their sorption isotherms as well as increase their sorption capacity. Noteworthy, there is so far a large array of hydrothermally stable and scalable MOFs with promising water sorption capacities and suitable hydrophilicity that appear as excellent candidates for heat transformation application.

The work reported in this thesis manuscript was performed in this research field within the frame of a **European FP7 Solar Thermochemical** Compact **Storage System (SoTherCo) project**. It deals with the preparation of a series of MOFs and $CaCl_2$-MOFs based composites for heat reallocation application.

This manuscript consists of General introduction, four chapters and Conclusion and perspectives:

-the first chapter covers recent advances in the field of heat transformation applications. It is also intended to give a useful survey of recent progresses concerning the water sorption properties of

MOFs and related applications.

-In the second chapter, we have studied a series of water stable porous metal carboxylates made from cheap metal cations (Fe^{3+}, Al^{3+}, Cr^{3+}, Ti^{4+}, Zr^{4+}) and polycarboxylate linkers as pure physical adsorbents. This series of hybrid porous solids (i. e. MIL-100(Fe), MIL-101(Cr), MIL-125(Ti)-NH_2, UiO-66(Zr)-NH_2, MIL-127(Fe) and MIL-160(Al)) presents a diversity in terms of composition (nature of metal and organic linker, presence of Lewis acid sites, hydrophilic-hydrophobic balance), framework topology, porosity (pore volume, pore size (microporous and mesoporous), pore shape)) and water sorption properties (water sorption capacity, cycling stability). We have studied the adsorption properties of those MOFs in conditions of thermal energy storage application. The most promising MOF from this series namely MIL-160(Al) has been prepared at a larger scale, processed as granulates and then evaluated in open-reactor prototype.

- In the third chapter, we have prepared composites by combining calcium chloride with the same series of MOFs. Composites differing by their composition (i. e. nature of the MOF matrix and the content of salt) were fully characterized with multiple techniques. The energy storage capacity of salt-MOFs composites has been evaluated in representative conditions of thermal storage devices.

- The fourth chapter is dedicated to the optimization of the synthesis of nanoparticles of MIL-127(Fe). Actually, the energy density of material for heat reallocation application is strongly dependent on the packing density of materials that is not only impacted by the crystallographic density, but also the particle size and shaping process. We have selected MIL-127(Fe) which is a highly water stable MOF and thus, very promising for different application fields related to water adsorption and also biomedicine.

Chapter I

Literature review

Chapter I: Thermochemical energy storage

1. Introduction

There are numerous technologies for the utilization of solar energy. They can be divided in solar thermal technologies and solar electrical systems. Solar electrical systems allow converting sunlight into electrical energy while solar thermal technologies - in thermal energy. The most notable example of solar electrical technologies is photovoltaic (PV) cells.[1] In this work we will focus on solar thermal technologies and more precisely on solar thermal storage technologies.

One of the possible ways to use solar thermal energy is warm domestic water providing. In North Western Europe, this system allows covering 60 – 70 % of the needed annual energy demand. These heat storage systems are commonly based on large insulated water tanks (sensible heat storage). However, current hot water stores have a relatively low energy storage density (~ 60 kWh/m³ at a temperature difference of $\Delta T = 50$ K), suffer considerable heat losses to the ambient during the storage period and only short-term storage time (several hours). Therefore, there are only some specific ways to apply this storage technology for long-term storage period e.g. in newly-built houses with a large hot water reserves (e.g. solar boiler) as an integral part of the building structure. Such systems yield only 20-30 % of solar fraction. The remaining heat demand is covered by a conventional fossil fueled backup heater.

In order to achieve higher solar fractions of at least 50 % and potentially up to 100 %, seasonal (long-term) energy storages are required. Thermochemical energy storage (TCES) is an excellent technology for space heating which allows the storage of solar heat from summer for use during the winter as the maximum heat demand occurs in colder months. Such a technology can significantly decrease the fossil energy demand in the building stock.

Concept of thermochemical energy storage includes the thermochemical storage material (TCM), design of the thermochemical energy storage and the integration of the thermochemical energy storage into the heat distribution (to the building and from the solar collectors) system.

Thermochemical energy storage approach has two important advantages in comparison with heat storage using water tanks. Energy storage densities in case of thermochemical heat storage could be higher (factor 2 to 6) as compared with heat storage using water. Additionally, the heat can be stored for a very long time without losses as soon as the thermochemical material has been charged. This opens up the opportunity for compact and highly efficient long-term thermal energy storages.

In 1970s, Swedish and Swiss researchers investigated thermochemical ES using chemical heat pump (CHP).[2] In 1970s, elaboration of long-distance thermal energy transportation system (EVA-ADAM) started and this technology was developed in 1980s becoming the first practical example of thermochemical heat storage.[2]

2. Definition of terms

Solar fraction is the amount of energy provided by the solar collectors and exploited by the user divided by the total energy required and could be defined as:
Solar fraction = Solar input / (Solar input + Supplementary input)

Energy storage density of material corresponds to stored energy per unit of volume [kWh/m^3]

Energy storage capacity of material corresponds to stored energy per unit of mass [Wh/kg]

Physical adsorption (physical sorption) implies Van-der-Waals or hydrogen bonding

Chemical sorption (chemisorption) implies valence bonding that provides new chemical compounds

Absorption is related to a transfer of a volume into a volume, i.e. it is a permeation or dissolution of a volume of energy or mass (absorbate) into another volume of energy or mass (absorbent).

Cycle loading lift is the working fluid exchange between the adsorption and desorption steps of the entire cycle in fixed conditions of T and p (conditions for the adsorption step on the one hand and conditions for the desorption step on the other hand), [g H_2O /g anhydrous material]

Adsorption loading lift is the adsorbed working fluid in fixed conditions of T and p,
[g H_2O /g anhydrous material]

Isosteric process is a process that occurs at a constant water loading

3. Thermal energy storage technologies and focus on thermochemical energy storage

3.1. Type of Thermal Energy Storage

Thermal energy storage (TES) is usually considered as an efficient energy conservation approach. Thermal energy storing could be effectuated by sensible TES, latent TES and thermochemical energy storage (TCES), which includes a wide range of physical-chemical process. Figure 1 shows an overview of the major techniques of thermal energy storage.

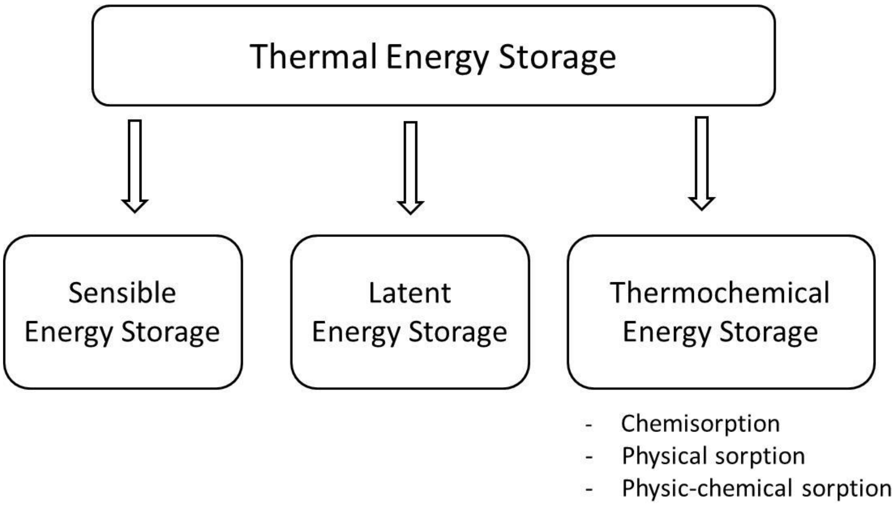

Figure 1. A classification of TES methods[3],[4],[5]

As mentioned above, generally TES includes technologies which allow storing heat and cold energy between day and night times and only thermochemical energy storage allows long-term storage period (several months).

3.2. Sensible and latent energy storage

Sensible and Latent Thermal Energy Storages are based on physical processes. **Sensible energy storage (SHS)** implies the heat absorbed or released when liquid (water, oil) or solid (molten salts, iron, rock, concrete) storage material undergoes a change in temperature, thus heat transfer interaction occurs. In case of sensible TES the stored energy depends on the mass of storage material, its heat capacity (C_p) and the temperature difference of the storage medium between its initial and final states. Mathematically this thermodynamic process can be expressed as follow:

$$E_{sens} = m \times C_p \times \Delta T$$

where E_{sens} is stored energy and m, C_p and ΔT are the mass, specific heat of the storage material, and the temperature difference before and after the storage operation, respectively.[6]
Storage of hot sanitary water in large insulated water tanks is the most common example of sensible energy storage.

Latent energy storage (LHS) implies the heat released or absorbed during a phase change (e.g. melting, evaporating and crystallization) at constant temperature. Latent heat storage materials also denoted Phase Change Materials (PCM) undergo phase change at constant temperature or in small temperature range (in case of non-eutectic mixture). In case of latent TES the stored energy depends on mass (m) and the specific latent heat of the phase change material (ΔH_{spec}) as follow[6]:

$$E_{lat} = m \times \Delta H_{spec}$$

Phase Change Materials exhibit a considerable storage density and store heat at a constant temperature corresponding to the phase transition temperature.[7] LHS materials allow storing more energy per unit of volume in comparison with sensible energy storage materials. Thus, LHS systems are much more promising as compared to SHS. Phase Change Materials can be classed in two types such as organic and inorganic PCM. For example, salt hydrates represent organic type of LHS materials while paraffin - inorganic LHS ones. **Figure 2** presents several examples of PCM depending on their melting temperature. In case of solar energy storage application with typical temperature of solar collectors of 80-120°C we can single out PCM with phase change temperature below 120°C. It concerns mainly paraffin, salt hydrates and fatty acids with enthalpy of fusion in the range of 150-600 kJ$\cdot$L^{-1}.

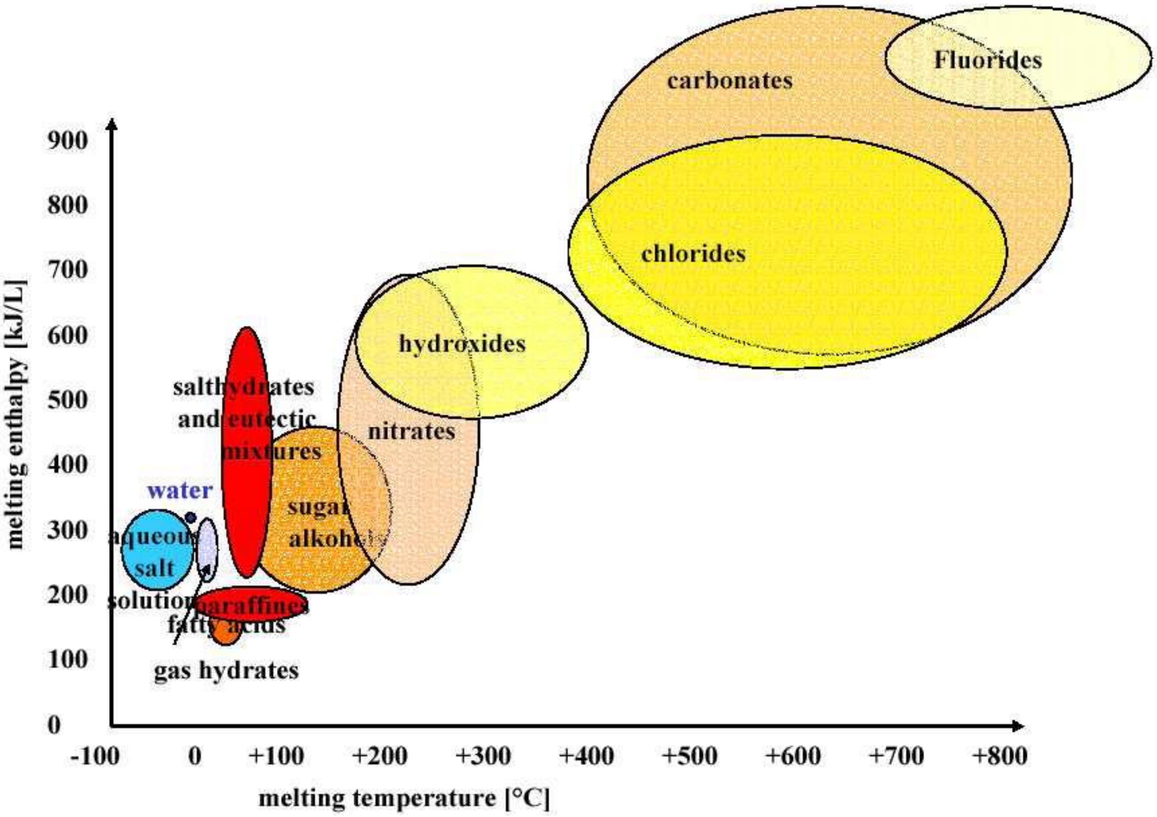

Figure 2. Enthalpy and fusion temperature of different phase change materials[8]

3.3. Thermochemical Energy Storage

Initially the term **Thermochemical Energy Storage** implied Thermal Energy Storage based on reversible chemical reaction $A + B \Leftrightarrow C + heat$, but recently many possibilities of reactants as porous sorbents or composite materials has been investigated as energy storage materials, that enchased the rage of phenomena involving this term. Several classifications suggested separating the term Thermochemical energy storage and Sorption energy storage. However, majority of articles includes term **Thermochemical Energy Storage** to define different phenomena such as physical sorption (adsorption), chemical reaction (absorption or chemisorption) and combination of both phenomena. As mentioned above, absorption is related to a transfer of a volume into a volume, while adsorption concerns the transfer process of a volume onto a surface when specific components of one phase of a fluid are transferred onto the surface of a solid adsorbent.[9],[10] Chemisorption processes often offer larger heat of sorption than physical sorption. The heat stored depends on the amount of storage material, the endothermic heat of reaction and the extent of conversion (mass of B that is transferred to A or form AB).[4]

Thermochemical ES is the most attractive approach compared to all other TES owing to higher energy density, long-term storage period, small thermal losses and wide temperature range. Due to these advantages thermochemical ES is particularly appropriate for seasonal storage of solar heat.

4. Principles of thermochemical ES

Reversible exo-/endothermic reaction $A + B \Leftrightarrow C + heat$ is the foundation of thermochemical storage systems. Adsorption process (zeolite, silica gel) or hydration process (salt) which is activated by bringing the dry storage material in contact with a working fluid such as water results in release of heat energy. Release of heat denoted as **energy discharging process** occurs during reaction $A + B \rightarrow C + heat$. A reverse reaction $A + B \leftarrow C + heat$ is endothermic and results in storage of heat or **energy charging process**.[11],[12]

Thermochemical material (TCM) C with heat supply can dissociate into components A and B, which are working pair or sorption couple. A and B can be stored separately in long-term until new cycle of heat release, then C will be formed.[12] Thermochemical ES cycle implies following processes:

1) Energy charging process: a required energy resource is used for dissociation of compound C during endothermic reaction
2) Energy storing process: after the charging process, A and B will be formed and both are stored in this stage
3) Energy discharging process: A and B are combined in an exothermic reaction and material C is regenerated together with heat release (Figure 3).[6]

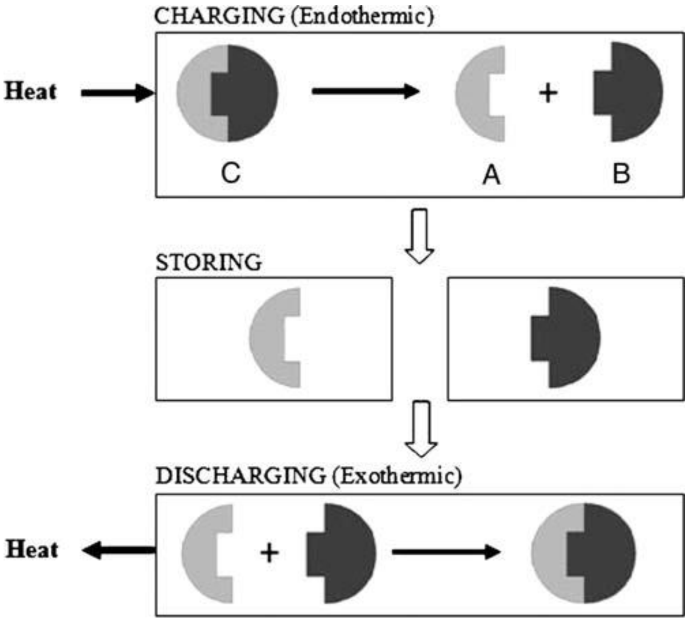

Figure 3. Processes involved in a thermochemical energy storage cycle: charging, storing and discharging[6]

4.1. Solid-gas process

As mentioned above, thermochemical energy storage processes corresponds to reversible reaction A + B ↔ C + (ΔH^0_r); ΔH^0_r being the standard enthalpy of the reaction (expressed by 1 mol). In case of chemical sorption the stoichiometry need to be considered. We will focus on the case of a solid-gas process where A is solid and B is the reactive gas (working fluid). The equilibrium conditions (p_{eq}, T_{eq}) of the solid-gas process can be described by the Clausius-Clapeyron relation. This relation is obtained considering the free Gibbs energy equal to zero in the condition of the thermodynamic equilibrium:

$$\Delta G_r = \Delta G^0_r + RT_{eq}\ln K = \Delta H^0_r - T_{eq}\Delta S^0_r + RT_{eq}\ln K = 0$$

K is the equilibrium constant, ΔH^0_r is standard enthalpy and ΔS^0_r is standard entropy of the reaction. If we consider the reactive gas as a perfect gas than K can be described as:

$$K = (p_{eq}/p^0)$$

p^0 is the reference pressure (1 bar).

Thus, the thermodynamic equilibrium conditions can be expressed mathematically as follow:

$$\ln(p_{eq}/p^0) = -\Delta H^0_r/RT_{eq} + \Delta S^0_r/R$$

T_{eq} and p_{eq} are equilibrium temperature and equilibrium pressure of the gas-solid system.

4.2. Closed and open thermochemical ES

Commonly, TCMS can be separated in open and closed systems.[5] Though, closed and open sorption systems suggest the same physical process, the engineering design of those is quite different. While in open systems, the storage material is exposed to the carrier gas flowrate that transports B to or from the solid, in closed systems, the storage material it is put in contact with pure working fluid B; the transport of B (from or to the storage material) is performed by a difference of total pressure (see Figure 4). Water is generally the working fluid and the carrier gas is very often air.

In fact, a closed Thermochemical Energy Storage is a heat pump which is operated under vacuum conditions. The basic steps are described below:

1) Charging process (desorption, drying of adsorbent): heat from a high temperature source (solar thermal collectors) is fed into the device, heats the adsorbent and vapor is desorbed from the adsorbent. The desorbed vapor condenses at a medium temperature level (medium temperature heat sink) and is stored in a separate reservoir. The heat of condensation has to be withdrawn to the environment (medium temperature heat sink).[6]
2) Storage period: the dry adsorbent is separated from the liquid working fluid (the connecting valve is closed). As long as these components stay separate, long-term heat storage without losses is possible if the sensible heat involved is neglected.[6]
3) Discharging process (adsorption of working fluid on adsorbent): water is evaporates taking up heat at a low temperature level (low temperature heat source). Vapor adsorbs and releases adsorption heat at a higher temperature level (medium temperature heat sink). This useful heat can be used for heating purposes.[6]

When the high temperature heat source is available at any time, steps 1, 2 and 3 are short and are repeated with a high frequency. Heat coming from the low and high temperature sources is provided to the medium temperature heat sink (during water condensation and adsorption). This known as a heat pump which can be considered, to a certain extent, as a very short term energy storage. If there is a time lift between the availability of the high temperature heat source and the heat demand from the medium temperature heat sink, than steps 1, 2 and 3 are long and are repeated with a low frequency (e.g. one per year). The process is thus known as a long term energy storage process.

The main differences between these two cases involving the same phenomena are:

- The frequency of the entire process
- The heat of condensation cannot be exploited in long term energy storage systems as there is no heat demand whereas it can when considering heat pumping
- Heat pumping requires fast kinetics to make the entire process as continuous as possible while providing the requested heat power to the heat sink.
- Long term heat storage requires suitable equilibrium characteristic so that a large quantity of energy may be stored in a small volume.

In closed systems, a heat exchanger allows heat transfer from/to the solid or liquid TCM. Expected energy density of closed systems is reduced as compared to one of open storage, mainly because the working fluid (water vapor) is the part of the storage system as it has to be stored as well.[13]The volume of the heat exchanger as well as the necessity to arrange a large quantity of solid in thin layers (for improving heat and mass transfers) also lower the energy density when calculated for the entire system compared to the energy density of the material. This is not a problem for high frequency heat pumping applications for which the required quantity of solid is low. It is a major bottleneck for a long term energy storage.

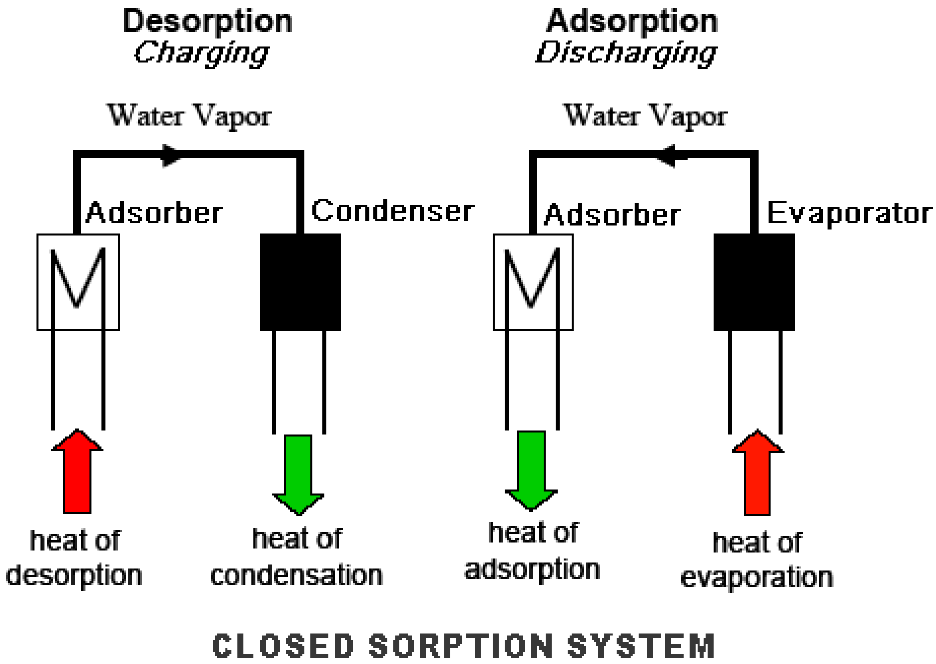

Figure 4. Operation principle of closed thermochemical TES[8]

In an open storage system sorption components are exposed to the atmosphere. An open sorption system includes a working fluid, a carrier gas and a thermochemical storage material (TCM) (Figure 5).[13] As gaseous working fluid and carrier gas of open system is directly released to the environment and operates at atmospheric pressure, thus, normally only water is a possible candidate as the working fluid and air as carrier gas.[6] TCMs of open systems need to be non-toxic and non-flammable.

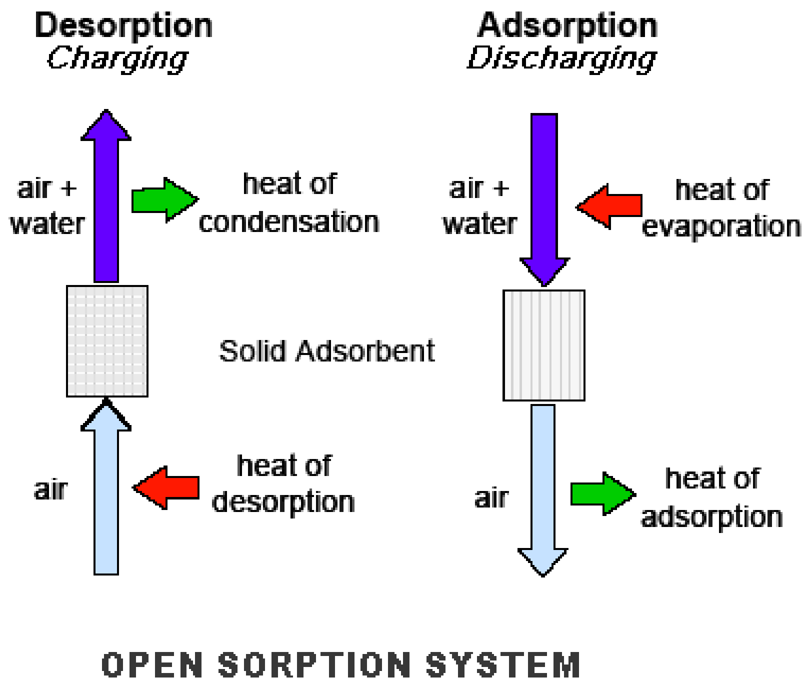

Figure 5. Operation principle of open thermochemical TES[8]

The basic steps are mentioned below:

1) Charging process (desorption, summer period): heat from a high temperature source (solar thermal collectors) is used to heat the air (carrier gas) which is subsequently injected to through the storage material resulting in a desorption process. Water vapor in the saturated warm air may be condensed at a medium temperature level (if there is a medium temperature heat demand) or humid air may just be expulsed outside.
2) Storage: The storage material is not supplied by air so that no transfer of water vapor from or to the material is possible.
3) Discharging process (adsorption, winter period): air (that may be exhaust air from the ventilation system) is injected in the adsorption column. At the outlet of column we obtain dry warm air due to the useful heat release. It may be used for heating the fresh air of the ventilation system. If the air at the column inlet is too dry, water may be injected and evaporated prior to the air admission into the column.

As for closed system this process (succession of steps 1 to 3) may also be imagined for heat pumping with some adaptation.

Using an open system may have the advantage of not requiring the storage of water in liquid state (use of natural humidity of air).

5. Thermochemical storage materials (TCMs): towards application

TCMs are the most capable materials in terms of energy storage densities compared to other thermal storage materials. Some of them may even offer storage density close to the properties of biomass[14], thus owing to high energy density thermochemical TES systems can provide more compact ES relative to latent and sensible TES (Figure 6) thus making possible their use for long term storage applications.[15]

Energy density of thermochemical storage is in range of 200-500 kWh·m^{-3}, and negligible heat losses between the storage period and the recovery period because the energy is stored as chemical potential, and the sensible heat of the elements is weak. Therefore, this kind of storage is relevant for seasonal storage for house heating.[16] As a matter of comparison, the energy density of latent storage is about 120 kWh·m^{-3} and the energy density of sensible water is about 54 kWh·m^{-3} (for a ΔT of 70 °C and heat losses of 25%).

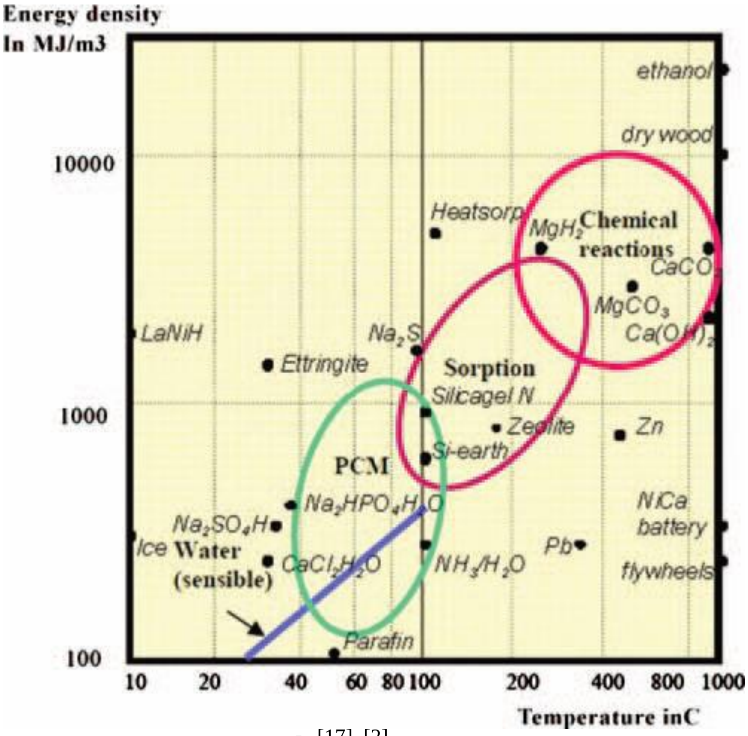

Figure 6. Different energy storage materials[17], [2]

Resent research data provides a wide range of TCMs and the some of them have already been investigated in real storage prototype systems. Working pairs for thermochemical storage systems can be classified by the nature of interaction as chemical sorption materials, physical sorption materials and emerging composite materials which may possess combination of both effects. The advantage of chemical sorption materials is the highest energy density (Figure 6), while physical sorption materials (adsorbents) have much more fast kinetics of adsorption cycle. At the moment the research in field of energy storage materials is particularly focused on recently investigated composites that can be considered as optimal sorbents due to numerous advantages that would be discussed below.

When considering appropriate TCM it is important to follow up the main criterion corresponding to the application domain. Further, we will consider in detail the requirements for TCM towards heat reallocation (heat storage and heat transformation) in case of use of solar energy source as well as each class of TCM materials with literature examples.

5.1. Requirements for TCM

The concept of heat reallocation requires hydrothermally stable materials with numerous parameters that we need to take into account. The main of them are mentioned below:

- energy storage density (energy storage capacity and packing density of material)
- regeneration temperature
- correlation between operating conditions and water sorption behavior of material

- kinetics
- hydrothermal multi-cycle behavior (stability over large numbers of cycles)
- corrosiveness
- cost
- toxicity and safety

Correlation between operating conditions and water sorption behavior of material means that depending on the operating conditions given by the application (desired evaporation and condensation temperatures, and available regeneration temperature), adsorption-desorption must take place at appropriate relative pressures p/p_0 in order to maximize the *cycle loading lift*.

The regeneration temperature range depends on the source of renewable energy and on the technology that is used for converting it into heat. In case of solar energy source/use of solar collector, temperature varies in the range of 80-100°C in summer period depending on type of solar collectors (for north western european country climate conditions).

All these criteria concern heat reallocation domain, however energy storage density is most important figure of merit for heat storage application, while kinetics has tremendous sense in heat transformation.

Energy density is a function of 3 parameters such as differential heat of adsorption (or heat of reaction), *cycle loading lift* and packing density of the material. The value of energy density of thermochemical storage materials typically varies in the range of 200-500 kWh/m^3. Besides, we need to keep in mind that energy density is always evaluated in the context of cycle boundary condition and design of energy storage device. For example, the increase of desorption temperature from 80°C to 100°C will provide the increase of cycle loading lift (for several materials) and, thus energy density. The packing density, which is important when considering of energy volume output, also could be optimized. It depends not only on crystallographic density, but also on particle size and shaping treatment. Thus, packing density could be increased by size-controlled synthesis or by shaping of material yielding enhance of energy density. Generally, energy density value is presented in bibliography in kWh/m^3, but there is also significant number of literature examples where it is presented in kWh/kg, that is more convenient in terms of further calculation of material price. This characteristic known from some literature source as energy density per unit of mass in kWh/kg will be denoted *energy storage capacity* in this manuscript. High *energy storage capacity* required high *cycle loading lift* and high differential heat of adsorption (or heat of reaction).

The question of optimal adsorbent for heat transformation can be considered using an Arrhenius diagram where the cycle is defined by the highest desorption temperature (driving temperature, point D), the minimum adsorption temperature (point B), and the condenser and evaporator pressure (Figure 7). The cycling loading lift can be presented by the difference between the richest and the weakest isostere of the cycle. Two pairs of temperature and pressure can characterize each isostere, namely, (T_B, P_e) and (T_C, P_c) in case of rich isostere (green) and (T_D, P_c) and (T_A, P_e) in case of week isostere (red). The promising adsorbent should exchange large amount of adsorbate under cycle conditions and thus, should have enhanced difference between the richest and the weakest isostere of the cycle.

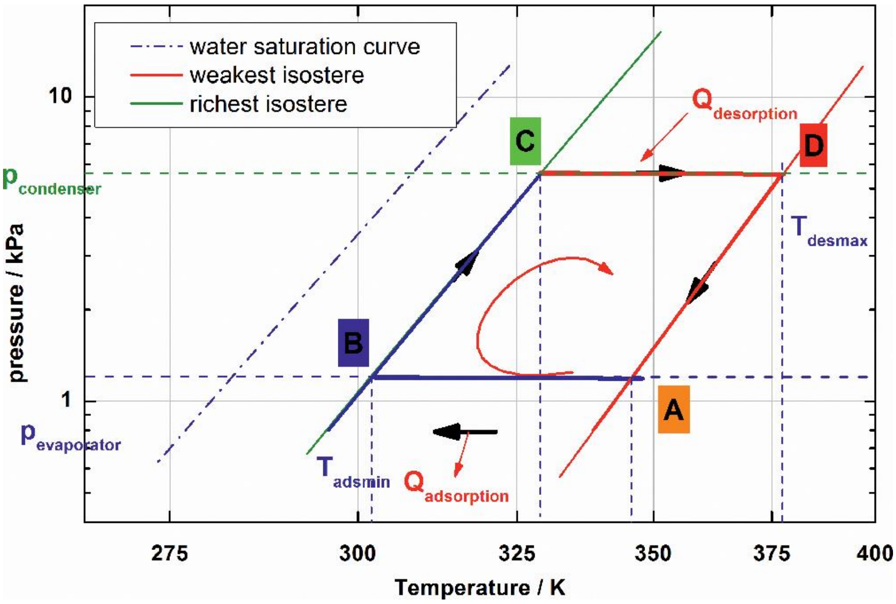

Figure 7. The van 't Hoff diagram of the ideal cycle.[18]

As mentioned above, highest desorption temperature in case of solar collector use, can reach 80-100°C. The minimum adsorption temperature is 30°C in case of space heating application, which is the minimum temperature required for space heating at winter period. The selection of the two pressure levels depends on application domain (heat transfer or seasonal heat storage) and reactor design (open or closed system). The water pressure in reactor is related to the air water content when using an open reactor, or to the evaporating or condensing temperature when using a closed reactor. For the space heating application in case of open reactor humid air (from the ventilation system) can reach RH of 50% at T=30°C.

For the space heating application in case of closed system typically boundary temperatures vary in the range of 5-10°C for T_e and 10°-15°C for T_c. For example, in present thesis we selected closed system for space heating with T_c=T_e where ground plays the role of low temperature source for evaporation and condensation (T_e=T_c=10°C that corresponds to saturated water pressure of p=12.5 mbar).

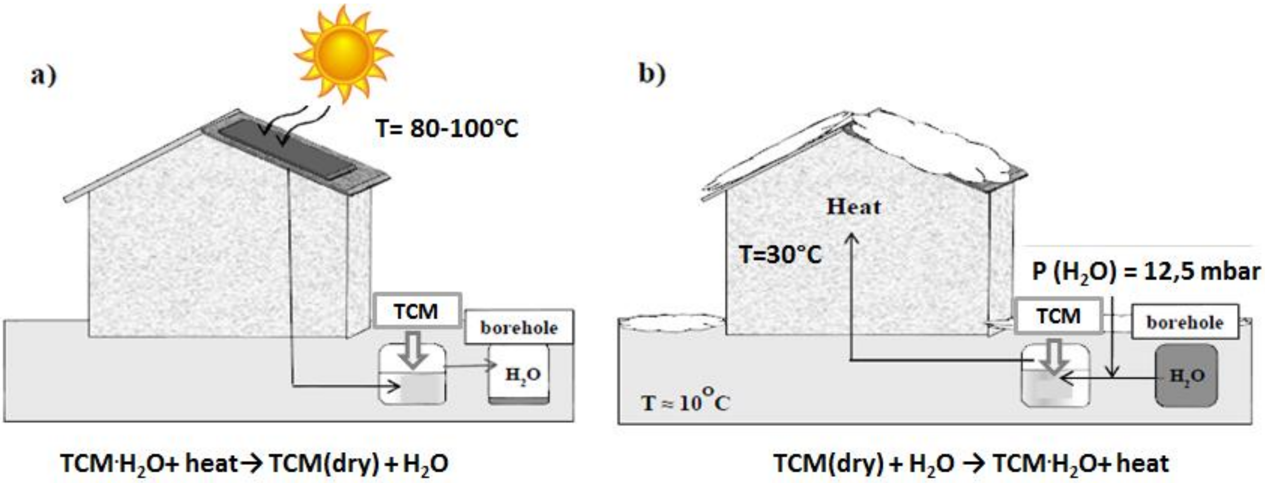

Figure 8. Representation of the practical conditions of the (a) energy charging and (b) energy discharging steps taking place in the seasonal heat storage system based on the water vapor sorption process in salt hydrates

The position of the adsorption step has to correlate with the cycle boundary temperatures of evaporation (T_e) because adsorption occurs at pressure corresponding to the temperature of evaporation. The desorption steps occurs at pressure corresponding to the temperature of condensation. Taking into account operating condition of cycle we can estimate the relative pressure region where adsorption has to exchange the maximum of sorption capacity. Generally, the most promising materials for heat storage application has high adsorption loading lift at p/p_0 below 0.3 and can be regenerated at relative pressure above 0.02.[19] The material which adsorbs water at p/p_o =0.30-0.45 requires the increase of evaporation temperature that requires a high temperature cold source/sink. Such sources are not naturally available and require the use of energy to be artificially created.

Summarizing, water sorption behavior of optimal adsorbent should correspond to selected cycle conditions (desired evaporation and condensation temperatures in case of closed system, and humidity in case of open system and available regeneration temperature). However, if limited flexibility in choice of cycle condition allows significant enhance of *cycling loading lift*, than this choice can be adapted according to sorption behavior of material in order to increase the efficiency. For example, in some cases energy expanses for enhancing p/p_o region or regeneration temperature could be compensated by impetuous increase of energy efficiency of material (condition of maximal *cycling loading lift*).

5.2. Chemical reaction

Generally, TCMs based on phenomenon of chemical reaction provide higher storage energy density compared to physical adsorbents, but kinetics of the process is slower. The first investigation of working pairs referred in 1990 provides several examples as ammoniate/ammonia, halogenated inorganic reactant/water materials and CaO/H_2O.[20] There are a huge number of possible reactions. For example, in 2009, Kato *et al.* investigated on medium temperature chemical heat storage materials with metal hydroxides.[21] In this part we will only consider the reactions of hydration of inorganic salt.

As mentioned above, it is important to consider the reaction in the context of temperature range required for each application. In order to follow application standards of solar thermochemical energy storage we will focus on the reactions in temperature range below 120°C, taking into account ideal regeneration temperature of 80-100°C and above 30°C taking into account the necessity to produce heat at suitable temperature for space heating. The determinative parameters are the energy density, the temperature of reaction at given pressures in accordance with the application.

Visscher *et al*. evaluated a group of salt hydrates as suitable TCM. The results suggested to use epsom (**$MgSO_4 \cdot 7H_2O$**) for such ES applications.[22],[23] The experimental evaluation of epsom capability as promising material for thermochemical ES is performed by Van Essen *et al.*[24], Posern and Kaps[25], Stach *et al.*[26] and is in good agreement. This salt presents numerous equilibriums as (7/0), (1/0), (7/1), (7/6), (6/0) according to Van de Voort *et al.*[27] The major advantage of this material is high energy density of 780 kWh/m^3. The significant drawback of this material apart from corrosiveness is that it cannot release totally all the stored heat under practical conditions.[28],[29] In addition, Hongois *S, et al.* showed that the pure magnesium sulphate is quite difficult to use practically because of its low power density.[30]

Magnesium chloride hydrates **$MgCl_2/H_2O$** was studied by Van Essen *et al.* and Opel *et al.*[28,31] The equilibria are indicated as follow: (6/4), (4/2), (2/1) . The best energy density of 574 kWh/m^3 was obtained for the reaction corresponding to transition 6→1. The major drawback of this material is the formation of HCl due to thermic decomposition of **$MgCl_2·6H_2O$** at 115°C. [28,31] In addition the low stability under numerous adsorption-desorption cycles was observed that proves the degradation of structure (Figure 9).[31]

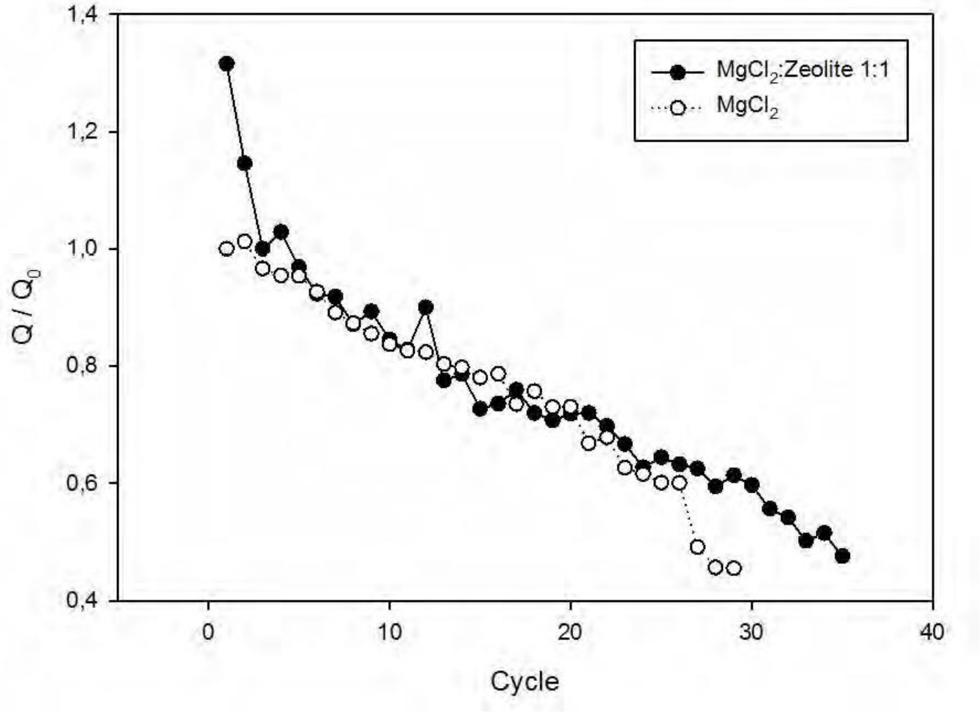

Figure 9. Decrease in reactivity of $MgCl_2$*6H2O and a zeolite composite, respectively, during subsequent hydration/dehydration cycles. The amount of heat released during hydration of the sample was measured.[31]

Another possible working pair is copper sulfate with water **$CuSO_4/H_2O$**. According to bibliography data this salt presents two equilibriums such as (5/3) and (3/1).[29,32] **$CuSO_4·5H_2O$** provides significantly high energy density of 574 kWh/m^3. The crystallographic analysis in-situ during dehydration was performed by Bertsch *et al.*[32] Copper sulfate changes color during the reaction that allows to visualize the reaction process. However, it has been shown that temperature standard required for heating in winter period could not be reached using this working pair.[32]

The hydration reaction of **$LiSO_4$** was also considered by Ferchaud 2012.[29] The X-ray analysis explains the mechanism of performance decrease on a long-term period. Another significant drawback of this salt is its quite low energy density of 197 kWh/m^3. This value is relatively low for chemical sorption materials.

Working pair based on aluminum sulfate **$Al_2(SO_4)_3/H_2O$** was also studied by Van Essen *et al.*[33] The energy density of this salt is 600 kWh/m^3.[33] However, it has been shown that temperature standard required for heating in winter period could not be reached using this working pair as in case **$CuSO_4$**.[33]

Sodium sulfide hydrates **Na_2S/H_2O** were studied by the Energy research Center of Netherlands (ECN). This salt presents three equilibriums such as (9/5), (5/2) and (2/0).[34] Sodium sulfide nonahydrate or pentahydrate gives a high thermal power density combined with a high energy storage density.[35] Even tough interesting energy density (Table 1), this material is undesirable for real application due to high toxicity. In addition Boer *et al.* revealed sodium sulfide is very corrosive.[35]

One the most efficient inorganic salt is $SrBr_2$. Abedin and Rosen[36] investigated a closed thermochemical TES using strontium bromide (**$SrBr_2 \cdot 6H2O$**) as the reactant and water as the working fluid. In 2006, Lahmidi *et al.* simulated a sorption process based on the use of strontium bromide, which is adapted to solar thermal systems.[37] The laboratory PROMES performed several studies in order to find the optimal inorganic salt for heat storage. The results allow standing out this material against other candidates owing to position of equilibrium step and high energy density (630 kWh/m^3).

$CaCl_2$ was also considered in the bibliography as interesting candidate owing to its low price.[37] It has been shown by van Essen *et al.* that temperature increase related to reaction of hydration corresponded completely to the temperature standard of heating for winter period.[33] However, after dehydration step material presented the kind of gel that was probably due to fusion temperature achievement. The equilibrium p-T curves of this salt are presented in Figure 10.[38,39]

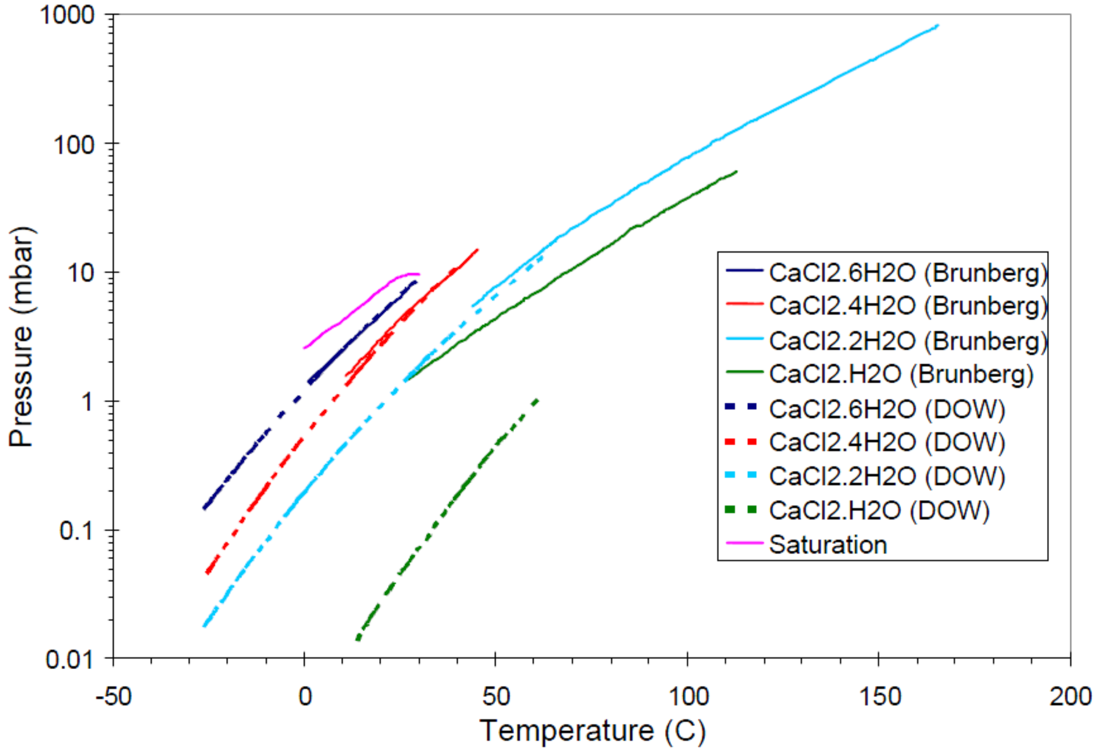

Figure 10. P-T curves of $CaCl_2$.[38–41]

According to equilibrium curves we can conclude that hydration temperature is suitable for heat providing purposes and dehydration temperature can be easily archived using vacuum tube solar collectors.

In 2010, Balasubramanian *et al.* estimated this capability via a mathematical model, which can help identify optimal materials for thermochemical storage within practical constraints.[42]

Foivos Epameinondas Marias in PhD thesis considered numerous examples of recently identified promising chemical storage materials underling the enthalpy and the entropy of reaction as well as energy density and temperature of sorption as determinative physic-chemical constants.[41] We will provide several examples considered by Foivos Epameinondas Marias, however focusing only on reaction of inorganic salt with water as working fluid corresponding to equation $A + \nu H_2O \leftrightarrow C + \Delta H_r$. The Table 2 includes the values of energy density, regeneration temperature, the enthalpy and the entropy of reaction, which are important factors for material selection. The enthalpy and the entropy determine the equilibrium curve p-T and the enthalpy affects the value of energy density.

Table 1. Examples of chemical sorption materials as TCM [41]

C	A	νH_2O	Energy density of material (kWh/m^3)^a	T_{eq} at 2500 Pa (°C)^b	T_{eq} at 1200 Pa (°C)^c	ΔH_r (J/mol $_{H2O}$)	ΔS_r (J/mol $_{H2O}\cdot K$)	References	Experimental(E) or theoretical (T) data
$MgSO_4\cdot 7H_2O$	$MgSO_4$	7 H_2O	780	110,3	108,2	411000	1041	[42][27][24][29][43]	E and T
$MgSO_4\cdot 7H_2O$	$MgSO_4\cdot 1H_2O$	6 H_2O	640	93	90,5	336000	887	[27][24][29][43]	E and T
$MgSO_4\cdot H_2O$	$MgSO_4$	1 H_2O	284	15,1	6,2	55000	160	[27][24][29][43]	E and T
$MgSO_4\cdot 7H_2O$	$MgSO_4\cdot 6H_2O$	1 H_2O	108	33,6	24,5	58070	-	[27][24][29][43]	E and T
$MgSO_4\cdot 6H_2O$	$MgSO_4\cdot H_2O$	5 H_2O	508	42,9	32,5	249880	-	[27][24][29][43]	E and T
$CaSO_4\cdot 2H_2O$	$CaSO_4$	2 H_2O	390	54,2	48,1	105000	290	[23][44][27][43]	T
$CuSO_4\cdot 5H_2O$	$CuSO_4\cdot 3H_2O$	2 H_2O	225	34,1	26,9	89070	-	[32][29][43] [44]	E and T
$CuSO_4\cdot 3H_2O$	$CuSO_4\cdot H_2O$	2 H_2O	331	38,5	31,1	89440	-	[32][29][43] [44]	E and T
$CuSO_4\cdot 5H_2O$	$CuSO_4\cdot H_2O$	4 H_2O	574	-	-	-		[32][29][43] [44]	E and T
$CaCl_2\cdot 2H_2O$	$CaCl_2\cdot H_2O$	1 H_2O	167	75,6	60,5	47000	104	[38][39] [45] [33][43]	E and T
$CaCl_2\cdot 2H_2O$	$CaCl_2$	2 H_2O	400	-	-	-	-	[38] [39] [40] [33][43]	E and T
$CaCl_2\cdot 1H_2O$	$CaCl_2$	1 H_2O	211	-	-	-	-	this manuscript	
$CaCl_2\cdot 2H_2O$	$CaCl_2$	2 H_2O	317	-	-	-	-	this manuscript	
$CaCl_2\cdot 4H_2O$	$CaCl_2$	4 H_2O	519	-	-	-	-	this manuscript	
$CaCl_2\cdot 6H_2O$	$CaCl_2$	6 H_2O	610	-	-	-	-	this manuscript	
$Al_2(SO_4)_3\cdot 18H_2O$	$Al_2(SO_4)_3\cdot 5H_2O$	13 H_2O	600	-	-	-	-	[44] [33] [45][43]	E and T
$MgCl_2\cdot 6H_2O$	$MgCl_2\cdot H_2O$	5 H_2O	590	-	-	-	-	[29] [44][43]	E and T
$MgCl_2\cdot 6H_2O$	$MgCl_2\cdot 4H_2O$	2 H_2O	219	70	61	102610	-	[44] [29] [43]	E and T
$MgCl_2\cdot 4H_2O$	$MgCl_2\cdot 2H_2O$	2 H_2O	306	109	96	117410	-	[44] [29] [43]	E and T
$MgCl_2\cdot 2H_2O$	$MgCl_2\cdot H_2O$	1 H_2O	-	131	117	-	-	[44] [29][43]	E and T
$LiSO_4\cdot H_2O$	$LiSO_4$	1 H_2O	197	-	-	41010	-	[29][43]	E

$SrBr_2\cdot 6H2O$	$SrBr_2\cdot H_2O$	$5\ H_2O$	630	54,4	45	67400	175	[6,37,46]	E
$Na_2S\cdot 9H_2O$	$Na_2S\cdot 5H_2O$	$4\ H_2O$	336	36,7	26,5	55400	148	[34,35,43,47,48]	E
$Na_2S\cdot 5H_2O$	$Na_2S\cdot 2H_2O$	$3\ H_2O$	493	77,3	65,8	63000	149	[34][43] [47]	E
$Na_2S\cdot 2H_2O$	Na_2S	$2\ H_2O$	98[d]	83	72,8	74000	177	[34][43] [47]	E
$Na_2S\cdot 9H_2O$	Na_2S	$9\ H_2O$	921	-	-	-	-	[34][43][47]	E
$KAl(SO_4)_2\cdot 12H_2O$	$KAl(SO_4)_2\cdot 3H_2O$	$9\ H_2O$	410	41,3	28,2	44237	110	[49][50]	E
$NH_4Al(SO_4)_2\cdot 12H_2O$	$NH_4Al(SO_4)_2$	$12\ H_2O$	560	44,4	31,6	46268	115	[51][52] [50][49]	E
$Na_2SiO_3\cdot 5H_2O$	Na_2SiO_3	$5\ H_2O$	445	49,8	36,3	45020	109	[50]	E
$NiSO_4\cdot 3H_2O$	$NiSO_4$	$3\ H_2O$	385	57,9	43,5	44408	103	[50]	E
$MgSO_4\cdot 6H_2O$	$MgSO_4\cdot H_2O$	$5\ H_2O$	435	51,1	38,2	48043	117	[50]	E

[a] Energy density of material in hydrated state (after reaction)

[b] corresponds to the temperature of condensation of 21°C

[c] corresponds to the temperature of condensation of 10°C

[d] Energy density of material in anhydrous state (before reaction)

5.3. Physical sorption

Physical sorption materials correspond to phenomena of adsorption. Recently several appropriate porous materials such as aluminophosphates (AlPOs), silica-aluminophosphates (SAPOs) and metal–organic frameworks (MOFs) have been investigated to match the demands of heat transformation processes.

5.3.1. Silica gel and zeolites

The present generation of adsorption chillers mostly employ as TCM silica gels synthesized either by polymerization of silicic acid, $Si(OH_4)$, or aggregation of colloidal silica particles. The disadvantage of this adsorbent is that most of the water adsorption occurs at high relative pressures and thus, the working fluid exchange over the cycle is only a small part of the total working capacity. There were numerous research aiming to improve silica gels features towards applications[53–55] with various modifications such as increase in amount of silanol groups on the surface or reducing the pore sizes that results in development of silica gels with enhanced water adsorption at low pressure.[54] This silica gel has very small pores (microporous silica) and contains trace impurities like aluminium or other metals.[56] Despite on this optimization, all the known silica gels present only 0.03-0.1 g/g of cycling loading lift within typical AHT cycle.[57]

On the contrary, zeolitic adsorbents are hydrophilic and they offer a large sorption uptake at quite low relative pressure region due to high affinity to water. Zeolites X and Y present the faujasite (FAU) crystal structure type. These synthetic zeolites are the most commonly used for adsorptive heat pumping and cooling cycles since the 1980's.[58,59] But the most critical point of these adsorbents is low fluid exchange within the cycle due to their strong hydrophilicity. In order to completely regenerate it during desorption high temperature above 140 °C is required[60]. Several modifications were applied to reduce the required desorption temperatures, for example ion exchange or de-alumination. In addition, the fabrication of materials without the use of any adhesive was investigated to reduce the inactive parts of, e.g., shaped materials. [59–61]

5.3.2. AlPO and SAPO

Zeolite-like crystalline aluminophosphates (AlPO) and silicaaluminophosphates (SAPO) are suggested to overcome the aforementioned problems of the classical adsorbents.[61] The most promising examples are AlPO-5, AlPO-17, AlPO-18 and APO-TRIC.[16,62–64] These materials consist of alternating AlO_4 and PO_4 tetrahedra. They demonstrate the optimal hydrophilic-hydrophobic balance providing s-shape adsorption isotherms.[65] Adsorption capacity of this materials is higher in comparison with zeolites and AlPO allow low desorption temperature (60-90°C) that makes them very attractive for solar energy storage.

The AlO_4 framework is more flexible than that of the zeolites and therefore their structure and thus sorption properties can be modulated by isomorphous substitution of metal atoms in the framework or P sites.[66,67] The most famous class of substituted AlPO is silica-aluminophosphates (SAPO) (Si inserted of P). Although the AlPO, framework is neutral, substitution of silicon at the phosphorus site leads to the negative charged framework and creation of Bronsted acids sites. Due to this polarity increase silica-aluminophosphates, SAPOs, are generally more hydrophilic than AlPOs. For example, SAPO-34, demonstrates an s-shaped isotherm with the steep increase shifted towards lower p/p_0. Majority of AlPOs and SAPOs show the excellent suitability of for heat reallocation. Due to the templated syntheses, these materials are unfortunately expensive, and thus, their application potential remains limited.

5.3.3. MOFs

Metal–organic frameworks (MOFs) are crystalline, three-dimensional porous hybrid networks that build from metal nodes coordinated by organic ligands. This class of porous materials was widely investigated for the range of applications based on adsorption processes. The potential of MOFs for heat reallocation systems would be discussed in details in Chapter 2.

5.4. Composites: inorganic salt in porous matrix

Nowadays one of the most efficient class of materials for heat storage is composites, which includes inorganic salt incorporated in a porous matrix (silica gel, activated carbon). This new generation of heat storage materials has been reported in 1996.[68–70] The objectives of such incorporation are optimization of thermal transfer parameters and/or mass transfer (thermal conductivity, surface of reaction) and also stability under numerous cycles. The matrix could be neutral or active part of composite in terms of interaction with adsorbent. That means that matrix may contribute to energy storage process or not. Composite material with active matrix provide a combination of chemical (inorganic salt) and physical sorption (matrix) that allows the final material to overcome the disadvantages of an individual component such as low energy output of physical sorption materials and slow kinetics in case of pure chemical reaction. Thus, this approach enhances energy density of physical sorption materials and mass transfer of chemical sorbents and also durability of material.

Composites enable to modify (or even tailor) their sorption properties by varying chemical nature of the confined salt, its particle size inside the matrix pores, amount of the confined salt.[43] It has been shown that regeneration temperature of composite material is lower than in case of pure salt.[21]. Aristov *et al.* studied water sorption behavior of composites with different pore size such as 8.5 nm ($CaCl_2$/SBA), 11.8 nm ($CaCl_2$/SBA) and 15 nm (SWS-1L). It was established that the hydration pressure was certainly lower in smaller pores, however the desorption temperature is higher due to stronger bonding.[23,24]

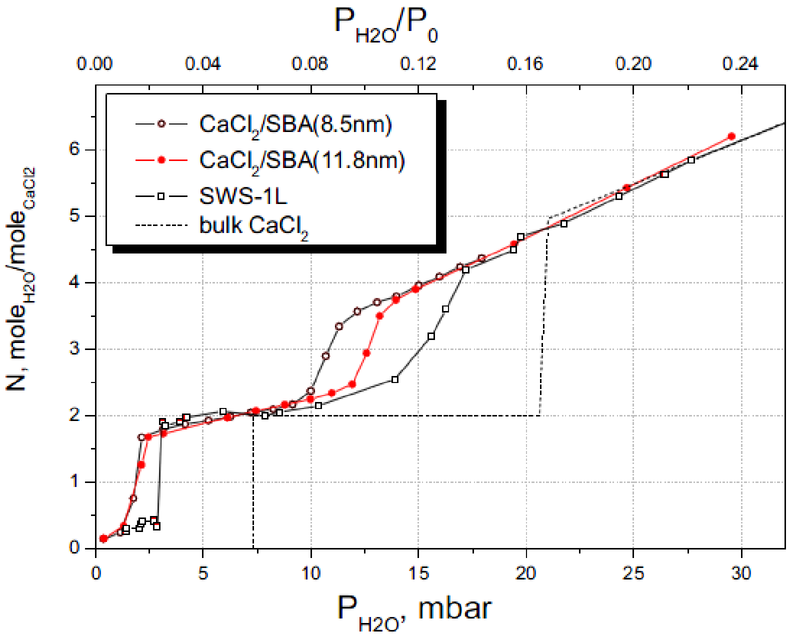

Figure 11. The isotherms of vapor sorption by the new composite $CaCl_2$/SBA with various pore size, SWS-1L and bulk $CaCl_2$. T=50°C. [18]

Thus, hydration temperature of the confined salt can be tuned in the low relative pressure region (up to 0.3), because it appears to depend on the pore size of the host matrix with uniform pore dimension. Another interesting tool for tailoring sorption properties of material is using binary salt systems such as LiCl/LiBr, $CaCl_2/CaBr_2$, $BaCl_2/BaBr_2$.[75]

Summarizing, this concept may completely modify the behavior of individual component affecting kinetics, packing density, stability and allow governing water sorption properties and regeneration temperature of final material.

In Solar World Congress (2011, Kassel, Germany) *Kerskes et al.* provided an overview of some storage materials for solar thermal application (Figure 12).[76] The charging step was performed at 20°C and water pressure of 20 mbar while the regeneration step was done at 120°C ($MgCl_2$), 150°C ($CaCl_2$) or 180°C (zeolite and $MgSO_4$) respectively. In the case of water energy storage density refers to a temperature deference of ΔT=50 K. The measurements were performed in Institute for Thermodynamics and Thermal Engineering (ITW) as well as by Hongois (2010, “EDF”)[77], and magnesium chloride on a passive matrix measured by Zondag (2010, “ECN”)[78]. As can be seen from Figure 12 composite materials such as zeolite + 7.5% $MgSO_4$, zeolite + 10% $MgSO_4$, bentonite + 41.7% $CaCl_2$ and $MgCl_2$ on supporting material provide high energy density in range 170-250 kWh/m^3.

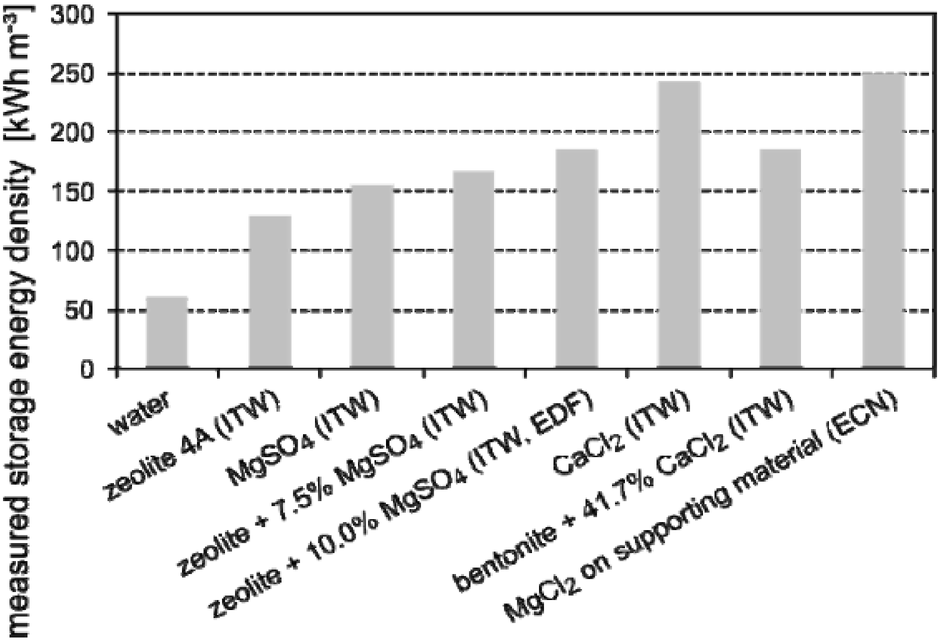

Figure 12. Overview of experimentally measured storage energy densities of selected materials for thermochemical energy storage.[76]

Herein, we will provide several examples of composites materials reported from 1992 till present time (Table 2).

Table 2. Examples of composite materials as TCM

Matrix	Salt	Supplementary data	Reference
GNE	$SrBr_2$	Different amount of salt	[79]
Graphite	Na_2S	Test in Prototype MCES	[48]
Copper, graphite, sand	$MgCl_2$	More than 30 cycles	[31]
Attapulgite	Mixture $MgSO_4$/$MgCl_2$ Mixture $MgSO_4$/LiCl	Salt mixtures with different ratio	[25]
Bentonite	$CaCl_2$	41.7% wt. of salt Energy density: 163 kWh/m^3	[80]
Zeolite 13X	$MgSO_4$	200g of material 15% wt. of salt Energy density: 166 kWh/m^3 3 cycles	[30,77]
Zeolite 4A	$MgSO_4$	10% wt. of salt Energy density: 178 kWh/m^3 (while 125 kWh/m^3 of pure zeolite)	[80]
Zeolites	$MgSO_4$	5-15% wt. of salt Correlation between reaction enthalpy and pore size of zeolite	[81]
Zeolite A	$MgCl_2$	More than 30 cycles	[31]
Different zeolites	$MgCl_2$	Highest energy density: 235	[82,83]

	$CaCl_2$	kWh/m^3	
Silica gel	$CaCl_2$	Variation of salt content	[68,69]
Silica gel with uniform size	$CaCl_2$	Variation of pore size of the matrix	[84,85]
Silica gel	$CaCl_2$ Na_2SO_4 $MgSO_4$ $CuSO_4$	Influence of synthesis procedure on sorption properties of composites	[86]
Silica gel	LiCl/LiBr, $CaCl_2/CaBr_2$, $BaCl_2/BaBr_2$	binary salt systems	[75]
Zeolite 13X	$CaCl_2$	10-46% wt. of salt	[87]
Iron silicate	$CaCl_2$	20 cycles	[88]
APO-Tric SAPO-34 AlPO-18	$CaCl_2$	50 cycles	[64]
Zeolite	$CaCl_2$	Maximal power of 0,6 kW/kg	[89]
Two types of zeolite	$CaCl_2$	Test in 3 prototypes	[90]

Chapter I: Metal Organic Framework towards heat reallocation

1. Introduction

The combination of the key-parameters such as adsorption capacity, position of adsorption step (p/p_0), easy and low energy demanding regeneration and stability towards water plays the main role in a view of selecting the best materials for heat storage and transfer systems as mentioned in Chapter I. Resent research in the field of heat reallocation have considered Metal Organic Frameworks (MOFs) as promising physical sorption materials.

Metal Organic Frameworks[91–93] also denoted hybrid porous solids are a one of the latest class of ordered porous solids with suitable features in terms of chemical and structural diversity together with their regular and tunable large accessible porosity. In comparison with other porous solids, MOFs display a higher degree of versatility that makes it possible to tune almost 'on-demand' their amphiphilic character, pore size, shape, etc. Therefore, one advantage for MOFs lies in the possibility to tune their sorption behavior in terms of sorption capacity as well as position of the adsorption step (p/p_0). The water uptake of several MOFs easily outperforms that of any inorganic porous material such as silica gel, zeolites, or SAPO/AlPO.[94] An illustration of the high potential of MOFs for heat transformation application is presented on the Figure 13.

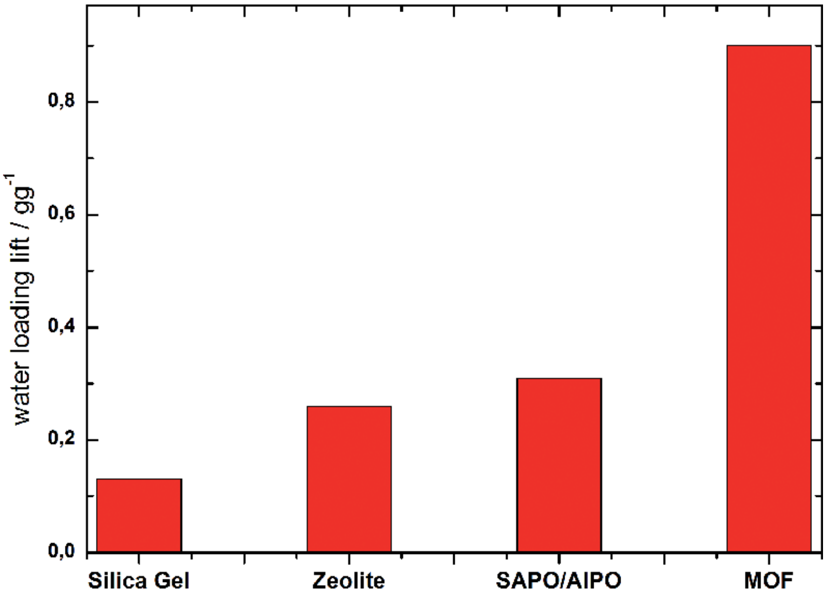

Figure 13. Illustration of the possible water loading lift for different material classes within a typical heat transformation cycle[94]

Apart from the tuning of adsorption loading lift and position of adsorption step (p/p_0) MOFs require relatively low energetic regeneration. Hydrothermal stability of hybrid porous solids is however one the most critical issue that restricts their use in real applications.[95,96] Presently, the available research data from the literature provide a large range of stable MOFs relatively easy to prepare and scale-up. In addition, the criteria affecting their hydrothermal stability are known which makes easier the design of new generation of highly stable and efficient hybrid porous materials for such applications.

All these features make them interesting candidates for heat storage and heat transformation based on adsorption method.

In this part of literature review we will consider the adsorption properties and stability aspect of Metal Organic Framework towards heat reallocation application. We will focus on water working fluid heat storage systems, and, thus, will consider only water vapor adsorption in MOFs.

Firstly we will briefly remind general information about MOFs. Secondly, we will consider their classification in terms of stability, the main parameters that drive their chemical stability while considering the stability level required for heat reallocation. In the third part we will provide a set of the most promising MOFs for heat reallocation, based on the existing experimental data including stability tests under numerous adsorption-desorption cycles. For some of them, structure and water sorption behavior will be considered in details.

2. Definition of MOFs and their application domains

Hybrid porous solids also named Metal–Organic Frameworks (MOFs) or Porous Coordination Polymers (PCPs) are the latest class of crystallized porous materials with tunable structures and multifunctional properties.[91–93] These materials combine inorganic and organic moieties resulting 3D networks (**Figure 14**).

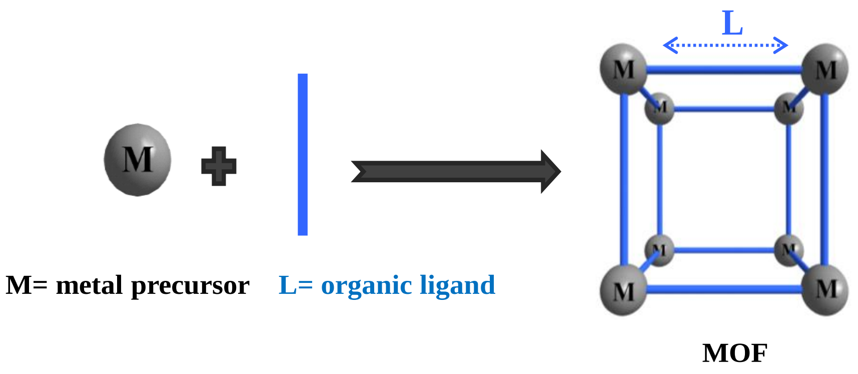

Figure 14. The formation of Metal–Organic Framework

The inorganic moieties also denoted Secondary Building Units (SBU)) can be presented by different examples such as simple polyhedrons, clusters, chains layers or even inorganic 3D arrangements. Several examples of SBU are shown in **Figure 15**.

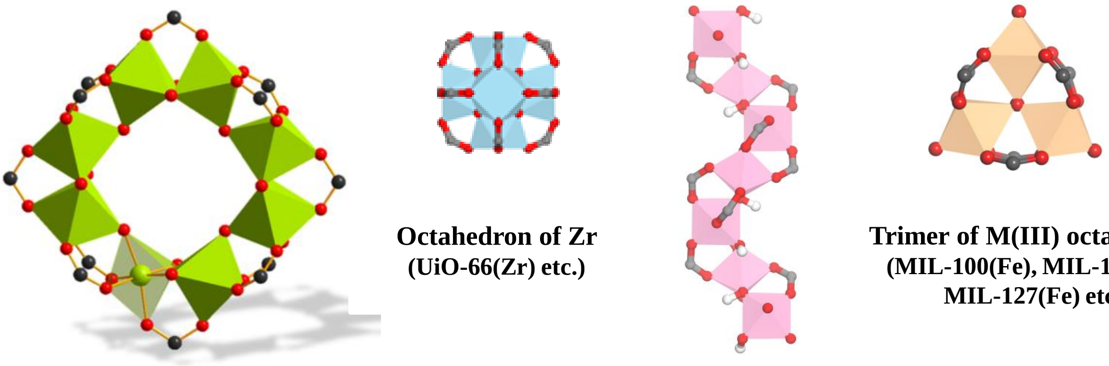

Octamers of Ti octahedrons
(MIL-125(Ti) etc.)

Octahedron of Zr
(UiO-66(Zr) etc.)

Helical chains of cis-connected
Al octahedrons
((MIL-160(Al), CAU-10)

Trimer of M(III) octahedrons
(MIL-100(Fe), MIL-101(Cr),
MIL-127(Fe) etc.)

Figure 15. Examples of Secondary building units of MOFs

SBU are bridged by the organic linkers which are mainly anionic O (polycarboxylates, polyphosphonates) and N (imidazolates, polypyrazolates, polytetrazolates) donors. The pore size of MOFs lies in the micro-meso-pores range. One of the main advantages of hybrid porous solids compared to inorganic crystalline porous materials (zeolites, metallophosphates) is that they can be built from almost any of the cations of the periodic table and considering the huge number of possible organic linkers, this leads to quasi-infinite possibilities of crystal structures and chemical compositions. Thus, their structures and therefore properties can be easily tuned by playing on the nature and coordination of the metal centers and the length and/or the functionalization of the organic linker. Such diversity provides an extremely broad range of tunable pore sizes and specific surface areas.

MOFs have being investigated for numerous potential applications[91,97–100] such as gas storage[101–103] and separation processes, drug delivery[104,105], heterogeneous catalysis[106,107] and recently heat reallocation[18,71,94,108–111]. Firstly the idea to use water sorption capacity of MOFs for heat transformation was suggested by Aristov in 2007.[71] Since 2011 several researches in this domain start to appear.[18,71,94,108–111] However, water stability issues strongly limits the numbers of MOFs potentially interesting for heat reallocation, because many of them are not hydrothermally stable at all or are kinetically stable only because of their hydrophobicity.[95,96] Nowadays recent researches possess a good number of reasonably hydrothermal stable MOFs such as for example MIL-100(Fe or Al), MIL-101(Cr), MIL-127(Fe), UiO-66(Zr) or its -NH_2 analoge, CAU-10, MIL-125(Ti)_NH_2 with good water sorption capacity, which thus can be considered as promising sorbents for heat transformation systems. It is notable that other numerous potentially interesting MOFs with desirable properties (high initial working fluid uptake) cannot be used in water-based heat pump processes due to their lack of multicycle hydrothermal stability.[60] For hydrothermally unstable materials (for example, MIL-53 and HKUST-1) the methanol as working fluid may therefore be used.[112]

3. Water vapor stability and stability under cycle conditions

In this part we will present the most noticeable experimental research in field of water stability of MOFs, consider different levels of water stability depending on application demands and provide the general classification of water stability depending on structural factors that was suggested by Burtch *et al.* in 2014.[113] Additionally, the cyclability of MOFs under operating conditions which also requires for heat transformation will be considered.

3.1. Water stability levels towards application demand

The water stability criterion strongly depends on the requirements for each application. For example, materials for drug delivery or aqueous phase separation required to be stable in aqueous phase. This is an issue since most of the MOFs that show good stability towards air moisture decompose in water. Application based on gas or vapor adsorption (e.g., flue gas treatment, air separation, gas purification) suppose require the stability in the presence of air moisture at different humidity rates under variable temperature conditions, and their practical use requires stability after numerous cycles. For each application type, water stability needs also to be evaluated by different techniques (XRPD, BET, IR analysis, cycling adsorption capacity under numerous cycles). To specify the definition of "water stability" in case of heat transfer application, we shall therefore consider the stability towards humid environment or water vapor stability together this thermal stability, because the regeneration cycle occurs at temperature about 80-100°C, thus, the combination of these two factors defines the required hydrothermal stability. Additionally, material for heat transfer must be stable at least during 40 adsorption-desorption cycles that implies very little change of adsorption capacity during this treatment.

3.2. Classification of water stability: structural factor governing water stability

Numerous factors which affect water stability of MOFs have been studied during the last decade. The most relevant structural parameters are the charge and coordination number of metal cation, redox properties of metal sites, the charge density (i.e. ratio of the charge/ionic radius), ratio of the cation and anion radius, pKa of complexing groups from the ligand, hydrophobicity of framework, the polarizability of ligand and a metal, steric factors etc. Burtch *et al.*[113] systemized all information relative to water stability and suggested the classification of structural factor governing thermodynamic and kinetic water stability. In this part, we will organize the bibliography research according this classification.[113] However, we will consider also speed of metal-ligand substitution reaction and crystal field stabilization energy effect for complexes with transition metal that were missing in the classification of Burtch et *al.*

3.2.1. Thermodynamic factors

The metal-linker connection bond in presence of water possesses the combination of electrophilic character of metal coordination center and nucleophilic character of functional group of linker that could lead to hydrolysis when exposed to water. Stable MOFs means a sufficient stability towards hydrolysis, e.g. stability in aqueous phase. In order to experimentally evaluate this stability one needs to compare the structural properties of material before and after prolonged water exposure performing XRPD and BET surface area analysis.

Among all the parameters controlling the water stability, the most crucial is the nature of the metal–ligand coordinative bond. We thus need to take into account coordination chemistry principles for the metal-linker combination and, thus, the properties of the metal species (the metal oxidation state and ionic radius) and nature of the linker.

The first article which is deals with the hydrothermal stability of MOFs was published by Low *et al.* in 2009.[95] Authors studied the thermal stability of series of MOF in presence of different amount of water steam. It was observed, that on the whole thermal and water steam stability increases with increasing of charge and number of coordination bonds of metal cation, which forms MOF.[95]

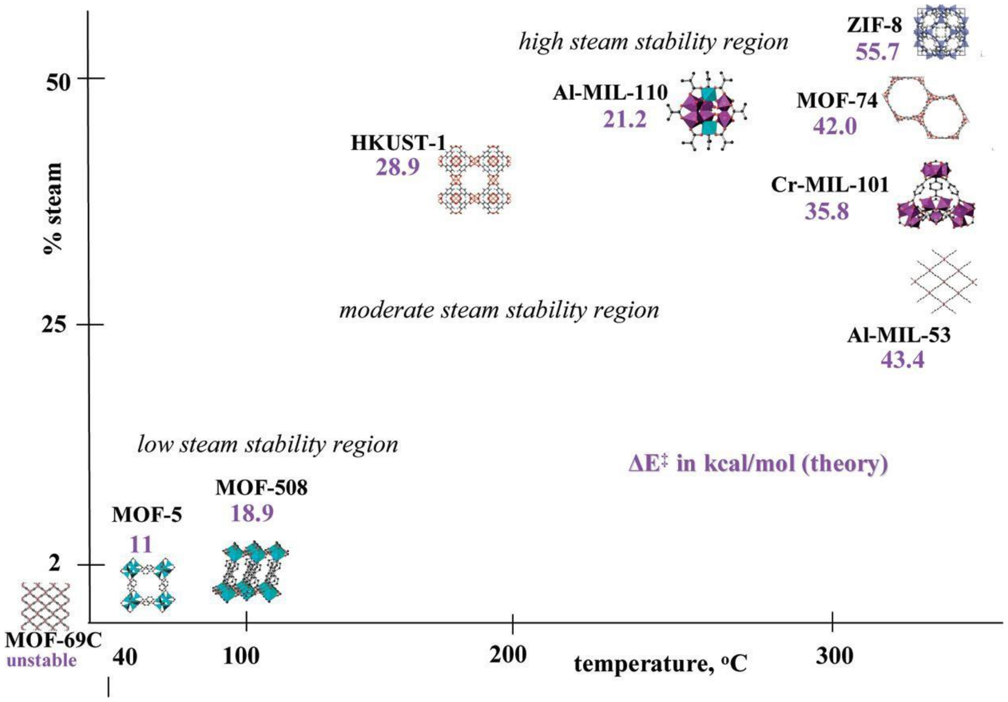

Figure 16. Steam stability map for the four families of PCPs discussed by *Low et al*. The position of the structure for a given MOF represents its maximum structural stability by XRD measurement, while the energy of activation for ligand displacement by a water molecule determined by molecular modelling is represented by the magenta number (in kcal/mol)[95]

Mainly because of the organic part of MOFs construction the long-time thermal metal–ligand framework stability lies typically between 150–250°C and seldom surpasses 300°C. It was proved by numerous independent research groups [108,110,114–121] that MOFs containing the metals of IV group in their highest oxidation state (Ti^{4+}, Zr^{4+} and Hf^{4+}) tend to be the most stable. In the contrary, metal clusters with +2 oxidation state tend to correlate with reduced level of stability. For example, zinc–carboxylate frameworks are generally unstable towards water (e.g. IRMOFs, MOF-5, DUT-4).[95,122] Irving–Williams studied the influence of metal nature on relative stability for the first row transition series bivalent metal ions (Mn < Fe < Co <Ni < Cu > Zn) using a wide variety of ligands.[123]

Moisture stability investigation of the MOF-74 (or CPO-27) series performed by Liu and Kizzie demonstrated, that the frameworks containing metal species that are poorly reducible tend to correlate with stronger stability level[124,125] that makes the reduction potential of the metal an potentially useful prediction factor. Another useful guideline is Pauling's rules which were applied to determine the favored crystal structures of ionic crystals from the ratio of the cation and anion radius.[126]

Lewis acid–base coordination chemistry is a foundation of MOFs assemblage and thus, the pK_a of the coordinating atom on the ligand is the useful characteristic of the metal–ligand bond strength. Initially, Long *et al.* suggested to use this parameter as predictor and applied their strategy in the synthesis of a series of highly stable Co-, Zn-, Ni-, and Cu based MOFs containing the pyrazolate ligand (pK_a 19.8).[127,128] Ligand pK_a can be determined by ligand pKa calculator[129] and thus this metric can rapidly provide the stability approximation of new structures before any synthesis attempt is made.

We need to keep in mind that the isolated properties of the ligand and metal species can serve only for first approximation of chemical stability of the resulting structure. In order to fully understand the metal─ligand bond strength, the combined metal─ligand properties need to be taken into account. The greater similarity between the polarizability of ligand and a metal (as a hard or soft acid and base) resulting in a stronger binding coordination complex is an example of such approach combined metal─ligand properties.[130] Ideally, we also need to consider the factors related to the ease of atomic orbital overlap between the metal and ligand in their specific coordination geometry.

3.2.2. Kinetic factors

While the free energy of a hydrolysis reaction relies on the thermodynamic stability of MOFs, the activation energy barrier governs the kinetic stability. The activation energy of a reaction depends on several parameters such as the product and reactant states, the specific reaction pathway and transition states involved.

It is noteworthy, that notwithstanding thermodynamically instability, in reality the structure could be stable under humid conditions owing to the presence of kinetic factors. The hydrolysis reaction occurs in case of two criterions execution. First, the possibility of interaction between the electron orbitals on the electrophilic metal and nucleophilic water need to be ensured by optimal and close location of water molecule on the metal sites. Second, the energetics of this interaction must be great enough to overcome the activation energy barrier of the reaction. The speed of metal-ligand (L-M) exchange (rate of reaction) is fundamental characteristic of kinetic stability. It depends on many parameters including size of cation, charge density, d-electron configuration, which can lead to crystal field stabilization energy effect (CFSE).

There are supplementary factors that govern kinetic stability and can increase the activation energy for hydrolysis (for example, hydrophobicity of framework and steric protection of metal clusters). In this part, we will provide some example of enhanced moist stability of framework supported by these factors.

The metal complexes L-M are generally divided into kinetically labile or inert, depending on constant of M-L water exchange. Complexes of the first row transition metal ions with the exception of Cr^{3+} and Co^{3+} are generally labile, whereas most of second and third row transition metal ions are inert. **Figure 17** represents the value of water-exchange rate depending on metal cation.[131] Complexes with reaction rate $k(H_2O)<10^{-1}$ are kinetically inert, while with $k\ (H_2O)>10^{-1}$ are kinetically labile.

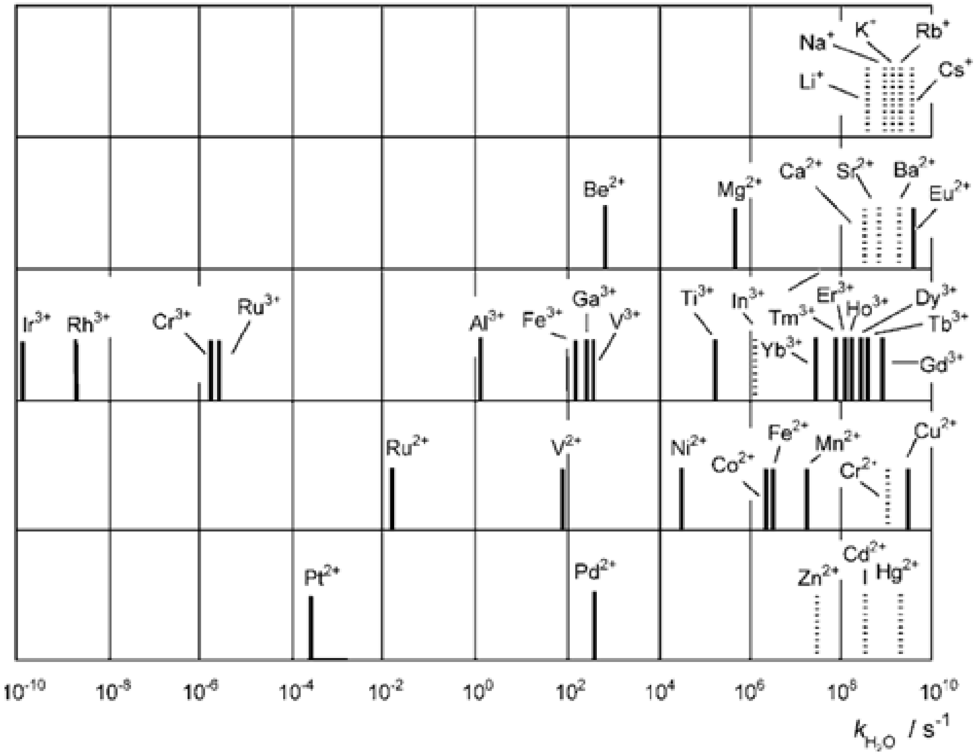

Figure 17. Water-exchange rate constants (k H_2O) in the first coordination sphere of $[M(H_2O)_n]^{m+}$.[131]

If we consider octahedral substitution in case of transition metal complexes, the factors affecting reaction rate are size and charge of metal, and the electronic configuration. It should be taken into account that the crystal field stabilization energy is generated by a set of ligands when placing a transition metal ion in the crystal field. The splitting of d-orbitals into octahedral field (initial state of substitution reaction) and square pyramidal field (transition state of substitution reaction) are different. Thus, if metal ion has electrons on d-orbital, the transition from octahedral to square pyramidal state of complexes can be more complicated and require more activation energy. This is, for example, the case of Cr^{3+} (d^3) where the activation barrier of exchange is enhanced by crystal fiend stabilization energy (CFSE), because the transition between octahedral d^3 complex to square pyramidal is not favorable. Thus, one of the explanations of the enhanced hydrothermal stability of MIL-101(Cr) in comparison with other MOFs is by electron configuration of metal (Cr^{3+} (d^3)).

The hydrophobicity of framework supported by incorporating hydrophobic (for example, perfluorinated or alky) functional groups on the ligand.[132–141] This shielding the metal-ligand bond from water vapor could provide two type of hydrophobicity effects. In the first case, pore hydrophobicity can prevent water from adsorbing into the pores providing super hydrophobic framework as ZIF-8.[137,142] This MOF shows improved hydrothermal stability due to absence of water sorption which is reached by interpenetration or pore blocking.[143,144] The second case is internal hydrophobicity which allows water to be adsorbed into the pores but not clustering around the metal center that prevents hydrolysis.[114,145]

The steric factors around ligands could also allow enhanced stability. For example, interpenetration in Zn-based pillared MOFs provides more water-stable MOFs even when the basicity of the pillar ligand is reduced.[146] The second example is higher stability of UiO-66 compared to UiO-67.[147] It has been suggested that UiO-67 with the 4,4′-biphenyldicarboxylate (BPDC) ligand is less stable than the BDC-based UiO-66 due to the greater torsional strain the BPDC linkers create around the metal cluster, while significant rotational dynamics of BDC in UiO-66 alters energy barrier of hydrolysis. Thus, ligand rotational effect could also class as steric factor.[114]

The high coordination number of metal cluster could be also considered as kinetic factor due to crowding effect which prevents water clusters from forming near the metal center. This high coordination number correlates with the better stability observed for the Zr-based MIL-140[115], DUT-51[119,120] (1), (2), (3), (4), (5), PCN-56- 59,222,224,225[116–118,148] and MOF-525,545[121], the Hf based DUT-51,67–69[119,120], and the La-based LaBTB[149]. Even if bond breaking takes place, higher metal coordination number can result in a greater tolerance for hydrolysis owing to numerous of other bound ligands which are available as support. Adsorption of guest molecules accompanied by structural transitions can also affect MOF water stability by changing the steric hindrance and accessibility for water around the metal center.[150–152]

3.3. Experimental investigation of water stability and stability under numerous adsorption-desorption cycles

The aspect of MOF stability towards water was considered for the first time in 2009 by Pia Küsgens.[153] Authors studied the water adsorption properties and the water stability of the metal-organic frameworks HKUST-1 (=($Cu_3(BTC)_2$) (BTC = benzene-1,3,5 tricarboxylate)), ZIF-8, MIL-101(Cr), MIL-100(Fe) and DUT-4 (=Al(OH)(NDC)) (NDC = naphthalene-2,6 dicarboxylate) and also estimated the chemical stability of these materials after water adsorption. Both HKUST-1 and DUT-4 turned out to be unstable in direct contact with water, while the MIL-materials and ZIF-8 did show a good stability. This research concerns stability of MOFs in aqueous phase, that is only required in case of drug delivery, catalysis or liquid separation applications.

There are numerous studies which provide water stability data of MOFs that was systemized by Burtch *et al*[113], but the question of stability under numerous cycles that requires for heat transfer application starts to be considered only since 2012. In this part we will focus not only on research of vapor stability but also on research of stability under cycle conditions of MOFs as essential criterion for heat transformation application.

One of the first systematical study of water vapor stability together with stability under numerous cycles was performed by Soubeyrand-Leonoir in her thesis project published in 2012.[154] In this work several Porous Solid such as HKUST-1(Cu), MIL-100(Al, Fe, Cr), MIL-101(Cr), MIL-127(Fe), UiO-66(Zr), UiO-66(Zr)_NH_2, MIL-125(Ti), MIL-125(Ti)_NH_2 have been investigated. Stability of these materials was evaluated by comparison of N_2 sorption isotherms and XRPD analysis before and after several cycles of water adsorption-desorption at T=25°C. It was established, that HKUST-1(Cu) degrades in presence of humidity, in good agreement with previous research.[95,153,155–157] According to Küsgen *et al.* the decrease of specific surface BET of HKUST-1 from 1340 m^2/g to 647 m^2/g was obtained.[153] The particular degradation of MIL-125(Ti) structure in presence of water was also observed for the first time (**Figure 18**).[154]

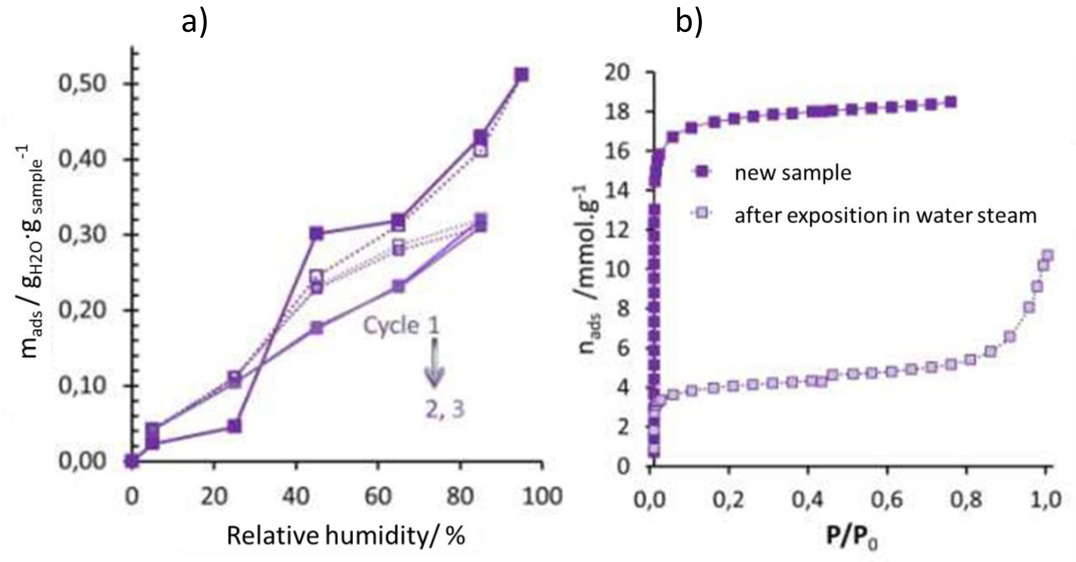

Figure 18. a) Water sorption cycles at T=25°C of MIL-125(Ti) before and after 3 cycles of exposition in water steam[154] b) N_2 sorption isotherms at 77K of MIL-125(Ti) before and after 3 cycles of exposition in water steam[154]

After three adsorption-desorption cycles the BET specific surface decreased from 1563 m^2/g to 341 m^2/g and pore volume from 0,54 to 0,13 m^2/g (**Figure 18**b). Summarizing, HKUST-1(Cu) and MIL-125(Ti) showed a significant decrease of adsorption capacity as well as one of BET surface area and pore volume. On the contrary, MIL-100(Al, Fe, Cr), MIL-101(Cr), MIL-127(Fe), UiO-66(Zr), UiO-66(Zr)_NH_2, MIL-125(Ti)_NH_2 presented a good stability under three adsorption cycles. The preservation of the crystallinity (PXRD), BET surface area and pore volume (N_2 sorption porosimetry) was observed for these MOFs.

The enhanced water stability of MIL-127(Fe) was established in 2015.[158]

Furukawa *et al.* investigated the cycling behavior of 23 porous solids including 20 MOFs, which consist of 6 new zirconium frameworks, MOF-802, MOF-805, MOF-806, MOF-812 and MOF-841.[159] They collected the water isotherms of these new MOFs and some other porous solids reported in literature. Five adsorption cycles were performed for each material (the evacuating after fist and following isotherms was performed at T=25°C and p=5 Pa for 2h). These results are shown below (Figure 19).

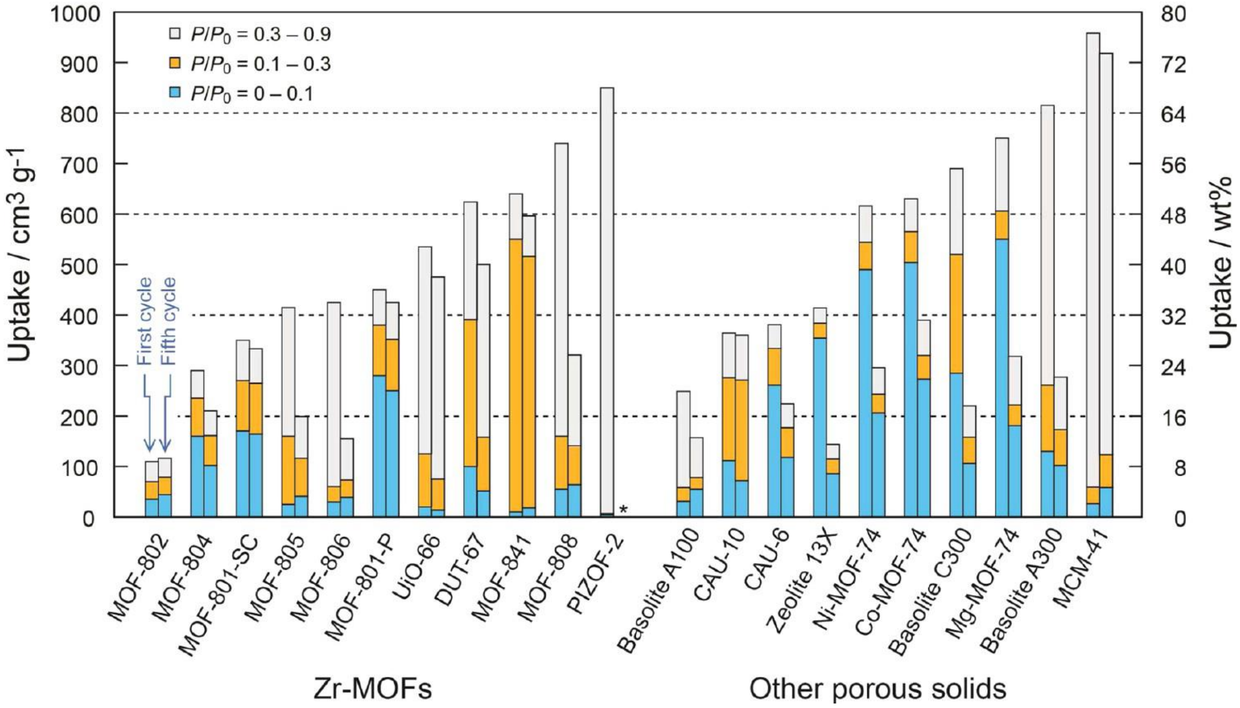

Figure 19. Water uptake capacity of zirconium MOFs (left) and other representative porous materials (right) in different pressure ranges. The large portion of water uptake capacity indicates that the pore filling or condensation occurs in this pressure range. Left and right bars represent first and fifth cycles, respectively. An asterisk (*) indicates no data. For MOF-801-SC, uptake capacities of first and second cycles were demonstrated.[159]

According to this study, one can select 6 MOFs with the best cycling behavior (5 cycles) such as MOF-801-P, MOF-802, MOF-841, UiO-66, CAU-10 and MCM-41.[159] Among these 6 stable MOFs the most interesting in terms of adsorption uptake in pressure range 0-0.3 are MOF-801-P, MOF-841, and CAU-10.

In 2012 Jeremias *et al.* studied the hydrothermal cycle stability of MIL-101(Cr), MIL-100(Fe), MIL-100(Cr), HKUST-1, ISE-1 and then in 2013 UiO-66(Zr)_NH$_2$, MIL-125(Ti)_NH$_2$ for heat pump application.[96] They evaluated stability of MOFs under numerous of adsorption-desorption cycles by comparing nitrogen porosimetry and PXRD analysis before and after adsorption-desorption cycles. Cycling stability tests were performed with a thermogravimetric apparatus at a constant water partial pressure of 5.6 kPa.[111] The samples were treated for 20 cycles by varying the temperature from 40 to 140 °C (Figure 20).

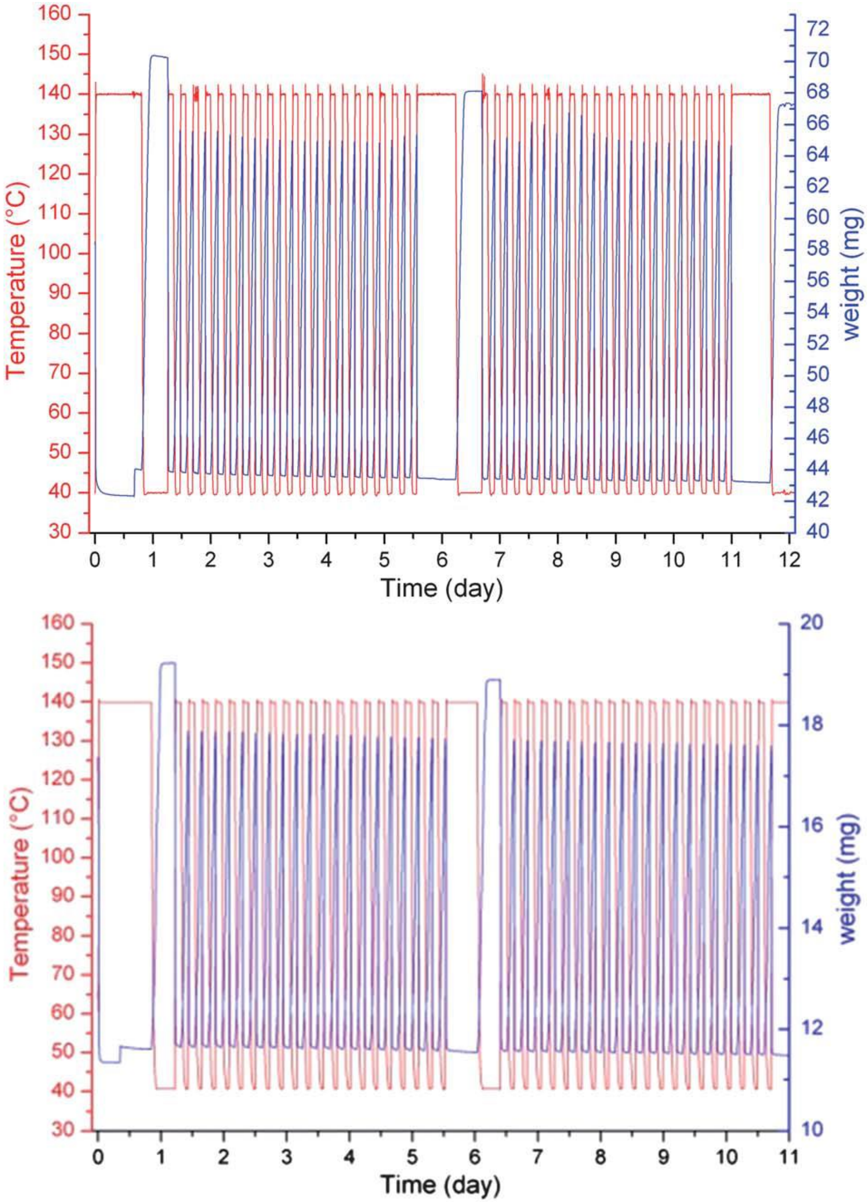

Figure 20. Temperature profile and load signal of the MIL-100(Al, upper, and Fe, lower graph) cycling experiment, acquired at pH_2O ¼ 5.6 kPa.[111]

In case of the HKUST-1 sample, the capacity is reduced by 53%, relative to the initial uptake. Basolite A100 [MIL-53Al] shows no dramatic loss, however desorption process is extremely slow and water uptake under the cycle conditions is very poor. ISE-1 also possesses a very poor water uptake in comparison with MIL-100(Fe) and MIL-101(Cr). Hydrothermal stability experiment of MIL-101(Cr) and MIL-100(Fe) have been performed with very promising results, showing only a slight degradation of approximately 3% compared to the initial load after 40 cycles. The same measurements for enhanced hydrophilic amino-functionalized MOFs UiO-66(Zr)_NH_2, MIL-125(Ti)_NH_2 indicate decrease of initial loading uptake of 38 and 17%, respectively. Nitrogen porosimetry analysis shows the decrease of BET surface area of 30% for UiO-66(Zr)_NH_2 and 29% for MIL-125(Ti)_NH_2 after cycling experiment. While UiO-66(Zr)_NH_2, seems to be not so stable during a multi-cycle hydrothermal stress test, stability of MIL-125(Ti)_NH_2 remains satisfied according to authors. **Figure 21** shows that MIL-101(Cr), MIL-100(Al, Fe), Aluminum fumarate A520, UiO-66(Zr)_NH_2 and MIL-125(Ti)_NH_2 are the most stable (40 cycles) compounds examined so far.[96]

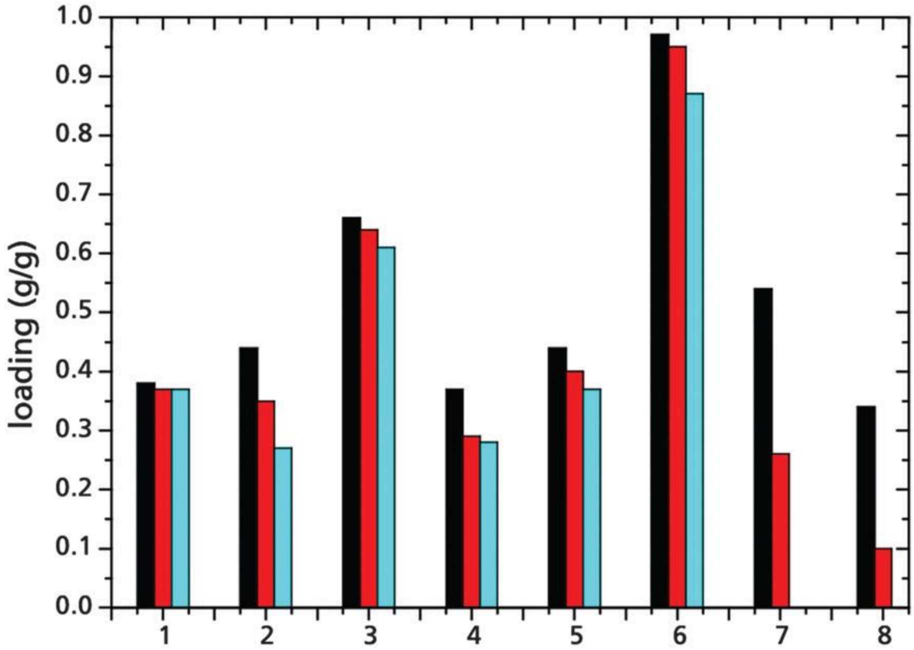

Figure 21. Water loading spread measured on aluminium fumarate (1), UiO-66 (2),[108] MIL-100Fe (3)[111] and Al (4)[111], MIL-125(Ti)_NH$_2$ (5),[108] MIL-101(Cr) (6),[18] HKUST-1 (7)[111] and Basolites F300 (8)[111] after activation (white), after 20 adsorption–desorption cycles with water vapor (red), and after 40 adsorption– desorption cycles (blue). [96]

Recently Cadiau et al. reported MIL-160[160] which is isostructural to CAU-10[16] consists of 5-membered ring including an O atom that provide enhanced hydrophilic character compared to CAU-10. The multiple cycle experiment demonstrates excellent hydrothermal stability of this MOF (adsorption at 303 K in humid nitrogen (RH 80%) and desorption at 373 K in nitrogen (RH 0.03%)).

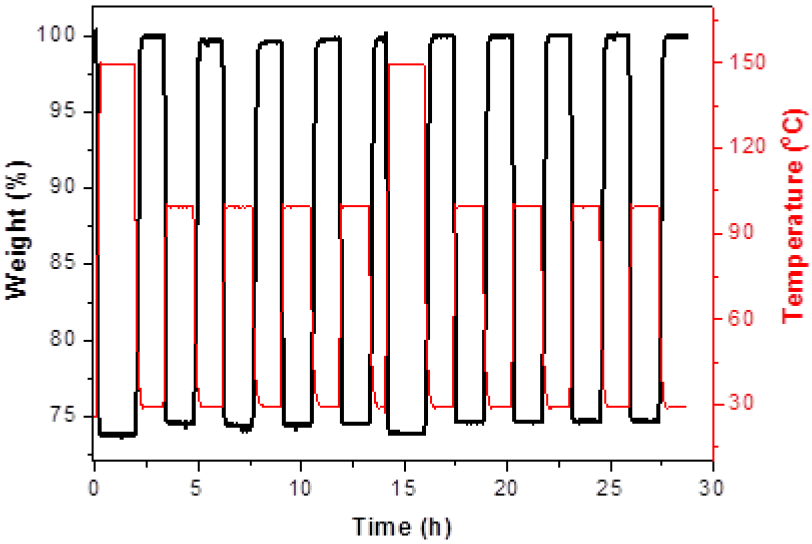

Figure 22. Thermogravimetric analysis profile for multiple cycles of water adsorption-desorption of MIL-160. Test conditions: adsorption at 303 K in humid nitrogen (RH 80%) and desorption at 373 K in nitrogen (RH 0.03%).[160]

According to the literature, MOFs such as aluminium fumarate, MOF-801-P, MOF-802, MOF-841, CAU-10, MIL-160(Al), MIL-101(Cr), MIL-100(Al, Fe), MIL-127(Fe), hydrophilic UiO-66(Zr)_NH_2 and MIL-125(Ti)_NH_2 possess therefore the most interesting hydrothermal stability and recyclability features for the first selection of materials promising for heat transformation and heat storage application. Selected MOF series shows high kinetics stability (MOF-801-P, MOF-802, MOF-841, CAU-10, MIL-160, MIL-100(Al, Fe), MIL-101(Cr), MIL-127(Fe), MIL-125(Ti)_NH_2, and UiO-66(Zr)_NH_2). MIL-101(Cr) was classified by Burtch *et al.*[113] as thermodynamically stable, while we consider that its enhanced stability refers to d^3 configuration of metal ion that provides water exchanged rate constant of $k=10^{-6}$ s^{-1}. We selected several MOFs from this series owing to highest adsorption capacity. Water adsorption behavior of these MOFs will be presented below and their potential for adsorption-based applications will be considered.

4. Water adsorption behavior of MOF

One of the most essential aspect to define MOF for adsorption-based application is their water sorption behavior, which could be illustrated by adsorption capacity and the amphiphilic balance, as defined by the position of adsorption step (p/p_0). In this part we will describe water sorption capacity of MOFs selected according to bibliography data owing to their stability under numerous adsorption-desorption cycles. We will also consider classification of water adsorption-based applications depending on amphiphilic balance of MOF, suggested by Furukawa *et al.*[159] with especial focus on heat transformation one.

The amphiphilic balance is the key-parameter governing application domain of water stable MOFs. Each water adsorption based application such as dehumidification, thermal batteries, delivery of water in remote areas, heat reallocation require high adsorption lift at different relative humidity condition. Therefore, the water sorption isotherm should exhibit a steep uptake at a specific relative pressure (p/p_0). For example, for thermal batteries water loading is desirable at low relative pressure ($p/p_0 \leq 0.1$). In order to consider the best material for heat reallocation application, we will remind the details of adsorption behavior requirement for this application. For ideal performance, a porous material should perform in the $0.05 < p/p_0 < 0.4$ relative pressure range and should have a desorption temperature at or below 80 °C.[71,94]

We will consider in detail the structural aspects and water adsorption behavior of MOF-series selected according to literature that correspond to criteria such as water stability, stability under numerous adsorption-desorption cycles, high adsorption lift. The choice of MOFs is following: MOF-801-P, MOF-841, CAU-10, MIL-160(Al), MIL-101(Cr), MIL-100(Al, Fe), MIL-127(Fe), UiO-66(Zr)_NH_2 and MIL-125(Ti)_NH_2.

4.1. CAU-10(Al) and MIL-160(Al)

The Al-carboxylate based MOF denoted CAU-10 (CAU stands for Christian-Albrechts-University) is a very promising candidate owing to highly hydrophilic character, high adsorption capacity, good hydrothermal stability, low cost and low toxicity.[160–162]

The inorganic building unit of this framework presents a chain of cis-connected, corner sharing AlO_6-polyhedra, built up from four oxygen atoms from four different carboxylate groups and two bridging OH-ions in cis-position to each other. Thus, inorganic building unit presents helical connectivity mode. (Figure 23).

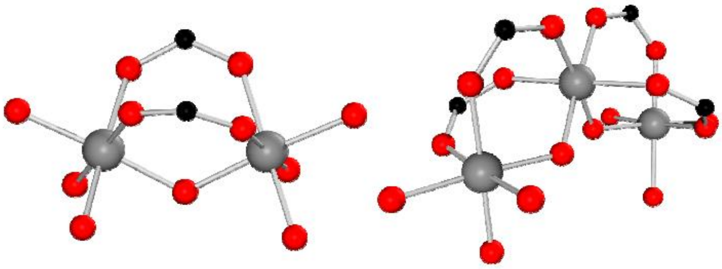

Figure 23. The dimeric unit of corner-sharing AlO_6-octahdera (on the left) and trimeric subunit (on the right) are shown. Aluminum atoms are shown in grey, oxygen in red and carbon in black.[163]

This helical inorganic building unit is remarkable because frequently linear chains of trans-connected $M(III)O_6$-polyhedra are observed in MOFs with one-dimensional inorganic units such as for example compounds with MIL-53 topology. But there are only two Sc-based MOFs which present such fourfold helical cis-connected chains of $M(III)O_6$-polyhedra.[164] In CAU-10 framework each helix is connected to four adjacent inorganic building units of alternating rotational orientation via the phenyl-based linker (Figure 24). This assemblage results in square-shaped, sinusoidal channels, which exhibit a maximum free diameter of ~ 5 A.

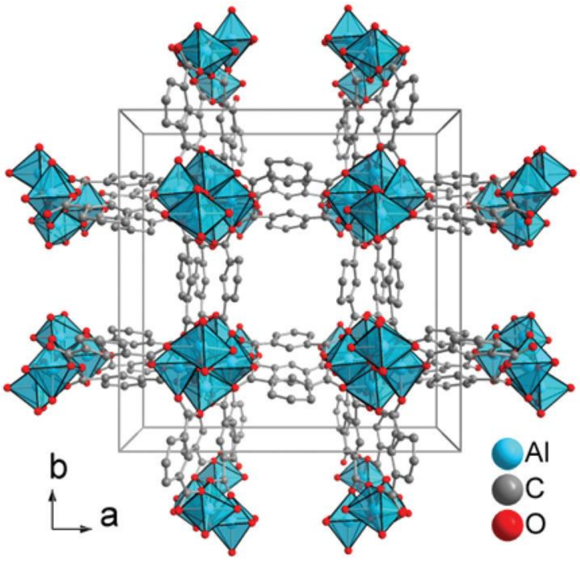

Figure 24. The framework of CAU-10-H (1) as seen along the *c*-axis, showing the fourfold connectivity of the helices and the square-shaped channels. Aluminum atoms are shown in blue, oxygen in red and carbon in grey.[161]

MIL-160(Al) is isostructural to the CAU-10. It relies on the same inorganic building unit however connected by linker with an aromatic ring incorporating a polar hetero-atom (2,5-furandicarboxylic acid (FDCA)) instead of phenyl-based linker. The advantage of this linker apart from enhanced hydrophilic character is that it derived from a renewable biomass feedstock that is already produced on an industrial scale,[160] which can significantly decrease the overall cost of MIL-160(Al). MIL-160(Al) presents 3-D framework with square shaped sinusoidal channels of ~5 Å in diameter.

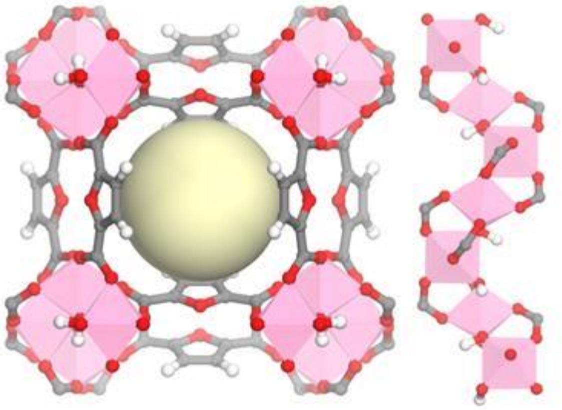

Figure 25. Framework of MIL-160: left: helical chains cis-connected by corner and surrounded by four carboxylate from four ligands, right: square shaped channels delimited via the ligands linking four chains. Aluminum atoms are shown in rose, oxygen in red and carbon in grey[160]

We will here consider the water sorption behavior of these two MOFs. A first strategy to enhance the hydrophilic character of CAU-10 consist of grafting diverse functional groups (-CH_3, -OCH_3, -NO_2, -NH_2, -OH) on the organic linkers.[163] Nevertheless if this led to an improvement of the affinity for water, the significant drop in the uptake capacity was observed due the significant decrease in pore volume of the corresponding solids. The increase in the heterogeneous character of the adsorption resulted in less steep water sorption isotherm.

The alternative concept for the hydrophilicity increase was demonstrated by MIL-160(Al). In this case, linker with an aromatic ring incorporating a polar hetero-atom instead of phenyl-based linker of CAU-10 allows not only hydrophilicity enhance of the solid but also keeping a highly accessible pore volume for the water molecules. Experimental water sorption isotherms of CAU-10 and MIL-160 clearly show that the furan-based material is more hydrophilic, the water uptake starting at lower p/p_0 (0.08 vs 0.18 for CAU-10).[160]

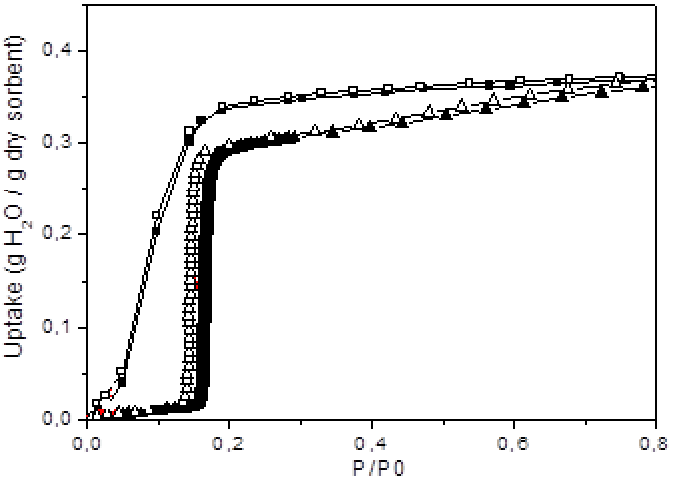

Figure 26. Water sorption isotherms at 303 K for MIL-160 (square) and CAU-10 (triangle): adsorption (full symbols), desorption (empty symbols).[160]

Moreover, the adsorption capacity of MIL-160 is slightly enhanced compared to CAU-10 (0.35 g/g dry MOF vs 0.30 g/g dry MOF at p/p_0=0.3).

4.2. NH_2- functionalized UiO-66(Zr) and MIL-125(Ti)

Hydrophilic UiO-66(Zr)_NH2 and MIL-125(Ti)_NH2 are other promising MOFs for heat reallocation due to their hydrophilic character and sufficient stability under cycle condition. We will consider their structures and water sorption behavior below.[166]

UiO-66(Zr) exhibits a closed packed cubic structure. Inorganic building unit which consists of $Zr_6O_4(OH)_4$ oxo-clusters are bridged by carboxylates ($-CO_2$) originating from the 1,4-benzenedicarboxylate resulting $Zr_6O_4(OH)_4(CO_2)_{12}$ cluster. Each inorganic building unit is linked with others by twelve dicarboxylic ligands resulting 3-D framework with two types of cages, tetrahedral and octahedral, of respectively 8 and 11 Å free apertures accessible through 4-6 Å windows (Figure 27).

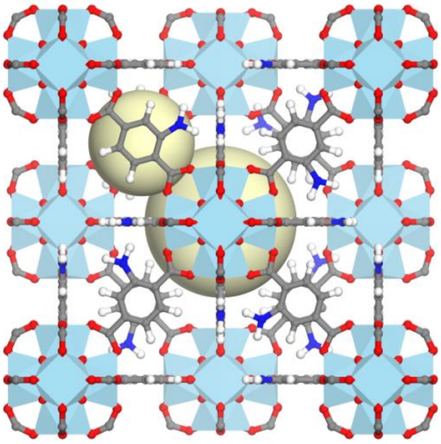

Figure 27. Structure of UiO-66(Zr)-NH_2 with two types of porosity (tetrahedral and octahedral cages). Zirconium atoms are shown in Cambridge blue, oxygen in red, nitrogen in Oxford blue and carbon in grey.

UiO-66(Zr)_NH_2 is isostructural to UiO-66(Zr). It consists on the same inorganic building unit however connected by 2-amino-functionalized benzenedicarboxylate linker.

The characteristics of the water adsorption isotherm of UiO-66(Zr)_NH_2 (Figure 28) reported by several independent research are in good agreement showing a water uptake of 0.36 g g^{-1} (20 mol kg^{-1}).[95,108,154,161] The water uptake of UiO-66 is also similar to the values given in the literature.[146,167–170]

The main loading step of UiO-66(Zr) occurs in a broad range from $p/p_0 = 0.2$ to 0.4 that corresponds to the filling of tetrahedral and octahedral cages. In case of UiO-66(Zr)_NH_2 main water uptake takes place in lower pressure range from $p/p_0 = 0.1$ to 0.3 owing to higher ligand hydrophilicity from amine–water interactions. This can be explained by the fact that the H_2N-group can serve as an H-bond donor. In addition, pores are somewhat narrowed due to the steric demand of the -NH_2 functionality, which also enhances the hydrophilicity.

We considered the example of UiO-66(Zr) to show the influence of functionalization on the water sorption behavior of MOF. However only UiO-66(Zr)_NH_2 can be considered as a candidate for heat reallocation due to mentioned above weaker hydrothermal stability of UiO-66(Zr) as well as its more hydrophibic character.

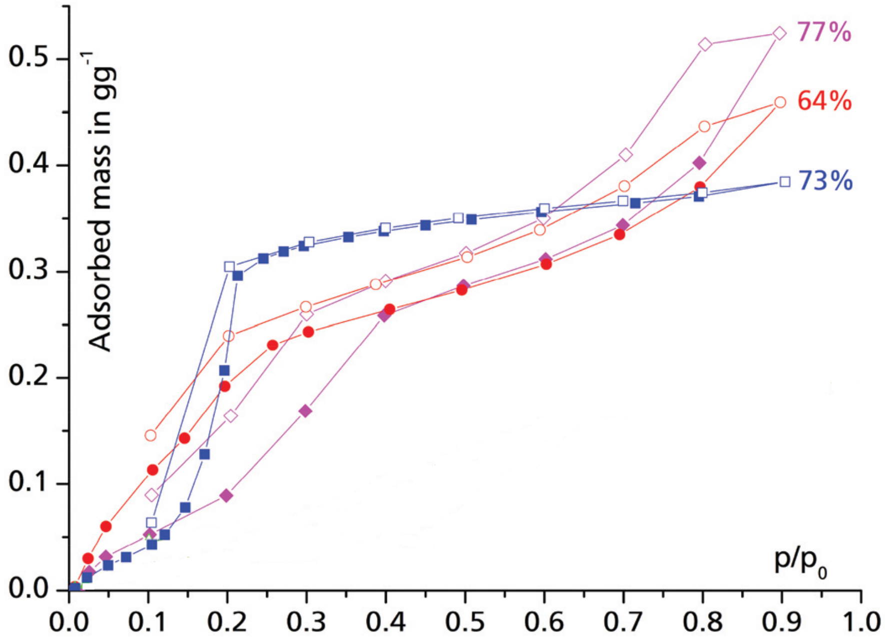

Figure 28. Water adsorption/desorption isotherms of UiO-66 (in violet), UiO-66(Zr)_NH$_2$ (in red) and H$_2$N-MIL-125 (in blue), acquired at T = 25 °C. Adsorption: filled symbols; desorption: empty symbols. Percentage of theoretical water loading is given at $p/p_0 = 0.8$ based on the calculated micropore volume ($V_{0.5}$) obtained from the Dubinin–Astakov model of N$_2$ adsorption at 77 K and assuming a density for condensed water of 1 g cm^{-3}.[166]

The MIL-125(Ti)_NH$_2$[171] exhibits a quasi-cubic tetragonal structure. Its inorganic building unit is built from a cyclic octamer of titanium octahedra that consists of edge- and corner-sharing $TiO_5(OH)$ octahedra. This SBU is 12 fold connected through 2-amino-benzene-1,4-dicarboxylate linkers. This structure can also be considered as an augmented version of the centered cubic structure.[172] This 3D porous framework possesses octahedral cages with a free diameter of 12.5 Å and tetrahedral cages of 6 Å diameter accessible through free apertures of 5–7 Å.

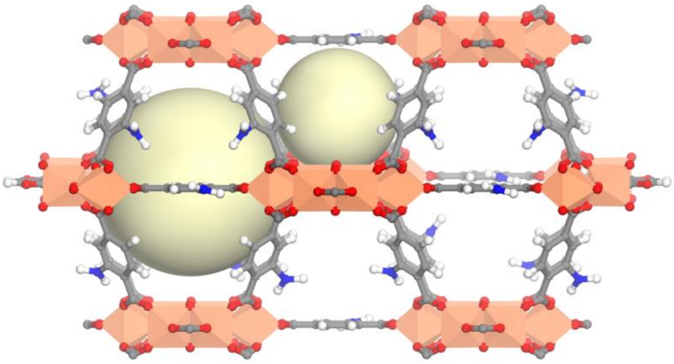

Figure 29. Structure of MIL-125(Ti)_NH$_2$ with two types of porosity – tetrahedral and octahedral cages. Titanium atoms are shown in orange, oxygen in red, nitrogen in Oxford blue and carbon in grey.

The enhanced hydrophilicity of this framework is due to the high density of hydrophilic active sites (Ti-OH and -NH$_2$ groups), as shown though its water sorption isotherms presented above, leading to an even more pronounced hydrophilic character compared to UiO-66(Zr)_NH$_2$. Thus, 73% of its total loading, together with a steep adsorption isotherm, at a relative pressure below $p/p_0 = 0.2$ (Figure 28). Such an increase of hydrophilic character in MIL-125(Ti)_NH$_2$, although possessing a similar pore sizes and linker as other amino-functionalized MOFs, can also be explained by its higher inorganic content (Ti/Linker=8/6 versus Zr/Linker=1 for UiO-66_NH$_2$).[108]

In 2014 Jeremias *et al*. investigated series of MOFs including hydrophilic amino-modified compounds UiO-66(Zr)_NH$_2$ and MIL-125(Ti)_NH$_2$ for heat transformation applications, pavng a particular attention to their stability under numerous short non-equilibrium cycles, sorption kinetics and heat of adsorption.[108] The water sorption kinetics studied on both MOFs during numerous adsorption-desorption cycles appeared to be substantially faster in case of MIL-125(Ti)_NH$_2$. Moreover, loading lift remains sufficiently stable for MIL-125(Ti)_NH$_2$ throughout the hydrothermal cycle stress test showing only 17% of adsorption capacity losses after 40 cycles (38% in case of UiO-66(Zr)_NH$_2$).[108]

Summarizing, UiO-66(Zr)_NH$_2$ and especially, MIL-125(Ti)_NH$_2$ are very promising for heat transformation based on adsorption method. The MIL-125(Ti)_NH$_2$ possesses a good hydrothermal stability on the whole comparable to mesoporous solids MIL-100(Fe) and MIL-101(Cr), but exhibiting a more pronounced hydrophilic character together with a higher heat of adsorption (56 kJ mol^{-1}), which provide additional advantages in terms of energy storage densities.[108]

4.3. Microporous MIL-127(Fe)

The stability of MIL-127(Fe) in aqueous phase was confirmed by Chevreau *et al*.[158] Earlier the water vapor stability of this MOF was studied under 3 adsorption isotherms.

The Secondary Building Unit (SBU) of MIL-127(Fe) consists of iron (III) octahedra trimers (Figure 30), sharing one central μ_3-oxo oxygen. In each octahedron, the apical position is occupied by 2/3 water molecules and 1/3 anions X (X = OH$^-$, ClO$_4^-$, Cl$^-$ depending on the synthesis route). Each SBU are bridged by six 3,3',5,5'-azobenzene tetracarboxylate ligands resulting in a 3D cubic framework, exhibiting a soc topology (Figure 30).

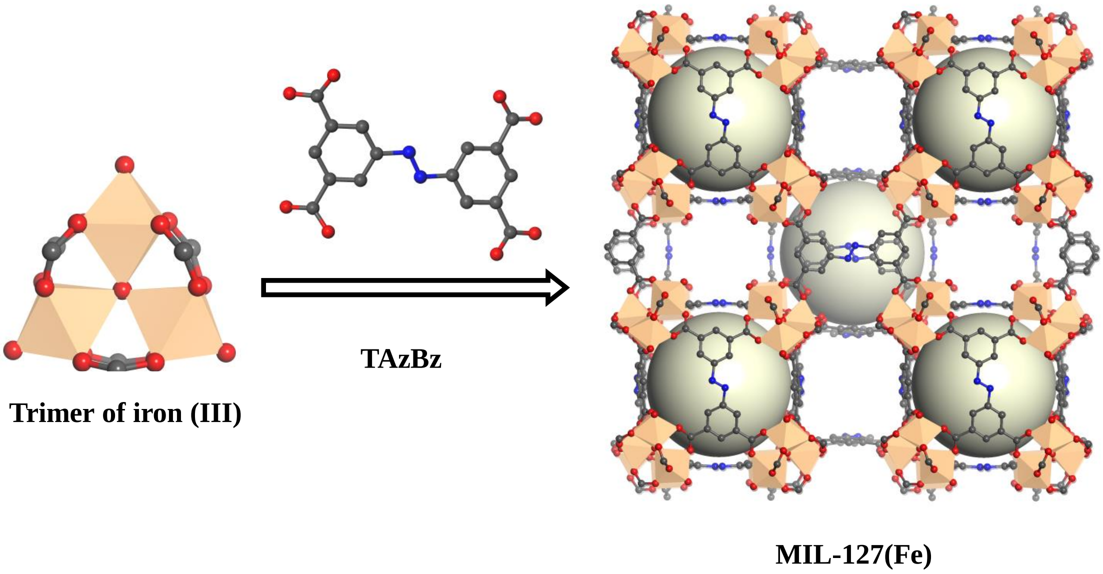

Figure 30. Structure of MIL-127 a) The secondary building unit (trimer of iron octahedron). b) The organic linker (3,3',5,5'-azobenzenetetracarboxylic acid). c) Unit cell of MIL-127. Iron atoms are shown in orange, oxygen in red, nitrogen in Oxford blue and carbon in grey.

The pore system of MIL-127(Fe) (Figure 30) consist of a 1D channels system (~ 5-7 Å) and hydrophilic cages of ca. 10 Å, only accessible for very small molecules (windows < 3 Å). Due to the presence of Lewis acid sites and organic spacers, two types of channels are present, either hydrophilic (~5 Å) or hydrophobic (~7 Å) pockets.

The water sorption behavior of MIL-127(Fe) was reported in the thesis of Soubeyrand-Lenoir.[154]

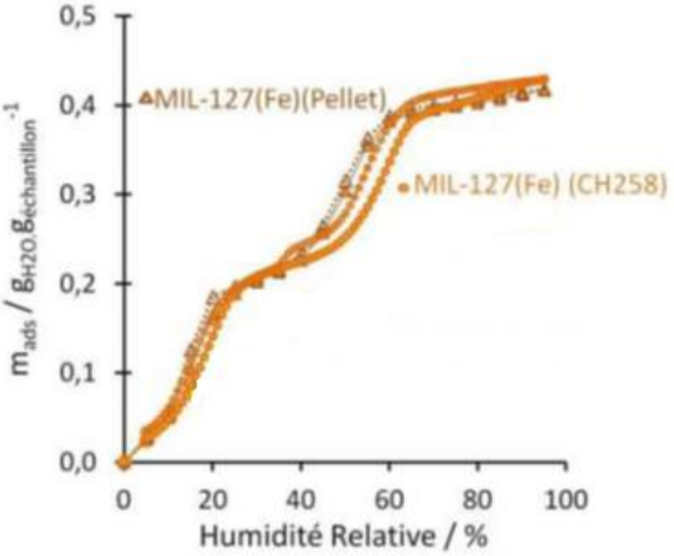

Figure 31. Water sorption isotherms for MIL-127(Fe) at 25 °C.[154]

Its adsorption behoaviour can be divided in two steps. At low relative pressure cluster formation at the hydrophilic metal sites, and likely at free doublet of azote (ligand), takes place. The first steep rise below RH=30% can be attributed to filling of small hydrophilic cages (windows of ~ 3 Å) and the hydrophilic channels. The second one with RH upper 40% corresponds to filling of hydrophobic channel system. This water sorption isotherm was measured in 2012 based on a MIL-127(Fe) synthesized in DMF. In this manuscript we will provide the optimized synthesis of this material in a more friendly solvent i-PrOH (see Chapter IV, article “Synthesis of the biocompatible and highly stable MIL-127(Fe): from large scale synthesis to particle size control”) and its water sorption isotherm (see Chapter III, article “Design of salt-Metal Organic Frameworks composites for heat storage applications”).

The main advantage of this MOF apart from excellent water stability (see Chapter III), including its stability under several adsorption-desorption cycles, lies in the presence of pores with a suitable hydrophilicity together with a high adsorption capacity and mainly in the presence of several types of pores with different sizes and hydrophilic character. This might be advantageous for separation but also for the preparation of composites which would consist of inorganic salt loaded MOF, which is the main objective of this thesis (Chapter III), due to the possibility to combine within the same composite physical sorption, that would occur in the small cages accessible only for water molecules, and chemical sorption that would take place in the channels filled by the inorganic salt.

4.4. Mesoporous MIL-100(Fe) and MIL-101(Cr)

As mentioned above, mesoporous MIL-100(Fe) and MIL-101(Cr) are of a great interest for heat reallocation owing to excellent stability under numerous adsorption-desorption cycles and high cycling loading lift that was demonstrated before.[94] Herein, we will provide their structures and water sorption behavior.

The inorganic building unit of these mesoporous MOFs consists of oxocentered trimers of metal(III) octaehdra (iron for MIL-100(Fe) and chromium for MIL-101(Cr)). The association of these trimers with the organic linker (1,3,5-benzene tricarboxylate for MIL-100(Fe) and benzene-1,4-dicarboxylate for MIL-101(Cr)) leads first to the so-called supertetrahedron (ST). These further assemble to provide a zeotype architecture. MIL-100(Fe) has two types of mesoporous cages such as smaller one of 24Å and larger one of 27 Å. Smaller mesoporous cage consists of pentagonal microporous windows (~4.7×5.5Å) only while larger mesoporous cage consists of both pentagonal and hexagonal windows (8.6 Å) (
Figure **32**).

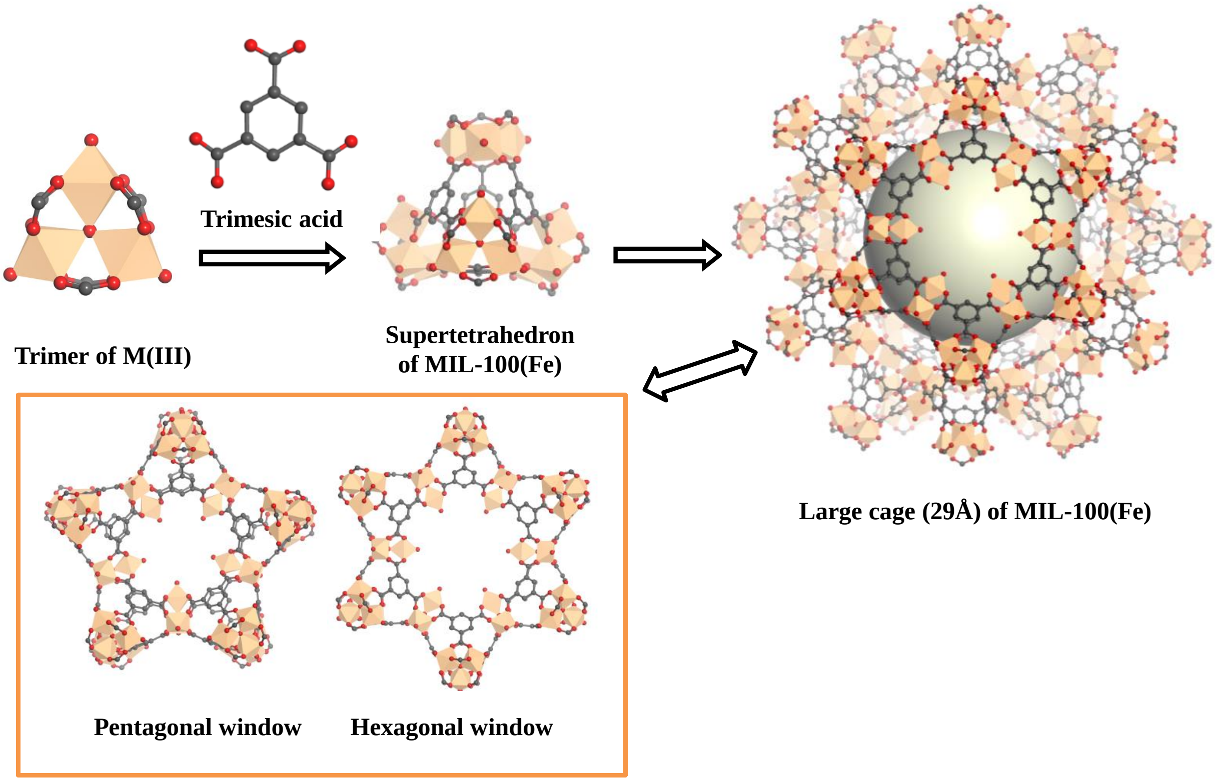

Figure 32. Structure of MIL-100(Fe), its pentagonal/hexagonal windows, and one large cage of 27 Å. Iron atoms are shown in orange, oxygen in red and carbon in grey.

MIL-101(Cr) possesses a similar structure as MIL-100(Fe), with the tricarboxylate lying at the faces of the ST being replaced by the 1,4-benzenedicarboxylate linkers occupying the edges of the ST. The ST being larger, this leads for MIL-101 to larger mesoporous cages of free diameter of 29Å and 34Å. The smaller mesoporous cage are accessible through pentagonal microporous windows (12 Å) while the larger ones are accessible through both pentagonal (12 Å) and hexagonal windows (14.7×16 Å).

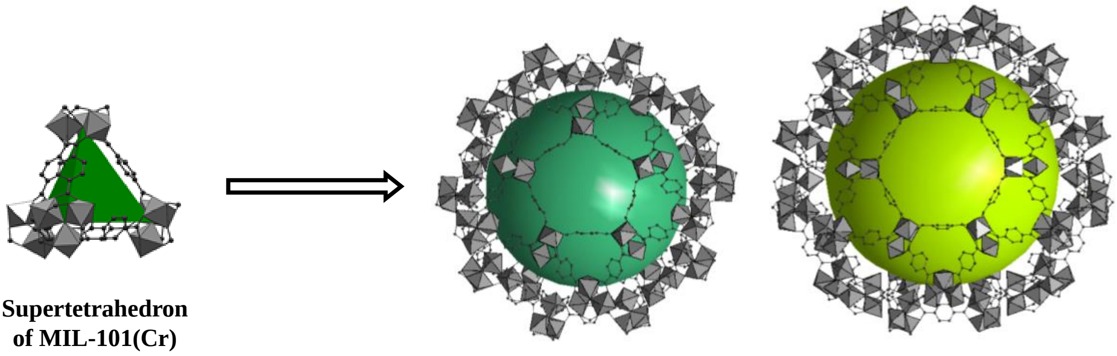

Supertetrahedron of MIL-101(Cr)

Small mesoporous cage (29Å) of MIL-101(Cr)

Large mesoporous cage (34Å) of MIL-101(Cr)

Figure 33. Structure of MIL-101(Cr) representing two mesoporous cages of 29Å and 34Å. Chromium atoms are shown in grey and others (carbon and oxygen) in black.

Water sorption isotherms of MIL-100(Fe) are presented in **Figure 34**. (6), (7) Its behavior can be explained as following: at low relative pressure range (p/p0 < 0.25), adsorption and cluster formation at the hydrophilic metal sites takes place. The steep rise at 0.25 < p/p0 < 0.45 corresponds to consecutive filling of first the 24 Å mesopores, then the 27 Å ones. A distinct hysteresis can be pointed out, particularly for the larger cages, as encountered typically in mesoporous materials. This phenomenon, although not very pronounced here, is undesired for the heat reallocation application because it significantly decreases the usable part of the loading lift.

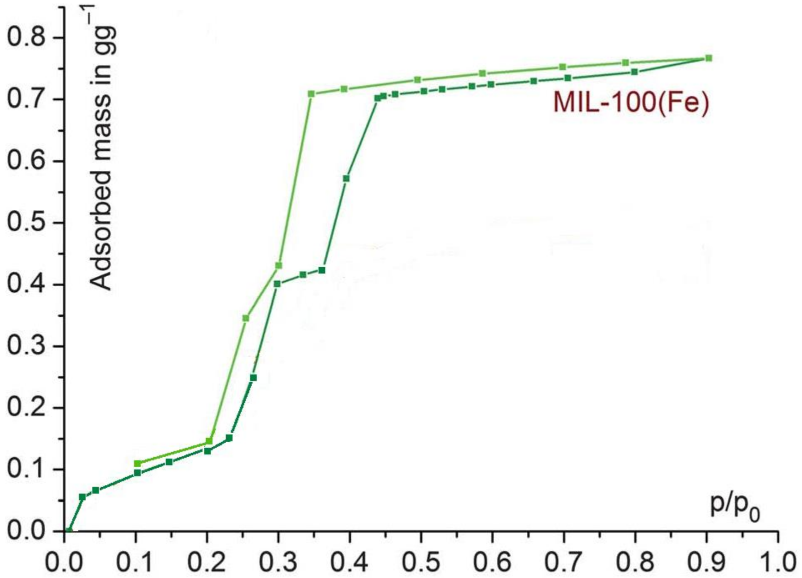

Figure 34. Water sorption isotherms for MIL-100(Fe and Al) at 25 °C (adsorption in dark and desorption in light green).[111]

MIL-101(Cr) possesses an enhanced water sorption capacity as well as a more hydrophobic character in comparison with MIL-100(Fe). Enhanced water sorption capacity can be easily explained by increased pore volume of MIL-101(Cr), while the reason of such increase of hydrophobic character is the higher organic content of this MOF (metal/linker=1 against 3/2 for MIL-100) leading to a shift to higher partial pressures of the isotherms up to p/p0 = 0.4.

Khutia et *al.* provide the comparison water sorption isotherms obtained by Henninger team and by other independent researchers.[173] The water adsorption isotherm presents a single adsorption step although there are two types of pores that are supposed to fill up consecutively as in case of MIL-100(Fe). Khutia et *al.* explained this phenomenon as follow: “as the difference in pore size is 5 Å which is bigger than the difference in pore size in MIL-100(Fe), the explanation for the missing step in the adsorption branch can only be attributed to the higher value of pores and windows in MIL-101.” The maximum water uptake for MIL-101(Cr) (8), (9), (10) reported by Henninger et *al.* (Figure 35) is 1.43 gg^{-1}.[173]

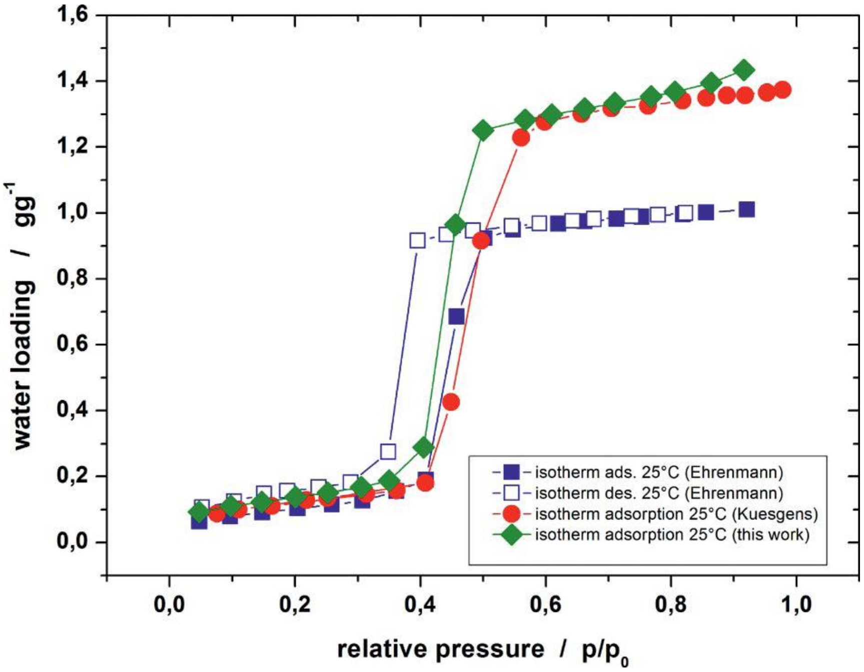

Figure 35. Water adsorption and desorption isotherms of different MIL-101(Cr) samples. Isotherms from Ehrenmann[18], calculated data from Küsgens[153] and in addition a newly synthesized sample showing the highest water uptake reported by Henninger.[174]

However, the water sorption measurements reported by Seo *et al.* indicated the presence of two steps, in agreement with supposed mechanism of consecutive filling of two mesoporous cages (see Chapter III).[175]

In summary, MIL-100(Fe) and MIL-101(Cr) through a combination of high water capacities, excellent cycle stabilities, suitable hydrophilicity and little hysteresis that considerably enlarges the boundary conditions, under which a heat storage systems can be operated which on the whole makes these MOFs highly suitable for heat transfer applications.

4.5. MOF-801-P and MOF-841 (11)

MOF-801-P and MOF-841 reported in 2014 by Furukawa *et al.* demonstrate excellent stability under 5 adsorption isotherms.[159]

Initially MOF-801-P was reported by Wißmann et al.[176], who elucidated its crystal structure by means of XRPD analysis, indicating that this MOF, a zirconium fumarate, was an analogue of UiO-66(Zr). Furukawa *et al*. succeed in growing crystals that allowed using SXRD analysis to solve this structure.[159] MOF-801-P is based on Zr6 oxo-clusters as inorganic building unit that are connected by fumarate ligands providing two independent tetrahedral cavities of 5.6 Å and 4.8 Å diameter and an octahedral cavity of 7.4 Å.

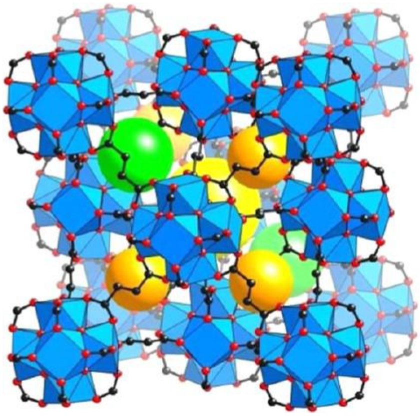

Figure 36. MOF-801 is the smallest Zr-MOF with fcu topology. Atom color scheme: C, black; O, red; Zr, blue polyhedra. Yellow, orange and green balls indicate the space in the framework.[159]

MOF-841 possesses similar inorganic building units as MOF-801-P and UiO-66(Zr)-NH_2. Each Zr oxo-cluster is bridged by eight tetrahedral MTB (4,4',4'',4'''-methanetetrayltetrabenzoic acid) linkers. Water and formate ligands complete the coordination of the SBU. Thus, MOF-841 presents the combination of octahedral and tetrahedral nodes as shown in **Figure 37**a. This 3D cubic structure is of a flu topology (Figure 37a) and possesses only one type of cage with a free diameter of 11.6 Å (without terminating formic acid) (Figure 37b).

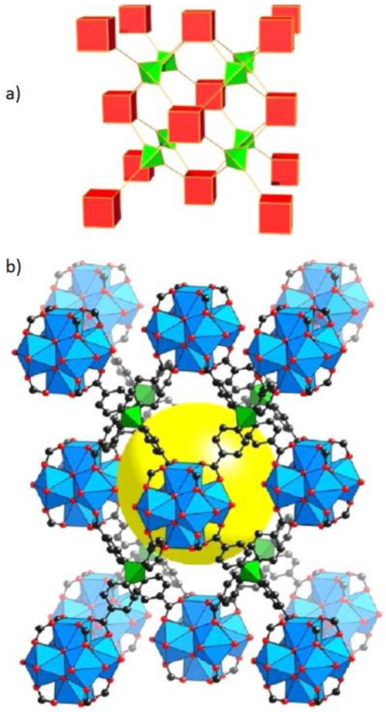

Figure 37. The flu network (c) is formed when tetrahedral units are combined with cubic ones, as in the case of MOF-841 (d). Atom color scheme: C, black; O, red; Zr, blue polyhedra. Green polyhedra represent central tetrahedral carbon. H atoms are omitted for clarity. Yellow balls indicate the space in the framework.[159]

The water adsorption-desorption isotherms of MOF-801 at 25°C are compared with isotherms of several others Zr-based MOFs (Figure 38). The hydrophilicity of this MOF is somehow intermediate between the one of zeolite 13X and UiO-66(Zr) with an adsorption occuring in P/P_0 = 0.05 to 0.1 range. There is significant difference in total water uptake of MOF-801-SC (single crystal) and MOF-801-P (powder) resulting in the maximum uptake of 350 $cm^3\ g^{-1}$ (28 wt %) at

P/P_0 = 0.9 for single crystals sample and 450 cm^3 g^{-1} (36 wt %) for powder sample. This phenomenon was also observed by the N_2 sorption measurements. Authors considered that a large amount of missing linker defects in MOF-801-P[159] can provide this this difference as it was already reported for UiO-66(Zr). In case of UiO-66(Zr) the correlation between the amount of acid modulator employed during the synthesis and the amounts of missing linker defects was observed. Taking into account that MOF-801-P was prepared using a higher concentration of formic acid than MOF-801-SC, we can expect a large number of such defects.[159]

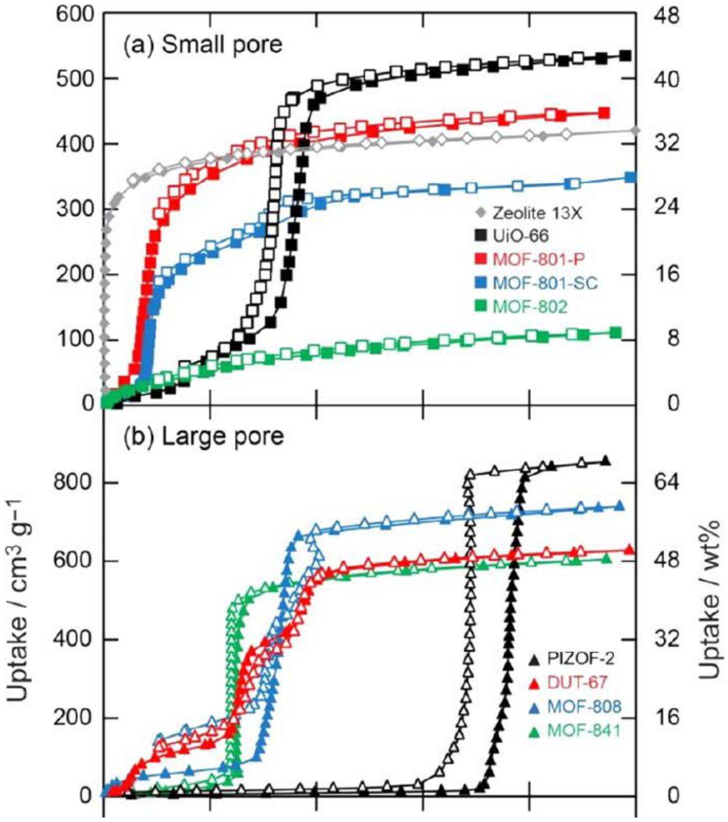

Figure 38. Water isotherms of zirconium MOFs with small pore (a), large pore (b) measured at 25 °C. The isotherm of zeolite 13X is also included in panel (a). [159]

The water sorption behavior of MOF-841 is shown in Figure 38. This MOF is also very hydrophilic, the steep adsorption commences at P/P_0 = 0.2 and reach 550 cm^3 g^{-1} at P/P_0 = 0.3 (640 cm^3 g^{-1} at P/P_0 = 0.9). Adsorption uptake of MOF-841 is the highest one compared to hydrophilic MOFs reported in this chapter such as MIL-160(Al), CAU-10, UiO-66(Zr)-NH_2, MIL-125(Ti)_NH_2. The combination of good stability (5 adsorption cycles), suitable hydrophilicity (P/P_0=0.2-0.3) and such high adsorption uptake can easily make MOF-841 one of the most promising hybrid porous solid for heat reallocation application although its expensive non commercially available linker might prevent from its practical use.

However, one shall take into account the next important requirement of heat storage and transformation applications such as easy low-energy regeneration process. As mentioned above high adsorption uptake is very important, but material need to release significant amount adsorbed of water at relatively low desorption temperature of 80-100°C. Thus, we need to look at cycling loading lift and not only on adsorption capacity of material. The strongly hydrophilic MOFs may provide problems of regeneration in this context due to high affinity towards water. In order to evaluate the potentiality of reported MOFs in terms of maximal cycling loading lift water sorption isotherms at different temperature need to be carried out. However, literature data generally provide only adsorption isotherms of MOFs at 25°C.

Conversely, adsorption behavior at different temperatures was published for MOF-801 and MOF-841 (11). Adsorption uptake of MOF-801 depends significantly on temperature showing the difference of about 100 cm^3/g between uptake at T=25°C and T=55°C. The ideal uptake between 30°C and 80°C need to be 0.4 g/g. The strong impact of temperature on the water sorption properties was established, confirming the potential of MOF-801 for thermochemical heat storage.

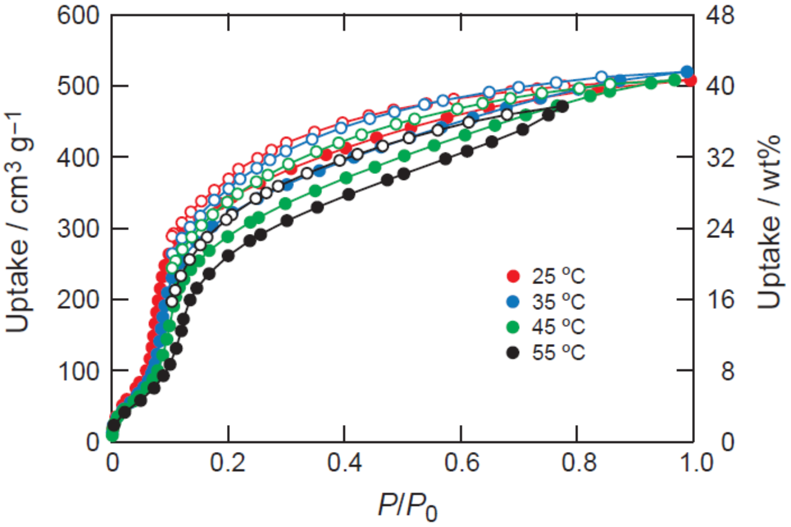

Figure 39. Water isotherms of MOF-801-P measured at 25, 35, 45, and 55 °C. [159]

In the contrary, MOF-841 presents a weak dependence of temperature on sorption properties (less than 0.08 g/g between 15 and 45°C), which could be due to the high water affinity for the framework.

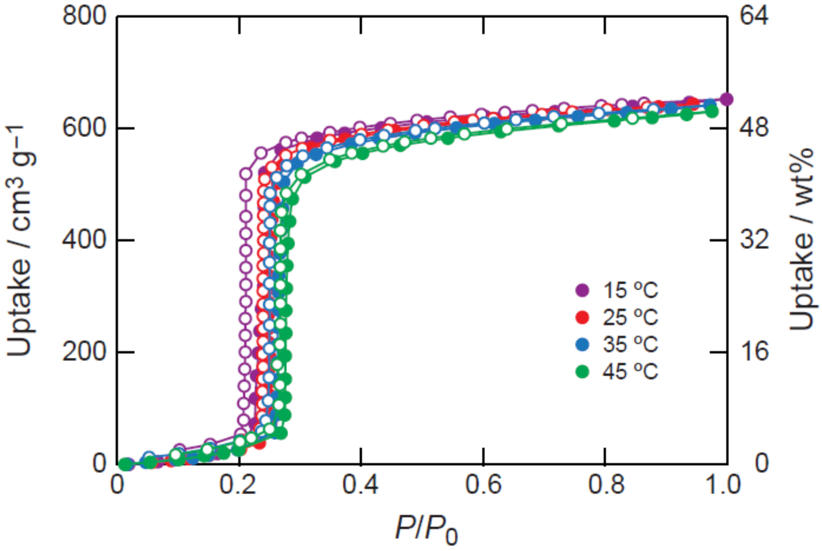

Figure 40. Water isotherms of MOF-841 measured at 15, 25, 35, and 45 °C.[159]

This data need to be completed by adsorption experiments at higher temperatures to insure the tendency and evaluate the potential towards thermochemical heat storage application.

4.6. Discussion

According to bibliography data MOFs such as aluminium fumarate, MOF-801-P, MOF-802, MOF-841, CAU-10, MIL-160(Al), MIL-101(Cr), MIL-100(Al, Fe), MIL-127(Fe), hydrophilic UiO-66(Zr)_NH_2 and MIL-125(Ti)_NH_2 possess good hydrothermal stability and also stability under several adsorption-desorption cycles (from 3 to 40 cycles depending on studied MOF). We considered in details the structure and water sorption behavior of several candidates from this list such as CAU-10, MIL-160(Al), MIL-101(Cr), MIL-100(Fe), MIL-127(Fe), hydrophilic UiO-66(Zr)_NH_2 and MIL-125(Ti)_NH_2, MOF-801-P, MOF-841. MOF-802 was not studied in details due to its lower adsorption uptake compared to others MOFs from this list.

Herein, we will compare these MOFs in terms of water adsorption capacity and amphiphilic balance. We will consider their adsorption capacity at different relative pressure ranges (Figure 41).

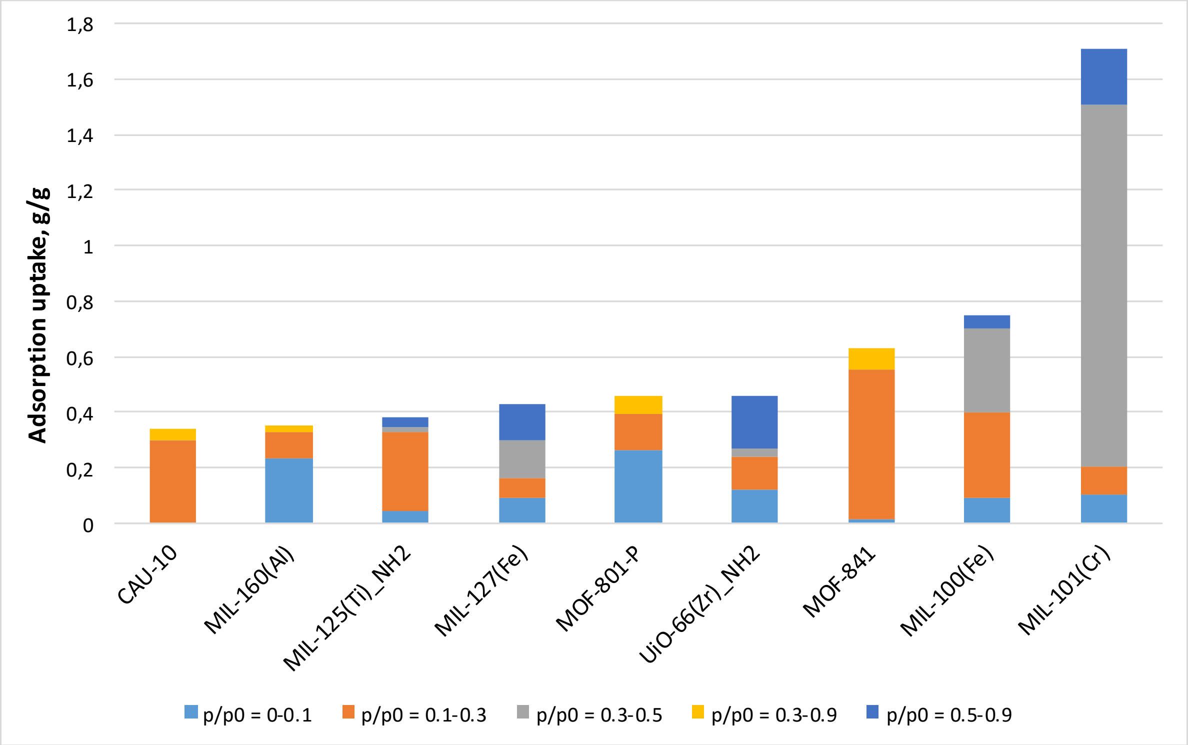

Figure 41. Water uptake capacity of water stable and recyclable MOFs in different pressure ranges: 0-0.1; 0.1-0.3; 0.3-0.5; 0.5-0.9. The large portion of water uptake capacity indicates that the pore filling or condensation occurs in this pressure range.

Furukawa *et al.* considered the potential of MOFs towards different type of application by separating three p/p_0 areas of adsorption: 0-0.1, 0.1-0.3 and 0.3-1 considering that only MOFs with adsorption below 0.3 are interesting for heat reallocation. However, Henninger *et al.* demonstrated that the relative pressure domain for heat transformation application could be extended up to 0.4 and even up to p/p_0=0.5 by using the minimal temperature of adsorption 20°C (see the example of MIL-100). In the other hand, for open system rector for space heating application adsorption loading may occur at p/p_0=0.5, since generally humid air (R.H. 50%, T=20°C) can be used for energy discharging step. Therefore, in order to compare the potential of

MOFs for heat reallocation we class it in terms of maximal uptake at p/p0=0.5 separating the new relative pressure area p/p0=0.3-0.5.

If one considers only relative pressure region below $p/p_0=0.3$, then water sorption capacity increases as follow: MIL-127(Fe), MIL-101(Cr), UiO-66(Zr)_NH_2, CAU-10, MIL-160(Al), MIL-125(Ti)_NH_2, MOF-801-P, MIL-100(Fe) and MOF-841. In case of enhanced relative pressure region (up to $p/p_0= 0.5$) the water uptake of these MOFs increases in the range: UiO-66(Zr)_NH_2, MIL-127(Fe), CAU-10, MIL-160(Al), MIL-125(Ti)_NH_2, MOF-801-P, MOF-841, MIL-100(Fe) and MIL-101(Cr).

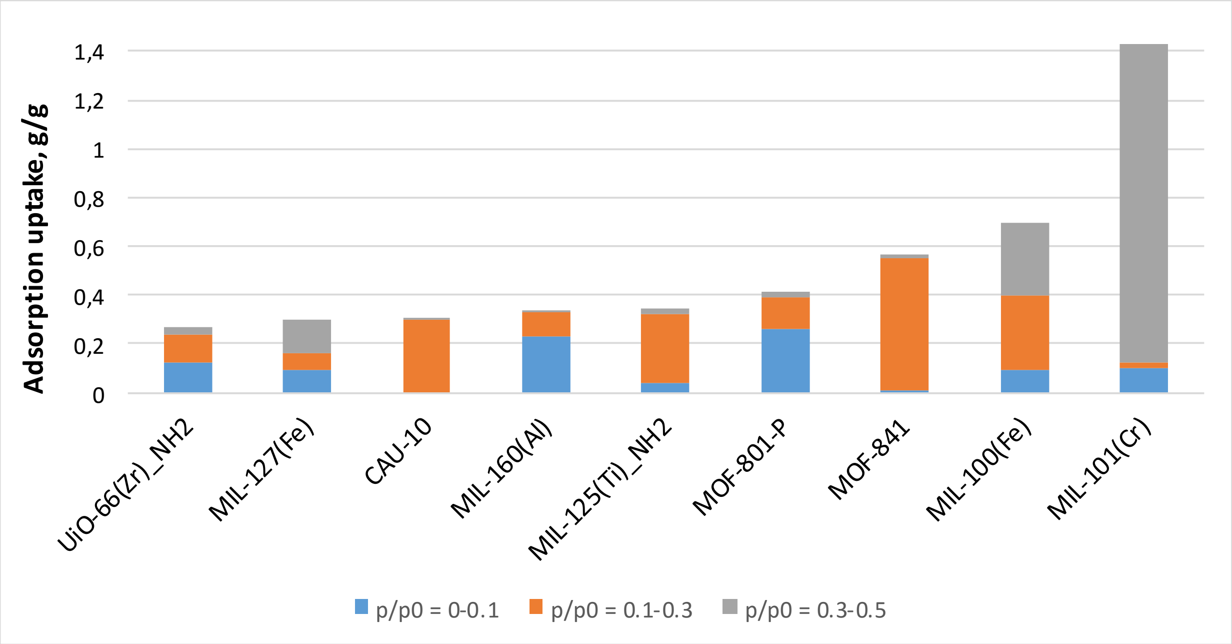

Figure 42. Water uptake capacity of water stable and recyclable MOFs in different pressure ranges: 0-0.1; 0.1-0.3; 0.3-0.5. The large portion of water uptake capacity indicates that the pore filling or condensation occurs in this pressure range.

For our experimental research we thus selected six MOFs with different features in terms of amphiphilic balance, porosity (mesoporous and microporous) and pore volume such as UiO-66(Zr)_NH_2, MIL-127(Fe), MIL-160(Al), MIL-125(Ti)_NH_2, MIL-100(Fe) and MIL-101(Cr). We didn't select CAU-10, but only MIL-160(Al), because MIL-160, isostructural form of CAU-10, possesses an improved water sorption capacity. We also didn't select MOF-801-P and MOF-841 for several reasons. First of all, these structures were reported recently (in 2014 then MOFs for our experimental work was already selected). Secondly, MOF-801-P has similar water sorption capacity compared to MIL-160(Al) and MIL-125(Ti)_NH_2. In case of MOF-841, its high cost together with low regeneration process precluded from its use.

Additionally, the stability of these two MOFs was studied during only five adsorption cycles, while in case of UiO-66(Zr)_NH_2, MIL-160(Al), MIL-125(Ti)_NH_2, MIL-100(Fe) and MIL-101(Cr) cycle stress experiment was effectuated during 10-40 cycles. Moreover, large-scale synthesis and procedure of shaping as pellets were already investigated for selected MOFs (UiO-66(Zr)_NH_2, MIL-160(Al), MIL-125(Ti)_NH_2, MIL-100(Fe) and MIL-101(Cr)).

References for Chapter I

[1] N. S. Lewis, *Science* **2007**, *315*, 798.

[2] Y. Ding, S. B. Riffat, *Int. J. Low-Carbon Technol.* **2013**, *8*, 106.

[3] Mehling H.,Cabeza L.F., *Heat and Cold Storage with PCM*, Springer Berlin Heidelberg, Berlin, Heidelberg, **2008**.

[4] A. Sharma, V. V. Tyagi, C. R. Chen, D. Buddhi, *Renew. Sustain. Energy Rev.* **2009**, *13*, 318.

[5] C. Bales, P. Gantenbein, D. Jaenig, H. Kerskes, K. Summer, M. van Essen, others, *Rep. IEA Sol. Heat. Cool. Programme-Task* **2008**, *32*.

[6] A. H. Abedin, M. A. Rosen, *Open Renew. Energy J* **2011**, *4*, 42.

[7] I. Dincer, *Int. J. Energy Res.* **2002**, *26*, 567.

[8] Hauer, A., Mehling, H., Schossig, P., Yamaha, M., Cabeza, L., *Implementing Agreement on Energy Conservation through Energy Storage, IEA Annex 17 Final Report*, **2001**.

[9] L. W. Wang, R. Z. Wang, R. G. Oliveira, *Renew. Sustain. Energy Rev.* **2009**, *13*, 518.

[10] N. C. Srivastava, I. W. Eames, *Appl. Therm. Eng.* **1998**, *18*, 707.

[11] H. Kawasaki, T. Watanabe, A. Kanzawa, *Appl. Therm. Eng.* **1999**, *19*, 133.

[12] Y. Kato, in *Therm. Energy Storage Sustain. Energy Consum.*, Springer, **2007**, pp. 377–391.

[13] H. Ö. Paksoy, Advanced Study Institute on Thermal Energy Storage for Sustainable Energy Consumption - Fundamentals, Case Studies and Design, Eds. , *Thermal Energy Storage for Sustainable Energy Consumption: Fundamentals, Case Studies and Design ; [proceedings of the NATO Advanced Study Institute on Thermal Energy Storage for Sustainable Energy Consumption - Fundamentals, Case Studies and Design, Izmir, Turkey, 6 - 17 June 2005]*, Springer, Dordrecht, **2007**.

[14] Hastings R, Wall M., *Sustainable Solar Housing: Exemplary Buildings and Technologies. IEA Energy Conservation in Buildings & Community Systems Programme*, **2007**.

[15] Hadorn J-C, **2005**.

[16] H. van Heyden, (Silico-) Aluminophosphates, lmu, **2008**.

[17] K. E. N'Tsoukpoe, H. Liu, N. Le Pierrès, L. Luo, *Renew. Sustain. Energy Rev.* **2009**, *13*, 2385.

[18] J. Ehrenmann, S. K. Henninger, C. Janiak, *Eur. J. Inorg. Chem.* **2011**, *2011*, 471.

[19] Y. I. Aristov, *Appl. Therm. Eng.* **2013**, *50*, 1610.

[20] Ogura, H., Miyazaki, M., Matsuda, H., Hasa tani, M., Yanadori, M. and Hiramatsu, M., **1991**, *17*, 916.

[21] Y. Kato, R. Takahashi, T. Sekiguchi, J. Ryu, *Int. J. Refrig.* **2009**, *32*, 661.

[22] Visscher K, Veldhuis JBJ, Oonk HAJ, **2004**.

[23] K. Visscher, J. B. J. Veldhuis, in *Ninth Int. IBPSA Conf. Montr. Can.*, **2005**.

[24] V. M. van Essen, H. A. Zondag, J. C. Gores, L. P. J. Bleijendaal, M. Bakker, R. Schuitema, W. G. J. van Helden, Z. He, C. C. M. Rindt, *J. Sol. Energy Eng.* **2009**, *131*, 041014.

[25] K. Posern, C. Kaps, *J. Therm. Anal. Calorim.* **2008**, *92*, 905.

[26] H. Stach, J. Mugele, J. Jänchen, E. Weiler, *Adsorption* **2005**, *11*, 393.

[27] C. C. M. Rindt, A. J. H. Frijns, J. G. Wijers, W. G. J. van Helden, **2007**.

[28] V. M. van Essen, M. Bakker, W. G. J. van Helden, **n.d.**

[29] C. Ferchaud, H. A. Zondag, R. de Boer, C. C. M. Rindt, in *Proc. 12th Int. Conf. Energy Storage Innostock 2012*, **2012**, pp. 16–19.

[30] S. Hongois, Stockage de Chaleur Inter-Saisonnier Par Voie Thermochimique Pour Le Chauffage Solaire de La Maison Individuelle, INSA de Lyon, **2011**.

[31] O. Opel, H. U. Rammelberg, M. Gérard, W. Ruck, in *Int. Conf. Sustain. Energy Storage IC-SES*, **2011**, pp. 21–24.

[32] F. Bertsch, B. Mette, S. Asenbeck, H. Kerskes, H. Müller-Steinhagen, in *Effstock Conf. Stockh.*, **2009**.

[33] van Essen VM, Gores C., Bleijendaal LPJ, Zondag HA, Schuitema R, van Helden WGJ, **2009**.

[34] de Boer R., Haije W.G., Veldhuis J.B.J., *Thermochim. Acta* **2003**, *395*, 3.

[35] Boer R.D., Haije W., Veldhuis J., **2004**.

[36] A. H. Abedin, M. A. Rosen, *Appl. Energy* **2012**, *93*, 18.

[37] H. Lahmidi, S. Mauran, V. Goetz, *Sol. Energy* **2006**, *80*, 883.

[38] Brunberg, *Method and System for Storing and Extracting Low-Temperature Heat Energy*, **1980**, US patent 4186794.

[39] DOW, *Chemical Brochure "Gas Dehydration with PELADOW Calcium Chloride,"* **n.d.**

[40] Zondag H.A., van Essen V.M., *Comparison of Reactors Concepts for Thermochemical Storage of Solar Energy*, **2008**.

[41] F. E. Marias, Analyse, Conception et Expérimentation de Procédés de Stockage Thermique Résidentiel de Longue Durée Par Réaction Thermochimique à Pression Atmosphérique, Université de Grenoble, **2014**.

[42] G. Balasubramanian, M. Ghommem, M. R. Hajj, W. P. Wong, J. A. Tomlin, I. K. Puri, *Int. J. Heat Mass Transf.* **2010**, *53*, 5700.

[43] B. Michel, Procédé Thermochimique Pour Le Stockage Intersaisonnier de L'énergie Solaire: Modélisation Multi-échelles et Expérimentation D'un Prototype Sous Air Humide, Université de Perpignan, **2012**.

[44] Wagman D., Evans W., Parker V., Schumm R., Halow I., Bailey S., Churney K., Nuttall R., *J. Phys. Chem. Ref. Data* **1982**, *11*.

[45] V. M. van Essen, L. P. J. Bleijendaal, B. W. J. Kikkert, H. A. Zondag, M. Bakker, P. W. Bach, in *Proc. EUROSUN*, **2010**.

[46] S. Mauran, H. Lahmidi, V. Goetz, *Sol. Energy* **2008**, *82*, 623.

[47] de Boer R., Haije W.G., Veldhuis J.B.J., *Determination of Structural, Thermodynamic and Phase Properties in the Na2S-H2O System for Application Ina Chemical Heat Pump*, **2002**.

[48] K. Iammak, W. Wongsuwan, T. Kiatsiriroj, in *Proceeding Jt. Int. Conf. Sustain. Energy Environ. SEE*, **2004**.

[49] M. Harmelin, *J. Therm. Anal.* **1969**, *1*, 137.

[50] D. Stitou, Transformation, Conversion, Stockage, Transport de L'énergie Thermique Par Procédés Thermochimiques et Thermo-Hydrauliques, Université de Perpignan, **2013**.

[51] F. Mauss, M. Murat, J.-M. Missiaen, B. Guilhot, *J. Therm. Anal. Calorim.* **1996**, *47*, 799.

[52] Mauss F., Murat M., Missiaen J.M., Guilhot B., *J. Therm. Anal.* **1996**.

[53] L. G. Gordeeva, A. Freni, Y. I. Aristov, G. Restuccia, *Ind. Eng. Chem. Res.* **2009**, *48*, 6197.

[54] Y. I. Aristov, M. M. Tokarev, A. Freni, I. S. Glaznev, G. Restuccia, *Microporous Mesoporous Mater.* **2006**, *96*, 65.

[55] K. C. Ng, H. T. Chua, C. Y. Chung, C. H. Loke, T. Kashiwagi, A. Akisawa, B. B. Saha, *Appl. Therm. Eng.* **2001**, *21*, 1631.

[56] B. Dawoud, Y. Aristov, *Int. J. Heat Mass Transf.* **2003**, *46*, 273.

[57] B. B. Saha, A. Chakraborty, S. Koyama, Y. I. Aristov, *Int. J. Heat Mass Transf.* **2009**, *52*, 516.

[58] G. Restuccia, G. Cacciola, R. Quagliata, *Int. J. Energy Res.* **1988**, *12*, 101.

[59] R. E. Critoph, R. Vogel, *Int. J. Ambient Energy* **1986**, *7*, 183.

[60] S. K. Henninger, F. Jeremias, H. Kummer, P. Schossig, H.-M. Henning, *Energy Procedia* **2012**, *30*, 279.

[61] S. T. Wilson, B. M. Lok, C. A. Messina, T. R. Cannan, E. M. Flanigen, *J. Am. Chem. Soc.* **1982**, *104*, 1146.

[62] S. Shimooka, K. Oshima, H. Hidaka, T. Takewaki, H. Kakiuchi, A. Kodama, M. Kubota, H. Matsuda, *J. Chem. Eng. Jpn.* **2007**, *40*, 1330.

[63] Kakiuchi H., Shimooka S., Iwade M., Oshima K., Yamazaki M., Terada S., Watanabe H., Takewaki T., *KAGAKU KOGAKU RONBUNSHU* **2005**, *31*, 361.

[64] A. Ristić, N. Z. Logar, S. K. Henninger, V. Kaučič, *Adv. Funct. Mater.* **2012**, *22*, 1952.

[65] S. G. Izmailova, E. A. Vasiljeva, I. V. Karetina, N. N. Feoktistova, S. S. Khvoshchev, *J. Colloid Interface Sci.* **1996**, *179*, 374.

[66] E.-P. Ng, S. Mintova, *Microporous Mesoporous Mater.* **2008**, *114*, 1.

[67] E. A. Vasil'eva, S. P. Zhdanov, S. Y. Zinov'ev, E. I. Smirnova, N. N. Feoktistova, *Bull. Acad. Sci. USSR Div. Chem. Sci.* **1989**, *38*, 2213.

[68] Y. I. Aristov, M. M. Tokarev, G. Restuccia, G. Cacciola, *React Kinet Catal Lett* **1996**, *59*, 325.

[69] Y. I. Aristov, M. M. Tokarev, G. Restuccia, G. Cacciola, *React Kinet Catal Lett* **1996**, *59*, 335.

[70] E. Levitskij, *Sol. Energy Mater. Sol. Cells* **1996**, *44*, 219.

[71] Y. I. Aristov, *J. Chem. Eng. Jpn.* **2007**, *40*, 1242.

[72] Y. I. Aristov, J. Di. Marco, M. M. Tokarev, N. V. Parmon, *React Kinet Catal Lett* **1997**, *61*, 147.

[73] I. A. Simonova, Y. I. Aristov, *Rus J Phys Chem* **2005**, *79*, 1307.

[74] I. A. Simonova, A. Freni, G. Restuccia, Y. I. Aristov, *Microporous Mesoporous Mater.* **2009**, *122*, 223.

[75] L. Gordeeva, A. Grekova, T. Krieger, Y. Aristov, *Appl. Therm. Eng.* **2013**, *50*, 1633.

[76] S. Hongois, Stockage de Chaleur Inter-Saisonnier Par Voie Thermochimique Pour Le Chauffage Solaire de La Maison Individuelle, INSA de Lyon, **2011**.

[77] Rambaud G., Mauran S., Mazet N., **2007**.

[78] Kerskes H., Mette B., Bertsch F., Asenbeck S., Druck H., *Thermische Solarenergie:: 19. Symposium; 06. bis 08. Mai 2009, Kloster Banz, Bad Staffelstein. Hauptbd. [...]*, OTTI, Regensburg, **2009**.

[79] G. Whiting, D. Grondin, S. Bennici, A. Auroux, *Sol. Energy Mater. Sol. Cells* **2013**, *112*, 112.

[80] J. Jänchen, D. Ackermann, H. Stach, W. Brösicke, *Sol. Energy* **2004**, *76*, 339.

[81] J. Jänchen, D. Ackermann, E. Weiler, H. Stach, W. Brösicke, *Thermochim. Acta* **2005**, *434*, 37.

[82] I. V. Ponomarenko, I. S. Glaznev, A. V. Gubar, Y. I. Aristov, S. D. Kirik, *Microporous Mesoporous Mater.* **2010**, *129*, 243.

[83] I. Glaznev, I. Ponomarenko, S. Kirik, Y. Aristov, *Int. J. Refrig.* **2011**, *34*, 1244.

[84] L. G. Gordeeva, I. S. Glaznev, E. V. Savchenko, V. V. Malakhov, Y. I. Aristov, *J. Colloid Interface Sci.* **2006**, *301*, 685.

[85] K. C. Chan, C. Y. H. Chao, G. N. Sze-To, K. S. Hui, *Int. J. Heat Mass Transf.* **2012**, *55*, 3214.

[86] A. Ristić, D. Maučec, S. K. Henninger, V. Kaučič, *Microporous Mesoporous Mater.* **2012**, *164*, 266.

[87] R. Cuypers, N. Maraz, J. Eversdijk, C. Finck, E. Henquet, H. Oversloot, H. van't Spijker, A. de Geus, *Energy Procedia* **2012**, *30*, 207.

[88] A. Lass-Seyoum, M. Blicker, D. Borozdenko, T. Friedrich, T. Langhof, *Energy Procedia* **2012**, *30*, 310.

[89] Ostbayerisches Technologie-Transfer-Institut, Ed. , *Thermische Solarenergie:: 19. Symposium; 06. bis 08. Mai 2009, Kloster Banz, Bad Staffelstein. Hauptbd. [...]*, OTTI, Regensburg, **2009**.

[90] H. A. Zondag, V. M. Van Essen, L. P. J. Bleijendaal, B. W. J. Kikkert, M. Bakker, in *Proc. IRES 2010 Conf. Berl.*, **2010**.

[91] G. Férey, *Chem Soc Rev* **2008**, *37*, 191.

[92] G. Férey, C. Mellot-Draznieks, C. Serre, F. Millange, *Acc. Chem. Res.* **2005**, *38*, 217.

[93] *Chem. Soc. Rev.* **2009**, *38*, 1201.

[94] S. K. Henninger, F. Jeremias, H. Kummer, C. Janiak, *Eur. J. Inorg. Chem.* **2012**, *2012*, 2625.

[95] J. J. Low, A. I. Benin, P. Jakubczak, J. F. Abrahamian, S. A. Faheem, R. R. Willis, *J. Am. Chem. Soc.* **2009**, *131*, 15834.

[96] F. Jeremias, D. Fröhlich, C. Janiak, S. K. Henninger, *New J. Chem.* **2014**, *38*, 1846.

[97] C. Janiak, *Dalton Trans.* **2003**, 2781.

[98] C. Janiak, J. K. Vieth, *New J. Chem.* **2010**, *34*, 2366.

[99] A. U. Czaja, N. Trukhan, U. Müller, *Chem. Soc. Rev.* **2009**, *38*, 1284.

[100] M. J. Prakash, M. S. Lah, *Chem. Commun.* **2009**, 3326.

[101] J.-R. Li, R. J. Kuppler, H.-C. Zhou, *Chem. Soc. Rev.* **2009**, *38*, 1477.

[102] M. P. Suh, H. J. Park, T. K. Prasad, D.-W. Lim, *Chem. Rev.* **2012**, *112*, 782.

[103] L. J. Murray, M. Dincă, J. R. Long, *Chem. Soc. Rev.* **2009**, *38*, 1294.

[104] J. Della Rocca, D. Liu, W. Lin, *Acc. Chem. Res.* **2011**, *44*, 957.

[105] P. Horcajada, R. Gref, T. Baati, P. K. Allan, G. Maurin, P. Couvreur, G. Férey, R. E. Morris, C. Serre, *Chem. Rev.* **2012**, *112*, 1232.

[106] *Chem. Soc. Rev.* **2009**, *38*, 1203.

[107] H.-C. Zhou, J. R. Long, O. M. Yaghi, *Chem. Rev.* **2012**, *112*, 673.

[108] F. Jeremias, V. Lozan, S. K. Henninger, C. Janiak, *Dalton Trans.* **2013**, *42*, 15967.

[109] C. Janiak, S. K. Henninger, *Chim. Int. J. Chem.* **2013**, *67*, 419.

[110] J.-P. Zhang, A.-X. Zhu, R.-B. Lin, X.-L. Qi, X.-M. Chen, *Adv. Mater.* **2011**, *23*, 1268.

[111] F. Jeremias, A. Khutia, S. K. Henninger, C. Janiak, *J Mater Chem* **2012**, *22*, 10148.

[112] M. F. de Lange, B. L. van Velzen, C. P. Ottevanger, K. J. F. M. Verouden, L.-C. Lin, T. J. H. Vlugt, J. Gascon, F. Kapteijn, *Langmuir* **2015**, *31*, 12783.

[113] N. C. Burtch, H. Jasuja, K. S. Walton, *Chem. Rev.* **2014**, *114*, 10575.

[114] J. B. DeCoste, G. W. Peterson, B. J. Schindler, K. L. Killops, M. A. Browe, J. J. Mahle, *J. Mater. Chem. A* **2013**, *1*, 11922.

[115] V. Guillerm, F. Ragon, M. Dan-Hardi, T. Devic, M. Vishnuvarthan, B. Campo, A. Vimont, G. Clet, Q. Yang, G. Maurin, G. Férey, A. Vittadini, S. Gross, C. Serre, *Angew. Chem. Int. Ed.* **2012**, *51*, 9267.

[116] H.-L. Jiang, D. Feng, K. Wang, Z.-Y. Gu, Z. Wei, Y.-P. Chen, H.-C. Zhou, *J. Am. Chem. Soc.* **2013**, *135*, 13934.

[117] D. Feng, Z.-Y. Gu, J.-R. Li, H.-L. Jiang, Z. Wei, H.-C. Zhou, *Angew. Chem. Int. Ed.* **2012**, *51*, 10307.

[118] D. Feng, W.-C. Chung, Z. Wei, Z.-Y. Gu, H.-L. Jiang, Y.-P. Chen, D. J. Darensbourg, H.-C. Zhou, *J. Am. Chem. Soc.* **2013**, *135*, 17105.

[119] V. Bon, V. Senkovskyy, I. Senkovska, S. Kaskel, *Chem. Commun.* **2012**, *48*, 8407.

[120] V. Bon, I. Senkovska, I. A. Baburin, S. Kaskel, *Cryst. Growth Des.* **2013**, *13*, 1231.

[121] W. Morris, B. Volosskiy, S. Demir, F. Gándara, P. L. McGrier, H. Furukawa, D. Cascio, J. F. Stoddart, O. M. Yaghi, *Inorg. Chem.* **2012**, *51*, 6443.

[122] J. A. Greathouse, M. D. Allendorf, *J. Am. Chem. Soc.* **2006**, *128*, 10678.

[123] H. Irving, R. J. P. Williams, *J. Chem. Soc. Resumed* **1953**, 3192.

[124] H. Liu, N. K. Edem, L. P. Nolwenn, L. Lingai, *Energy Convers. Manag.* **2011**, *52*, 2427.

[125] A. C. Kizzie, A. G. Wong-Foy, A. J. Matzger, *Langmuir* **2011**, *27*, 6368.

[126] L. Pauling, *J. Am. Chem. Soc.* **1929**, *51*, 1010.

[127] H. J. Choi, M. Dincă, A. Dailly, J. R. Long, *Energy Env. Sci* **2010**, *3*, 117.

[128] V. Colombo, S. Galli, H. J. Choi, G. D. Han, A. Maspero, G. Palmisano, N. Masciocchi, J. R. Long, *Chem. Sci.* **2011**, *2*, 1311.

[129] Hilal, S. H., (Prénom) Karickhoff, S. W., Carreira, L. A., *Quant Struct-Act Relat* **1995**, *14*, 348.

[130] R. G. Pearson, *J. Am. Chem. Soc.* **1963**, *85*, 3533.

[131] S. Lincoln, *Helv. Chim. Acta* **2005**, *88*, 523.

[132] J. M. Taylor, R. Vaidhyanathan, S. S. Iremonger, G. K. H. Shimizu, *J. Am. Chem. Soc.* **2012**, *134*, 14338.

[133] T. Wu, L. Shen, M. Luebbers, C. Hu, Q. Chen, Z. Ni, R. I. Masel, *Chem. Commun.* **2010**, *46*, 6120.

[134] T. A. Makal, X. Wang, H.-C. Zhou, *Cryst. Growth Des.* **2013**, *13*, 4760.

[135] J. G. Nguyen, S. M. Cohen, *J. Am. Chem. Soc.* **2010**, *132*, 4560.

[136] J. Yang, A. Grzech, F. M. Mulder, T. J. Dingemans, *Chem. Commun.* **2011**, *47*, 5244.

[137] T.-H. Chen, I. Popov, O. Zenasni, O. Daugulis, O. Š. Miljanić, *Chem. Commun.* **2013**, *49*, 6846.

[138] C. Serre, *Angew. Chem. Int. Ed.* **2012**, *51*, 6048.

[139] T. Li, D.-L. Chen, J. E. Sullivan, M. T. Kozlowski, J. K. Johnson, N. L. Rosi, *Chem. Sci.* **2013**, *4*, 1746.

[140] Y. Cai, Y. Zhang, Y. Huang, S. R. Marder, K. S. Walton, *Cryst. Growth Des.* **2012**, *12*, 3709.

[141] H. Liu, Y. Zhao, Z. Zhang, N. Nijem, Y. J. Chabal, X. Peng, H. Zeng, J. Li, *Chem. - Asian J.* **2013**, *8*, 778.

[142] T.-H. Chen, I. Popov, W. Kaveevivitchai, O. Š. Miljanić, *Chem. Mater.* **2014**, *26*, 4322.

[143] H. Jasuja, K. S. Walton, *Dalton Trans.* **2013**, *42*, 15421.

[144] T. Birsa Čelič, M. Mazaj, N. Guillou, E. Elkaïm, M. El Roz, F. Thibault-Starzyk, G. Mali, M. Rangus, T. Čendak, V. Kaučič, N. Zabukovec Logar, *J. Phys. Chem. C* **2013**, *117*, 14608.

[145] L. Bellarosa, J. J. Gutiérrez-Sevillano, S. Calero, N. López, *Phys. Chem. Chem. Phys.* **2013**, *15*, 17696.

[146] H. Jasuja, Y. Huang, K. S. Walton, *Langmuir* **2012**, *28*, 16874.

[147] D. I. Kolokolov, A. G. Stepanov, V. Guillerm, C. Serre, B. Frick, H. Jobic, *J. Phys. Chem. C* **2012**, *116*, 12131.

[148] H.-L. Jiang, D. Feng, T.-F. Liu, J.-R. Li, H.-C. Zhou, *J. Am. Chem. Soc.* **2012**, *134*, 14690.

[149] J. Duan, M. Higuchi, S. Horike, M. L. Foo, K. P. Rao, Y. Inubushi, T. Fukushima, S. Kitagawa, *Adv. Funct. Mater.* **2013**, *23*, 3525.

[150] F.-X. Coudert, *Chem. Mater.* **2015**, *27*, 1905.

[151] G. Férey, C. Serre, *Chem. Soc. Rev.* **2009**, *38*, 1380.

[152] C. R. Murdock, B. C. Hughes, Z. Lu, D. M. Jenkins, *Coord. Chem. Rev.* **2014**, *258-259*, 119.

[153] P. Küsgens, M. Rose, I. Senkovska, H. Fröde, A. Henschel, S. Siegle, S. Kaskel, *Microporous Mesoporous Mater.* **2009**, *120*, 325.

[154] Soubeyrand-Leonoir, Estelle, Adsorption et Separation de Gaz En Mode Dynamique Sur Des Materiaux Hybrides, **2012**.

[155] Y. Cheng, A. Kondo, H. Noguchi, H. Kajiro, K. Urita, T. Ohba, K. Kaneko, H. Kanoh, *Langmuir* **2009**, *25*, 4510.

[156] F. Gul-E-Noor, B. Jee, A. Pöppl, M. Hartmann, D. Himsl, M. Bertmer, *Phys. Chem. Chem. Phys.* **2011**, *13*, 7783.

[157] B. Mu, K. S. Walton, *J. Phys. Chem. C* **2011**, *115*, 22748.

[158] Hubert Chevreau, Anastasia Permyakova, Farid Nouar, Paul Fabry, Carine Livage, Florence Ragon, Alfonso Garcia-Marquez, Thomas Devic, Nathalie Steunou, Christian Serre, Patricia Horcajada, *CrystEngComm* **n.d.**, Manuscript ID: CE.

[159] H. Furukawa, F. Gándara, Y.-B. Zhang, J. Jiang, W. L. Queen, M. R. Hudson, O. M. Yaghi, *J. Am. Chem. Soc.* **2014**, *136*, 4369.

[160] A. Cadiau, J. S. Lee, D. Damasceno Borges, P. Fabry, T. Devic, M. T. Wharmby, C. Martineau, D. Foucher, F. Taulelle, C.-H. Jun, Y. K. Hwang, N. Stock, M. F. De Lange, F. Kapteijn, J. Gascon, G. Maurin, J.-S. Chang, C. Serre, *Adv. Mater.* **2015**, *27*, 4775.

[161] D. Fröhlich, S. K. Henninger, C. Janiak, *Dalton Trans* **2014**, *43*, 15300.

[162] M. F. de Lange, C. P. Ottevanger, M. Wiegman, T. J. H. Vlugt, J. Gascon, F. Kapteijn, *CrystEngComm* **2015**, *17*, 281.

[163] H. Reinsch, M. A. van der Veen, B. Gil, B. Marszalek, T. Verbiest, D. de Vos, N. Stock, *Chem. Mater.* **2013**, *25*, 17.

[164] C. Volkringer, T. Loiseau, M. Haouas, F. Taulelle, D. Popov, M. Burghammer, C. Riekel, C. Zlotea, F. Cuevas, M. Latroche, D. Phanon, C. Knöfelv, P. L. Llewellyn, G. Férey, *Chem. Mater.* **2009**, *21*, 5783.

[165] **n.d.**

[166] F. Jeremias, V. Lozan, S. K. Henninger, C. Janiak, *Dalton Trans.* **2013**, *42*, 15967.

[167] G. E. Cmarik, M. Kim, S. M. Cohen, K. S. Walton, *Langmuir* **2012**, *28*, 15606.

[168] H. Jasuja, J. Zang, D. S. Sholl, K. S. Walton, *J. Phys. Chem. C* **2012**, *116*, 23526.

[169] P. M. Schoenecker, C. G. Carson, H. Jasuja, C. J. J. Flemming, K. S. Walton, *Ind. Eng. Chem. Res.* **2012**, *51*, 6513.

[170] A. D. Wiersum, E. Soubeyrand-Lenoir, Q. Yang, B. Moulin, V. Guillerm, M. B. Yahia, S. Bourrelly, A. Vimont, S. Miller, C. Vagner, M. Daturi, G. Clet, C. Serre, G. Maurin, P. L. Llewellyn, *Chem. - Asian J.* **2011**, *6*, 3270.

[171] C. Zlotea, D. Phanon, M. Mazaj, D. Heurtaux, V. Guillerm, C. Serre, P. Horcajada, T. Devic, E. Magnier, F. Cuevas, G. Férey, P. L. Llewellyn, M. Latroche, *Dalton Trans.* **2011**, *40*, 4879.

[172] M. Dan-Hardi, C. Serre, T. Frot, L. Rozes, G. Maurin, C. Sanchez, G. Férey, *J. Am. Chem. Soc.* **2009**, *131*, 10857.

[173] A. Khutia, H. U. Rammelberg, T. Schmidt, S. Henninger, C. Janiak, *Chem. Mater.* **2013**, *25*, 790.

[174] S. K. Henninger, G. Munz, K.-F. Ratzsch, P. Schossig, *Renew. Energy* **2011**, *36*, 3043.

[175] Y.-K. Seo, J. W. Yoon, J. S. Lee, Y. K. Hwang, C.-H. Jun, J.-S. Chang, S. Wuttke, P. Bazin, A. Vimont, M. Daturi, S. Bourrelly, P. L. Llewellyn, P. Horcajada, C. Serre, G. Férey, *Adv. Mater.* **2012**, *24*, 806.

[176] G. Wißmann, A. Schaate, S. Lilienthal, I. Bremer, A. M. Schneider, P. Behrens, *Microporous Mesoporous Mater.* **2012**, *152*, 64.

Chapter II

Laboratory pilot scale evaluation of the heat reallocation properties of the robust hydrophilic Al dicarboxylate Metal Organic Framework MIL-160(Al)

Chapter II: Laboratory pilot scale evaluation of the heat reallocation properties of the robust hydrophilic Al dicarboxylate Metal Organic Framework MIL-160(Al).

This work is described in the format of a research article. In this chapter we analyse the energy storage capacity of a hydrophilic water stable Al dicarboxylate MOF through a laboratory pilot scale prototype. As mentioned in Chapter I, previous studies were mainly focused on the development of MOFs for heat transformation purposes. First, we will provide a brief introduction to clarify the contribution of each collaborator.

Author contribution

In a first step, following our initial selection of MOFs materials (Chapter I), we have evaluated the thermochemical energy storage properties of a series of stable MOFs bearing mesopores (i. e. MIL-100(Fe), MIL-101(Cr)), or micropores (i. e. MIL-127(Fe), MIL-160(Al), MIL-125-(Ti)-NH_2, UiO-66(Zr)-NH_2) materials, before paying a particular attention to the highly hydrophilic microporous MIL-160(Al) candidate.

This work implies the synthesis of MOFs, assessment of their water sorption properties under operating cycle conditions (adsorption and cycling loading lifts), measurements of their heats of adsorption and water sorption isotherms, calculation of their energy storage capacities. In a second step, a scale-up of the synthesis and shaping of the best candidate was performed followed finally by the evaluation of its energy storage properties in a laboratory pilot-scale prototype.

I have synthesized and characterized the MIL-100(Fe), MIL-101(Cr), MIL-127(Fe) and MIL-160(Al) solids while the synthesis of MIL-125-(Ti)-NH_2 and UiO-66-NH_2 was performed by Dr. Sujing Wang (post doctoral fellow at UVSQ). I have measured the cycling loading lifts of all the MOFs under operating cycle conditions of energy storage device at the University of Mons. The heat of adsorption measurements and water sorption isotherms at 25°C of MOFs were carried out by Dr. Sandrine Bourrelly (MADIREL, University Aix-Marseille UMR CNRS 7246). Basing on the cycle loading lifts and heat of adsorption measurements, I have calculated the energy storage capacities. According to the energy storage capacity values, MIL-160(Al) was selected as the most promising MOFs. Moreover, this material is of special interest due to its very good hydrothermal stability, low cost and low toxicity as well as its possible scale-up production and shaping. The optimal synthetic conditions at the multi gram scale were developed by Maame Affram (Master 1 student project, UVSQ) under the supervision of Dr. Georges Mouchaham and Dr. Thomas Devic (UVSQ). I have optimized the larger scale synthesis of this MOF (200 gram scale). In order to get enough material for the shaping, a similar synthesis at the large scale was carried out in the team of Dr Jong-San Chang, by Dr U-Hwang Lee and Anil H. Valekar (Korea Research Institute of Chemical Technology, KRICT, Daejon, Korea). They also carried out the shaping of MIL-160(Al) in the form of pellets through a wet granulation method. The water sorption isotherms of pellet-shaped MIL-160(Al) at different temperatures (T=20-80°C with step of 10°C) were measured by Dr. Emilie Courbon (University of Mons). I have finally studied with Dr. Alexandre Srylnyk the heat reallocation properties of MIL-160(Al) using the pilot scale prototype in University Mons (UMons, Department of thermodynamics).

Article: Laboratory pilot scale evaluation of the heat reallocation properties of the robust hydrophilic Al dicarboxylate Metal Organic Framework MIL-160(Al)

1. Introduction

Nowadays the need for a better use of renewable heat appeals for energy storage, heat pumping and heat transformation technologies with increased performances. As far as sorption technologies are concerned, new developments require novel adsorption materials with enhanced properties. Energy reallocation concept is based on a heat storage process at very short (minutes), short (hours) and middle to long term (days to inter seasonal). All applications are based on the same principle of the adsorption heat release (adsorbent), when considering physical adsorbent as energy storage material. Among currently investigated physical sorption materials for energy reallocation such as zeolites, silica gel, and aluminophosphates, Metal Organic Frameworks (MOFs) are a recent class of highly promising hybrid crystalline sorbents. Besides a suitable stability under numerous working cycles, the major requirements for energy storage materials are a high adsorption uptake at relatively low relative pressure and regeneration under mild conditions (desorption with the 80-100°C range). For example, silica gels can be regenerated at very low temperature (< 45-50 °C), whereas its low sorption capacity results in poor loading lift (0.03-0.10 g/g) within typical adsorption heat pump (AHP) cycle.[1] On the contrary, high water affinity of cationic zeolites yields typically to large sorption uptakes at low values of the relative pressure, with however an energy demanding regeneration (> 140°C).[2] Silico-aluminophosphates provide better features for AHT with loading lifts close to 0.20 g/g at low relative pressure together with a moderate regeneration temperature of 90°C; however, one could point out their relatively costly synthesis compared to zeolites or silica gels.[3]

MOFs are porous crystalline hybrid materials that could be considered as interesting alternative candidates for heat reallocation. Owing to their higher degree of versatility in terms of chemical functionality, (micro)structural properties (high specific surface, pore size, and shape), and physico-chemical properties (hydrophilicity, water stability), MOFs can be regenerated in most cases at relatively low temperatures while their water sorption behavior can be easily tuned in terms of water sorption capacity as well as position of the adsorption step (p/p_0).[4] All these features make them promising candidates for heat reallocation based on water adsorption.

As recently reported[5], one of the most promising MOF candidates for heat reallocation is the highly hydrophilic and hydrothermally stable bio-sourced porous Al dicarboxylate solid MIL-160(Al) or $Al(OH)[O_2C-C_4H_2O-CO_2]$ (Figure 1) (MIL stands for Materials from Institut Lavoisier).

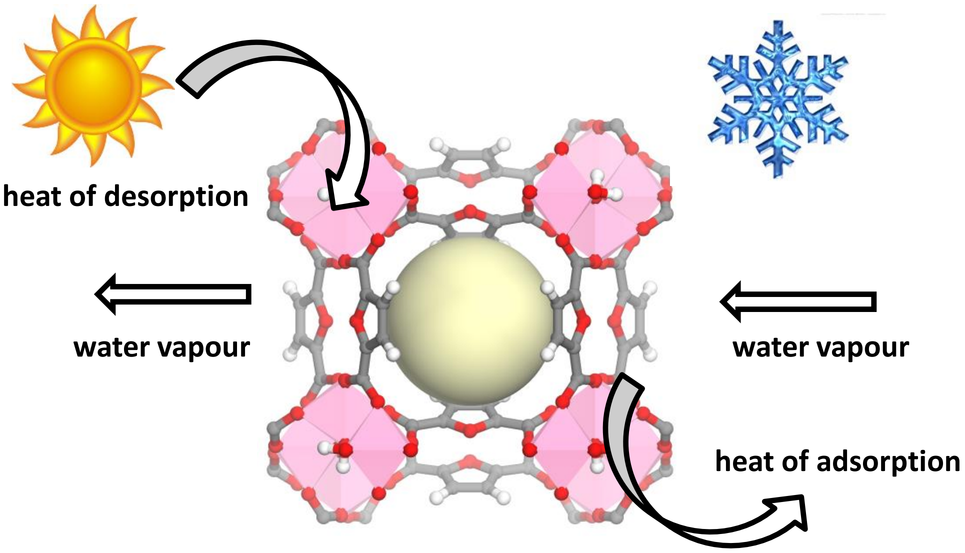

Figure 1. Schematic view of MIL-160(Al) for seasonal energy storage application. Al polyhedra, oxygen, carbon and hydrogen atoms are in pink, red, grey and white, respectively.

Its structure consists of helical cis-corner-sharing chains of $AlO_4(OH)_2$ octahedra connected via 2,5-furandicarboxylate groups. This delimits 1D microporous square shaped sinusoidal channels of free aperture close to ~5 Å in diameter. Besides its enhanced hydrophilic character mainly due to the concomitant presence of weak Brønsted -OH sites, an heterocyclic ring within narrow pores, it is noteworthy that the linker is derived from a renewable biomass feedstock, and is already on the way to be produced at a large industrial scale which might lead in a near future to a strong decrease the overall production cost of MIL-160(Al).

This MOF has previously demonstrated its strong interest for heat reallocation due to its very a high loading lift within typical adsorption heat pump (AHT) cycle (adsorption at 40°C and 1.2 kPa, and desorption at 95°C and 5.6 kPa) exceeding slightly the value of the commercial porous solid SAPO-34, as well as its excellent stability.[5]

In the present study, water cycling loading lifts of a series of water stable porous MOFs, based on high valence metal cations (Al^{3+}, Fe^{3+}, Ti^{4+}, Zr^{4+}, Cr^{3+}) and polycarboxylates aromatic linkers have been considered. This includes the mesoporous MOFs MIL-100(Fe)[6], and MIL-101(Cr)[7], and microporous solids such as MIL-160(Al)[5], MIL-127(Fe), MIL-125(Ti)_NH_2[4] and UiO-66(Zr)_NH_2[4]). The sorption tests were performed in the typical conditions of seasonal energy storage device. We calculated the energy storage capacity of these MOFs-series using data of cycling loading lifts and heat of adsorption measurements in order to select the most promising candidate. It turned out that MIL-160(Al) and MIL-125(Ti)_NH_2 provided the highest energy storage capacity. However, due to its eco-compatible (water as solvent, biosourced linker), hydrothermal stability, cheap and easy scalable synthesis (reflux, high Space Time Yield (STY)), MIL-160(Al) was finally selected in a view of a pilot scale heat reallocation laboratory prototype.

In order to obtain a sufficient amount of this MOF for the pilot test, we optimized its synthesis route prior to perform its larger scale synthesis (~400 g scale). The powder was then shaped through a wet granulation route in order to obtain 250 g of granules of a 0.5-1 mm size suitable for the pilot scale open reactor prototype tests to probe its performances for space heating applications. These experiments have revealed that MIL-160(Al) exhibits one of the best energy storage density (~140 kWh/m^3) among physical sorption materials (Table 1).

2. Experimental

2.1. Synthesis

Optimized synthetic conditions and large scale production of MIL-160(Al):

In a round bottom flask (250 ml) containing 75 ml of distilled water were introduced 75 mmol of $Al(OH)(CH_3COO)_2$ (11.71 g) (Aldrich, 90%) and 75 mmol of 2,5-furandicarboxylic acid (12.16 g). Then, the mixture was stirred under reflux for *ca.* 24 hrs. The resulting white solid was recovered by filtration, washed with of ethanol and dried in the oven at 100°C to give 13.9 g of dry MIL-160(Al) (yield = 93% and STY = 185 $kg{\cdot}m^{-3}{\cdot}day^{-1}$). This procedure was then used to prepare a larger amount of MIL-160(Al) multiplying all amounts by *ca.* 10 times using 2L round bottom flask.

Shaping of MIL-160(Al)

The shaping of MIL-160(Al) was prepared using the conventional wet granulation method recently reported for MIL-100(Fe).[8] A known amount of MIL-160 powder was mixed with a 10% silica sol (Aldrich Co.) solution as a binder using a pan-type granulator (GebruderLodige, Maschinenbau GmbH D-33102). Typically, the granulation is performed by a wetting process of the mixture in the rotating fan (Marumerizer, FUJI PAUDAL Co. LTD, QJ-230) to enhance the spherical shape. Finally, the granules (spheres) were dried at 100°C for 12 h in order to remove the residual water.

2.2 Characterization of MIL-160(Al)

Powder X-ray diffraction patterns were collected on a Siemens D5000 diffractometer using CuKα1,2 radiation (λ=1.5406Å).

Nitrogen adsorption-desorption isotherms measured on Belsorp Mini (Bel, Japan) at liquid nitrogen temperature (77 K). Prior to the analysis, samples were degassed for 12 h at 150°C under primary vacuum. BET surface areas and micropore volumes were calculated at a relative pressure below 0.25.

Thermogravimetric (TG) measurements were carried out on thermogravimetric analyzer (Perkin Elmer Diamond TGA/DTA STA 6000) with oxygen flow of 200 ml/min. The temperature was increased from 30°C to 600°C.

SEM-EDX analysis was performed on a JEOL JSM-7001F microscope using gold-coated samples equipped with an energy-dispersive X-ray (EDX) spectrometer and a X-Max SDD (Silicon Drift Detector) by Oxford.

Cycling loading lift measurements

The cycling loading lift measurements (water exchange between the production cycle (adsorption) and regeneration cycle (desorption)) were performed using thermogravimetric analyzer (TG-DSC111) connected with generator of humidity Setaram with RH stability of ±

0.3 %. The operating conditions of cycle were selected as following: water pressure p=1.25 kPa, adsorption temperature T_a=30°C, desorption temperature T_d=80°C. The sample was first dried for 12 h under vacuum at T=150°C. After this drying step, the sample was cooled down to 30°C and previously humidified nitrogen gas flow (humidity generator at T=40°C and relative humidity RH=17.4%) was passed through the thermogravimetric balance. The adsorption profiles were collected at 30°C in humid nitrogen at 1.25 kPa during 20-30 hours (depending on the sample). The desorption step was performed at 80 °C at 1.25 kPa during 12 hours.

Water sorption isotherm measurements (IGASorp)

Water sorption isotherms at different temperatures (20-80°C) were recorded using an Intelligent Gravimetric Analyzer (IGASorp Moisture Sorption Analyzer). The IGASorp allows precisely controlling the water vapor pressure (1-95 RH% with the accuracy of ± 0.1% RH) and temperature (5-80°C with the accuracy of ±0.1°C). For the first step, sample was dried for 12 h under N_2 flow at T=150°C. Then, adsorption measurement was performed at fixed temperature in defined RH range. After each isotherm measurement the sample was dehydrated (T=150°C, 8h) before being submitted to the next adsorption measurement.

Experiments in open system reactor prototype

The pilot test was performed on 201 gram of dry MIL-160 (pretreatment in an oven at T=150°C , 12h) shaped into granules in a prototype which represents an open heat storage system (adsorption column with air as a carrier gas). The energy production cycle (adsorption) was performed with the following controlled inlet air conditions (temperature: 30°C, air relative humidity of 50% (calculated at 20 °C) and air volume flow rate of 215 l/min. For the details of prototype experimental set-up see SI (Figure S6).

3. Results and discussion

Cycling loading lift of a series of MOFs and zeolite 13X

The structures of the selected water stable polycarboxylate based MOFs (MIL-100(Fe), MIL-101(Cr), MIL-125(Ti)_NH_2, UiO-66(Zr)-NH_2, MIL-127(Fe) and MIL-160(Al) strongly differ in terms of composition (presence or not of Lewis or Brønsted acid sites, tunable hydrophilic-hydrophobic character), pore volume and structural features (framework topology (1D or 3D pores), micropores or mesopores).[4,9–12] Except MIL-127(Fe), their water sorption properties were previously reported with interesting results in terms of water sorption capacity and low temperature regeneration. Moreover, the hydrophilic character of some MOFs (i. e. MIL-125(Ti)_NH_2, UiO-66(Zr)-NH_2) could be enhanced through the introduction of hydrophilic amino groups on the organic spacer. Herein, we aimed at comparing the potentiality of these MOFs and zeolite 13X as physical adsorbent materials for energy storage application. We have first measured their cycling loading lifts following the typical conditions of a seasonal energy storage device. The energy storage capacity of these materials was calculated based on cycling loading lift data and calorimetric measurements reported in the literature (i. e. MIL-160(Al)[5], MIL-125(Ti)_NH_2[13], MIL-100(Fe) [14] MIL-101(Cr)[14] and zeolite 13X[15]) (for the first estimation the energy storage densities of MIL-127(Fe) and UIO-66(Zr)_NH_2 were calculated using heat of adsorption values of MIL-100(Fe) and MIL-125(Ti)_NH_2, respectively) (Figure 2).

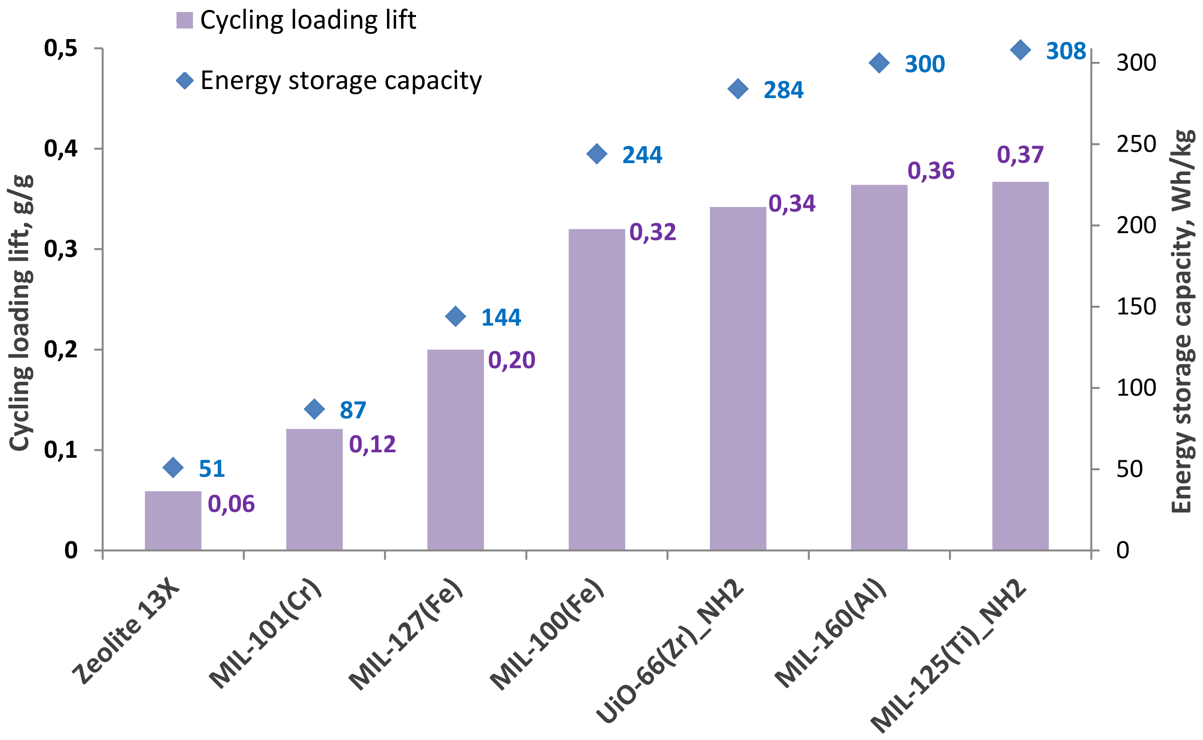

Figure 2. Cycling loading lifts and calculated energy storage capacities of MOF series and zeolite 13X. Cycle conditions: adsorption at 30°C and 1.25 kPa and desorption at 80°C and 1.25 kPa. Adsorption condition: 30°C and 1.25 kPa

Figure 2 displays the cycling loading lift and the calculated energy storage capacity of MOFs and zeolite 13X. The values of our cycling loading lifts for MOF series are fully consistent with that previously reported data under similar operating conditions [“Design of salt-Metal Organic Framework composites for heat storage application”]. Since a heat storage application implies water adsorption at low relative pressure ($p/p_0=0.3$), hydrophilic MOFs are supposed to be the most efficient water sorbents. Figure 2 shows clearly that (i) the cycling loading lift of all these MOFs is enhanced compared to zeolite 13X and (ii) the cycling loading lift of MOFs grows with the increase of the hydrophilic character of the framework, with the less interesting candidate being the hydrophobic MIL-101(Cr) to the best solids for the hydrophilic solids UiO-66(Zr)_NH_2, MIL-160(Al) and MIL-125(Ti)_NH_2. As indicated in Figure 2, the best calculated energy storage capacities, up to 300 and 308 Wh/kg, are obtained for MIL-160(Al) and MIL-125(Ti)_NH_2, respectively which is superior to that for modern zeolites (71-225 Wh/kg) with regeneration temperature of 150°C.[16] In this study, we selected MIL-160(Al) for the next step, i.e. prototype evaluation, two reasons. Firstly, the heat storage application required a sorbent with a sufficient cycling stability and from this point of view the MIL-160(Al) outperforms MIL-125(Ti)_NH_2 (no degradation has been observed for MIL-160 under 10 adsorption-desorption cycles[5], while 17% of losses under 40 cycles have been reported for MIL-125(Ti)_NH_2[4]). Secondly, the synthesis of MIL-125(Ti)_NH_2 requires toxic solvents (Dimethylformamide, Methanol), a linker derived from non-renewable feedstocks and a rather expensive metal source (Ti alcoxide) while the synthesis of MIL-160(Al) is carried out in pure water using a cheap Al salt precursor and a bio-derived renewable linker (2,5-furandicarboxylic acid).

Optimization of synthesis, scale-up, and shaping of MIL-160(Al)

The synthesis of MIL-160(Al) which was reported previously implies the use of a corrosive aluminium(III) chloride source as well as the addition of equimolar amounts of NaOH as a pH modulator. We aimed at replacing this reactant by the more eco-compatible and friendly $Al(OH)(CH_3COO)_2$ source in a view of a scale-up of the synthesis of MIL-160(Al). This less acidic precursor allowed us to avoid adding a base to tune the pH of the synthesis of the reaction media. To optimize the purity and yield, an initial high throughput synthesis methodology, based on 24*1.5 ml Teflon lined hydrothermal micro-reactors, was used for a fast screening of possible reaction parameters such as pH and reactant concentration. The time (12-72 h) and temperature (100-150°C) were also varied systematically. By exploring systematically these parameters, the synthesis of pure MIL-160(Al) was scaled-up to the 13.9 gram scale using a larger glass reactor (250 ml) together with a good crystallinity, a high yield (93% based on Al) and a good STY (185 $kg \cdot m^{-3} \cdot day^{-1}$).

In a second step, based on a even larger glass reactor (2L), three large scale synthesis were performed following this new recipe, and resulted as a whole into 400 g of powder with a good purity and surface area of 1150 $m^2.g^{-1}$. The shaping of the powder was carried out leading to 250 gram of granules of MIL-160(Al) with size distribution of 0.5-1.8 mm (Figure S3). As mentioned above, silica gel was used for this shaping and might affect the adsorption properties of the MOF compared to the pure powdered form. Therefore, the comparative analysis of microstructural properties of both the powder and the shaped MIL-160(Al) was performed including thermogravimetric analysis, nitrogen sorption porosimetry, XRPD, and infrared spectroscopy. Water sorption properties were also compared by measuring cycling loading lifts. The XRPD patterns look identical for both samples with no decrease of relative intensity of the Bragg peaks (Figure S1). Infrared spectroscopy (IR) patterns are also similar for both samples indicating the absence of residual free ligand ($\upsilon(CO) = 1695\ cm^{-1}$) (Figure S4). Thermogravimetric analysis indicates a very slight excess of inorganic residue at 450°C for pellet-shaped sample compared to the powder one (33% versus 28%) in agreement with the presence of about 6-8% of silica gel in granules of MIL-160(Al) (Figure S5). For the same reason the BET surface area and pore volume of the powder are slightly higher (S_{BET}=1150 $m^2.g^{-1}$, V_{pore}=0.479 $cm^3.g^{-1}$) than for pellet-shaped sample (S_{BET}=1010 $m^2.g^{-1}$, V_{pore}=0.443 $cm^3.g^{-1}$) (Figure S2).

The water sorption behavior of the powder and pellet-shaped MIL-160(Al) was studied under conditions of a seasonal energy storage application; the cycling loading lifts are respectively equal to 0.36 and 0.32 g/g while the adsorption loading lifts are 0.37 and 0.35 g/g, respectively (Figure 3). These results show that the shaping procedure has no significant impact on the water uptake of MIL-160(Al) in our conditions.

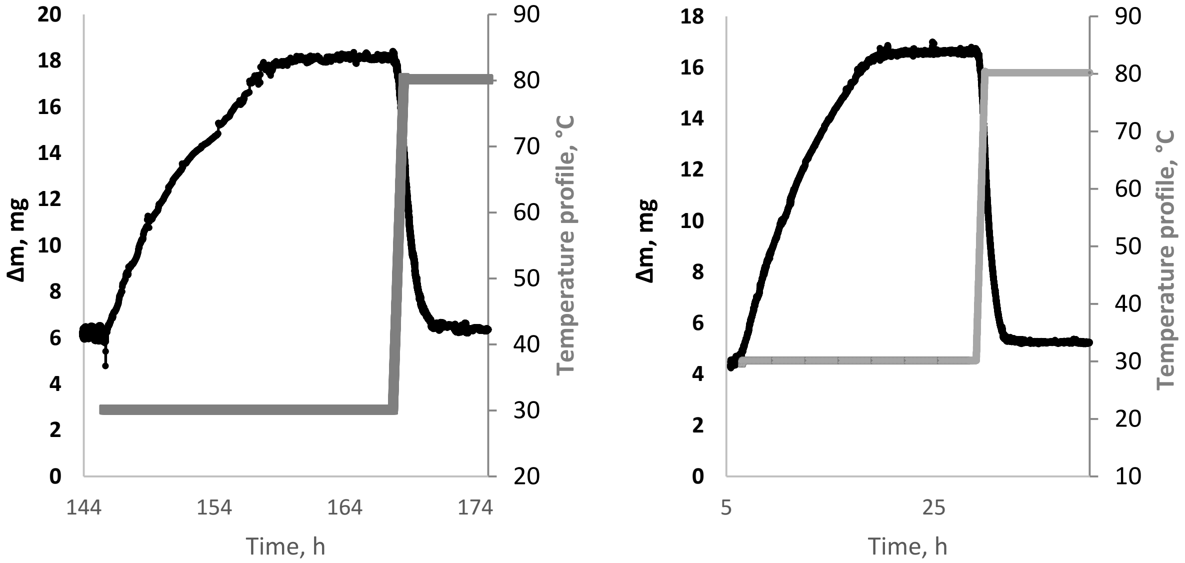

Figure 3. Adsorption and cycling loading lift on 32.11 mg of anhydrous powder MIL-160(Al) (left) and on 35.69 mg of anhydrous pellet-shaped MIL-160(Al) (right). Condition of lift: adsorption at 30°C and p=1.25 kPa mbar, desorption at 80°C and p=1.25 kPa.

In order to confirm the performances of the shaped material, the water sorption isotherms at different temperatures (30-80°C, step of 10°C) were collected (Figure 4). This is also critical if later one could like to model different operating conditions for this material.

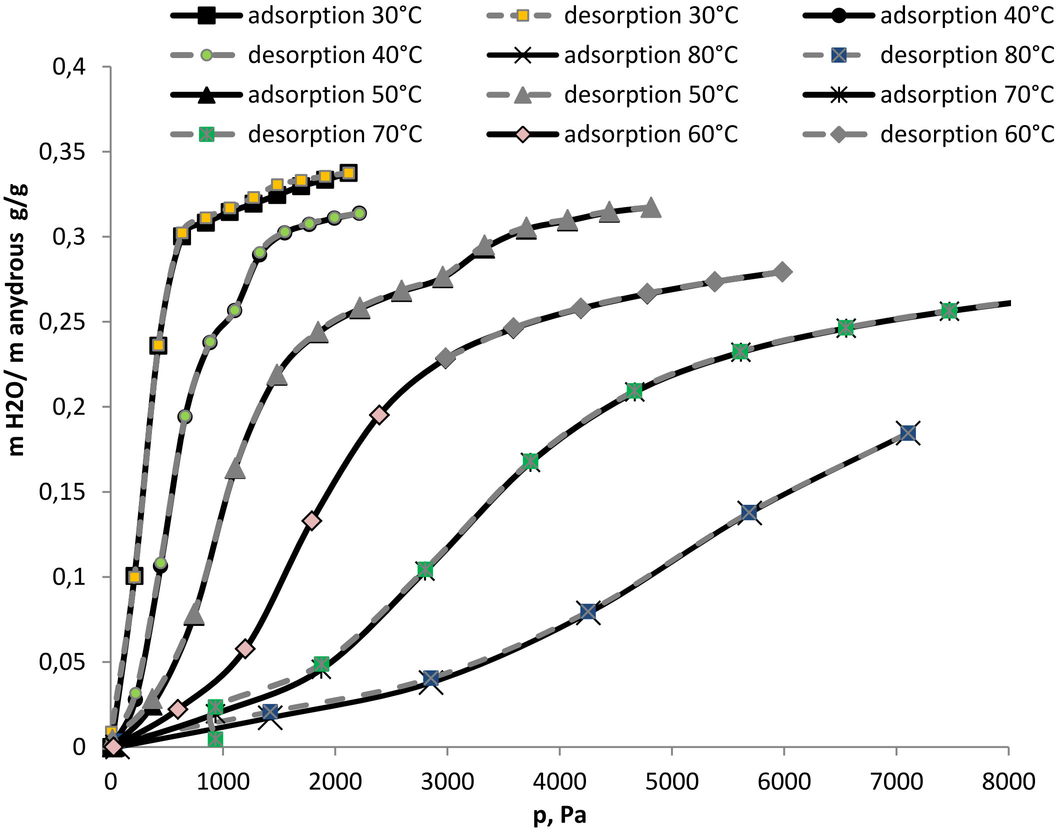

Figure 4. Water sorption isotherms at T=30-80°C (step of 10°C) of shaped MIL-160(Al).

The water sorption isotherm (T=30°C) is first in fair agreement with what was reported previously for powdered MIL-160(Al).[12] The adsorption loading lift from water sorption isotherm (T=30°C) at p = 1.25 kPa (0.32 g/g) is also comparable with that obtained from TG-DSC (0.35 g/g). Thus, this confirms that these data can be used as a reference for adsorption and cycling loading lift performed at different (T-p) conditions.

In summary, MIL-160(Al) has been selected among above mentioned series of physical sorption MOFs materials owing to its high cycling loading lift and energy storage capacity, green, cheap and friendly synthesis conditions and excellent stability under numerous adsorption-desorption cycles[12]. An optimized eco-compatible large scale synthesis and shaping of MIL-160(Al) was performed at the 250 gram scale with properties similar to the one of the small scale powdered form. Thus, MIL-160(Al) is eligible for next investigation step as pilot test in energy storage device.

Pilot test open-system prototype

The performance of shaped MIL-160(Al) was evaluated under conditions mimicking the ones of long term heat storage applications by performing experiments in a pilot scale open-reactor prototype. The measured energy storage capacity of MIL-160(Al) was compared to that of calculated from loading lift experiments (TG-DSC) and from water sorption isotherms. It is important to point out that the conditions in the open-system prototype differ from conditions of adsorption loading lift (TG-DSC). This is difficult to control the inlet air conditions for the pilot tests in a way that is as efficient as for the cycling loading lift tests. As a consequence, the water pressure in the inlet air during adsorption process in prototype is of 1.32 kPa (instead of 1.25 kPa).

In addition, we performed here only energy production cycle in the open-system prototype, but cycling loading lift measurements (TG-DSC) confirmed the easy regeneration character of MIL-160(Al) under low temperature conditions (80°C). Indeed, the very close values of adsorption lift (0.37g/g) and cycling loading lift (0.36 g/g) of MIL-160(Al) (Figure 3) are indicative of an almost complete regeneration of MIL-160(Al) at 80°C.

The air flow rate has also an impact on the rate of water adsorption and hence, on the thermal power. Thermal power and speed of reaction grow with increase of air flow rate. Therefore, we selected the highest flow rate of 215 l/min among three tested flow rates (108 l/min, 152 l/min and 215 l/min) for energy capacity measurement. Noteworthy, the adsorption experiment was repeated twice showing good reproducibility. Adsorption loading lifts of 0.36 g/g (1.32 kPa, T=30°C) were measured during energy production cycle in agreement with that obtained from the cycling loading lift tests on TG-DSC (Figure 5) (0.35 g/g at p=1.25 kPa, T=30°C) and from water sorption isotherm at 30°C (0.32 g/g at p=1.32 kPa, T=30°C) (Figure 3). The measurement of input and output air temperatures allows obtaining the thermal power curve (Figure 5) calculated by using the equation:

$$\mathbf{H = A * Cp * \Delta T}$$

where **H** is thermal power (W), **A** is air mass flow rate (kg/s), **Cp** is the air heat capacity (J/kg*K) and **ΔT** is the temperature difference between input and output air.

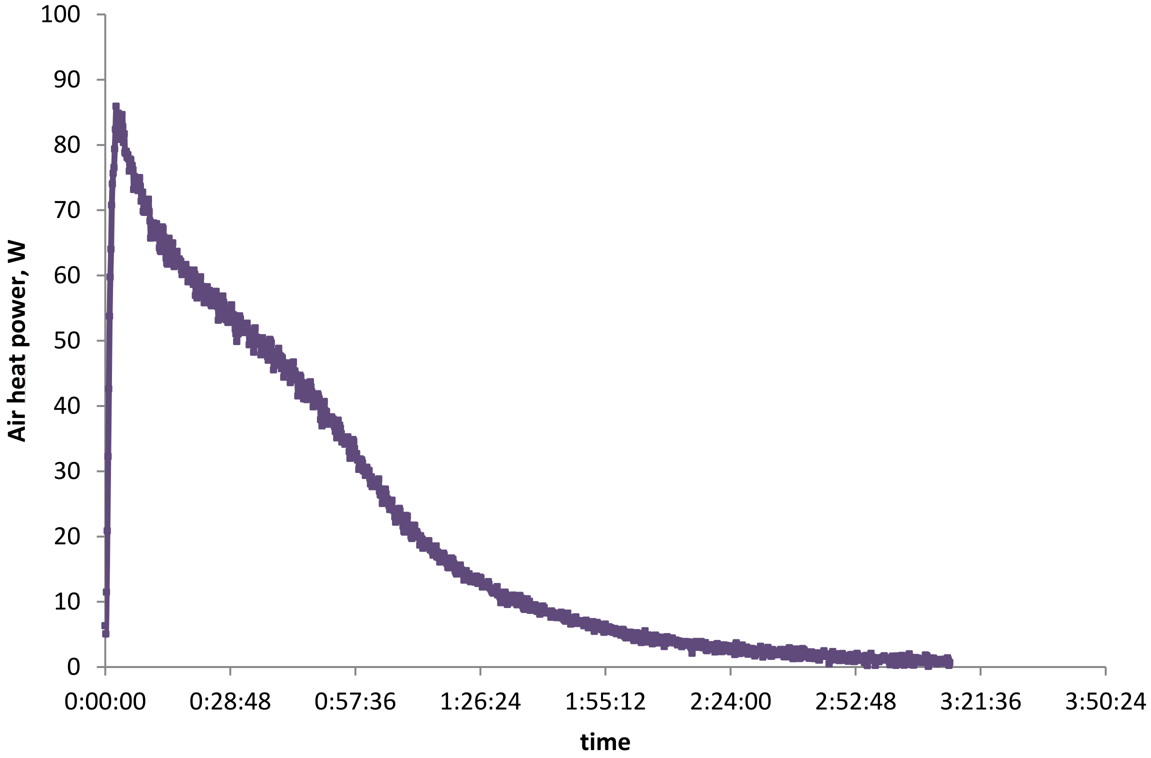

Figure 5. Thermal power profile of MIL-160(Al) granules (pilot test on 201 gram).

The integration (from t=0 to t=2h 40 min) of the heat power curve finally provides a rather high energy storage capacity value of 343 Wh/kg (141 kWh/m^3) in agreement with that obtained from the cycling loading lift (292 Wh/kg at T=30°C, p=1.25 kPa). The slight higher value of energy storage capacity derived from the open-system is certainly due to the resolution of temperature sensor ($\Delta T=0.2°C$) that provides an inaccuracy on the integrated value of the thermal power.

Interestingly, the energy storage density value of shaped MIL-160(Al) is high compared to other physical adsorbents, although conditions are not exactly the same here and thus, any direct comparison of storage capacity is complicated (Table 1). Zeolites show interesting energy storage density up to 180 kWh/m^3 in the conditions of high desorption temperature (180°C).[17] However, their performance in low desorption temperature conditions is poor (37 Wh/kg[18] and 51 Wh/kg (this work) for zeolite 13X and 118 Wh/kg[18] for FAM-Z02) compared to MIL-160(Al) (292-300 Wh/kg). Moreover, the energy storage capacity of MIL-160(Al) (T_d=80°C) outperforms by at 19-32 % that of SAPO-34 and AlPO-18 (T_d=90°C).

Table 1. Energy storage capacities and energy storage densities of different physical sorption materials for heat storage application.

Adsorbents for energy storage	Operating conditions	Regeneration conditions, °C	Energy storage capacity, Wh/kg	Energy storage density, kWh/m^3	Reference
MIL-160(Al)	T=30°C, p=1.32 kPa	Complete evacuation	343	141	this work
	T=30°C, p=1.25 kPa	80°C	292-300	118-123	this work
Zeolite 13X	T=30°C, p=1.25 kPa	80°C	51		this work
	T= 25°C, p=1.59 kPa	Complete evacuation	-	131	[19]
	T=22°C p=2.48 kPa	180°C	-	180	[17]
	Ta=40°C p=1.70 kPa	90°C 160°C	37 110	-	[18]
FAM-Z02 zeolite based molecular sieve	Ta=40°C p=1.70 kPa	90°C 160°C	118 172	-	[18]
Zeolite 4A	T=25°C P=2.00 kPa	150°C	-	98	[19]
SAPO-34	T=40°C P=1.20 kPa	90°C	203 (heat transfer)	-	[20]
AlPO-18	T=40°C P=1.20 kPa	90°C	243 (heat transfer)	-	[20]

In order to control the stability of shaped MIL-160(Al) under conditions of a seasonal energy storage prototype, MIL-160(Al) after 6 adsorption-desorption cycles in reactor was characterized by a combination of PXRD, thermogravimetric analysis, IR spectroscopy and nitrogen sorption porosimetry (Figure S9-Figure S12). These results are fully consistent with that obtained for the fresh shaped MIL-160(Al), showing the excellent stability of this material for heat reallocation application.

4. Conclusions

In this work, a series of robust MOFs with different chemical and structural features (MIL-101(Cr) and MIL-100(Fe), MIL-127(Fe), MIL-160(Al), MIL-125(Ti)_NH_2, and UiO-66(Zr)_NH_2) was evaluated for seasonal heat storage application and compared with the commercial zeolite 13X. Best calculated energy storage capacities were obtained with the most hydrophilic MOFs (MIL-160(Al), MIL-125(Ti)_NH_2, and UiO-66(Zr)_NH_2) which appear as interesting candidates for such an energy storage application. The synthesis optimization, scale-up and shaping of the most interesting solid, MIL-160(Al), was demonstrated leading to a high purity, an excellent yield (93%), a good STY (>180). More than 200 gram of shaped MIL-160(Al) was then evaluated in a laboratory pilot scale heat reallocation open system reactor prototype. First, a very good agreement was reached between the adsorption loading lift and energy storage capacities obtained in pilot test compared to results previously calculated from the small scale powder. Secondly, the energy output of the shaped MOF material slightly exceeded the performances of the best inorganic porous solids reported so far. This paves the way for the integration of MIL-160(Al) in future energy physisorption based reallocation systems.

5. Notes and references

[1] B. B. Saha, A. Chakraborty, S. Koyama, Y. I. Aristov, *Int. J. Heat Mass Transf.* **2009**, *52*, 516.
[2] F. Jeremias, D. Fröhlich, C. Janiak, S. K. Henninger, *New J. Chem.* **2014**, *38*, 1846.
[3] S. Shimooka, K. Oshima, H. Hidaka, T. Takewaki, H. Kakiuchi, A. Kodama, M. Kubota, H. Matsuda, *J. Chem. Eng. Jpn.* **2007**, *40*, 1330.
[4] F. Jeremias, V. Lozan, S. K. Henninger, C. Janiak, *Dalton Trans.* **2013**, *42*, 15967.
[5] A. Cadiau, J. S. Lee, D. Damasceno Borges, P. Fabry, T. Devic, M. T. Wharmby, C. Martineau, D. Foucher, F. Taulelle, C.-H. Jun, Y. K. Hwang, N. Stock, M. F. De Lange, F. Kapteijn, J. Gascon, G. Maurin, J.-S. Chang, C. Serre, *Adv. Mater.* **2015**, *27*, 4775.
[6] F. Jeremias, A. Khutia, S. K. Henninger, C. Janiak, *J Mater Chem* **2012**, *22*, 10148.
[7] A. Khutia, H. U. Rammelberg, T. Schmidt, S. Henninger, C. Janiak, *Chem. Mater.* **2013**, *25*, 790.
[8] P.-J. Kim, Y.-W. You, H. Park, J.-S. Chang, Y.-S. Bae, C.-H. Lee, J.-K. Suh, *Chem. Eng. J.* **2015**, *262*, 683.
[9] F. Jeremias, A. Khutia, S. K. Henninger, C. Janiak, *J Mater Chem* **2012**, *22*, 10148.
[10] G. Akiyama, R. Matsuda, H. Sato, A. Hori, M. Takata, S. Kitagawa, *Microporous Mesoporous Mater.* **2012**, *157*, 89.
[11] G. E. Cmarik, M. Kim, S. M. Cohen, K. S. Walton, *Langmuir* **2012**, *28*, 15606.
[12] A. Cadiau, J. S. Lee, D. Damasceno-Borges, P. Fabry, T. Devic, M.T. Wharmby, C. Martineau, D. Fouchet, F. Taulelle, C.-H. Jun, Y. K. Hwang, N. Stock, M. F. De Lange, F. Kapteijn, J. Gascon, G. Maurin, J.-S. Chang, C. Serre, *Adv. Mater.* **2015**, *27*, 4775.
[13] L. G. Gordeeva, M. V. Solovyeva, Y. I. Aristov, *Energy* **2016**, *100*, 18.
[14] Y.-K. Seo, J. W. Yoon, J. S. Lee, Y. K. Hwang, C.-H. Jun, J.-S. Chang, S. Wuttke, P. Bazin, A. Vimont, M. Daturi, S. Bourrelly, P. L. Llewellyn, P. Horcajada, C. Serre, G. Férey, *Adv. Mater.* **2012**, *24*, 806.
[15] F. B. Cortés, F. Chejne, F. Carrasco-Marín, C. Moreno-Castilla, A. F. Pérez-Cadenas, *Adsorption* **2010**, *16*, 141.
[16] N. Yu, R. Z. Wang, L. W. Wang, *Prog. Energy Combust. Sci.* **2013**, *39*, 489.
[17] C. Bales, *Laboratory Prototypes of Thermo-Chemical and Sorption Storage Units*, Bales, **2007**.
[18] C. Bales, P. Gantenbein, D. Jaenig, H. Kerskes, K. Summer, M. van Essen, others, *Rep. IEA Sol. Heat. Cool. Programme-Task* **2008**, *32*.
[19] B. Mette, H. Kerskes, H. Drück, *Energy Procedia* **2012**, *30*, 321.
[20] S. K. Henninger, F. Jeremias, H. Kummer, P. Schossig, H.-M. Henning, *Energy Procedia* **2012**, *30*, 279.

Supporting Information

1. Characterization of powder and shaped MIL-160(Al)

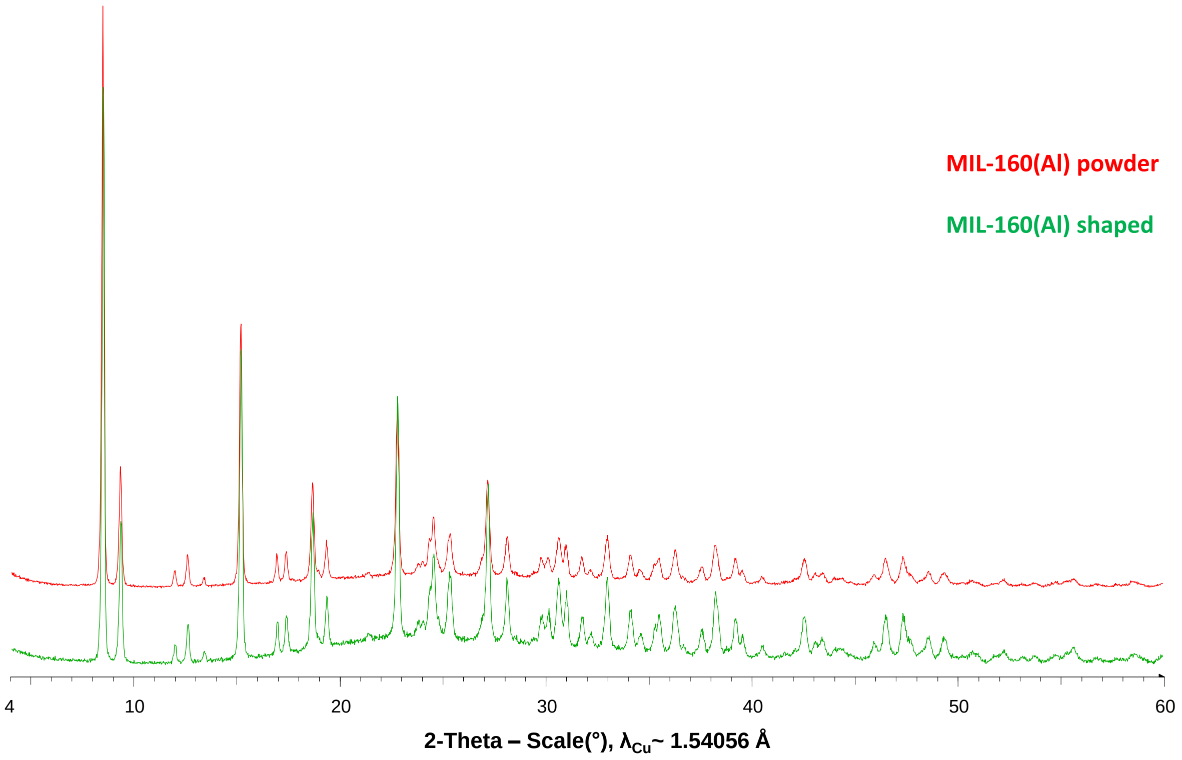

Figure S1. PXRD patterns of MIL-160(Al) as powder (red) and pellet-shaped sample (green)

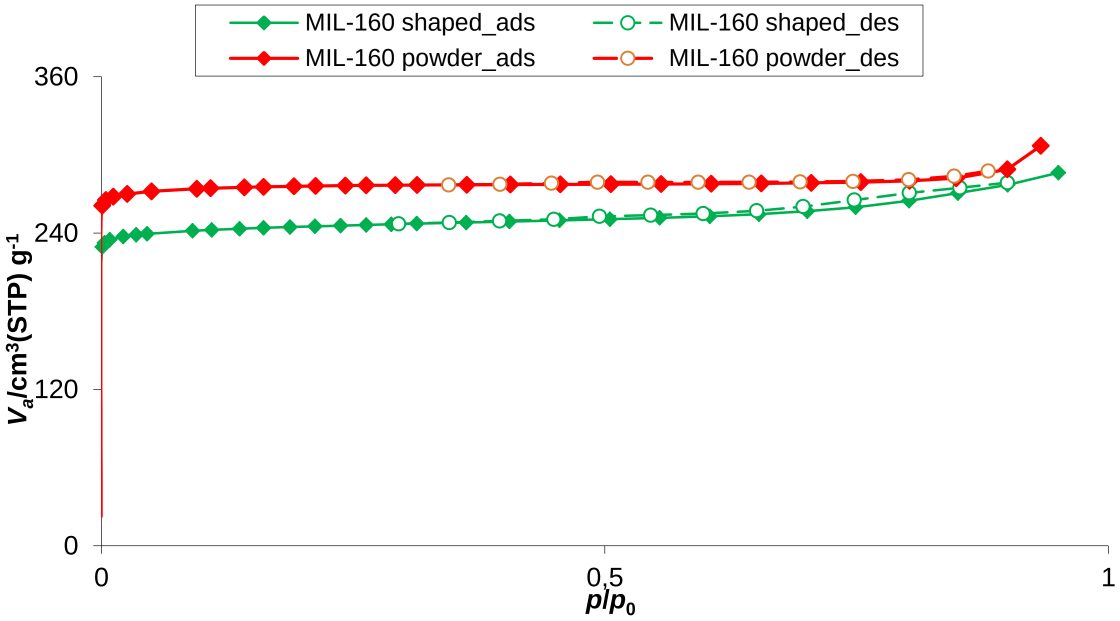

Figure S2. Nitrogen adsorption-desorption isotherms of MIL-160(Al) powder (red) and shaped (green) at 77K.

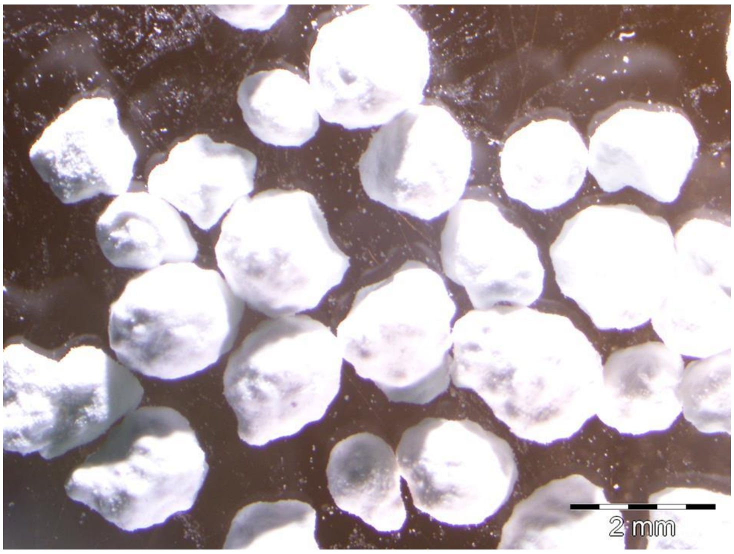

Figure S3. Picture of granule MIL-160(Al) (0.5-1.8 mm)

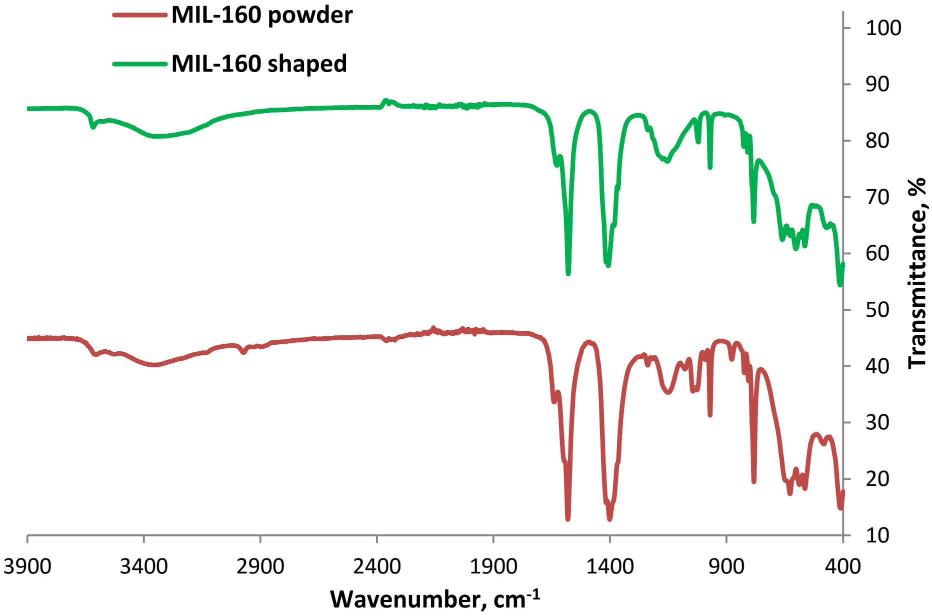

Figure S4. Infrared spectrum of powder (in red) and shaped (in green) MIL-160(Al).

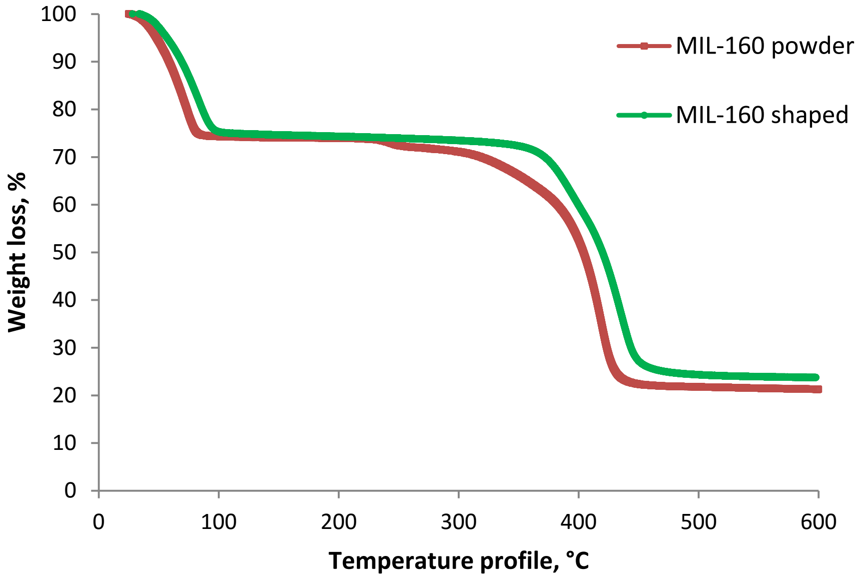

Figure S5. Thermogravimetric analysis of powder (in red) and shaped (in green) MIL-160(Al) under oxygen flow.

2. Open reactor prototype instrumentation

The experimental set-up consists of the dry air generator to deliver the air at different flow rates, controlled air humidification system to prepare the moist air within the controlled conditions, and adsorption column assembly. The general and complete instrumentation scheme and the supplemental information about its elements are described in Figure S6.

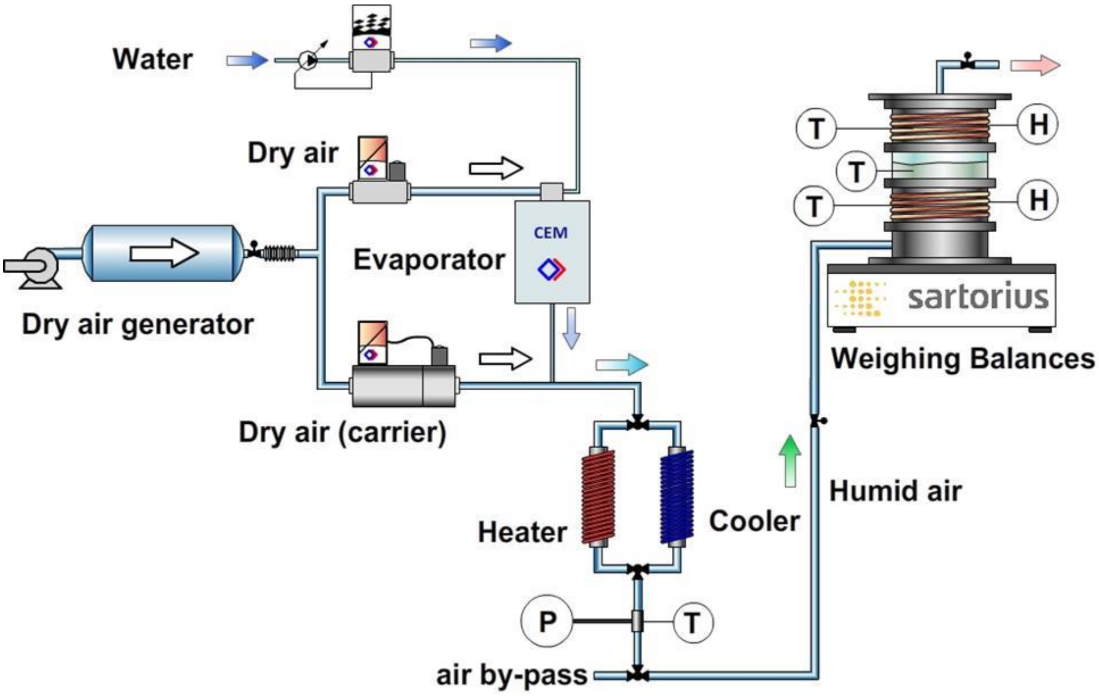

Figure S6. Instrumentation scheme of open reactor prototype

Dry air was generated by a compressor equipped with a dryer. To generate the humidity (0-100%), we used a controlled evaporator and mixer (CEM) connected with Bronkhorst mass flow controllers (volumetric flow of 0-800 L/min). The fluid pressure and fluid temperature were measured by a pressure gauge and a thermocouple, respectively. The air could be heated or cooled by an electrical air heater or air cooler (tube in serpentine in a bath at constant temperature), respectively.

The adsorption column assembly is composed of thermally isolated input and output air spacer units, and the adsorption cell placed between spacers. The air temperature and humidity were measured at the inlet and outlet of the adsorption column by Rotronic probes. The pressure drops induced by the column were measured by a differential pressure gauge (0-0.13 bar). The temperature of material inside the column was also measured by thermocouple. The adsorption column assembly is mounted onto a balance to measure precisely (weight resolution of 0.5 g) the variation of the material mass.

3. Adsorption test on MIL-160(Al) in open system prototype

The pilot test was carried out on dry granuled MIL-160(Al). Initially, some parameters such as air volume flow rate (108 l/min, 152 l/min and 215 l/min) and input air humidity (50% and 70% at 20°C) were varied (6 adsorption-desorption experiments). As mentioned above, the selected conditions for adsorption process are following: input air at T=30 °C with 50 % of relative humidity (calculated at 20°C) and 215 l/min of air volume flow rate. The air temperature profiles measured at input and output of the adsorption column are given (Figure S7).

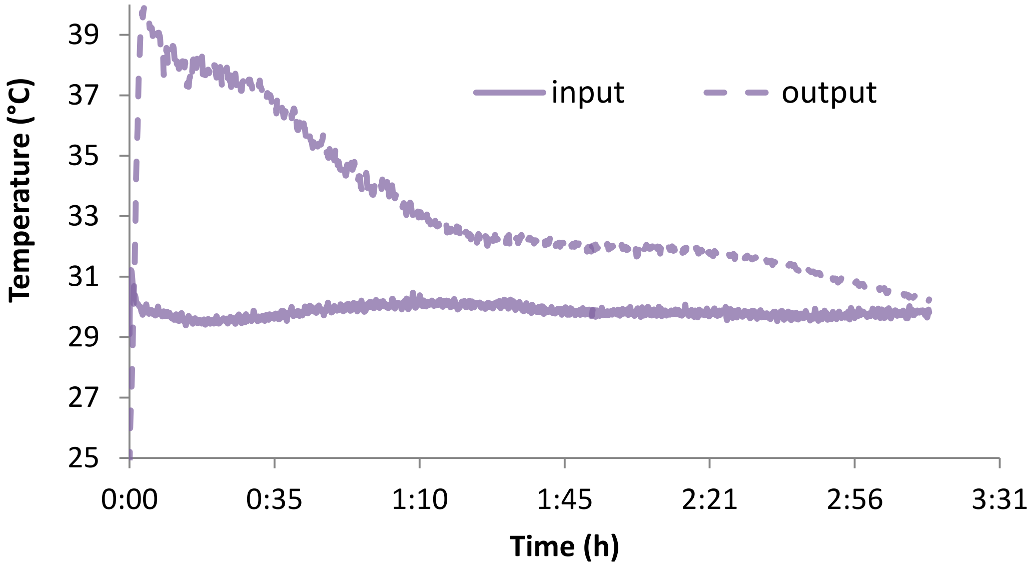

Figure S7. Temperature profile profile at the inlet and outlet of the adsorption column (pilot test on 201 g of MIL-160(Al)).

After 3h 10 min inlet and outlet temperatures became equal corresponding to equilibrium condition and indicating the end of adsorption process. The water pressure profile in the adsorption column is illustrated in Figure S8.

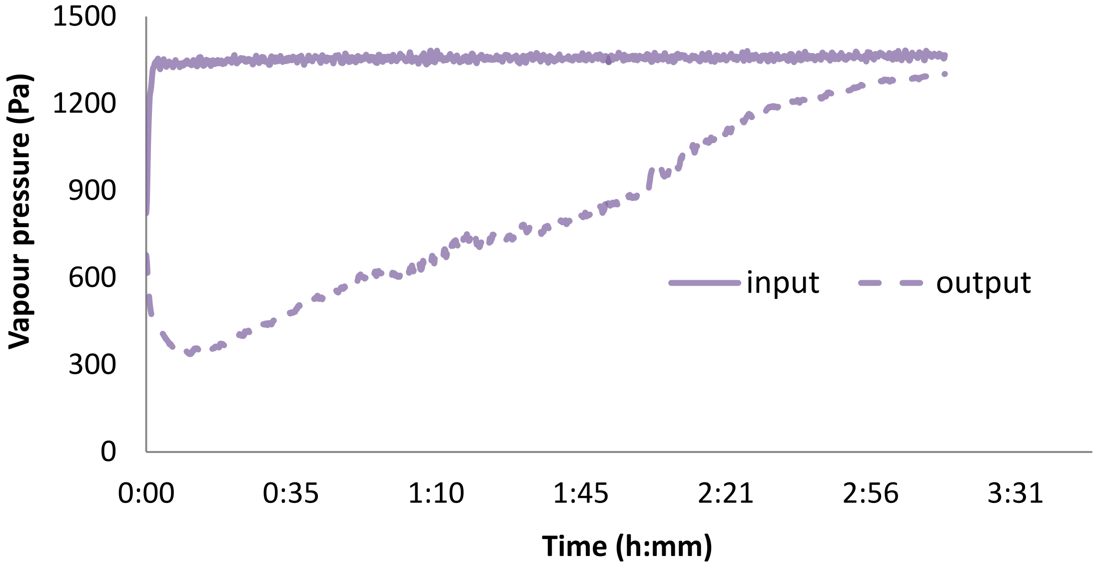

Figure S8. Water pressure profile at the inlet and outlet of the adsorption column (pilot test on 201 g of MIL-160(Al)).

The stability of granuled MIL-160 (Al) after performing adsorption-desorption test in prototype (6 test in total) was controlled by means of thermogravimetric analysis, nitrogen sorption porosimetry, PXRD, and IR. The comparison of (micro)structural properties of granuled MOFs before and after prototype experiments shows that the stability of this pellet-shaped material is excellent. The characterizations are given below.

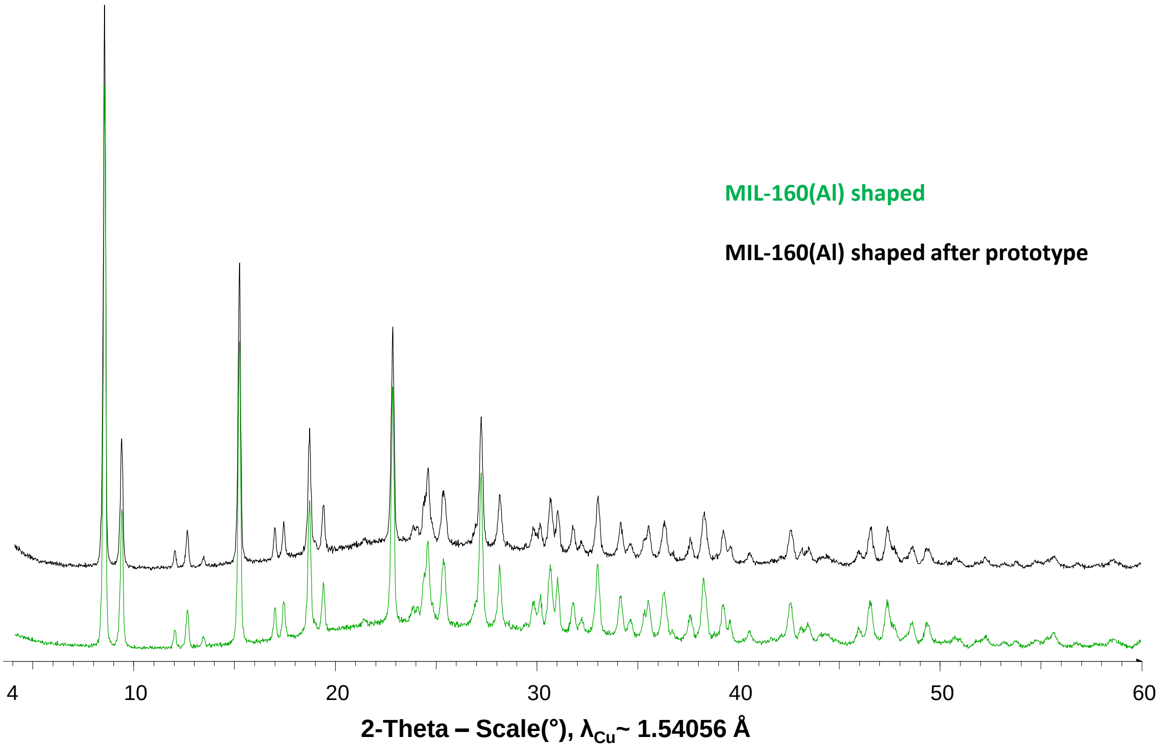

Figure S9. PXRD patterns of shaped MIL-160(Al) before (in green) and after (in black) 6 adsorption-desorption cycles in prototype.

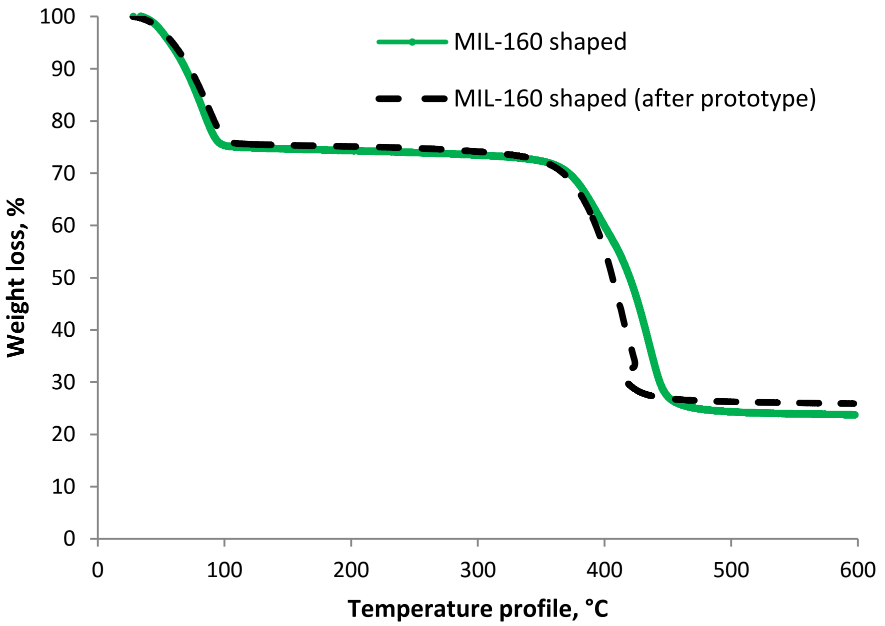

Figure S10. Thermogravimetric analysis of shaped MIL-160(Al) under oxygen flow before (in green) and after (in black) 6 adsorption-desorption cycles in prototype.

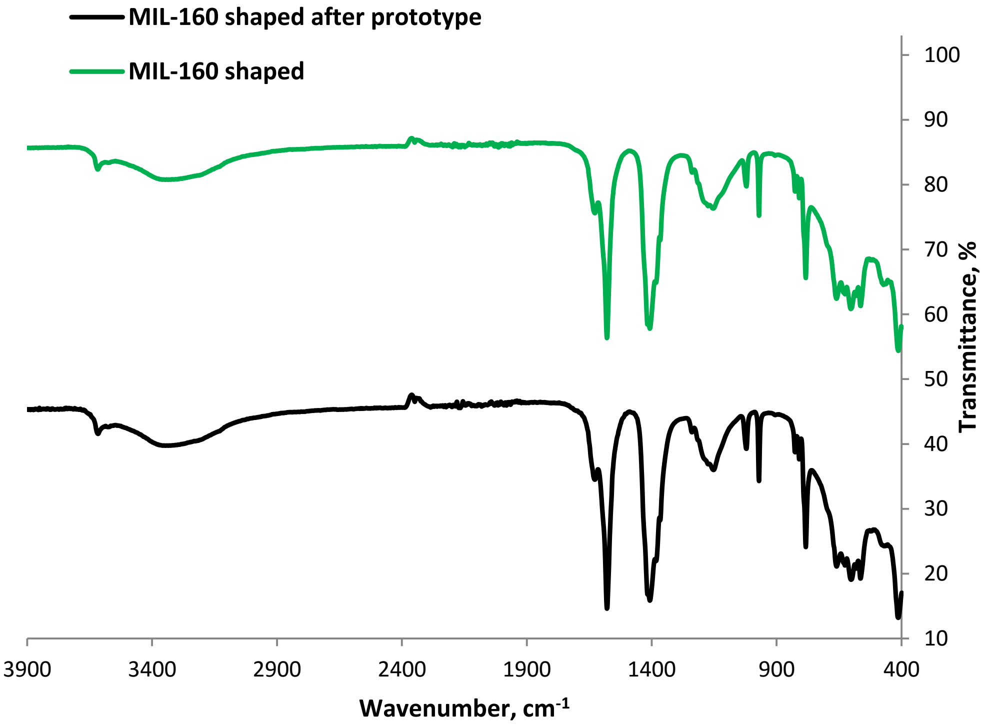

Figure S11. . Infrared spectrum of shaped MIL-160(Al) before (in green) and after (in black) 6 adsorption-desorption cycles in prototype.

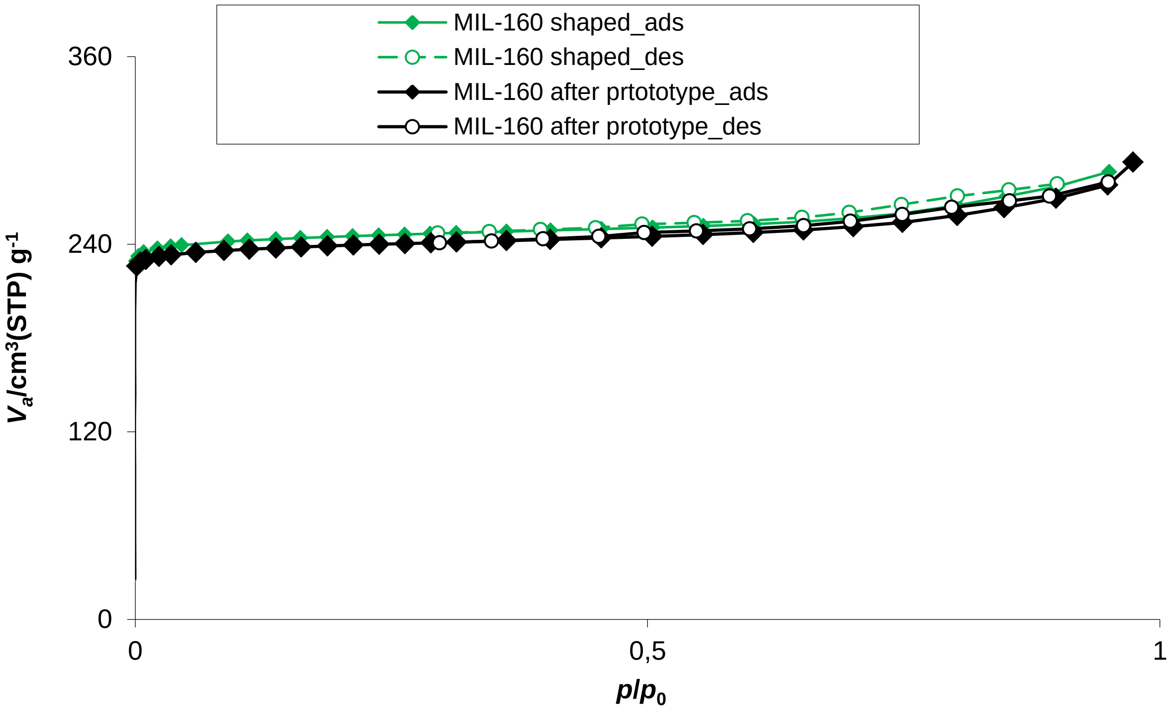

Figure S12. Nitrogen adsorption-desorption isotherms of shaped MIL-160(Al) before (in green) and after (in black) 6 adsorption-desorption cycles in prototype.

Chapter III

Design of salt-Metal Organic Framework composites for heat storage applications

Chapter III: Design of salt-Metal Organic Framework composites for heat storage applications

The work reported in this chapter is described in the format of an article accompanied by an annex 'Supplemental experimental data on salt-MOF composites'. This study was performed in the frame of a European FP7 Solar Thermochemical Compact Storage System (SoTherCo) project. The Chapter III is focused on the design of MOFs-salt composites for energy storage application. The author contribution is provided below.

Author contribution

This chapter constitutes the "core" of my thesis work. It aims at developing a series of MOFs-salt composites by varying the nature of MOFs and their composition (i. e. mainly salt content) and at investigating the impact of the physico-chemical and microstructural properties of composites on their water adsorption properties and potentiality for heat reallocation application. The selection of MOF series including mesoporous (i. e. MIL-100(Fe), MIL-101(Cr)), or microporous (i. e. MIL-127(Fe), MIL-160(Al), MIL-125-(Ti)-NH_2, UiO-66(Zr)-NH_2), is derived from Chapter I according to their full characterization in terms of water sorption properties and water stability.

This work implies several steps such as the synthesis MOF-composites with desirable salt content, their full micro-structural characterization, the study of their water sorption properties in the context of operating cycle conditions, the calculation and measurement of their energy storage capacity and energy storage density, followed by the selection of the best candidates, and the evaluation of their stability with time and under adsorption-desorption cycles. I have particularly investigated the MOF-composites based on the microporous MIL-127(Fe) and mesoporous MIL-100(Fe). I have proposed a synthesis approach of those composites that was then applied for all others MOFs (MIL-101(Cr), MIL-125-(Ti)-NH_2, UiO-66(Zr)-NH_2, MIL-160(Al)) from the series. The synthesis of composites based on hydrophilic MOFs *(i. e.* UiO-66-NH_2, MIL-125-(Ti)-NH_2 and MIL-160(Al)) was carried out by Dr. Sujing Wang (post-doc, UVSQ). I performed the synthesis of composites based on MIL-101(Cr). I have studied the energy storage properties for all composites (i. e. measurement of cycling loading lift, calculation of energy sorption capacity and energy storage density, stability with time). Nicolas Heymans (post-doc, UMons) and I have studied together the stability under several adsorption-desorption cycles of MIL-100(Fe) and MIL-101(Cr) based composites.

Before article submitting we will check the calculated energy density of composites by performing the micro calorimetric measurements (TG-DSC, UMons).

WILEY-VCH

DOI: 10.1002/((please add manuscript number))
Article type: Communication

Design of salt-Metal Organic Frameworks composites for heat storage applications

Anastasia Permyakova, [a,b] *Sujing Wang,*[a] *Emilie Courbon,*[b] *Farid Nouar,*[a] *Nicolas Heymans,*[b] *Pierre Billemont,*[b] *Guy De Weireld,*[b] *Nathalie Steunou,*[a*]*Marc Frère* [b*] *and Christian Serre* [a*]

[a] Institut Lavoisier, UMR CNRS 8180, Université de Versailles St-Quentin en Yvelines, 45 Avenue des Etats-Unis, 78035 Versailles Cedex, Université Paris-Saclay, France.
E-mail: nathalie.steunou@uvsq.fr, marc.frere@umons.ac.be, christian.serre@uvsq.fr.
[b] Institut de Recherche en Energie, Service de Thermodynamique et de Physique mathématique, Université de Mons, 31, boulevard Dolez, 7000 Mons, Belgique

Keywords: heat storage, Metal-Organic-Frameworks, calcium chloride, composites

Nowadays, the increasingly austere problems of excessive fossil fuel consumption and greenhouse gas emissions produced by combustion processes are pushing for the development of efficient and affordable alternative energy solutions. Thermochemical energy storage, based on reversible reactions involving working fluids, is a very efficient way of heat reallocation with extremely low losses, tunable cycle times, from months for seasonal applications or minutes for heat transformation, heat pumping or refrigerating applications (see Fig.S1 for more information). So far, only heat pumping and refrigeration applications are mature and water is the most widespread working fluid used due to its high evaporation enthalpy (i. e. 2500 $kJ.kg^{-1}$), non-toxicity and availability. Water is also considered to be an interesting working fluid for seasonal storage potential applications mainly for its absence of toxicity. Therefore, if in both cases, one requires hydrothermally stable and scalable materials with a high energy density or energy capacity (especially for seasonal storage applications), fast adsorption kinetics (especially for heat transformation/pumping and refrigerating applications), stability under numerous adsorption-desorption cycles, the water sorption characteristics of materials have to match those of the operating conditions of the application. In case of closed system configurations, this is defined by the cycle boundary temperatures of water evaporation (T_e) and condensation temperatures (T_c) as well as the regeneration temperature. For heat pumping applications, the most interesting materials should present a high water uptake (i. e. high cycle loading lift) at typical relative working pressure p/p_0 below 0.3 (depending on the process temperature).[1] For seasonal heat storage applications, high quantities of energy have to be handled in one cycle so that high values of the cycle loading lift are targeted to ensure affordable size of the storage system.

Inorganic porous materials have been investigated so far for such applications based on water sorption, showing fast kinetics typical of pure physical sorption. While silica gels can be regenerated at very low temperature (down to 45-50 °C), they exhibit generally a low sorption capacity, in the range 0.03-0.10 g/g within a typical adsorption heat pump (AHT).[2] Due to their high hydrophilic character, zeolites present a large water sorption uptake at quite low values of the relative pressure, but high regeneration temperature is required (over 140°C).[3] Aluminophosphates (AlPOs) and silica-aluminophosphates (SAPOs) were also considered for heat transformation application with however limited interest for seasonal storage due to their high cost and low water adsorption capacity.[3][4] Inorganic porous materials exhibit energy output of 50-100 kWh/m^3[1] which is considered as too low for seasonal storage application. In contrast, chemical sorption materials (hygroscopic salt) present generally higher energy output (up to ~600 kWh/m^3), but slower water sorption kinetics, highly suitable for seasonal storage applications. However, their stability under multiple adsorption-desorption cycles remains the key issue for their practical use. Therefore, the design of composite materials in which an inorganic salt is confined in a porous host matrix was recently reported as an interesting approach since a synergy between the physical sorption of the host matrix and chemical sorption of salt as well as possible absorption of water vapor by super-concentrated salt solution may be expected.[5–7] In composites, the behavior of the individual components (inorganic salt and porous matrix) may be completely modified in terms of water sorption properties, kinetics, packing density, stability and regeneration temperature. In particular, the sorption properties of composites can be tuned by varying the chemical nature of the confined salt, its amount and particle size and depend strongly on the microstructural and physic-chemical properties of the porous host matrix (pore diameter, specific surface area, hydrophilic/hydrophobic balance).[8–11]

Metal–organic frameworks (MOFs)[12] represent a new class of crystalline hybrid porous materials obtained by assembling metal nodes and organic ligands. They possess tunable properties in terms of internal surface area and pore volume as well as structural and chemical diversity due to the large variety of possible metal cations, organic linkers and building blocks and to the almost infinite number of possible combinations. The surface area values of such MOFs typically range from 1000 to 6000 m^2/g, exceeding in most cases the values of “traditional” porous materials. As a result of their fascinating physico-chemical properties, these materials present potential applications in gas storage/separation[13–15], catalysis[16–20], drug delivery[21,22], sensors[23–27] among others. Recently, this class of hybrid materials has emerged as promising water sorption materials for heat transformation[3,28,29]. For instance, it is noteworthy that the position of the adsorption loading lift (p/p_0) in composites strongly depends on pore size of the host matrix[1,10] and from this point of view MOFs could offer a rich variability. One critical issue of this study concerns the chemical and thermodynamic compatibility between MOFs and salt. Actually, the stability and water sorption properties of composites are strongly dependent on the interfacial properties between the porous matrix and salt that drives both the salt dispersion /aggregation and the free pore volume of the sorbent. In particular, a series of MILs (MIL stands for Materials from Institut Lavoisier) or UiO’s (UiO stands for materials from University of Oslo) that comprised of three- and four-valent metal cations (Cr^{3+}, Al^{3+}, Fe^{3+}, Zr^{4+} and Ti^{4+}) and aromatic polycarboxylate linkers was investigated for water sorption (see Figure 1).[28,30,31]

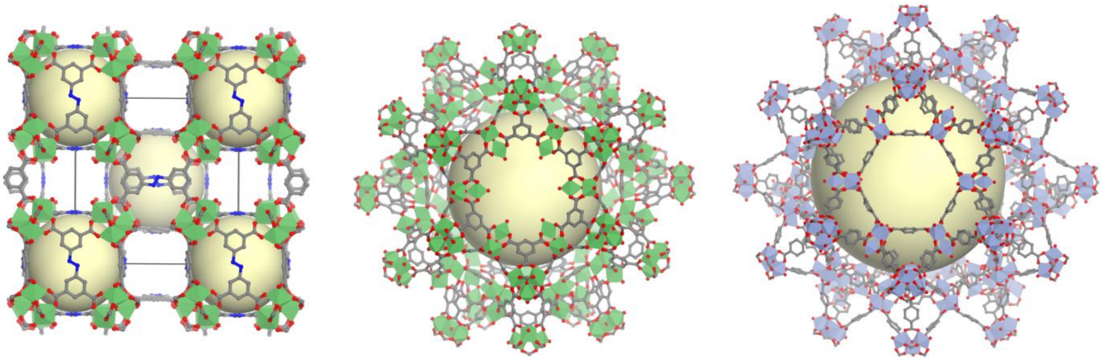

MIL-127(Fe) **MIL-100(Fe)** **MIL-101(Cr)**

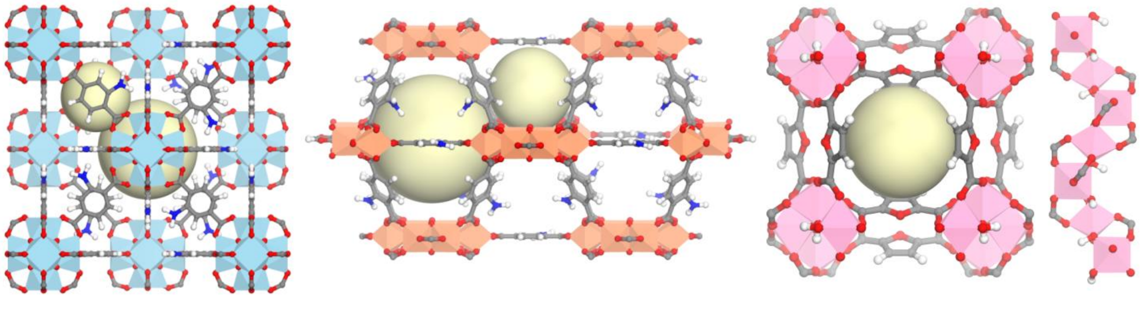

UiO-66(Zr)-NH_2 **MIL-125(Ti)-NH_2** **MIL-160(Al)**

Figure 1. Structures of MOFs

These materials (i. e. MIL-101(Cr), MIL-100(Fe, Al, Cr), MIL-160(Al), UiO-66(Zr)_NH_2, MIL-125(Ti)-NH_2) present a good hydrothermal stability, water adsorption isotherms with a “S” shape profile and water uptake ranging from 0.5 to 1.5 $g.g^{-1}$.[28–33] In addition, the modification of the organic linker of MOFs by using hydrophilic amino- or hydroxo groups from the inorganic core enables to tune their sorption behavior in terms of water uptake (i. e. adsorption loading lift) as well as their hydrophilic character (position of step in p/p_0). This wide choice of hydrothermally stable MOFs with promising water sorption capacities, suitable hydrophilicity and relatively low regeneration temperatures is therefore particularly suitable for heat reallocation applications.

The present paper deals with the first exploitation of this series of stable MOFs as host matrices of salts for the preparation of composite sorbents for seasonal heat storage, in order to investigate the impact of the physico-chemical and structural properties of MOFs on the energy density of composites sorbents, thereby optimizing their performances.

Prior to such an investigation, the sorption properties of MOFs (see Fig. S2-S19 for full characterization) have been studied in conditions close to the application, allowing the sorption properties and energy storage performance (energy density) of composites to be compared with those of hosts matrices. Sorption isotherms or cycling loading lifts were measured in conditions of a seasonal energy storage system (Table 1).

Table 1. Structural and sorption characteristics of MOFs

MOF	Pore diameter, [Å]	S_{BET} [m^2/g]	Total pore volume [cm^3/g]	Structural characteristics	Adsorption loading lift at 30°C, g/g	Cycling loading lift, g/g
MIL-100(Fe)	25/29	1828	0.81	acid Lewis sites	0.39	0.32
MIL-101(Cr)	29/34	3721	1.51	acid Lewis sites	0.17	0.12
MIL-127(Fe)	5/8/10	1342	0.57	-	0.28	0.20
UiO-66(Zr)_NH_2	7.5/12	1112	0.44	hydrophilic centers (-NH_2)	0.36	0.34
MIL-125(Ti)_NH_2	6/12	1480	0.64	hydrophilic centers (-NH_2)	0.39	0.37
MIL-160(Al)	5	1150	0.46	hydrophilic centers (O-heteroatom)	0.37	0.36

Standard deviations of adsorption and cycling loading lifts are ~1%.

The adsorption temperature (T_a) was of 30°C, which is the minimum temperature for space heating at winter period while a desorption temperature (T_d=80°C) for loading lift measurements, typical of a solar collector, was selected. A closed system with evaporating and condensing temperatures of 10°C (T_c, T_e) corresponding to a pressure of 12.5 mbar was chosen. Finally, the operating conditions are here the following: T_d=80°C, T_a=30°C, T_e=10°C, T_c =10°C.

Two main parameters have been considered here for the MOFs: (i) their hydrophilic/hydrophobic balance and (ii) their pore size. Firstly, we have considered a selection of microporous MOFs bearing a high hydrophilic character, due to a combination of hydroxylated inorganic building units and the polarity of the organic linker: UiO-66(Zr)-NH_2, MIL-125(Ti)-NH_2 (amino group) or MIL-160(Al) (2,5-furandicarboxylic acid (FDCA)). UiO-66(Zr)_NH_2 and MIL-125(Ti)_NH_2 exhibit both a 3D network made up of two tetrahedral or octahedral cages with pore sizes of 7.5/12 Å and 6/12 Å, respectively. In both structures, the framework is built by connecting metal oxo/hydroxo clusters (i. e. $Zr_6O_4(OH)_4$ and $Ti_8O_8(OH)_4$) and terephthalate based linkers. In MIL-160(Al) the helical cis-corner-sharing chains of $AlO_4(OH)_2$ octahedrons are connected via carboxylate groups of FDCA resulting in a 3-D framework with square shaped sinusoidal channels of ~5 Å in diameter. As previously reported[28,31,33], these solids present similar one-step S-shaped isotherms with steep uptake at relative pressure p/p_0= 0.30, 0.25 and 0.20, respectively. In this work, we have shown that their adsorption loading lifts (T=30°C, 12.5 mbar) and cycling loading lifts (12.5 mbar, T_a=30°C, T_d=80°C) are equal to 0.36 and 0.34 g/g, 0.39 and 0.37 g/g, 0.37 and 0.36 g/g, respectively (Fig. S20). In contrast, if one considers the more hydrophobic microporous MIL-127(Fe) and mesoporous MIL-100(Fe) and MIL-101(Cr) MOFs, a shift of their sorption steps towards higher $p/p_0$is observed together with a two-steps isotherms due to their bimodal pore size distribution.[29,30,34] These solids are built by oxo-centered trimers of metal octahedra and polycarboxylate ligands (terephthalate for MIL-101, trimesate for MIL-100, 3, 3', 5, 5'-azobenzenetetracraboxylate for MIL-127(Fe)). MIL-127(Fe) exhibits a microporous cubic structure with a soc topology and its two-steps water sorption isotherm can be explained by the consecutive filling of hydrophilic cages (~10 Å) or channels (~5 Å) and then hydrophobic pores (~7 Å) leading to two uptakes at p/p_0=0.30 and at p/p_0=0.60, respectively (T=30°C).[34] MIL-100(Fe) and MIL-101(Cr) present a MTN zeolite topology with two types of mesoporous cages of 24/27 Å and 27/34 Å, respectively, and high specific surface areas (Table 1). These structural properties can explain the step-wise shape of the water adsorption isotherms and the large water uptake. For MIL-100(Fe), as reported before, two steep rise uptakes of 0.49 g/g at p/p_0=0.35 and 0.35 g/g at p/p_0=0.45 correspond to the consecutive filling of the 25 Å and 29 Å mesoporous cages, respectively.[30] Due to its more hydrophobic character, MIL-101(Cr) exhibits a water uptake close to 1.20 g/g but shifted to higher relative pressure of p/p_0=0.4-0.5 in agreement with previous studies.[30] Similarly to MIL-100(Fe), the water adsorption proceeds in a stepwise manner with consecutive filling of the two different mesopores of 29 and 34 Å. (i. e. first adsorption lift of 0.97g/g at p/p_0=0.40 and total adsorption lift of 1.55 g/g at p=0.50). The adsorption loading lifts and cycling loading lifts of MIL-127(Fe), MIL-100(Fe) and MIL-101(Cr) are respectively of 0.28 and 0.20 g/g, 0.39 and 0.32 g/g and 0.17 and 0.12 g/g (Fig. S20). In addition to their interesting water sorption properties, these MOFs present a suitable stability under numerous adsorption-desorption cycles. It has been previously reported that the mass loss of exchanged water is of 3.2 % (40 cycles), 6.37 % (40 cycles), 17 % (40 cycles), 38 % (40 cycles) and 0 % (10 cycles) for respectively MIL-101(Cr), MIL-100(Fe), MIL-125(Ti)-NH_2, UiO-66(Zr)-NH_2 and MIL-160(Al).[28,29,35,36] This series of MOFs (see Fig S2-S19 for the full characterization of MOFs) shows also great promises for the application of interest due to the possibility to easily scale-up them up at the laboratory scale up to at least 200 g. Moreover, MIL-100(Fe)[37], MIL-101(Cr)[38] can be synthesized using H_2O as solvent, MIL-127(Fe)[39] in alcohols while MIL-160(Al)[31] is obtained through a green route using a bio-derived linker.

In a second step, composites combining MOF matrices and $CaCl_2$ were synthesized. The MOFs were dried 3 hours in an oven at 100 °C, followed by impregnation of aqueous solutions of $CaCl_2$ of different concentrations (Table S1). To the best of our knowledge, the synthesis of such materials has not been reported elsewhere. Composites with a $CaCl_2$ content varying between 30 and 62 wt% were fully characterized by combining powder X-ray diffraction (PXRD), thermogravimetric analysis (TGA), scanning electron microcopy (SEM), energy dispersive X-ray (EDX) elemental mapping and N_2 sorption and elemental analysis (see Fig S29-S60). The influence of the soaking time, sample washing, concentration of $CaCl_2$, temperature, number of encapsulation steps on the microstructural properties and composition of composites was investigated. Washing of composites with H_2O or EtOH, initially to remove the excess of salt at the outer surface of MOF particles, was ruled out due to the removal of most of the salt initially encapsulated. The temperature during encapsulation process was fixed to ambient values since higher temperatures led to a very high amount of salt in the matrix but with a large amount of salt located at the surface of MOF particles with unstable resulting composites. Two methods of encapsulation were studied with one or several encapsulation steps. In the first one, each encapsulation step was followed by centrifugation and removal of the liquid phase with however a negligible increase of the salt content with the number of encapsulation steps. The second method used a drying of the composites after each encapsulation which led to an enhancement of the salt content but a recrystallization of the salt at the surface of MOF particles. Finally, we selected a one-step encapsulation procedure and modulated the concentration of the initial salt solution to tune the salt content in the composites with homogeneously distributed salt on a reproducible manner.

Powder X-ray diffraction (PXRD) patterns of composites were collected at room temperature and high temperature (150°C). First, for the whole series of composites, the X-ray diffraction patterns are in good agreement with that of pure MOFs indicating, that the structure of MOFs is preserved in composites (see Fig. S27-S34). Secondly, for the composites with the highest salt content (i. e. MIL-127(Fe)/$CaCl_2$ (40 wt%)), the presence of $CaCl_2 \cdot 2H_2O$ (25°C) or anhydrous $CaCl_2$ at 150°C is clearly evidenced and is likely to be due to a recrystallization of a small amount of salt at the outer surface of MOFs particles (Fig. S28). Finally, in the case of composites based on large pores MIL-100(Fe) and MIL-101(Cr), a significant decrease of relative intensity of diffraction Bragg peaks can be observed at RT and 150°C, especially at low angle, which is probably due both to a modification of the electronic density (and thus a strong absorbance of the X-ray by the materials) as well as an increase of the disorder within the pores as a result of the encapsulation of the hydrated salt in very large pores.[37,40] To prove such assumption, we carried out a similar PXRD analysis using the same samples but washed in water to remove the salt. The PXRD patterns recorded on these composites obtained after washing in water exhibit the same diffraction peaks typical of the parent MOFs (see Fig. S35-S36) confirming the preservation of their structure after the salt loading. In addition, SEM images of composites show that the morphology of MOFs crystallites is not altered after the salt encapsulation, confirming the absence of any MOF degradation (see Figures S45-S52). The salt rate was determined by thermogravimetric analysis, EDX analysis and elemental analysis (these data are presented in Table S4). According to SEM and EDX elemental mapping, no $CaCl_2$ crystallites can be observed in the samples, either at the surface of MOFs particles or in the inter-particle space.

The Calcium/Metal (Ca/M) ratio obtained by EDX (Table S4) is on the whole similar for 3 areas of composite, confirming the homogeneously distribution of salt among the different MOFs particles, although in the case of UiO-66(Zr)-NH_2/$CaCl_2$ (43%) and MIL-125(Ti)-NH_2/$CaCl_2$ (45%), a slightly heterogeneous Ca/M ratio may arise from a significant distribution of MOFs particle size, thereby affecting the diffusion and location of salts. Nevertheless, for all MOF based composites, the total salt content for each composite determined by thermogravimetric analysis, EDX and elemental analysis is comparable (see Table S4). Nitrogen sorption isotherms of composites show as expected a strong decrease of pore volume and surface area BET as a result of the salt entrapment. Noteworthy, both depending on the salt content and the type of MOFs, a residual porosity remains after salt incorporation, which may play a significant role in the final water sorption capacity of composites (however, nitrogen sorption porosimetry indicates the residual porosity when salt is in anhydrous state, thus we can discuss about the impact of physical sorption of MOFs only after comparison the water sorption capacity of composite with one of bulk salt).

In order to shed light on the influence of $CaCl_2$ content on the water sorption properties of composites, two series of MOFs-$CaCl_2$ composites with different salt contents were further prepared: i) a first one with a similar salt content, i.e. close to 31-34 wt%, and ii) a second series with an increased salt loading between 40 and 64 wt%. The analysis of the first series of composites highlighted the impact of the water physical sorption in MOFs on the water uptake of composites, in direct relationship with the hydrophilic character and the free pore volume of the MOFs. The second series, which includes composites with higher salt content, shows the effect of their amphiphilic character, residual pore volume and salt loading capacity on the water uptake. Noteworthy, for each MOF structure and considering their theoretical pore volume, it was possible to estimate three limits of salt content to be encapsulated that corresponds to volume of anhydrous $CaCl_2$ and its tetra and hexahydrate. The first limit takes into account the maximum amount of anhydrous $CaCl_2$ that can be encapsulated in the MOF matrix without recrystallization of salt outside of MOF porosity. The good way to control the absence of such recrystallization is PXRD analysis. However, we need also to take into account the volume that encapsulated $CaCl_2$ will occupy in adsorption step. It is difficult to predict the state of the salt in composite in adsorption step (solution, tetra or hexahydrate) but we however calculated the second and third limits (Table 2) as maximal amount of anhydrous $CaCl_2$ encapsulated in each MOF taking into account its further transformation in tetra or hexahydrate, respectively.

Table 2. Properties of MOF-salt composites

MOF-martix	$CaCl_2$ content [a], [%, wt]	Limit 2-Limit 3[b], [%, wt]	V pore of matrix (theor.) [cm^3/g]	S_{BET} of composite [m^2/g]	V pore of composite [cm^3/g]	Ads. loading lift, g/g	Cycling loading lift, g/g	Calculated energy storage capacity [Wh/kg]	Measured energy storage capacity, [Wh/kg]	Calculated energy storage density [kWh/m^3]
MIL-160(Al)	34	27-36	0.50	523±16[c]	0.240±0.006	0.35	0.21			
UiO-66 (Zr)_NH_2	43	27-36	0.50	309±10[d]	0.130±0.004	0.47	0.34	248	-	-
MIL125 (Ti)_NH_2	45	35-46	0.78	356±13[c]	0.240±0.004	0.46	0.35	254	-	-
MIL-127(Fe)	31	38-48	0.83	517±15[c]	0.228±0.009	0.46	0.33			
MIL-127(Fe)	40	38-48	0.83	516±3[c]	0.223±0.005	0.43	0.33	243	-	-
MIL-100(Fe)	34	43-53	1.02	365±46[c]	0.119±0.005	0.48	0.34			
MIL-100(Fe)	46	43-53	1.02	291±13[c]	0.133±0.016	0.56	0.48	357	-	222
MIL-101(Cr)	62	59-68	1.95	323±1[c]	0.170±0.010	0.75	0.60	439	-	280

[a] Salt content are presented according chemical analysis; [b] Limit 2 and 3 of salt content based on tetra and hexahydrate state (respectively) of salt in the porosity of MOF [c] standard deviation on 3 measurements; [d] standard deviation on 10 measurements

However, one could point out that these values might be slightly overestimated since one could expect that not all the pore volume is accessible to such a bulky guest salt. For instance, MIL-127(Fe) exhibits two types of porosity: 1-D channel systems (~5-8 Å) and cages accessible only through very narrow windows (~3 Å). Thus, the filling of the latter pores by the salt is impossible and as a consequence the experimental loading capacity in MIL-127(Fe) is less than 48 wt%. Only in the case of UiO-66(Zr)_NH_2/$CaCl_2$ (43 wt%), the experimental exceeds the theoretical, with no evidence of recrystallized salt detected by PXRD (see Fig. S29), which is probably due to the presence of linker's defects leading to a larger pore volume sample. Noteworthy, increasing the porosity through the use of mesoporous MOFs such as MIL-100(Fe) (1.02 $cm^3.g^{-1}$ theor.) and MIL-101 (1.95 $cm^3.g^{-1}$ theor.), leads to higher salt loadings (i. e. 46 and 62 wt%), far beyond the values obtained with composites based on silica gel (28-34 wt%).[41,42]

The water sorption behavior of the first series of composites with similar salt contents (31-34 wt%) was studied using conditions of a seasonal energy storage namely, adsorption condition at T=30°C and p=12.5 mbar (adsorption loading lift) and above mentioned cycle condition (cycling loading lift) (Fig. 1).

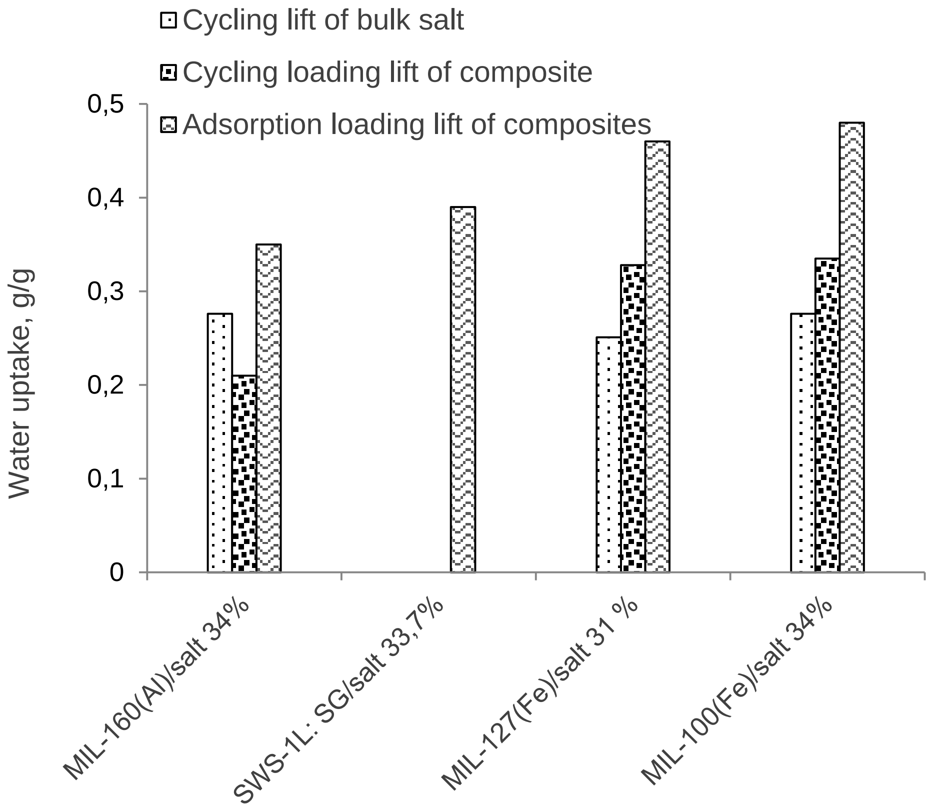

Figure 2. Adsorption (p=12.5 mbar), cycling loading lift (p=12.5 mbar) and energy storage capacity of MOF based composites with $CaCl_2$ (31-34 wt%) and adsorption lift of silica gel based composite SWS-1L (p=12.3 mbar)

For a better understanding, we report a comparison with composites based on silica gel host matrix (i. e. SWS-1L) with a 33.7 wt% $CaCl_2$ loading is proposed,[42] as well as the corresponding cycling loading lift due to salt hydration with the same salt content, calculated by considering the behavior of bulk $CaCl_2$ at 12.5 mbar between 30°C and 80°C as a monohydrate to hexahydrate transition.

One can first notice that the water uptake of composites is not improved by using a hydrophilic host matrix. For instance, for the most hydrophilic MOF in play here, MIL-160(Al), a significantly lower (or comparable) performance was observed compared with those of composites based on amphiphilic MOFs (i. e. MIL-127(Fe) and MIL-100(Fe)). Noteworthy, this is striking for MIL-160(Al) that (i) no improvement in water uptake is even evidenced upon the salt encapsulation (0.36 g/g) compared to the pure MOFs (0.38 g/g) and (ii) the cycling loading lift of the composite (34 wt%) is even lower (0.21 g/g) than that of pure MIL-160(Al) (0.37 g/g). Such phenomenon may be explained by the high hydrophilic character of MIL-160(Al)/$CaCl_2$ composite (34 wt%) which possesses both a very hydrophilic framework and adsorbed guests (salt, water), leading to a much lower desorption efficiency at 80°C. Moreover, the 1D pore system of MIL-160(Al), combined with the large amount of entrapped salt, whose loading close to the upper limit salt content of this MOF, might restrict non only the desorption of water but also its accessibility and diffusion and probably also the complete transition of salt from hexahydrate to monohydrate state (see Table 1).

In contrast, when dealing with amphiphilic MOFs based composites, i. e. MIL-127(Fe)/$CaCl_2$ (31 wt%) and MIL-100(Fe)/$CaCl_2$ (34 wt%), the adsorption and cycling loading lifts are enhanced compared to the pure MOFs. Moreover, these values are also superior than that of the pure bulk salt (see Fig. 2), as a result of a beneficial synergy between the chemical sorption of salt and the physical sorption of MOFs, derived from the residual pore volume of the composites, whose salt content is lower than the upper salt limit (i. e. 48-53 wt%).

To gain further understanding, a second series of composites was prepared with salt loadings higher than 30 wt%, i.e. MIL-125(Ti)-NH_2/$CaCl_2$ (45% wt), UiO-66(Zr)_NH_2/ $CaCl_2$(43% wt), MIL-127(Fe)/$CaCl_2$ (40% wt), MIL-100(Fe)/$CaCl_2$ (46% wt) and MIL-101(Cr)/$CaCl_2$ (62% wt) (for MIL-160, the salt rate already reached the upper limit of $CaCl_2$ content in the first series of composites). The amount of $CaCl_2$ is directly here linked to the pore volume of MOFs: the higher the pore volume of MOFs, the higher the $CaCl_2$ amount is encapsulated. Therefore, particularly for the mesoporous MOFs based composites issued from MIL-100(Fe) and MIL-101(Cr), the amount of loaded $CaCl_2$ is much higher than that reported for silica gel composites such as SWS-1L/$CaCl_2$ (33 wt%)[42], SBA (8.7nm)/$CaCl_2$ (28.2 wt%)[21] or SBA

(11.8 nm)/$CaCl_2$ (29.5 wt%)[41] . Furthermore, the cycling loading lift increases strongly with increasing the salt content as shown by comparing 40-46 wt% composites and 62 wt% MIL-101(Cr)/$CaCl_2$ (Figure 3), and composites based on MIL-100(Fe) with 34 wt% and 46 wt% of $CaCl_2$ (Fig. 2 and 3).

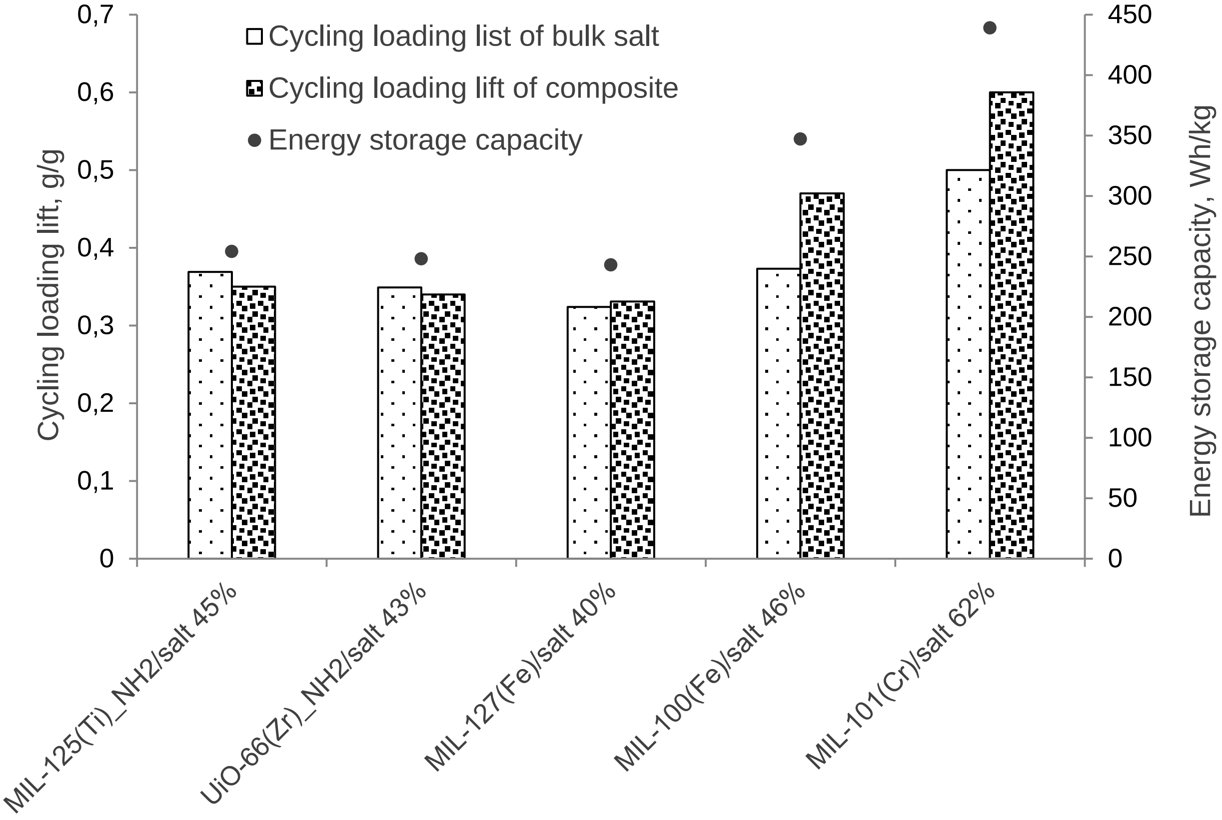

Figure 3. Cycling loading lift and energy storage capacity (Wh/kg) of composites MIL-125(Ti)-NH_2/$CaCl_2$ (44% wt), UiO-66(Zr)_NH_2/ $CaCl_2$ (43% wt), MIL-127(Fe)/$CaCl_2$ (40% wt), MIL-100/$CaCl_2$ (46 wt%), MIL-101(Cr)/CaC_2 (62 wt%). Cycle conditions: adsorption at 30°C and p=12.5 mbar, desorption at 80°C and p=12.5 mbar

In case of composites 31 and 40 wt% MIL-127(Fe)/$CaCl_2$ there is no difference in cycling loading lift due certainly to an overestimated salt limit for composite with 40 wt% as expected for the MIL-127(Fe) porous system.

As observed for the first series of composites, lower cycling loading lift values are typically observed for hydrophilic MOFs based composites (i. e. MIL-125(Ti)-NH_2/$CaCl_2$ (45 wt%), UiO-66(Zr)_NH_2/$CaCl_2$ (43 wt%) or composites with the lowest amount of salt (i. e. MIL-127(Fe)/$CaCl_2$ (40 wt%) (see Fig. 3). Once again, the cycling loading lifts of composites were compared to those derived by the hydration process of the bulk salt. It is remarkable that for amphiphilic MOF based composites, the cycling loading lift of the composites is larger than that of pure salt, showing that the water uptake of composites results from a complex interplay between the amphiphilic balance and residual pore volume of MOFs and the content and location of salt. In particular, the amphiphilic character of MOFs may favor the desorption process while their residual pore volume may enhance the adsorption process. One can expect also here a full transition between mono to hexahydrate during adsorption/desorption processes. For instance the MIL-101(Cr)/$CaCl_2$ (62 wt%) composite, which exhibits to our knowledge the best performance so far in the field of $CaCl_2$ porous solids composites, illustrates the ideal structural and physic-chemical requirements for seasonal heat storage applications. This material combines a huge salt content, a moderate hydrophilic character and a significant residual accessible pore volume. The 3D mesoporous pore system of MIL-101 may also enhance a fast water sorption diffusivity. Such influence of the pore size of the host matrix on the water sorption behavior of composites was previously reported for other host matrices.[41]

In a last step, cycling loading lifts of composites and microcalorimetric measurements were both used to calculate the energy storage capacity (Wh/kg) of the second series of salt-MOF composites (see Figure 3). The calculated energy capacity for the second series of composites give are 254, 248, 243, 357 and 439 Wh/kg for composites based on MIL-125(Ti)-NH_2, UiO-66(Zr)_NH_2, MIL-127(Fe), MIL-100(Fe), MIL-101(Cr), respectively.

For the two most promising composites MIL-100(Fe)/$CaCl_2$ (46 wt%) and MIL-101(Cr)/$CaCl_2$ (64 wt%), the energy storage volumetric density (kWh/m^3) was evaluated by taking into account the packing density of composites in their powdered forms (see SI). The values of MIL-100/$CaCl_2$ (46 wt%) and MIL-101(Cr)/$CaCl_2$ (62 wt%), are respectively equal to 222 kWh/m^3 and 280 kWh/m^3 (Table 2). Although the shaping and packing of the MOFs-$CaCl_2$ composites have not been yet optimized, their performances are higher or comparable to that of the most promising composites reported so far in the literature (see Table 3).[41–44]

Table 3. The comparison of composites (literature) with MOF based composite (this work) for space heating application

matrix	salt	salt content [%, wt]	Energy storage capacity [Wh/kg]	Energy storage density [kWh/m^3]	Adsorption temperature [°C]	Additional data on adsorption	Desorption temperature [°C]	Ref.
MIL-100(Fe)	$CaCl_2$	46	357	222	30	12.5 mbar	80	this work
MIL-101(Cr)	$CaCl_2$	62	439	280	30	12.5 mbar	80	this work
Silica gel KSK	**$CaCl_2$**	**33.7**	**132**	**85**	**40**	**17.0 mbar**	**90**	[47]
Silica gel	**LiCl**	**35**	**254**	**163**	**40**	**17.0 mbar**	**90**	[48]
Silica gel	**$CaCl_2$**	**-**	**283**	**-**	**30**	**33.9 mbar**	**90**	[44,45]
Zeolite 13X	$MgSO_4$	15	180	166	30	15.9 mbar	150	[44]
attapulgite	$MgSO_4$/$MgCl_2$	-	397	-	30	31.8 mbar	130	[46]

Aluminosilicate	$CaCl_2$	30	240	-	40	20 mbar	120	[49]
FeKIL2 iron silicate	$CaCl_2$	7	155	-	25	12 mbar	150	[50]

Besides, we need to bear in mind that any direct comparison of storage capacity is complicated, because it strongly depends on cycle boundary condition and design of energy storage device. For example, the increase of desorption temperature from 80°C to 100°C will enhance the cycling loading lift and, thus the energy storage density. Nevertheless, the state of the art of composite materials (inorganic salt in porous matrix) developed for space heating application is presented in Table 3. If considering the low desorption temperature below 100°C the energy storage capacity values of reported materials ($CaCl_2$ or LiCl encapsulated in silica gel matrix) are in range of ~130-280 Wh/kg that are lower than for salt-MOF composites. The highest energy storage density was found for silica gel/$CaCl_2$ composite.[45] This silica gel matrix and MIL-100(Fe) have equal pore volume (0.81 cm^3/g) and composites based on these matrices were prepared using similar synthesis conditions (using 35 wt% and 40 wt% $CaCl_2$ solution, respectively). It is interesting to underline, that despite the more efficient cycling conditions of the silica gel based composite compared to MIL-100(Fe)/$CaCl_2$ (46 wt%) (i. e. higher pressure of adsorption (RH=80% versus 30% at 30°C) and temperature of regeneration (90°C versus 80°C)), the storage capacity of this composite is lower than that of MOF-based one (283 Wh/kg versus 357 Wh/kg).

If considering operating conditions with regeneration temperature of 120-150°C the higher energy storage capacity below 400 Wh/kg can be found for reported composites based on zeolite 13X, attapulgite, alumosilicate and iron silicate matrices. For example, the highest energy storage capacity (397 Wh/kg) which is comparable with our composite was reported for composite of attapulgite with $MgSO_4$ and $MgCl_2$ (mass ratio 20/80).[46] However, this energy storage capacity refers to higher pressure conditions of adsorption compared to our conditions (31.8 versus 12.5 mbar, respectively).

The packing density parameter, which is of primary importance when considering the volume of the storage device, depends not only on the crystallographic density, but also on the particle size and shaping process of the host matrix. Thus, the packing density could be optimized by tailoring the particle size during the MOF synthesis or through an appropriate processing and shaping of the composite.

Finally, in order to evaluate the cycling stability of MIL-100(Fe)/$CaCl_2$ (46 wt%) and MIL-101(Cr)/$CaCl_2$ (62 wt%) composites, these materials were exposed to continuous water adsorption and desorption cycles in representative conditions of seasonal energy storage devices. MIL-100(Fe)/$CaCl_2$ (46 wt%) shows a decrease of about 11 % of initial performance after 11 adsorption-desorption cycles (Figure 4) but reaches a steady state after 7 cycles. The same phenomenon was already reported for pure MIL-100(Fe) and water sorption.[13]

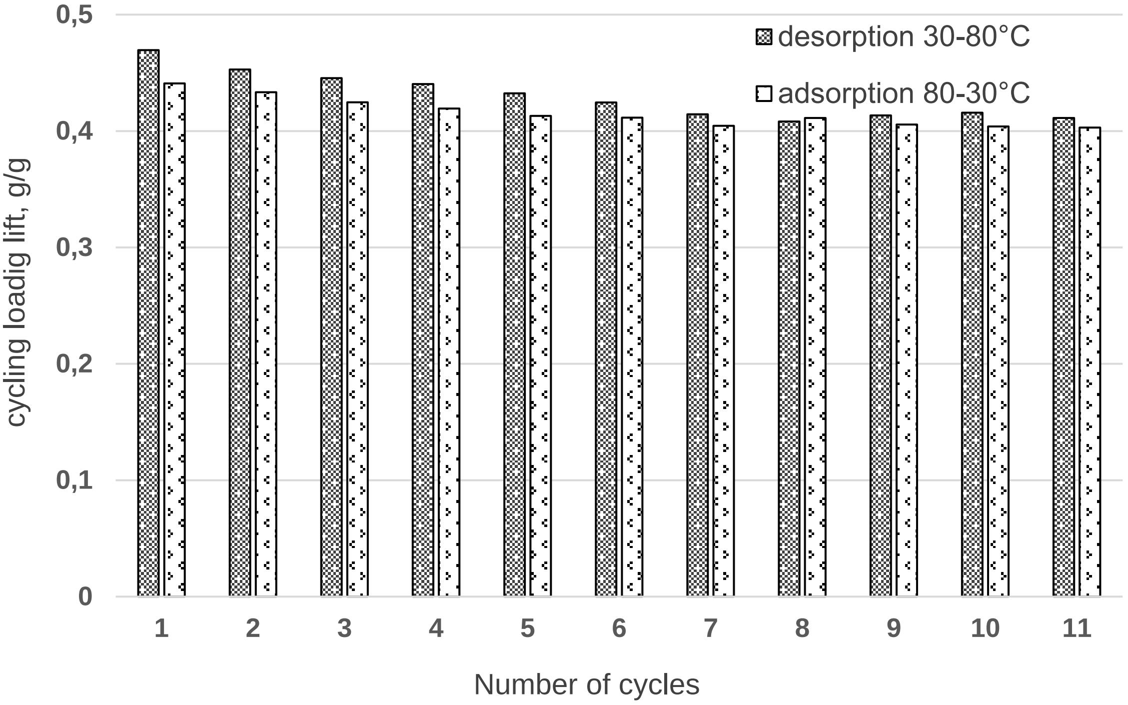

Figure 4. Stability under numerous adsorption-desorption cycles of composite MIL-100/$CaCl_2$ (46 wt%).

MIL-101(Cr)/$CaCl_2$ (62 wt%) present only 8% of losses under 10 adsorption-desorption cycles (Figure 5) but reaches a steady state after 4 cycles.

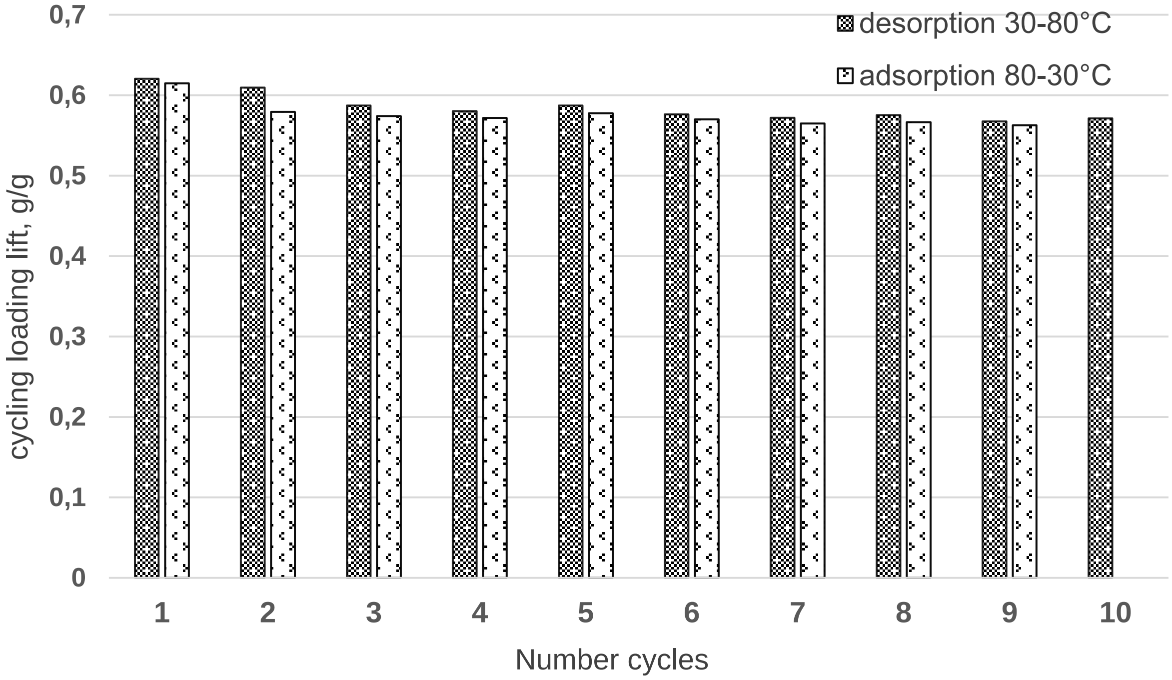

Figure 5. Stability under numerous adsorption-desorption cycles of composite MIL-101(Cr)/$CaCl_2$ (62 wt%).

The ageing stability of MIL-100(Fe)/$CaCl_2$ (46 wt%) and MIL-101(Cr)/$CaCl_2$ (62 wt%) was studied by collecting PXRD, SEM, TGA and nitrogen sorption porosimetry measurements after ageing the samples for about 18 and 6 months, respectively, with no evidence of framework degradation (see Fig. S68-S73). The high water stability of these composite suggest that these materials can pave the way towards highly efficient water sorbent for heat reallocation.

Conclusions

A systematic synthesis and characterization study of series of high loading $CaCl_2$ composites based on robust MOFs bearing various chemical and structural features, has been carried out in a view of energy reallocation applications. It has been shown first that the increase of salt content in composites significantly enhances the water adsorption capacity of material, while the hydrophilicity character of the MOF-matrix does not improve the overall water uptake due to regeneration or salt hydration limitations. Secondly, the use of an amphiphilic MOF at intermediate salt loadings enables a synergetic effect between the salt water chemisorption and the physisorption of the residual pore volume of the MOF, leading to better performances compared with the pure MOF or salt. Finally, the use of mesoporous robust MOFs is an efficient strategy to achieve higher encapsulation rates and thus, higher loading lifts in comparison with silica gel matrix. This results into very promising MOF-salt composites, with a good cycling performance, for seasonal storage application with energy volumetric density up to 280 kWh/m^3, a value which could be still enhanced by optimizing the packing density of the composites. Moreover, one could also expect a more suitable choice of boundary conditions (e.g. desorption temperature) leading to even more efficient materials. Given the large variety of stable MOFs candidates already available, this paves the way for the design of advanced composites based on new MOF matrices for energy reallocation applications.

Supporting Information

Supporting Information is available from the Wiley Online Library or from the author.

Acknowledgements

The authors acknowledge the financial support of the European Community within the FP7 Program (Project SOTHERCO).

Received: ((will be filled in by the editorial staff))
Revised: ((will be filled in by the editorial staff))
Published online: ((will be filled in by the editorial staff))

[1] Y. I. Aristov, *Appl. Therm. Eng.* **2013**, *50*, 1610.

[2] B. B. Saha, A. Chakraborty, S. Koyama, Y. I. Aristov, *Int. J. Heat Mass Transf.* **2009**, *52*, 516.

[3] F. Jeremias, D. Fröhlich, C. Janiak, S. K. Henninger, *New J. Chem.* **2014**, *38*, 1846.

[4] S. Shimooka, K. Oshima, H. Hidaka, T. Takewaki, H. Kakiuchi, A. Kodama, M. Kubota, H. Matsuda, *J. Chem. Eng. Jpn.* **2007**, *40*, 1330.

[5] Y. I. Aristov, M. M. Tokarev, G. Restuccia, G. Cacciola, *React Kinet Catal Lett* **1996**, *59*, 325.

[6] Y. I. Aristov, M. M. Tokarev, G. Restuccia, G. Cacciola, *React Kinet Catal Lett* **1996**, *59*, 335.

[7] E. Levitskij, *Sol. Energy Mater. Sol. Cells* **1996**, *44*, 219.

[8] Y. I. Aristov, J. Di. Marco, M. M. Tokarev, N. V. Parmon, *React Kinet Catal Lett* **1997**, *61*, 147.

[9] Y. I. Aristov, *J. Chem. Eng. Jpn.* **2007**, *40*, 1242.

[10] I. A. Simonova, Y. I. Aristov, *Rus J Phys Chem* **2005**, *79*, 1307.

[11] I. A. Simonova, A. Freni, G. Restuccia, Y. I. Aristov, *Microporous Mesoporous Mater.* **2009**, *122*, 223.

[12] G. Férey, *Chem Soc Rev* **2008**, *37*, 191.

[13] L. J. Murray, M. Dincă, J. R. Long, *Chem. Soc. Rev.* **2009**, *38*, 1294.

[14] P. L. Llewellyn, M. Garcia-Rates, L. Gaberová, S. R. Miller, T. Devic, J.-C. Lavalley, S. Bourrelly, E. Bloch, Y. Filinchuk, P. A. Wright, C. Serre, A. Vimont, G. Maurin, *J. Phys. Chem. C* **2015**, *119*, 4208.

[15] Q. Yang, S. Vaesen, F. Ragon, A. D. Wiersum, D. Wu, A. Lago, T. Devic, C. Martineau, F. Taulelle, P. L. Llewellyn, H. Jobic, C. Zhong, C. Serre, G. De Weireld, G. Maurin, *Angew. Chem. Int. Ed.* **2013**, *52*, 10316.

[16] J. Lee, O. K. Farha, J. Roberts, K. A. Scheidt, S. T. Nguyen, J. T. Hupp, *Chem. Soc. Rev.* **2009**, *38*, 1450.

[17] P. Horcajada, S. Surblé, C. Serre, D.-Y. Hong, Y.-K. Seo, J.-S. Chang, J.-M. Grenèche, I. Margiolaki, G. Férey, *Chem. Commun.* **2007**, 2820.

[18] J. Gascon, U. Aktay, M. Hernandezalonso, G. Vanklink, F. Kapteijn, *J. Catal.* **2009**, *261*, 75.

[19] M. A. Nasalevich, R. Becker, E. V. Ramos-Fernandez, S. Castellanos, S. L. Veber, M. V. Fedin, F. Kapteijn, J. N. H. Reek, J. I. van der Vlugt, J. Gascon, *Energy Env. Sci* **2015**, *8*, 364.

[20] C. Rösler, R. A. Fischer, *CrystEngComm* **2015**, *17*, 199.

[21] P. Horcajada, T. Chalati, C. Serre, B. Gillet, C. Sebrie, T. Baati, J. F. Eubank, D. Heurtaux, P. Clayette, C. Kreuz, J.-S. Chang, Y. K. Hwang, V. Marsaud, P.-N. Bories, L. Cynober, S. Gil, G. Férey, P. Couvreur, R. Gref, *Nat. Mater.* **2010**, *9*, 172.

[22] P. Horcajada, R. Gref, T. Baati, P. K. Allan, G. Maurin, P. Couvreur, G. Férey, R. E. Morris, C. Serre, *Chem. Rev.* **2012**, *112*, 1232.

[23] M. Meilikhov, S. Furukawa, K. Hirai, R. A. Fischer, S. Kitagawa, *Angew. Chem. Int. Ed.* **2013**, *52*, 341.

[24] L. E. Kreno, K. Leong, O. K. Farha, M. Allendorf, R. P. Van Duyne, J. T. Hupp, *Chem. Rev.* **2012**, *112*, 1105.

[25] S. S. Nagarkar, B. Joarder, A. K. Chaudhari, S. Mukherjee, S. K. Ghosh, *Angew. Chem. Int. Ed.* **2013**, *52*, 2881.

[26] B. Joarder, A. V. Desai, P. Samanta, S. Mukherjee, S. K. Ghosh, *Chem. - Eur. J.* **2015**, *21*, 965.

[27] A. V. Desai, P. Samanta, B. Manna, S. K. Ghosh, *Chem Commun* **2015**, *51*, 6111.

[28] F. Jeremias, V. Lozan, S. K. Henninger, C. Janiak, *Dalton Trans.* **2013**, *42*, 15967.

[29] F. Jeremias, A. Khutia, S. K. Henninger, C. Janiak, *J Mater Chem* **2012**, *22*, 10148.

[30] Y.-K. Seo, J. W. Yoon, J. S. Lee, Y. K. Hwang, C.-H. Jun, J.-S. Chang, S. Wuttke, P. Bazin, A. Vimont, M. Daturi, S. Bourrelly, P. L. Llewellyn, P. Horcajada, C. Serre, G. Férey, *Adv. Mater.* **2012**, *24*, 806.

[31] A. Cadiau, J. S. Lee, D. Damasceno Borges, P. Fabry, T. Devic, M. T. Wharmby, C. Martineau, D. Foucher, F. Taulelle, C.-H. Jun, Y. K. Hwang, N. Stock, M. F. De Lange, F. Kapteijn, J. Gascon, G. Maurin, J.-S. Chang, C. Serre, *Adv. Mater.* **2015**, *27*, 4775.

[32] G. Akiyama, R. Matsuda, H. Sato, A. Hori, M. Takata, S. Kitagawa, *Microporous Mesoporous Mater.* **2012**, *157*, 89.

[33] G. E. Cmarik, M. Kim, S. M. Cohen, K. S. Walton, *Langmuir* **2012**, *28*, 15606.

[34] Soubeyrand-Leonoir, Estelle, Adsorption et Separation de Gaz En Mode Dynamique Sur Des Materiaux Hybrides, **2012**.

[35] A. Khutia, H. U. Rammelberg, T. Schmidt, S. Henninger, C. Janiak, *Chem. Mater.* **2013**, *25*, 790.

[36] A. Cadiau, J. S. Lee, D. Damasceno-Borges, P. Fabry, T. Devic, M.T. Wharmby, C. Martineau, D. Fouchet, F. Taulelle, C.-H. Jun, Y. K. Hwang, N. Stock, M. F. De Lange, F. Kapteijn, J. Gascon, G. Maurin, J.-S. Chang, C. Serre, *Adv. Mater.* **2015**, *27*, 4775.

[37] R. Canioni, C. Roch-Marchal, F. Sécheresse, P. Horcajada, C. Serre, M. Hardi-Dan, G. Férey, J.-M. Grenèche, F. Lefebvre, J.-S. Chang, Y.-K. Hwang, O. Lebedev, S. Turner, G. Van Tendeloo, *J Mater Chem* **2011**, *21*, 1226.

[38] D.-Y. Hong, Y. K. Hwang, C. Serre, G. Férey, J.-S. Chang, *Adv. Funct. Mater.* **2009**, *19*, 1537.

[39] H. Chevreau, A. Permyakova, F. Nouar, P. Fabry, C. Livage, F. Ragon, A. Garcia-Marquez, T. Devic, N. Steunou, C. Serre, P. Horcajada, *CrystEngComm* **2016**, DOI 10.1039/C5CE01864A.

[40] G. Férey, *Science* **2005**, *309*, 2040.

[41] I. Glaznev, I. Ponomarenko, S. Kirik, Y. Aristov, *Int. J. Refrig.* **2011**, *34*, 1244.

[42] Y. I. Aristov, G. Restuccia, G. Cacciola, V. N. Parmon, *Appl. Therm. Eng.* **2002**, *22*, 191.

[43] Kerskes H., Mette B., Bertsch F., Asenbeck S., Druck H., *Thermische Solarenergie:: 19. Symposium; 06. bis 08. Mai 2009, Kloster Banz, Bad Staffelstein. Hauptbd. [...]*, OTTI, Regensburg, **2009**.

[44] S. Hongois, Stockage de Chaleur Inter-Saisonnier Par Voie Thermochimique Pour Le Chauffage Solaire de La Maison Individuelle, INSA de Lyon, **2011**.

[45] H. Wu, S. Wang, D. Zhu, *Sol. Energy* **2007**, *81*, 864.

[46] K. Posern, C. Kaps, *Thermochim. Acta* **2010**, *502*, 73.

[47] C. Bales, P. Gantenbein, A. Hauer, H.-M. Henning, D. Jaenig, H. Kerskes, T. Núñez, K. Visscher, *Rep. IEA Sol. Heat. Cool. Program.* **2005**, *32*.

[48] N. Yu, R. Z. Wang, Z. S. Lu, L. W. Wang, *Chem. Eng. Sci.* **2014**, *111*, 73.

[49] J. Jänchen, D. Ackermann, H. Stach, W. Brösicke, *Sol. Energy* **2004**, *76*, 339.

[50] A. Ristić, D. Maučec, S. K. Henninger, V. Kaučič, *Microporous Mesoporous Mater.* **2012**, *164*, 266.

Supporting Information

Design of salt-Metal Organic Frameworks composites for heat storage applications

Anastasia Permyakova, [a,b] *Sujing Wang,*[a] *Emilie Courbon,*[b] *Farid Nouar,*[a] *Pierre Billemont,*[b] *Nicolas Heymans,*[b] *Guy De Weireld,*[b] *Nathalie Steunou,*[a*] *Marc Frère* [b] *and Christian Serre* [a*]

[a] Institut Lavoisier, UMR CNRS 8180, Université de Versailles St-Quentin en Yvelines, Université Paris-Saclay, 45 Avenue des Etats-Unis, 78035 Versailles Cedex, France. E-mail: christian.serre@uvsq.fr, nathalie.steunou@uvsq.fr

[b] Faculté Polytechnique de UMONS, Service de Thermodynamique et de Physique mathématique, 31, boulevard Dolez, 7000 Mons, Belgique

Keywords: heat storage materials, Metal-Organic-Frameworks, composites

I. Thermochemical energy storage

Thermochemical energy storage is based on reversible exo-/endothermic reaction of storage material with working fluid (generally, water). Adsorption process (zeolite, silica gel) or hydration process (salt) which is activated by bringing the dry storage material in contact with a working fluid results in release of heat energy. The seasonal space heating applications imply energy charging in summer period and heat release (energy discharging process) in winter. The Figure S1 shows the scheme of closed-system device for seasonal heat storage.

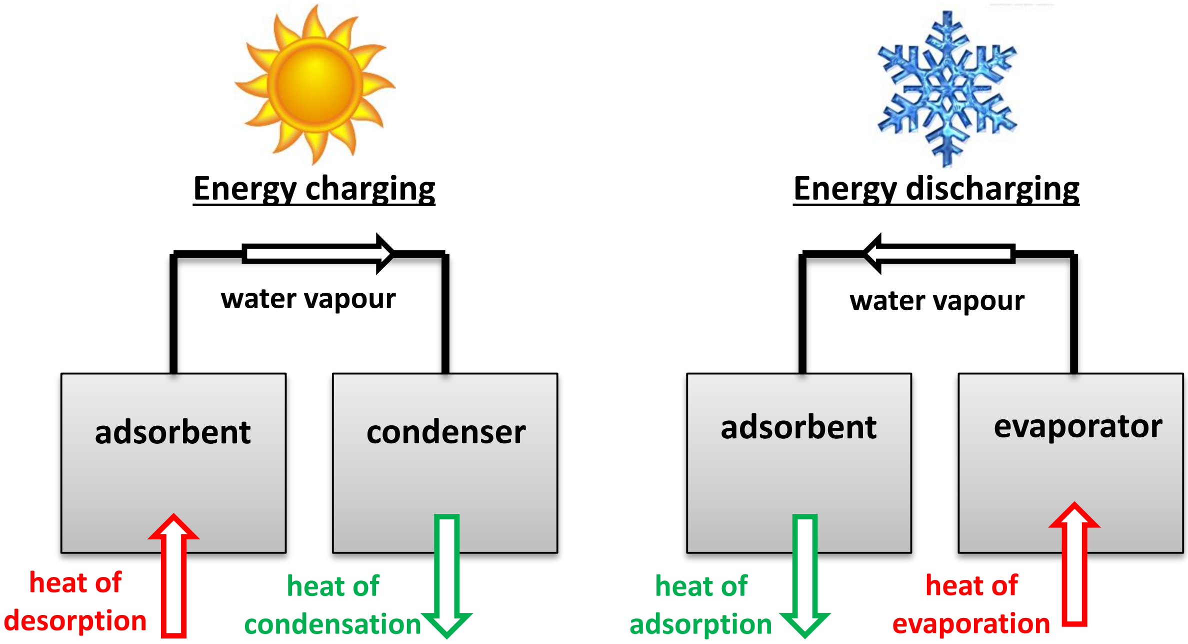

Figure S1. Closed-system device for seasonal heat storage

II. Analysis and equipment

1. Characterization of materials

Powder X-ray diffraction patterns of MIL-100(Fe), MIL-127(Fe), MIL-101(Cr), MIL-125(Ti)-NH_2, UiO-66(Zr)-NH_2 and MIL-160(Al) samples were obtained on a Siemens D5000 diffractometer using CuKα1,2 radiation (λ=1.5406Å). The pattern was recorded within the 0.2 – 60° 2θ range, with a step of 0.02°. Powder X-ray diffraction patterns of salt-MOF composites were performed on Thermal diffractometer (Bruker D8 Advance) (CuKα1 radiation (λ = 1.540598 Å) at T=25 and 150°C.

The BET surface area was calculated from N_2 adsorption-desorption isotherms measured on Belsorp Mini (Bel, Japan) at liquid nitrogen temperature (77 K). Prior to the analysis, samples were dried for 12 h at temperature mentioned below for each sample under primary vacuum. BET surface and micropore volume were estimated at a relative pressure below 0.25.

Thermogravimetric (TG) measurements were carried out on thermogravimetric analyzer (Perkin Elmer Diamond TGA/DTA STA 6000) with oxygen flow of 200 ml/min. The temperature was increased from 303 K to 873 K.

SEM-EDX analysis was performed on a JEOL JSM-7001F microscope using gold-coated samples equipped with an energy-dispersive X-ray (EDX) spectrometer and a X-Max SDD (Silicon Drift Detector) by Oxford.

2. Water sorption experiments (gravimetric method)

Water sorption isotherm measurements were carried out using an Intelligent Gravimetric Analyzer (IGASorp Moisture Sorption Analyzer). The IGASorp allows to precisely control the water vapor pressure (1-95 RH% with the accuracy of ± 0.1% RH) and temperature (5-80°C with the accuracy of ±0.1°C). Prior to the analysis, samples were dried for 12 h under N_2 flow at the same temperature as for N_2 sorption measurements for each sample. At first adsorption measurement was carried out at temperature 30°C and R.H. range 5-50% with step of 5% (the point at R.H. 30% corresponds to p=12.5 mbar). Then the sample was dehydrated before being submitted to an adsorption measurement at 80°C and R.H. range of 2.6-7.8% with step of 3% (the point at R.H. 2.6% corresponds to p=12.5 mbar).

The cycling loading lift under cycle boundary condition (p=12.5 mbar, T_a=30°C, T_d=80°C) and multiple cycles of water adsorption-desorption were carried out using a thermogravimetric analyzer (TG-DSC111) connected with generator of humidity Setaram with RH stability of ± 0.3%. The sample was first dried for 12h under vacuum at the same temperature as for N_2 sorption measurements for each sample. Nitrogen gas flow was firstly humidified in the generator of humidity (T=40°C, RH=17.4%) and then was passed through thermogravimetric balance. The adsorption profiles were collected at 30°C in humid nitrogen at 12.5 mbar during 48 hours. The desorption step were performed at 80 °C at 12.5 mbar during 12 hours.

III. Characterization of MOFs

1. X-ray powder diffraction

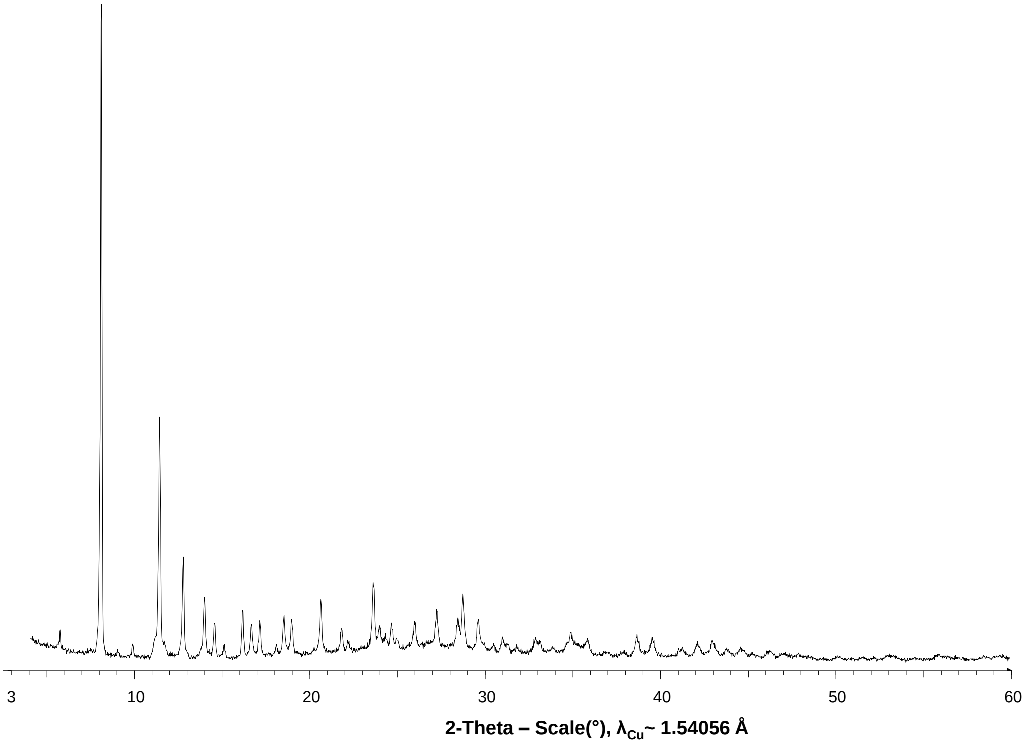

Figure S2. PXRD pattern of MIL-127(Fe) in 2Θ range 4-60° (step 0.02°, 17 s per step)

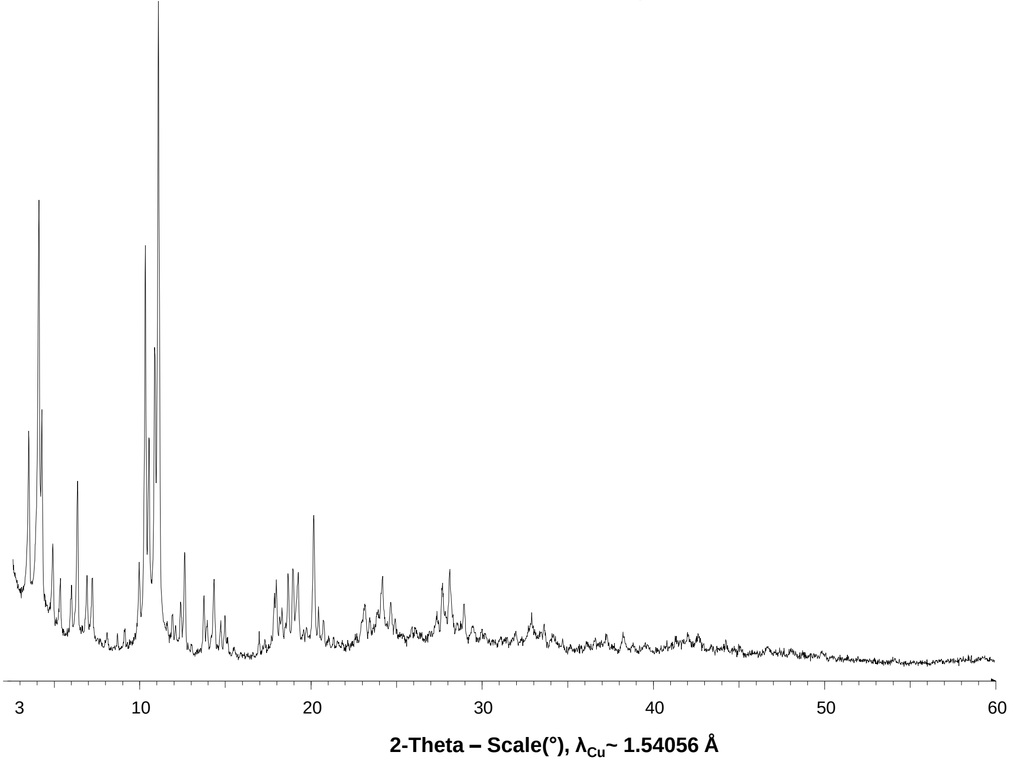

Figure S3. PXRD pattern of MIL-100(Fe) in 2Θ range 2.5-60° (step 0.02°, 17 s per step)

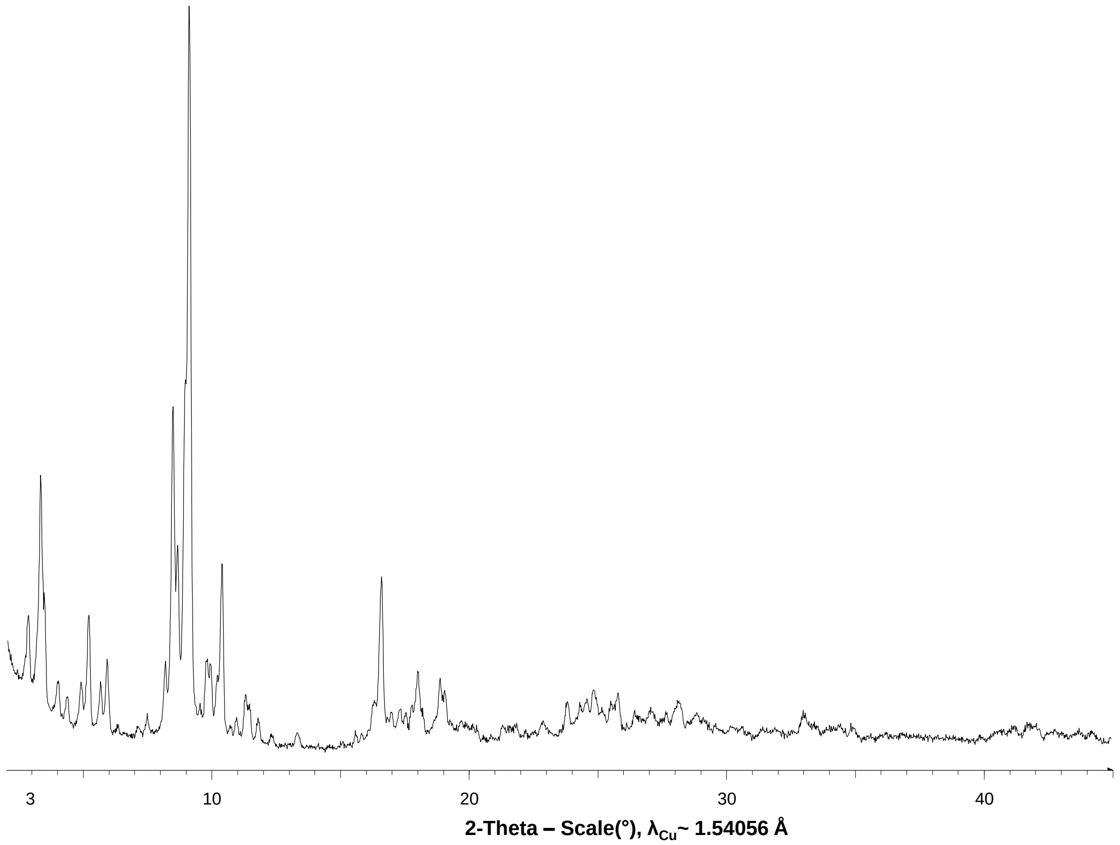

Figure S4. PXRD pattern of MIL-101(Cr) in 2ϴ range 2-45° (step 0.02°, 17 s per step)

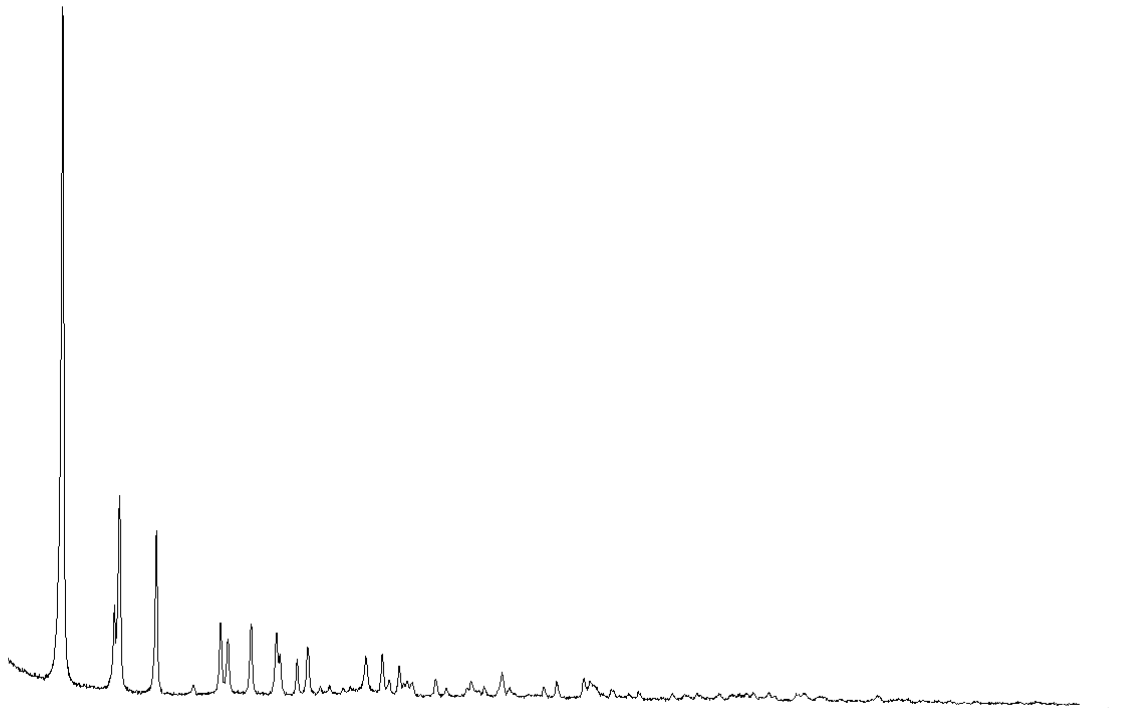

Figure S5. PXRD pattern of MIL-125(Ti)-NH_2 in 2ϴ range 4-60° (step 0.02°, 17 s per step)

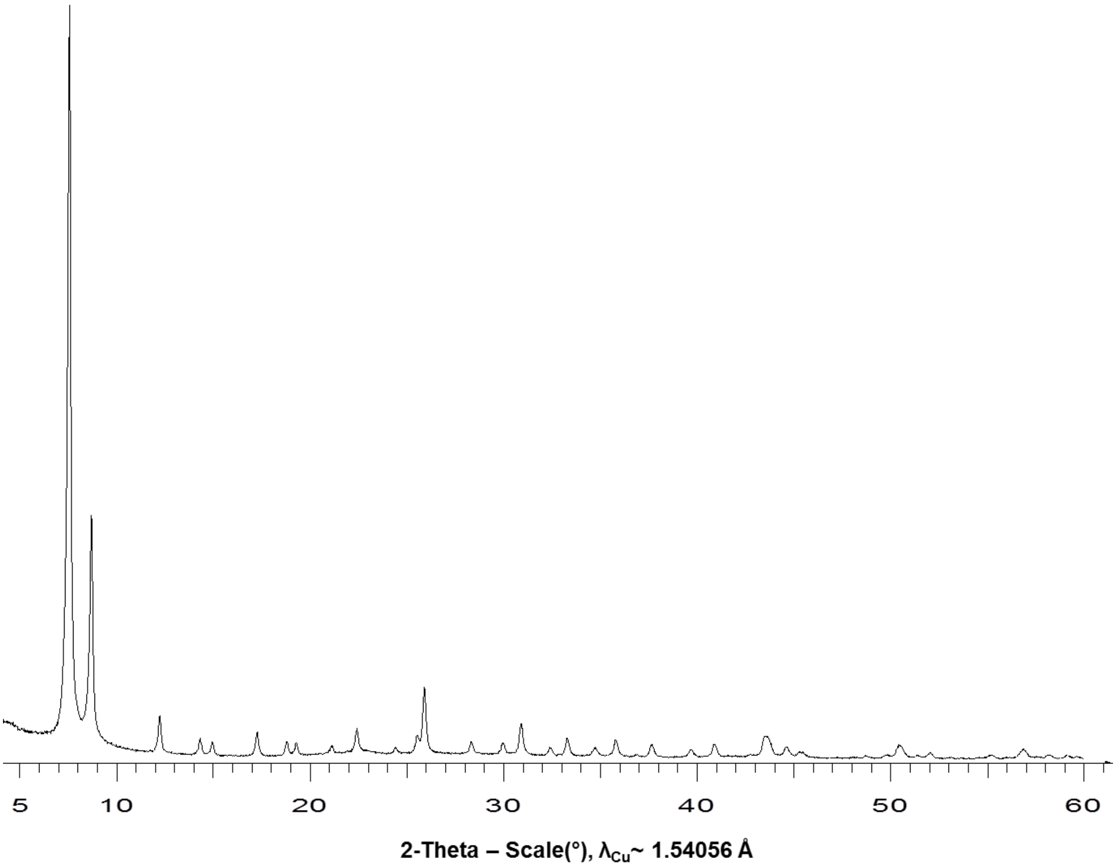

Figure S6. PXRD pattern of UIO-66(Zr)-NH_2 in 2Θ range 4-60° (step 0.02°, 17 s per step)

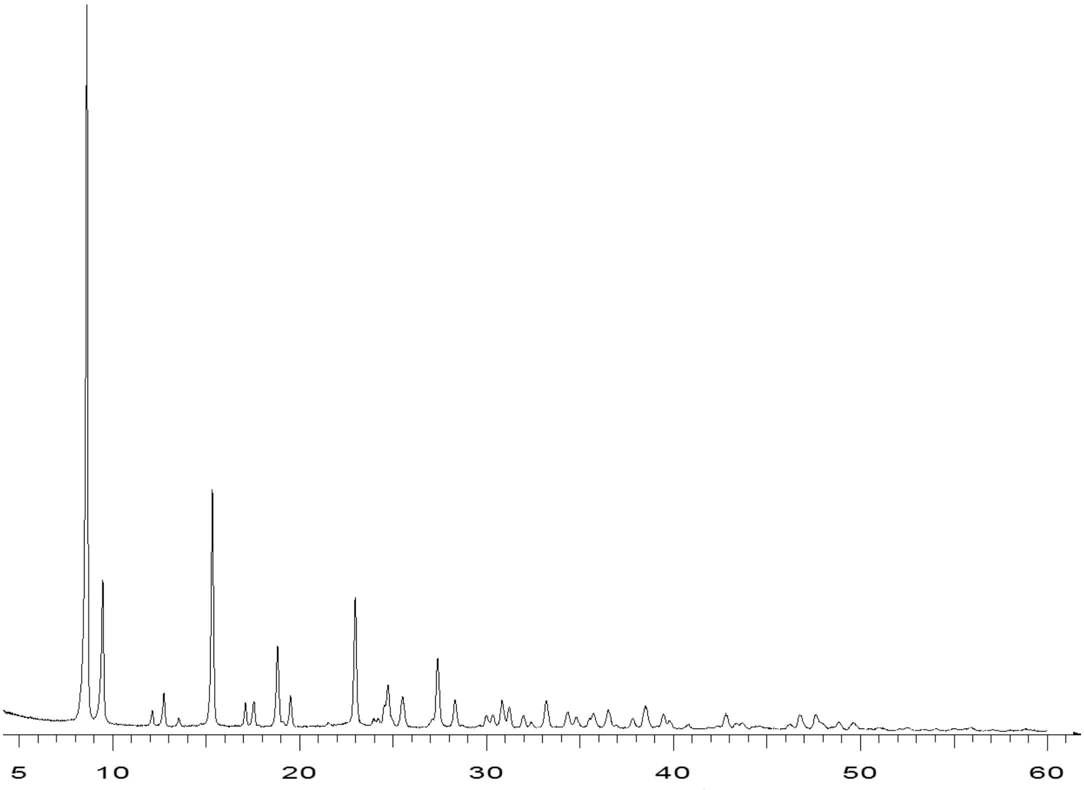

Figure S7. PXRD pattern of MIL-160(Al) in 2Θ range 4-60° (step 0.02°, 17 s per step)

2. Thermogravimetric analysis

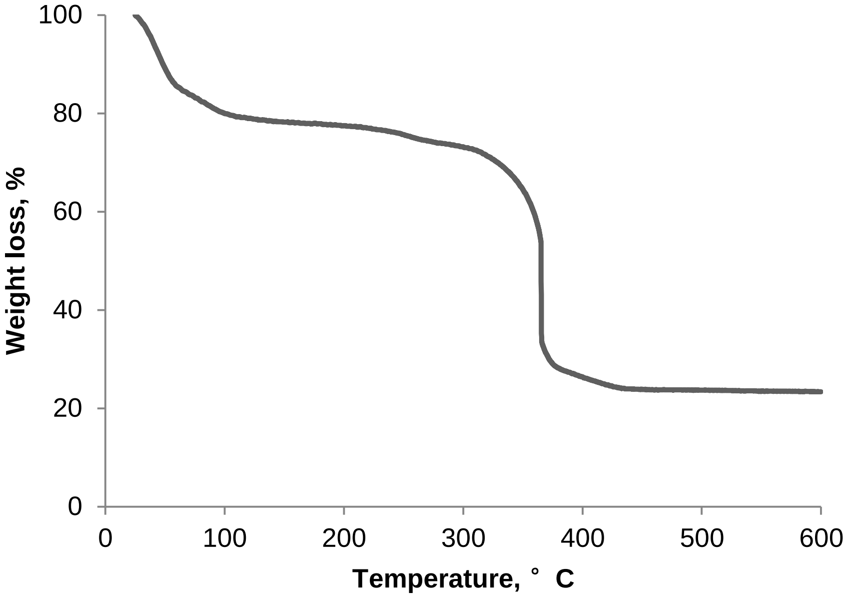

Figure S8. Thermogravimetric analysis profile of MIL-127(Fe) under oxygen flow (carrier gas flow rate: 200 ml/min).

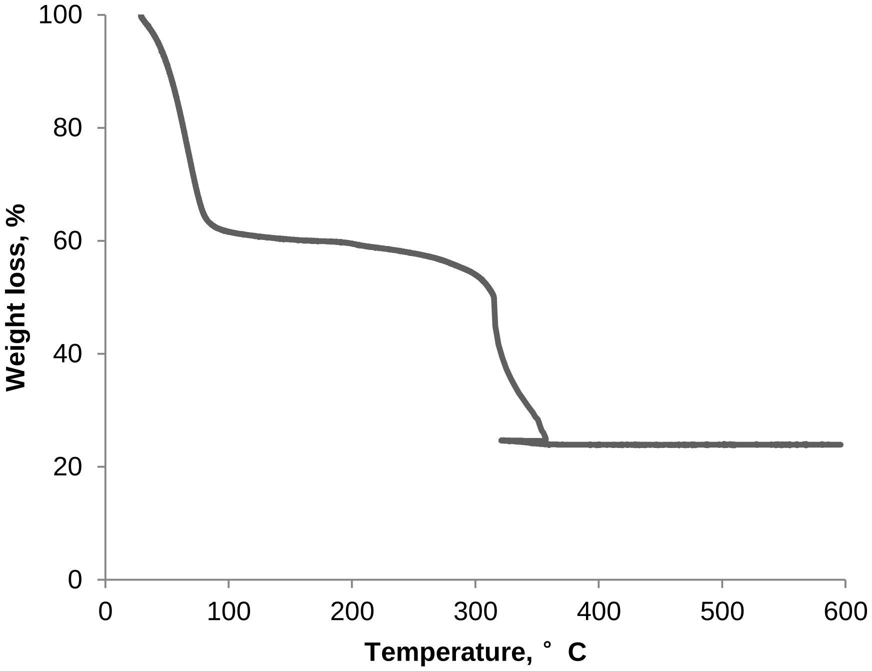

Figure S9. Thermogravimetric analysis profile of MIL-100(Fe) under oxygen flow (carrier gas flow rate: 200 ml/min).

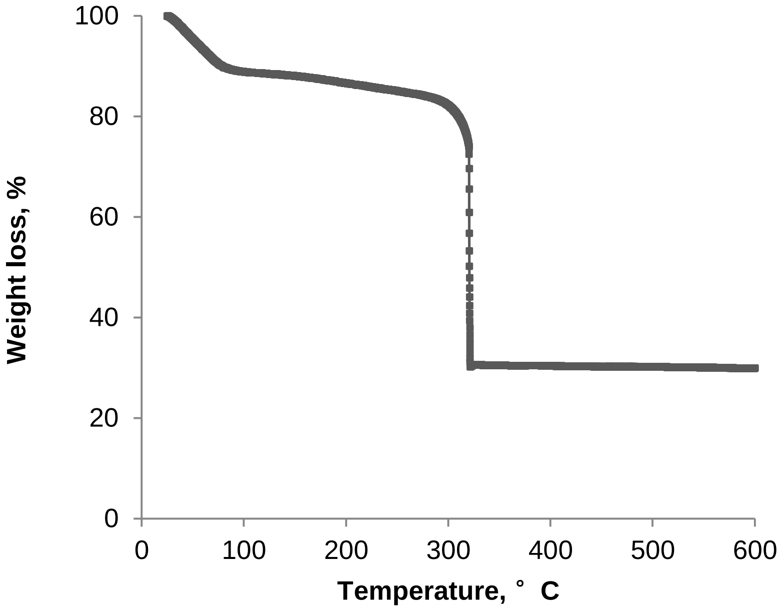

Figure S10. Thermogravimetric analysis profile of MIL-101(Cr) under oxygen flow (carrier gas flow rate: 200 ml/min).

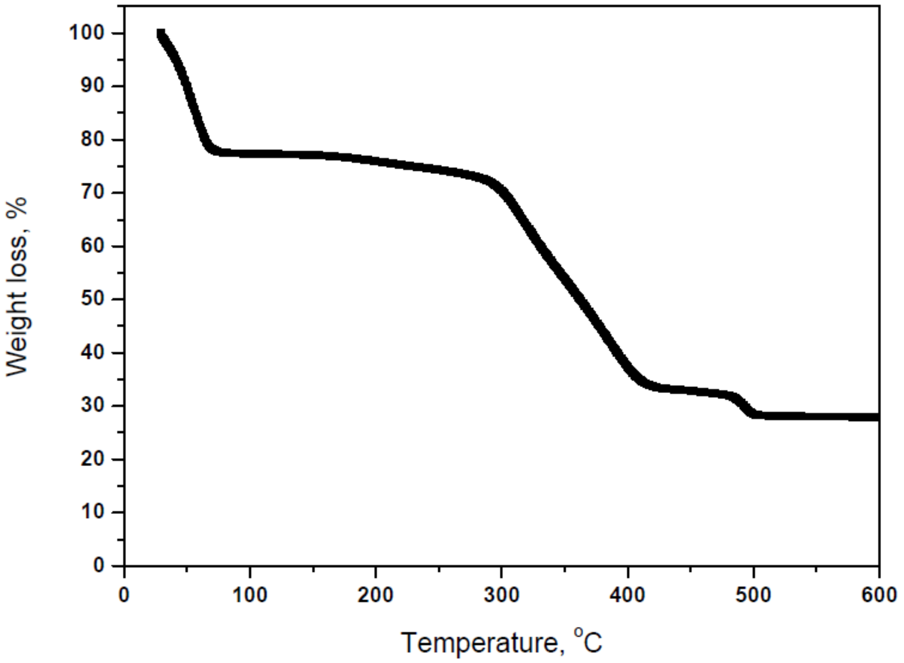

Figure S11. Thermogravimetric analysis profile of MIL-125(Ti)-NH_2 under oxygen flow (carrier gas flow rate: 200 ml/min).

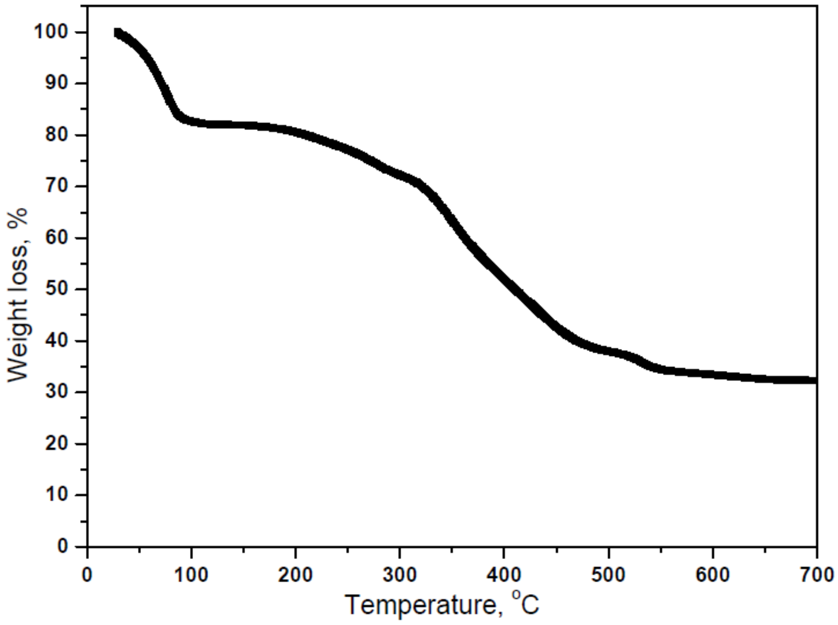

Figure S12. Thermogravimetric analysis profile of UIO-66(Zr)-NH$_2$ under oxygen flow (carrier gas flow rate: 200 ml/min).

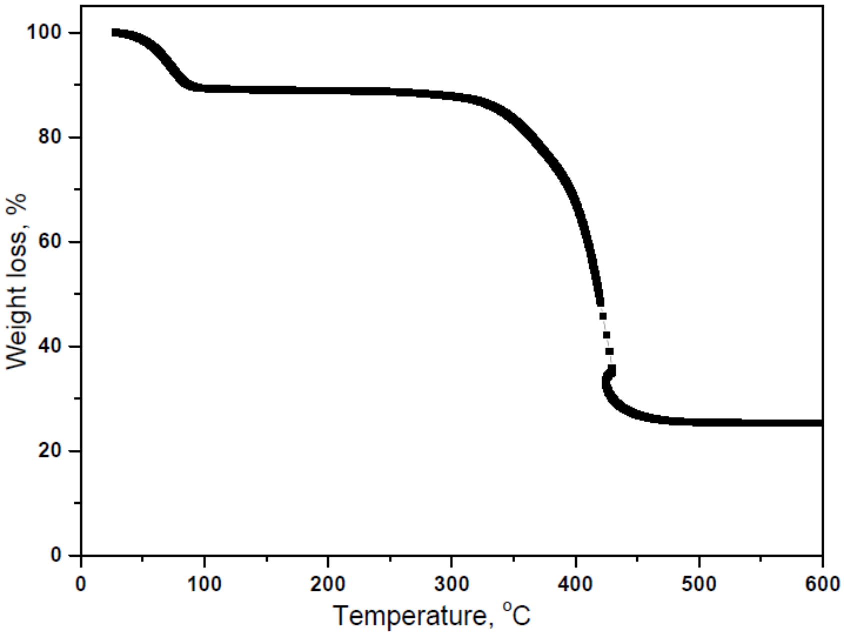

Figure S13. Thermogravimetric analysis profile of MIL-160 under oxygen flow (carrier gas flow rate: 200 ml/min).

3. N$_2$ sorption porosimetry

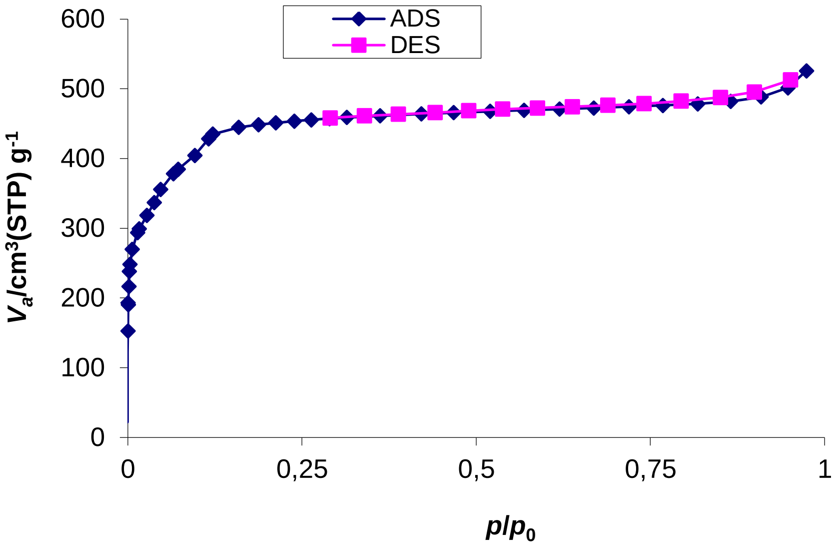

Figure S14. Nitrogen sorption isotherm of MIL-100(Fe) at 77 K (S_{BET} = 1828 m^2/g, V_{pore} = 0.81 cm^3/g). Temperature of pretreatments is 180°C.

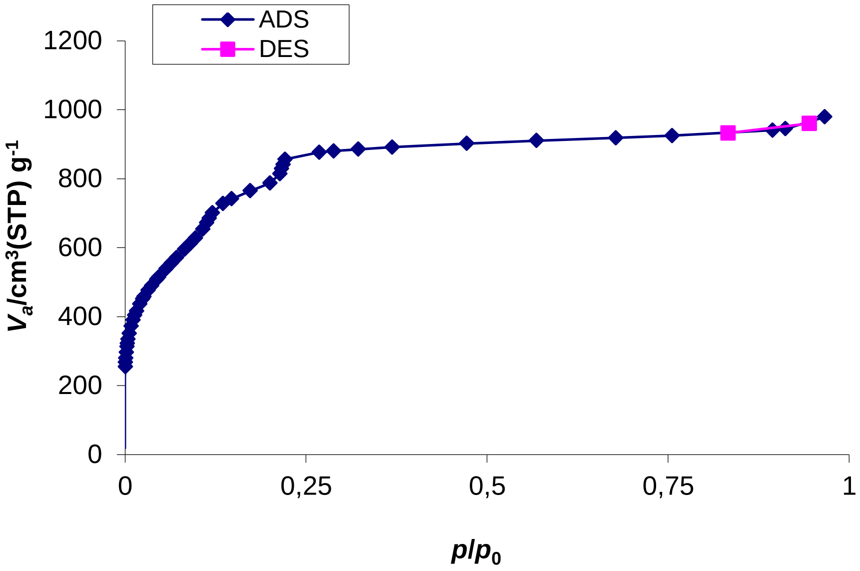

Figure S15. Nitrogen sorption isotherm of MIL-101(Cr) at 77 K (S_{BET} = 3721 m^2/g, V_{pore} =1.51 cm^3/g). Temperature of pretreatments is 200°C.

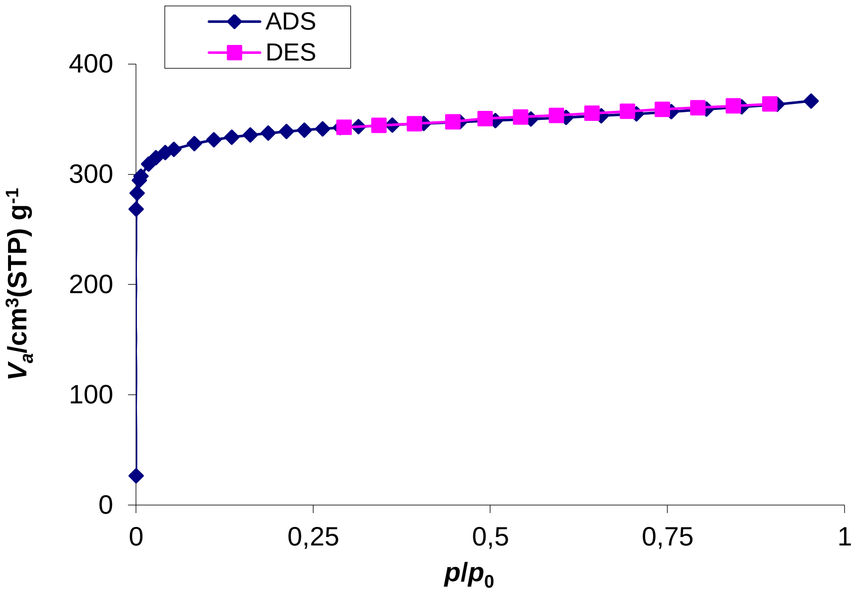

Figure S16. Nitrogen sorption isotherm of MIL-127(Fe) at 77 K (S_{BET} = 1342 m^2/g, V_{pore} =0.57 cm^3/g). Temperature of pretreatments is 180°C.

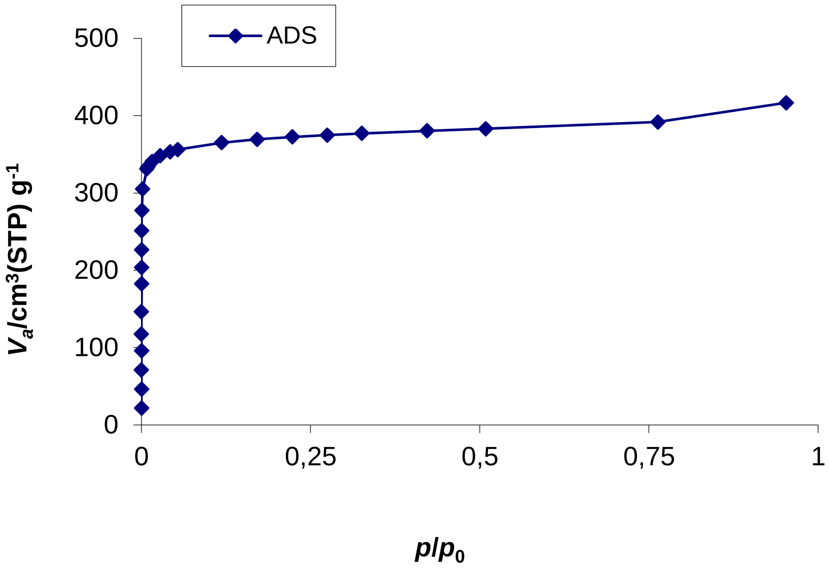

Figure S17. Nitrogen sorption isotherm of MIL-125(Ti)-NH_2 at 77 K (S_{BET} = 1450 m^2/g, V_{pore} =0.64 cm^3/g). Temperature of pretreatments is 180°C.

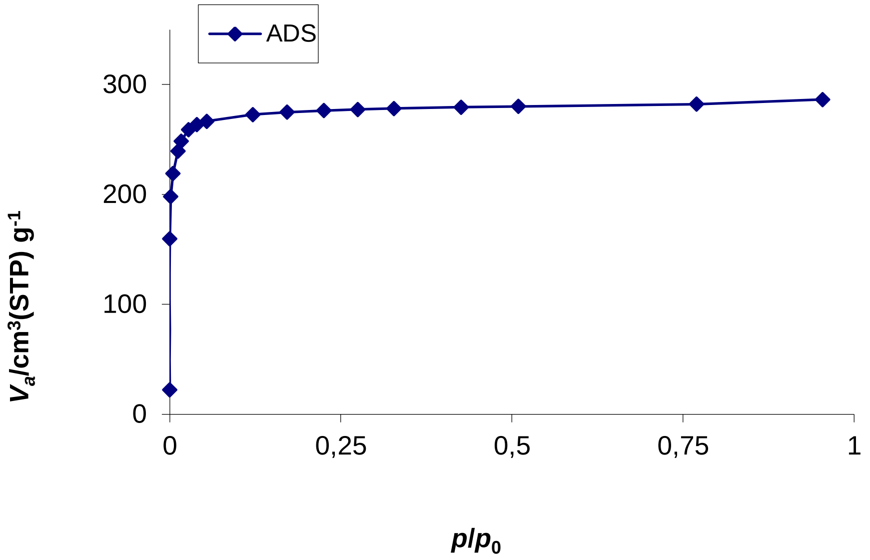

Figure S18. Nitrogen sorption isotherm of UiO-66(Zr)-NH$_2$ at 77 K (S$_{BET}$ = 1119 m^2/g, V$_{pore}$ =0.44 cm^3/g). Temperature of pretreatments is 150°C.

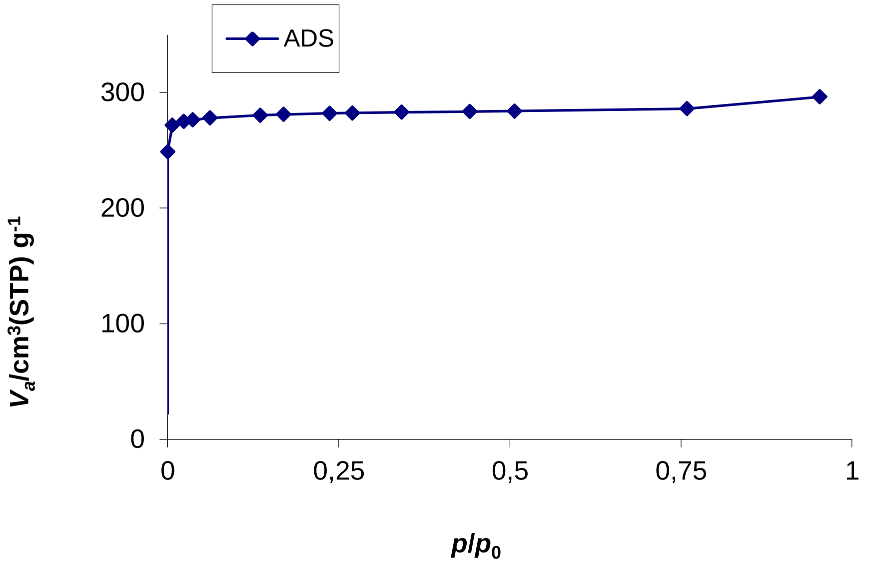

Figure S19. Nitrogen sorption isotherm of MIL-160 at 77 K (S$_{BET}$ = 1148 m^2/g, V$_{pore}$ =0.46 cm^3/g). Temperature of pretreatments is 150°C.

4. Water sorption of MOFs

The achievable cycle loading lift is the working fluid exchange between the production cycle (adsorption) and the regeneration cycle (desorption). As mentioned above (SI I.2.) information about cycling loading lift under boundary conditions could be obtained by two equipment: IGASorp and TGA. Information about cycling loading lift can be extracted directly from test on TGA. In case of IGASorp analysis adsorption-desorption at 30°C was carried out on anhydrous material whereupon adsorption-desorption at 80°C was performed on material without complete drying (only by dry N_2 at 30°C) in order to correspond to the real condition in the reactor. The exchanged mass of water between adsorption at 30°C and desorption at 80°C was considered as cycling loading lift.

Figure S2 summaries the adsorption loading lift (T=30°C, p=12.5 mbar) and cycling loading lift (between T=30°C and T=80°C, p=12.5 mbar) of MIL-101(Cr), MIL-127(Fe), MIL-100(Fe), UiO-66(Zr)-NH_2, MIL-125(Ti)-NH_2, MIL-160(Al).

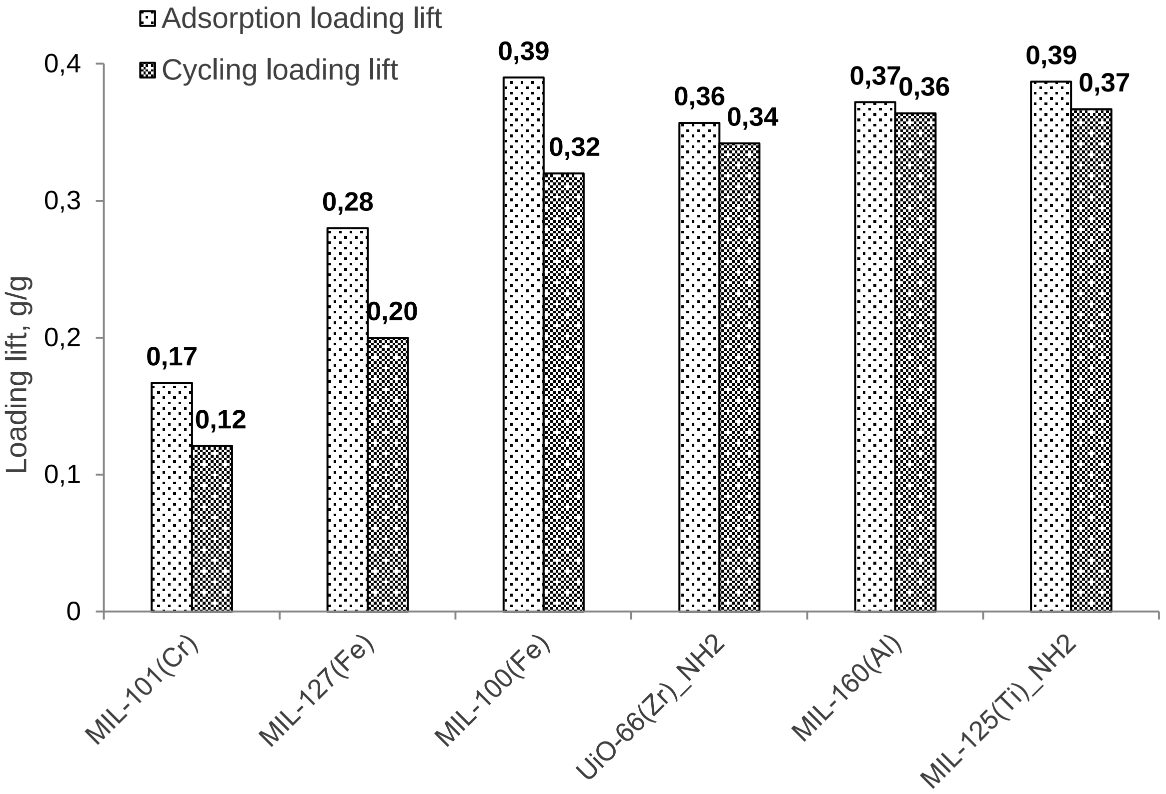

Figure S20. Adsorption and cycling loading lifts of MOFs. Cycle conditions: adsorption at 30°C and 12.5 mbar and desorption at 80°C and 12.5 mbar. Adsorption condition: 30°C and 12.5 mbar

Further we will provide water sorption tests of MOFs in the condition of adsorption and cycling using one of these techniques: TGA or IGASorp.

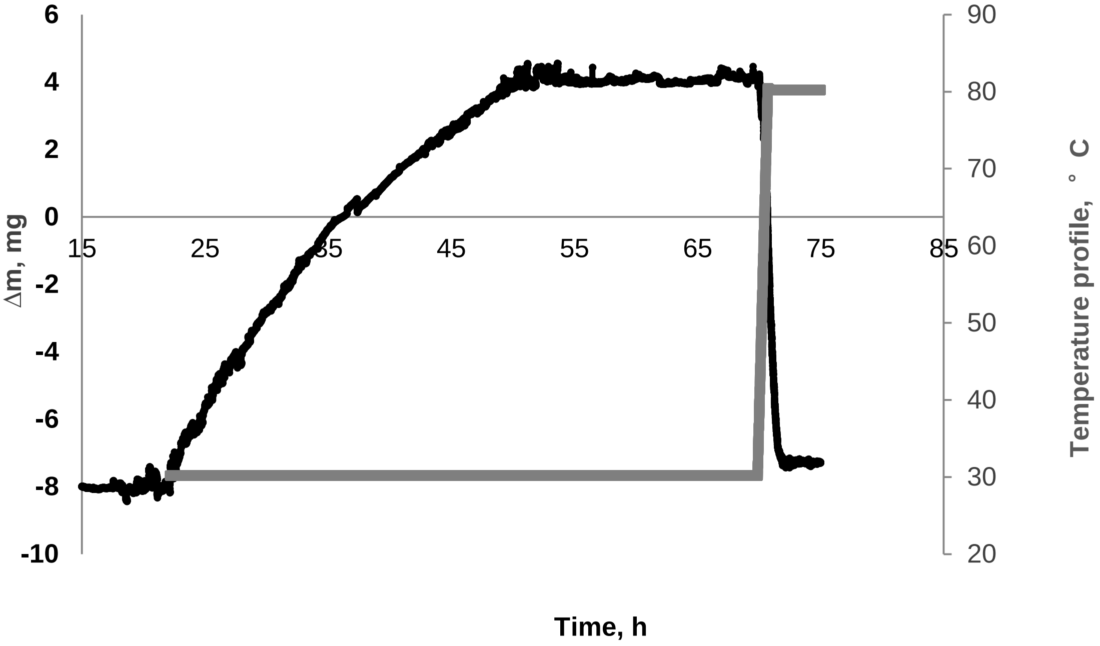

Figure S21. Cycling loading lift (TGA) on 30.90 mg of anhydrous MIL-125(Ti)-NH_2. Condition of lift: adsorption at 30°C and p=12.5 mbar, desorption at 80°C and p=12.5 mbar.

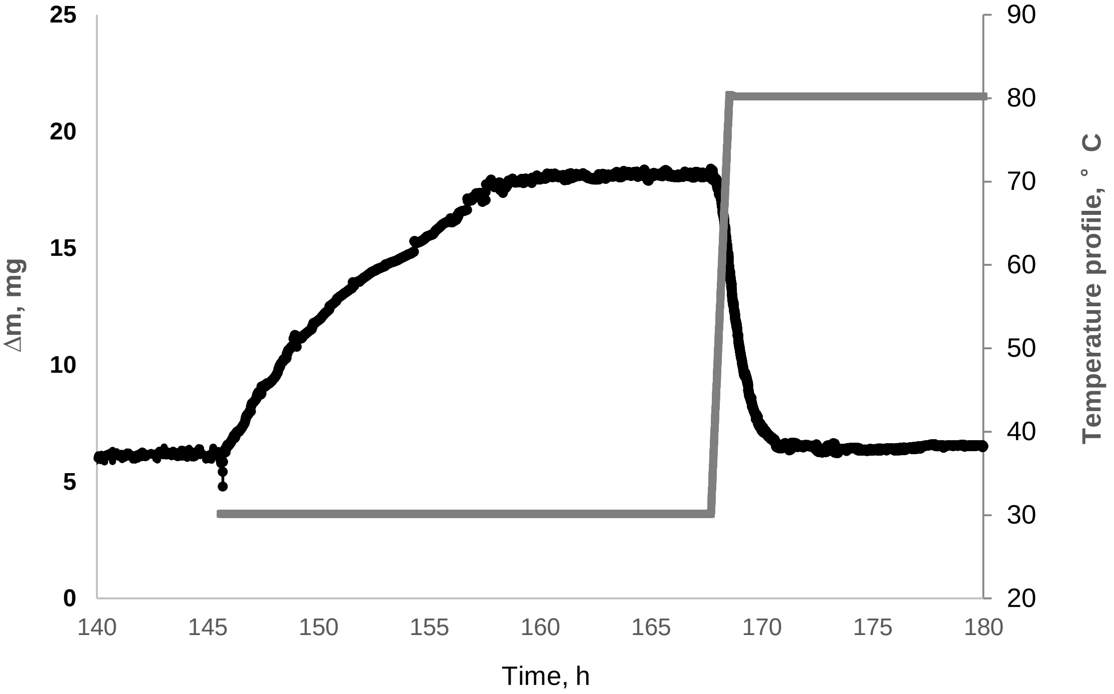

Figure S22. Cycling loading lift (TGA) on 31.83 mg of anhydrous MIL-160(Al). Condition of lift: adsorption at 30°C and p=12.5 mbar, desorption at 80°C and p=12.5 mbar.

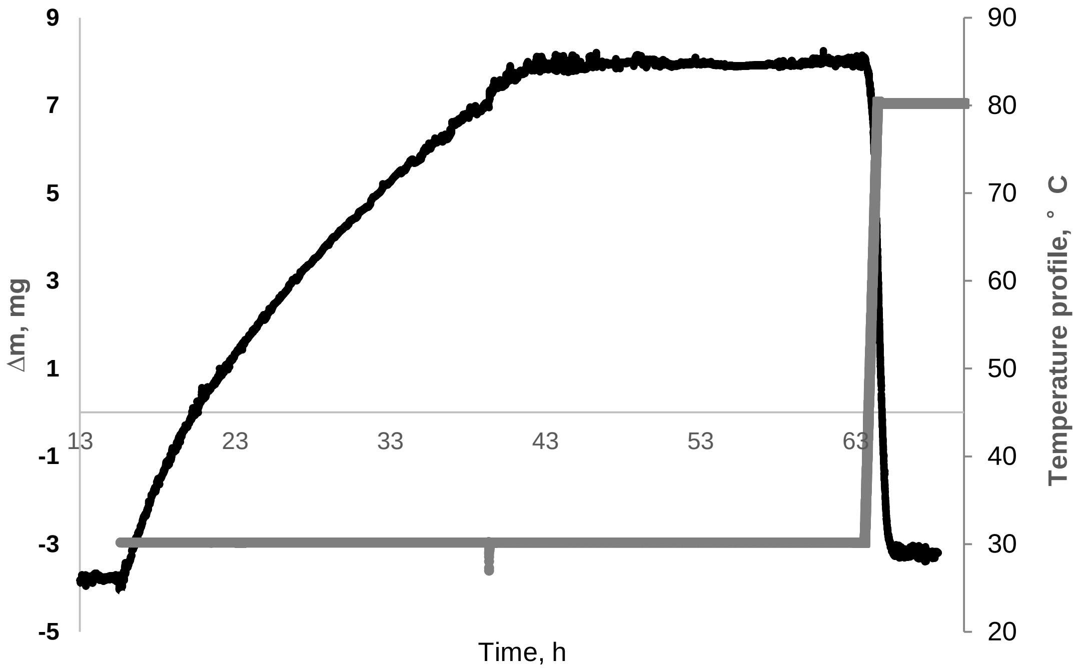

Figure S23. Cycling loading lift (TGA) on 33.10 mg of anhydrous UiO-66(Zr)-NH_2. Condition of lift: adsorption at 30°C and p=12.5 mbar, desorption at 80°C and p=12.5 mbar.

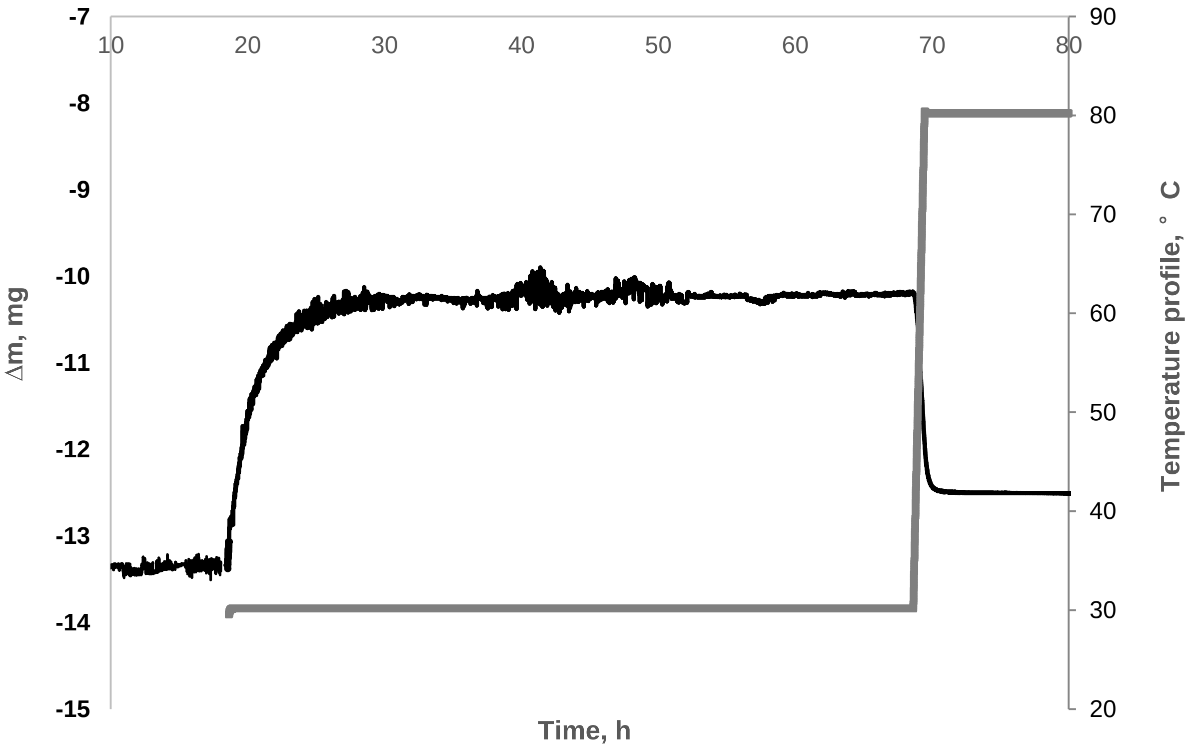

Figure S24. Cycling loading lift (TGA) on 19.00 mg of anhydrous MIL-101(Cr). Condition of lift: adsorption at 30°C and p=12.5 mbar, desorption at 80°C and p=12.5 mbar.

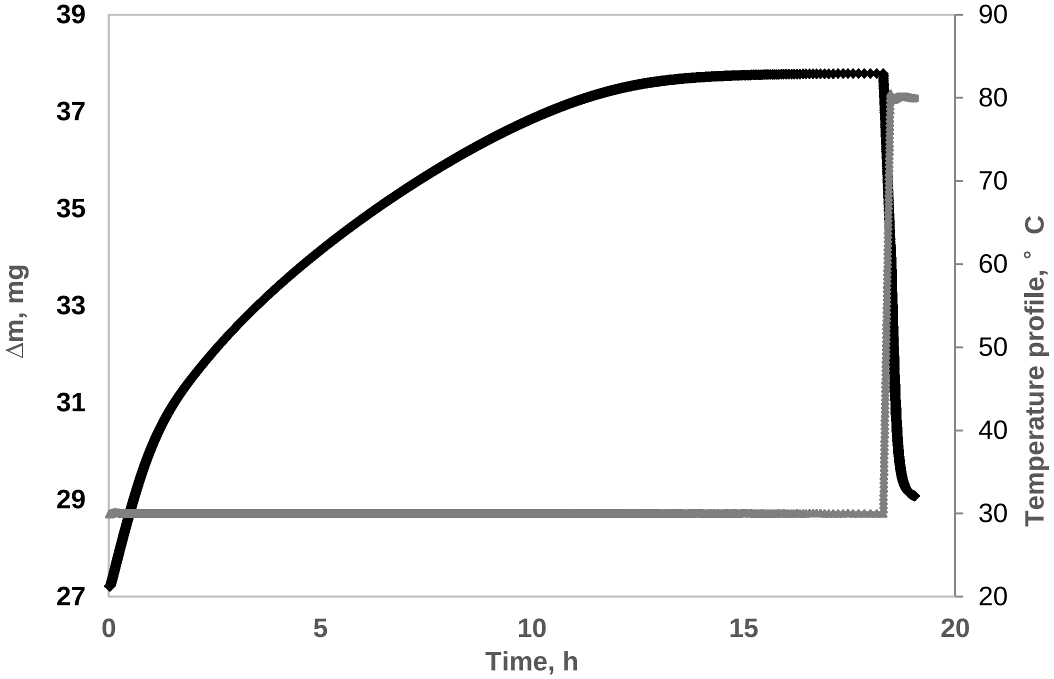

Figure S25. Cycling loading lift (IGASorp) on 27.21 mg of anhydrous MIL-100(Fe). Condition of cycling loading lift: adsorption at 30°C and p=12.5 mbar, desorption at 80°C and p=12.5 mbar.

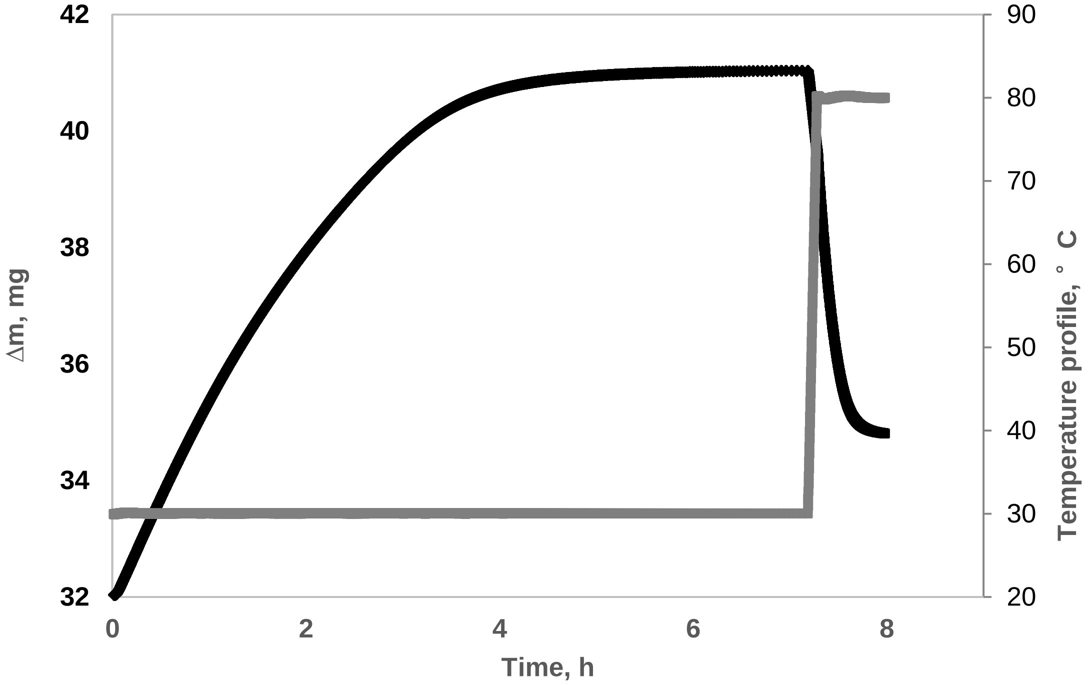

Figure S26. Cycling loading lift (IGASorp) on 32.04 mg of anhydrous MIL-127(Fe). Condition of cycling loading lift: adsorption at 30°C and p=12.5 mbar, desorption at 80°C and p=12.5 mbar.

IV. Characterization of salt-MOF composites

1. Synthesis of salt-MOF composites

The detailed preparation process includes soaking MOFs in inorganic salt solution and drying afterwards. Several parameters of the preparation condition, including concentration of the inorganic salt solution, the volume of inorganic salt solution used for soaking, soaking time, soaking temperature, cycles of soaking, drying temperature was investigated in order to achieve the optimal sample with controlled salt content, good stability and reproducibility. We provide herein the details of composite synthesis indicated in Table S1.

Prior to the encapsulation step MOF sample was dried during 3 hours in an oven at 100 °C. MOF sample was involved in one encapsulation step using $CaCl_2$ solution with soaking time of 2 hours. The sample was collected following the removal of excessive $CaCl_2$ solution by centrifugation and was completely dried at 100 ºC in an oven for overnight.

Table S1. Synthesis of salt-MOF composites

Name of composite	MOF-matrix	m of MOF sample, [mg]	V of salt solution [ml]	Concentration of salt solution [%]
MIL-100/$CaCl_2$ (46% wt.)	MIL-100(Fe)	200	0.8	35
MIL-100/$CaCl_2$ (34% wt.)	MIL-100(Fe)	200	0.8	25
MIL-127/$CaCl_2$ (31% wt.)	MIL-127(Fe)	200	0.8	20
MIL-127/$CaCl_2$ (40% wt.)	MIL-127(Fe)	200	0.8	30
UiO-66-NH_2/$CaCl_2$ (43% wt.)	UiO-66(Zr)-NH_2	80	0.8	40
MIL-125(Ti)-NH_2/CaCl2 (45% wt.)	MIL-125(Ti)-NH_2	80	0.8	30
MIL-101(Cr)/CaCl2 (62%)	MIL-101(Cr)	200	0.8	28
MIL-160/$CaCl_2$ (34%)	MIL-160(Al)	80	0.8	40

3. X-ray powder diffraction of composites

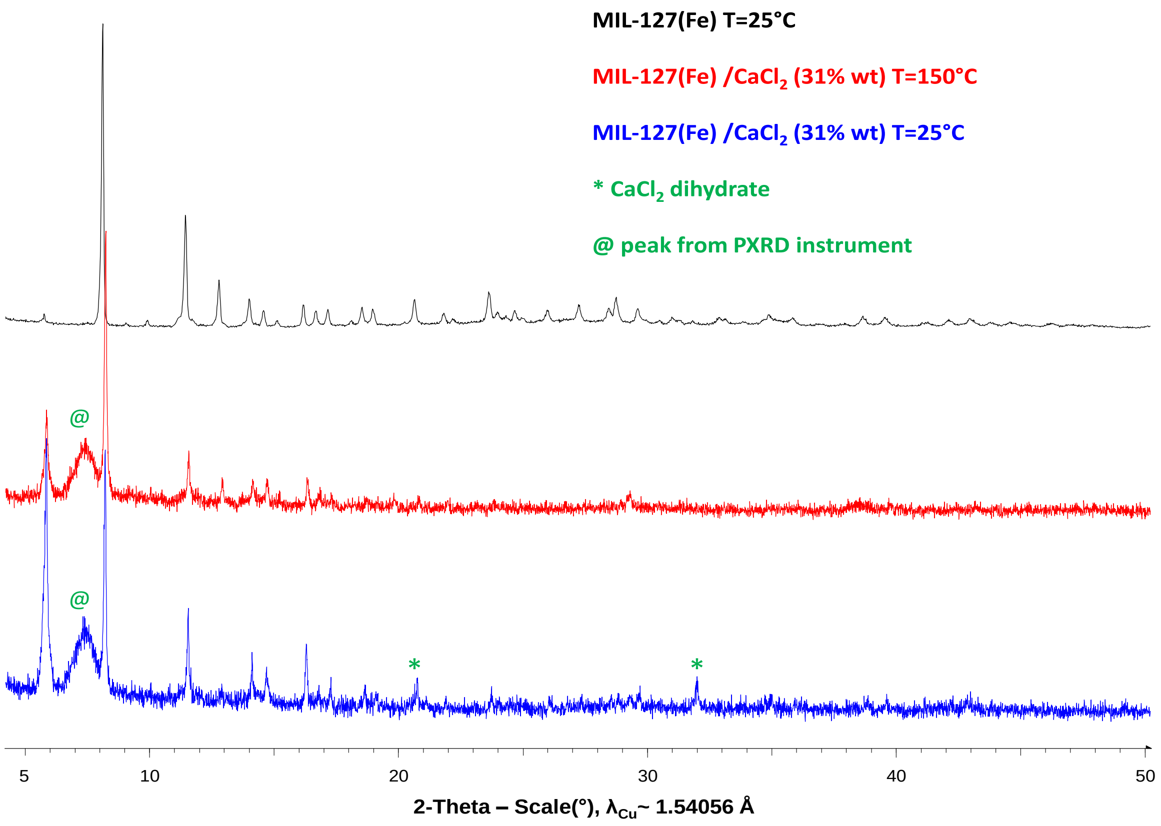

Figure S27. PXRD patterns of MIL-127(Fe) and composite MIL-127(Fe)/$CaCl_2$ (31% wt).

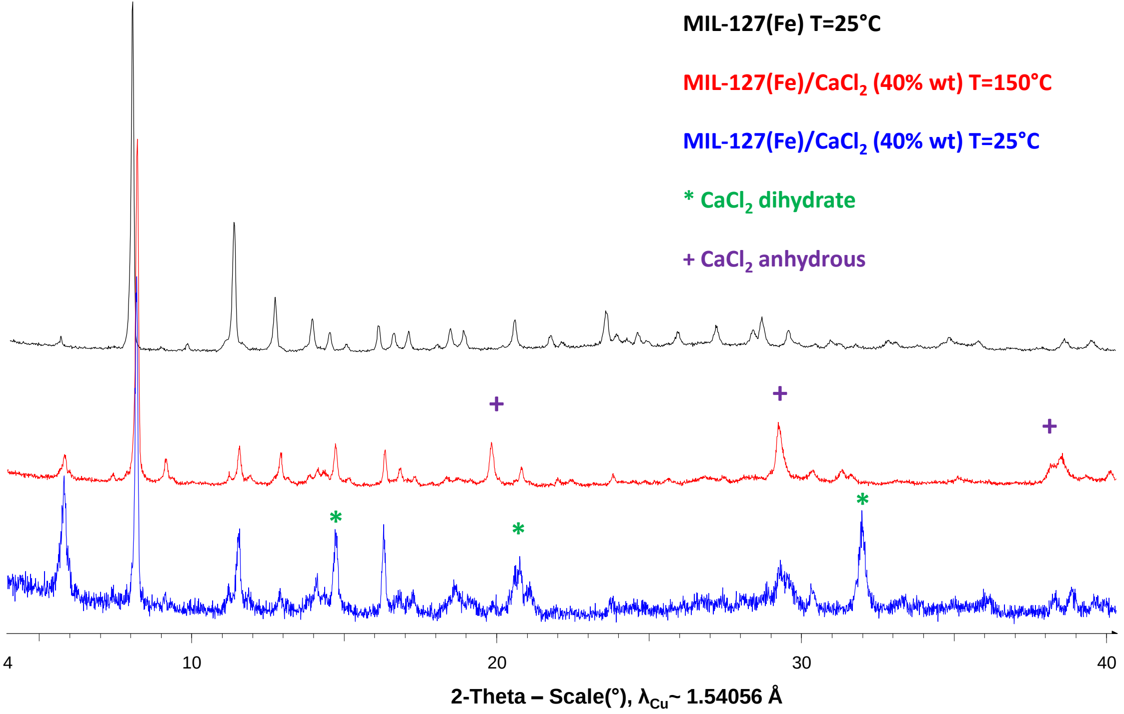

Figure S28. PXRD patterns of MIL-127(Fe) and composite MIL-127(Fe)/$CaCl_2$ (40% wt).

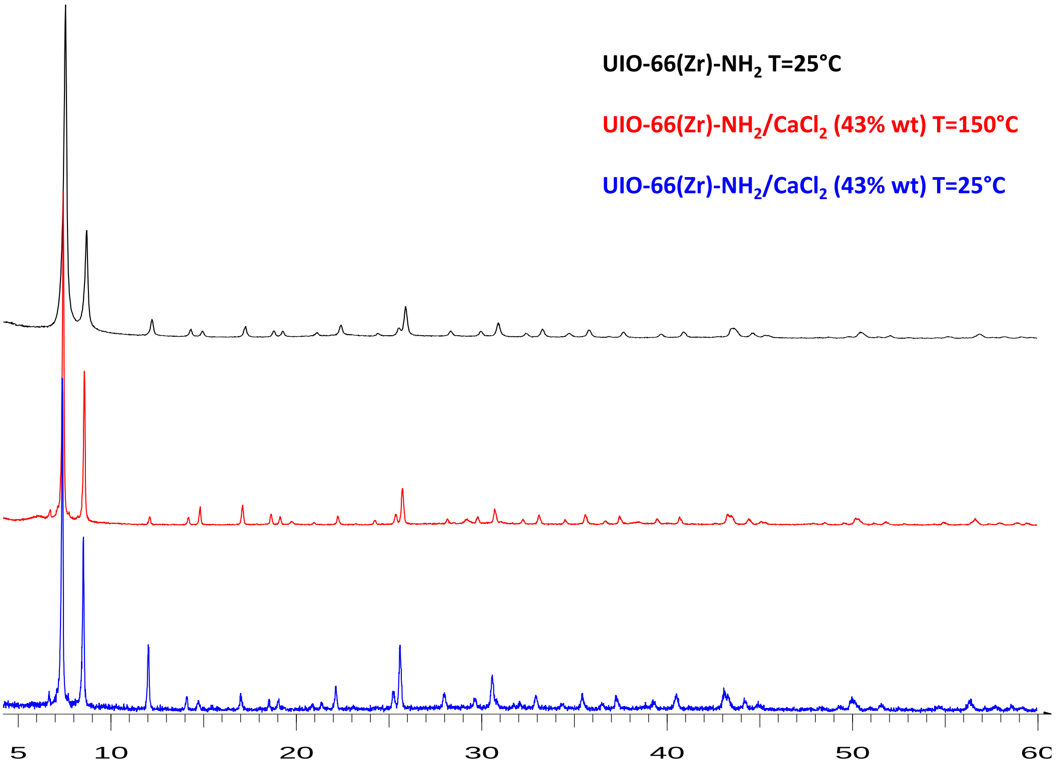

Figure S29. PXRD patterns of UIO-66(Zr)-NH$_2$ and composite UIO-66(Zr)-NH$_2$/CaCl$_2$ (43 %).

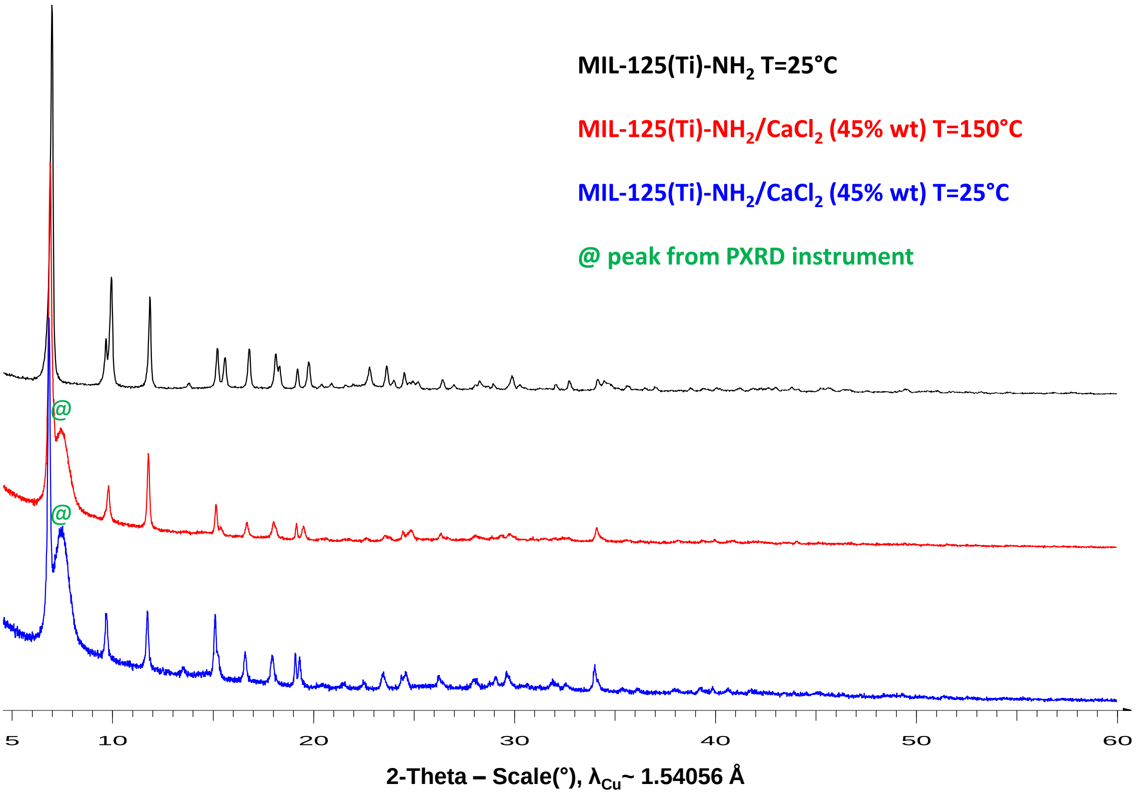

Figure S30. PXRD patterns of MIL-125(Ti)-NH$_2$ and composite MIL-125(Ti)-NH$_2$/CaCl$_2$ (45 %).

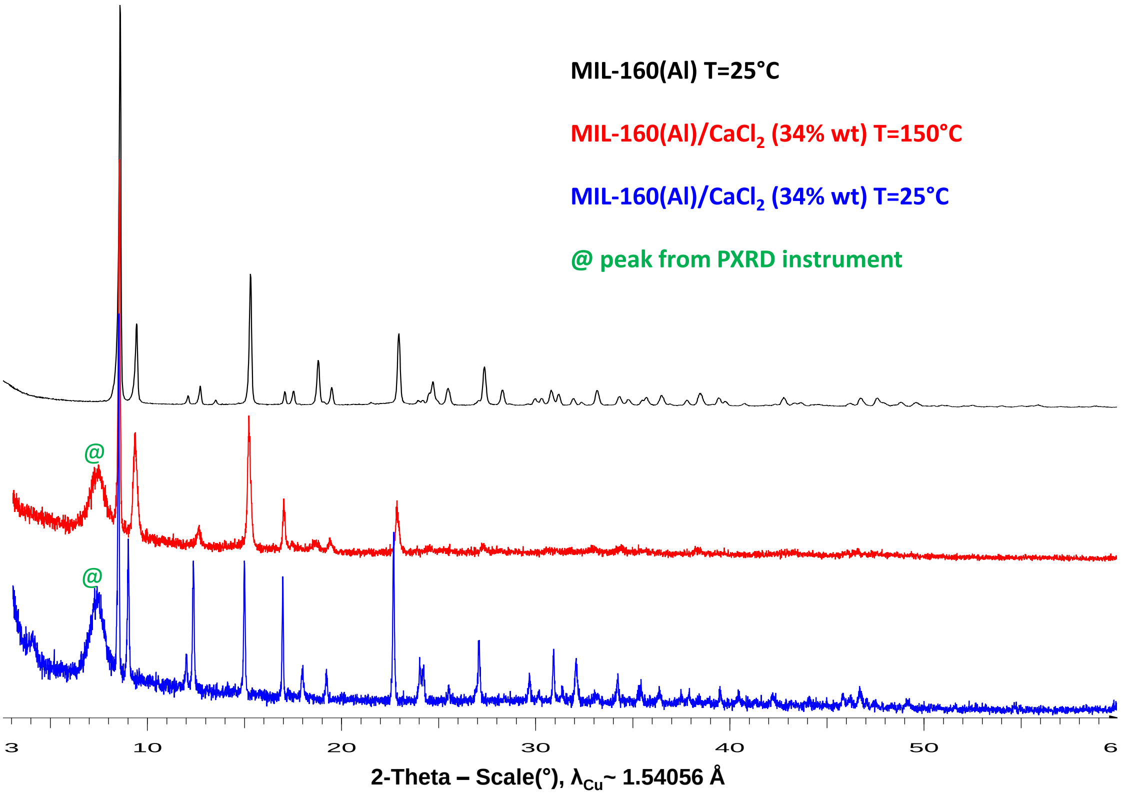

Figure S31. PXRD patterns of MIL-160(Al) and composite MIL-160(Al)/$CaCl_2$ (34 %).

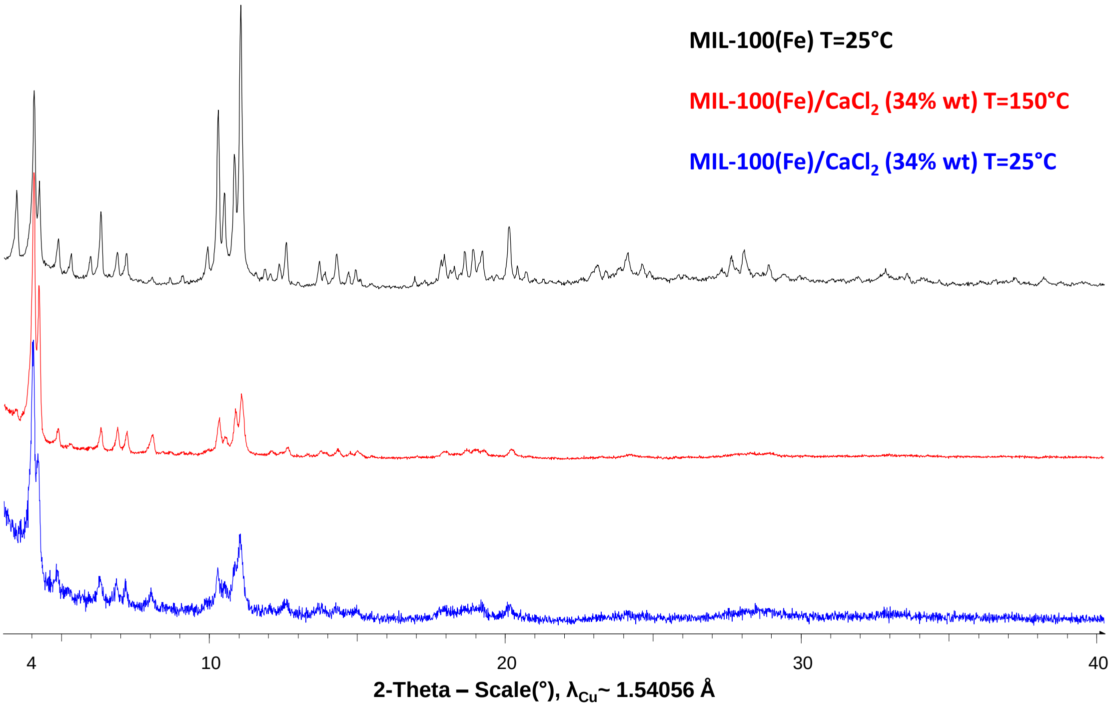

Figure S32. PXRD patterns of MIL-100(Fe) and composite MIL-100(Fe)/$CaCl_2$ (34% wt).

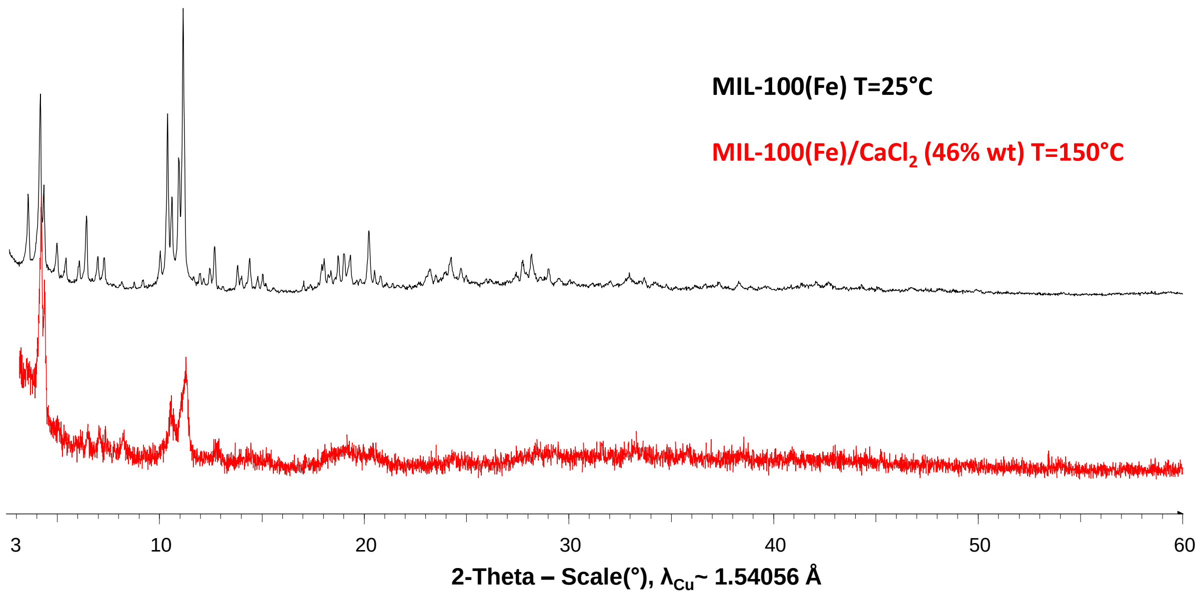

Figure S33. PXRD patterns of MIL-100(Fe) and composite MIL-100(Fe)/CaCl$_2$ (46% wt).

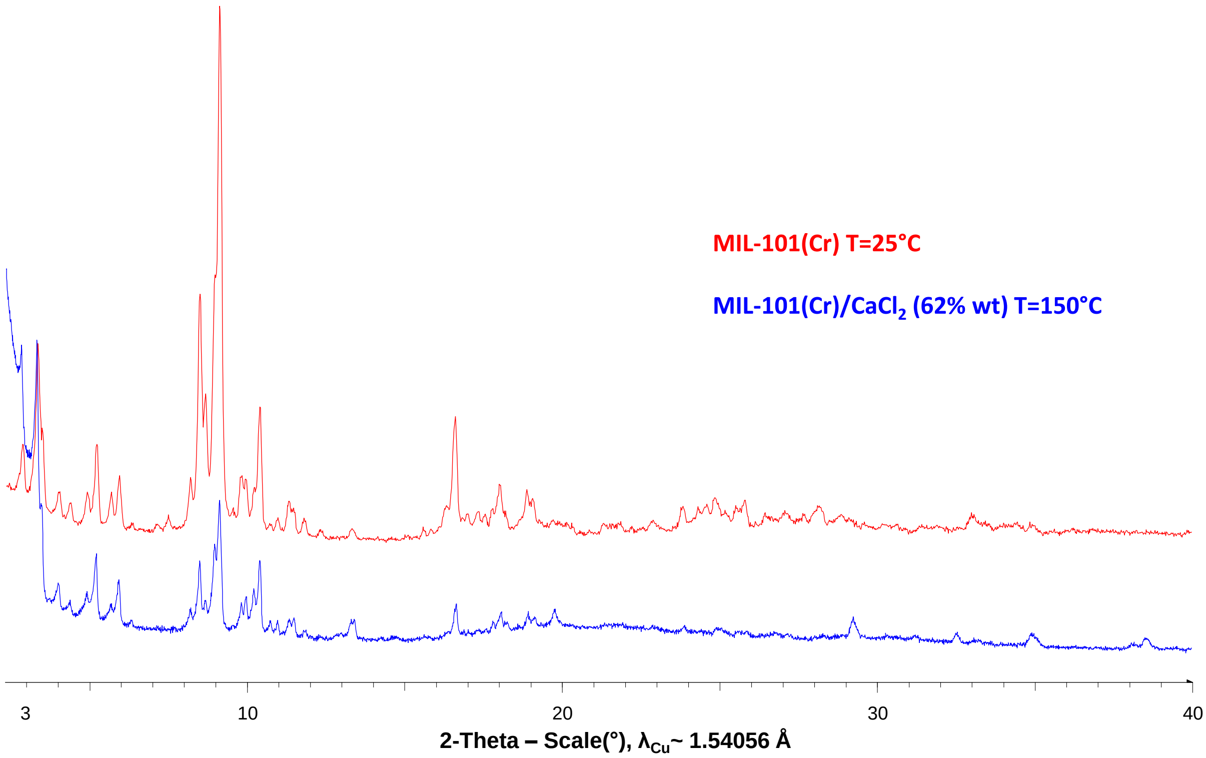

Figure S34. PXRD patterns of MIL-101(Cr) and composite MIL-101(Cr)/CaCl$_2$ (62% wt).

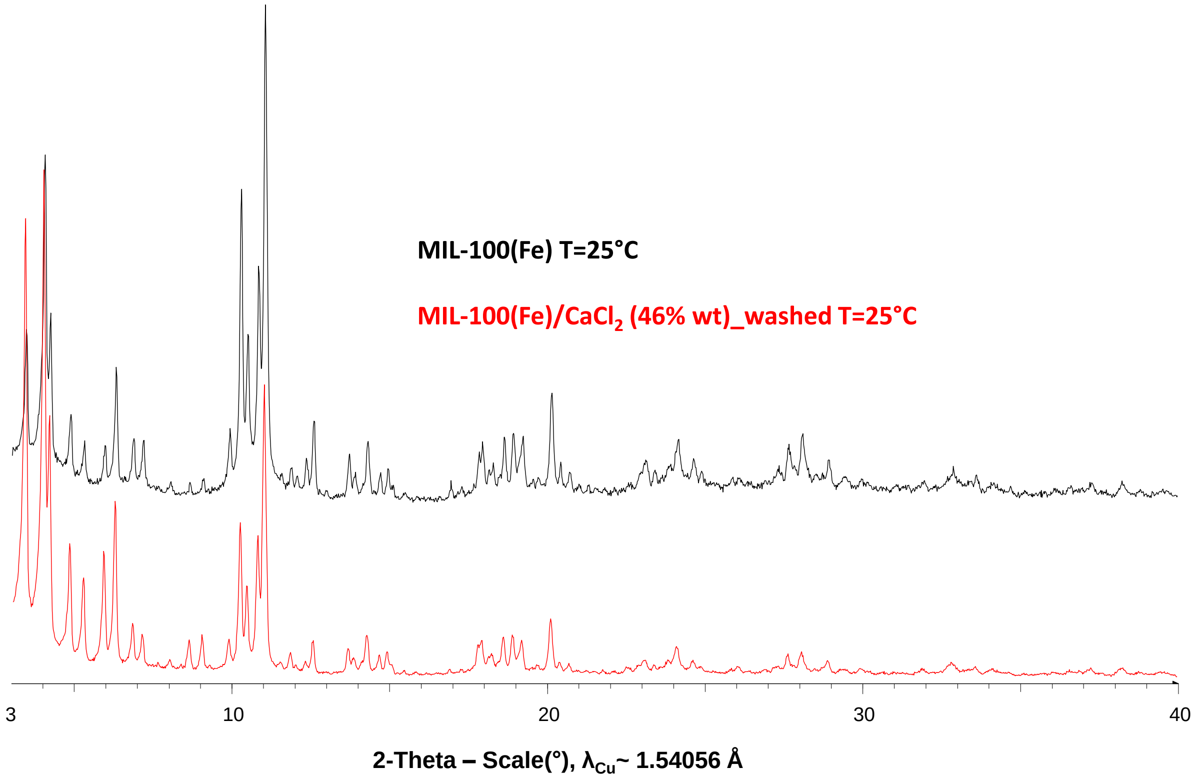

Figure S35. PXRD patterns of MIL-100(Fe) and composite MIL-100(Fe)/CaCl$_2$ (46% wt) after washing

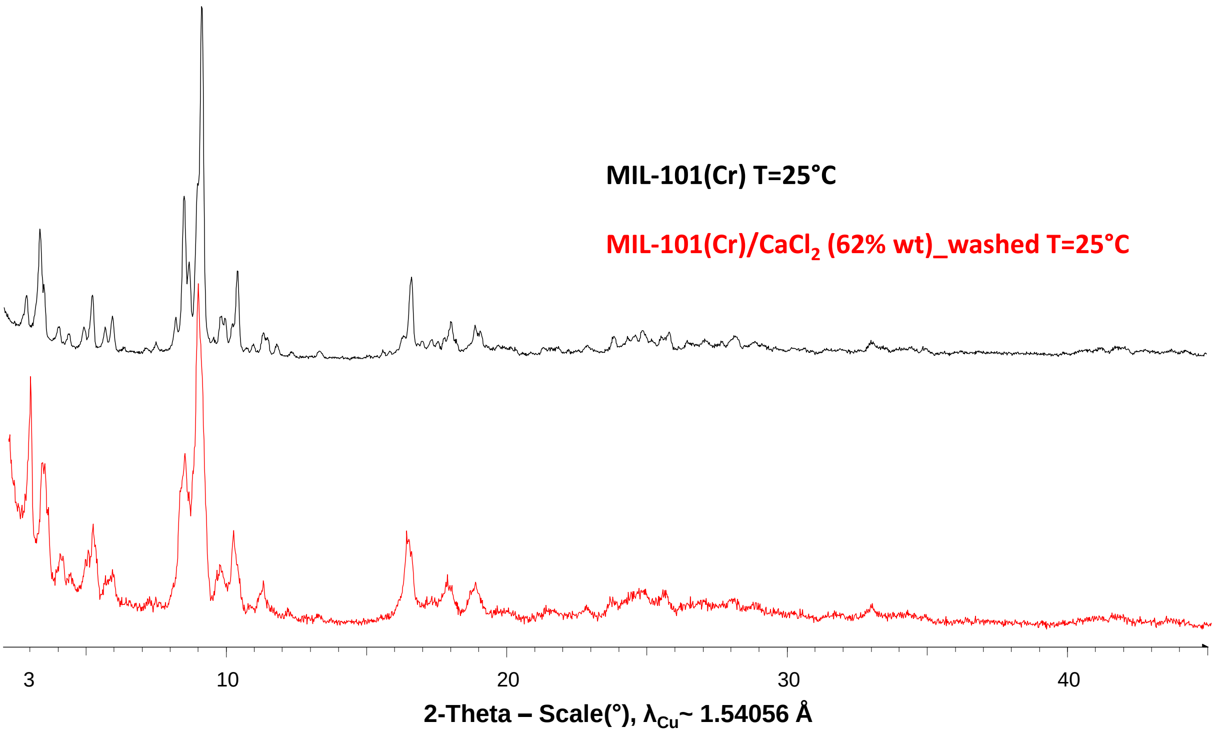

Figure S36. PXRD patterns of MIL-101(Cr) and composite MIL-101(Cr)/CaCl$_2$ (62% wt) after washing

4. Calculation of the salt content

Thermogravimetric analysis

For each composite, three identical samples prepared with the same synthesis conditions were considered and the chemical composition of $CaCl_2$-MOFs composites given in Table S1 is the average of that of the three samples. Thermogravimetric analysis of composites was performed in order to estimate the $CaCl_2$ content and thermal stability of composites. Thermogravimetric profile of composite consists of two weight losses. The first one between 25°C and 260°C corresponds to water departure. The second continuous weigh loss from 260 to 600°C can be assigned to the departure of the organic ligand. Taking into account the melting point of $CaCl_2$ at 773 °C we can consider that metal oxide (Fe_2O_3, Cr_2O_3, TiO_2, ZrO_2, Al_2O_3) and $CaCl_2$ are presented in the mixture at T=600°C. According to the molar amount of the organic and inorganic moiety for each MOF it is possible to extract the expected inorganic residual meatal oxide in composite, whereupon calculate the amount of $CaCl_2$ in composite considering inorganic part of composite at T=600°C as mixture of metal oxide from each MOF and $CaCl_2$. It can be presented as follow:

$$\boldsymbol{\omega_{salt}} = \mathbf{x}_{\boldsymbol{inorg}} - \frac{\mathbf{x}_{\boldsymbol{org}}}{R}$$

Here $\boldsymbol{\omega_{salt}}$ is the salt content of anhydrous composite, x_{inorg} is the content of inorganic mixture in the anhydrous composite calculated from thermogravimetric analysis of composite at T=600°C, x_{org} is the content of organic moiety in the anhydrous composite calculated from thermogravimetric analysis of composite, and R is the organic/inorganic ratio of anhydrous MOF calculated from thermogravimetric profile of MOF.

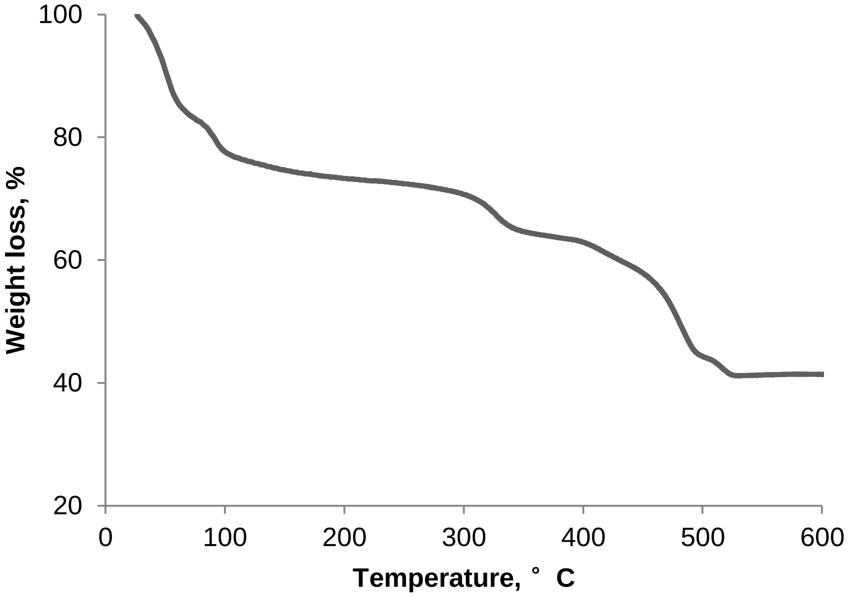

Figure S37. Thermogravimetric analysis profile of MIL-127(Fe)/$CaCl_2$ (40% wt.) under oxygen flow (carrier gas flow rate: 200 ml/min).

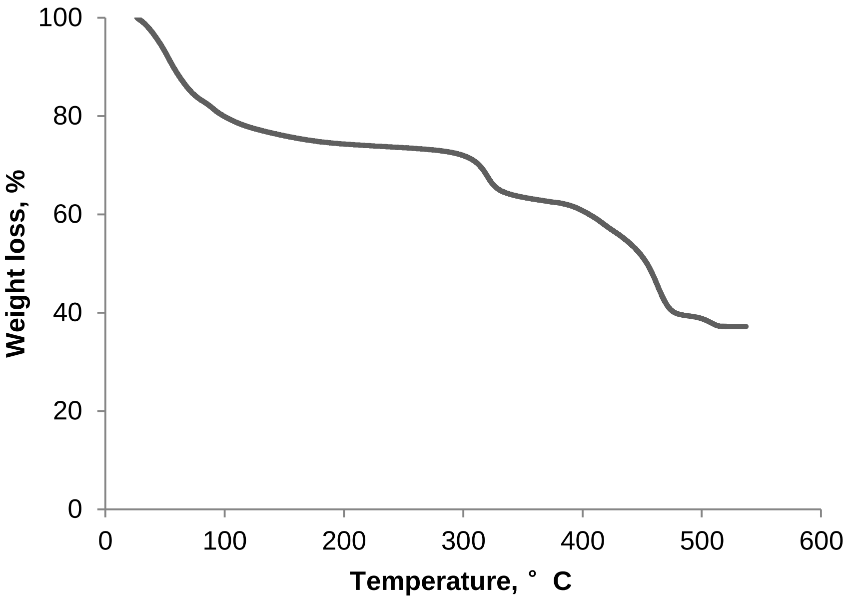

Figure S38. Thermogravimetric analysis profile of MIL-127(Fe)/$CaCl_2$ (31% wt.) under oxygen flow (carrier gas flow rate: 200 ml/min).

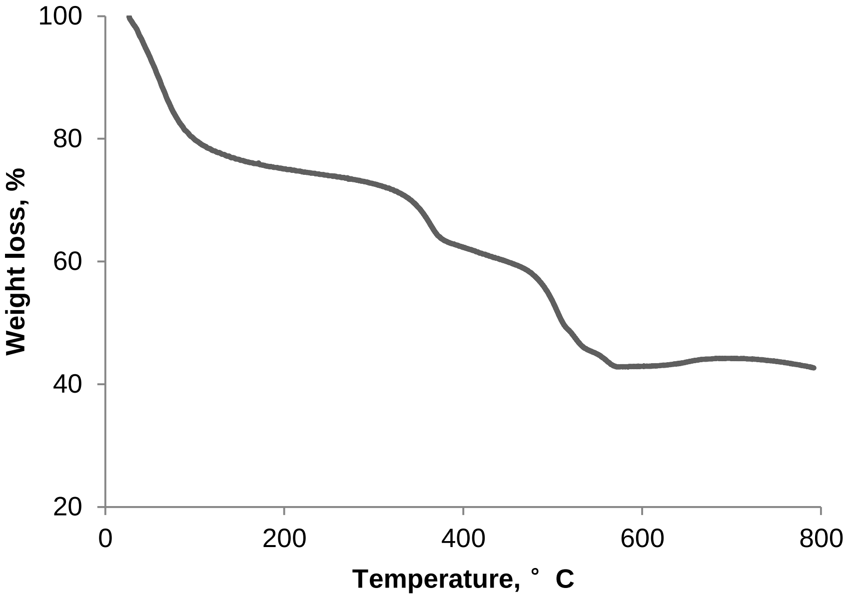

Figure S39. Thermogravimetric analysis profile of MIL-100(Fe)/$CaCl_2$ (34% wt.) under oxygen flow (carrier gas flow rate: 200 ml/min).

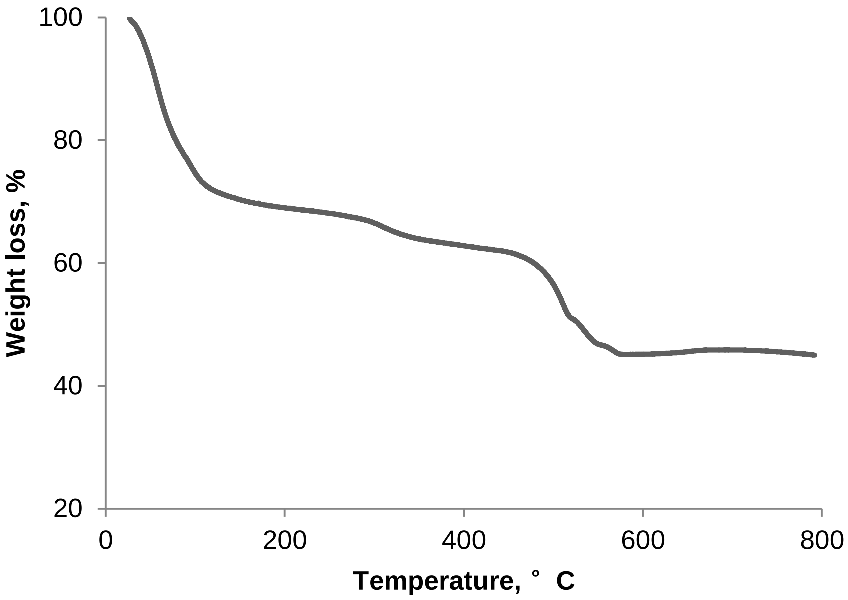

Figure S40. Thermogravimetric analysis profile of MIL-100(Fe)/$CaCl_2$ (46 % wt.) under oxygen flow (carrier gas flow rate: 200 ml/min).

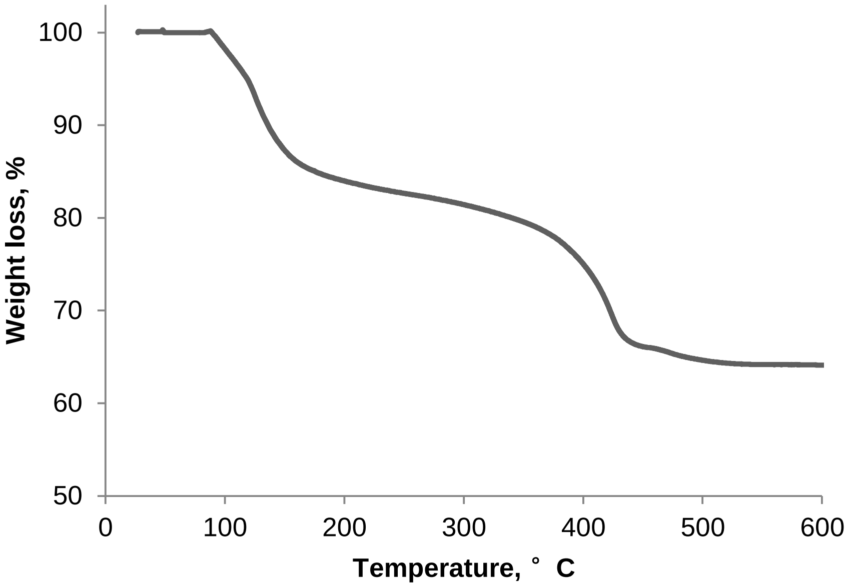

Figure S41. Thermogravimetric analysis profile of MIL-101(Cr)/$CaCl_2$ (62 % wt.) under oxygen flow (carrier gas flow rate: 200 ml/min).

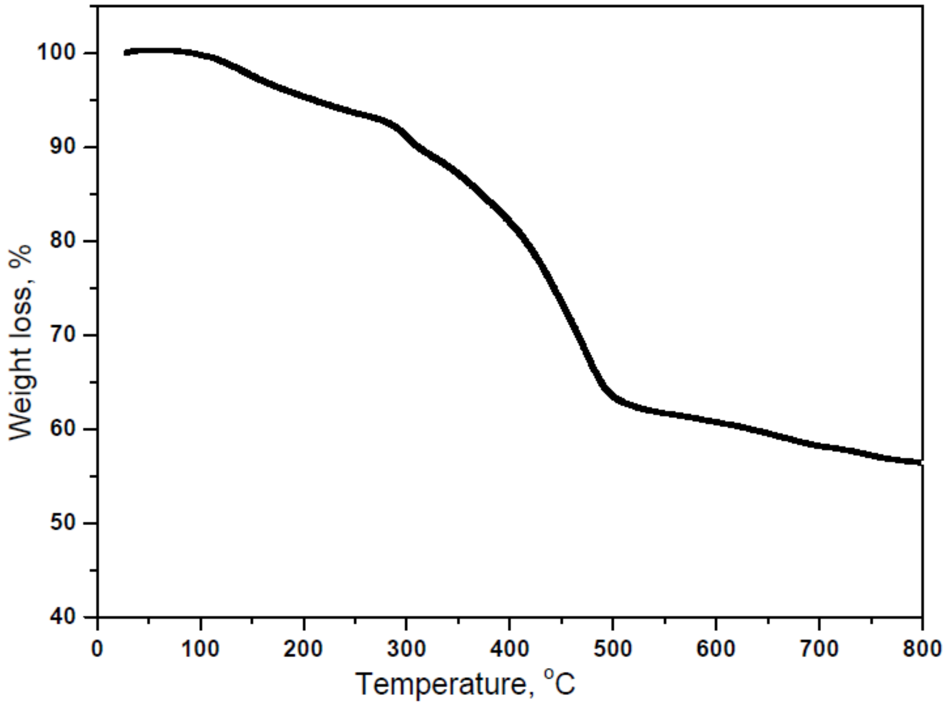

Figure S42. Thermogravimetric analysis profile of MIL-125(Ti)-NH_2/$CaCl_2$ (45% wt.) under oxygen flow (carrier gas flow rate: 200 ml/min).

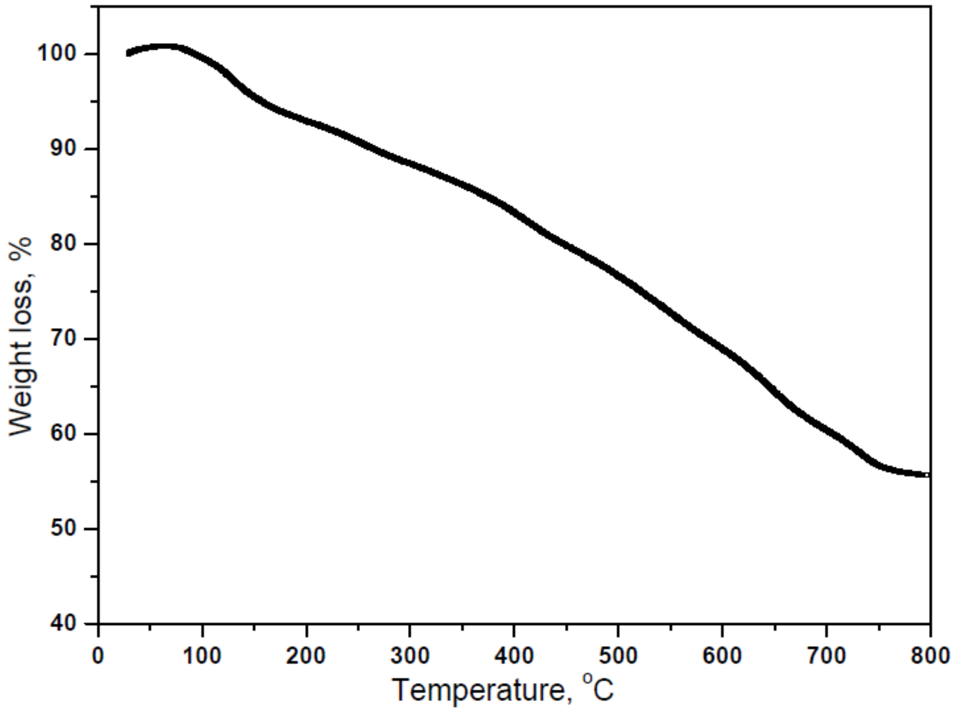

Figure S43. Thermogravimetric analysis profile of UIO-66(Zr)-NH_2/$CaCl_2$ (43% wt.) under oxygen flow (carrier gas flow rate: 200 ml/min).

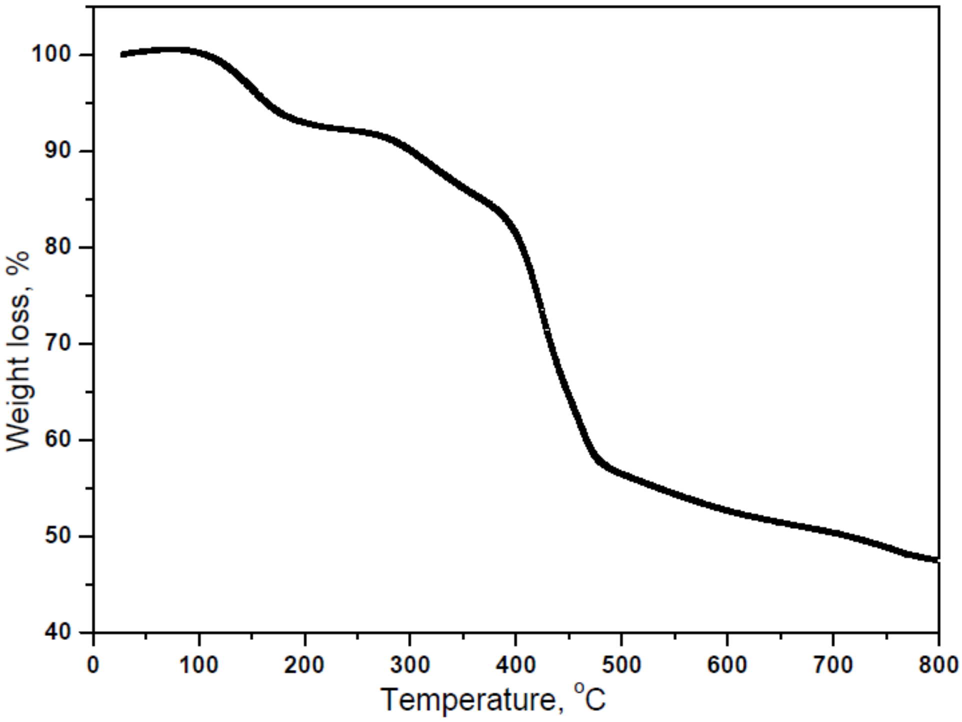

Figure S44. Thermogravimetric analysis profile of MIL-160(Al)/$CaCl_2$ (34% wt.) under oxygen flow (carrier gas flow rate: 200 ml/min).

The good correlation between results of TGA and elemental analysis proves that TGA is an accurate method to determine the salt content of composites.

Elemental analysis of composites

Salt content in composites was calculated twice. The first estimation considers only Ca/Fe ratio from elemental analysis (considering molar ratio Cl/Ca equal 2 according to the salt formula as $CaCl_2$). This salt content is mentioned in the Table S2 as ω_{CaCl2} (Ca/Fe ratio) and it was used to compare with salt content obtained by TGA. The second estimation takes into account real content of Ca^{2+} and Cl^- in the MOF and is mentioned as ω_{CaCl2} (Ca/Fe and Cl/Fe ratio). It is appeared that there is a lack of Cl in composite compared to molar ratio of $CaCl_2$ that in case of MIL-100(Fe) can be attributed to interaction between Lewis cites of matrix with Cl^- providing exchange of OH^- of matrix by Cl^-. During the drying step HCl could be eliminated out of the material. The rate (%) mentioned in the title of each composite refers to the sum of Ca and Cl atoms in composite detected by elemental analysis.

SEM-EDX of composites

SEM and EDX analysis (points and mapping) were carried out for 3 areas of each composite. SEM analysis confirms the crystallinity of MOF after salt incorporation and preserving of the same morphology. Moreover, SEM was repeated on best composites in order to study the ageing (after 0.5 and 1.5 years for MIL-101(Cr)/$CaCl_2$ (64%) and MIL-100(Fe)/$CaCl_2$ (46%), respectively). It appeared that both composites remain crystalline after long term storing. The repartition of Me, Ca, Cl elements given by EDS mapping for all composites is quite homogeneous. No region of the images contains the sole presence of Ca and Cl atoms which is in agreement with the absence of $CaCl_2$ crystals as suggested by SEM images. These results suggest that most of the $CaCl_2$ crystals are distributed inside the pores of MOF matrix. It is notable, that the Ca/Fe ratio differs significantly from one region to the other in several composites, suggesting that the $CaCl_2$ salt is not always homogeneously distributed inside the pores of MOF. However, Ca/Fe ratio is reproducible in MIL-100(Fe) based composites that allows calculating $CaCl_2$ content. It is in agreement with salt content determined by chemical analysis.

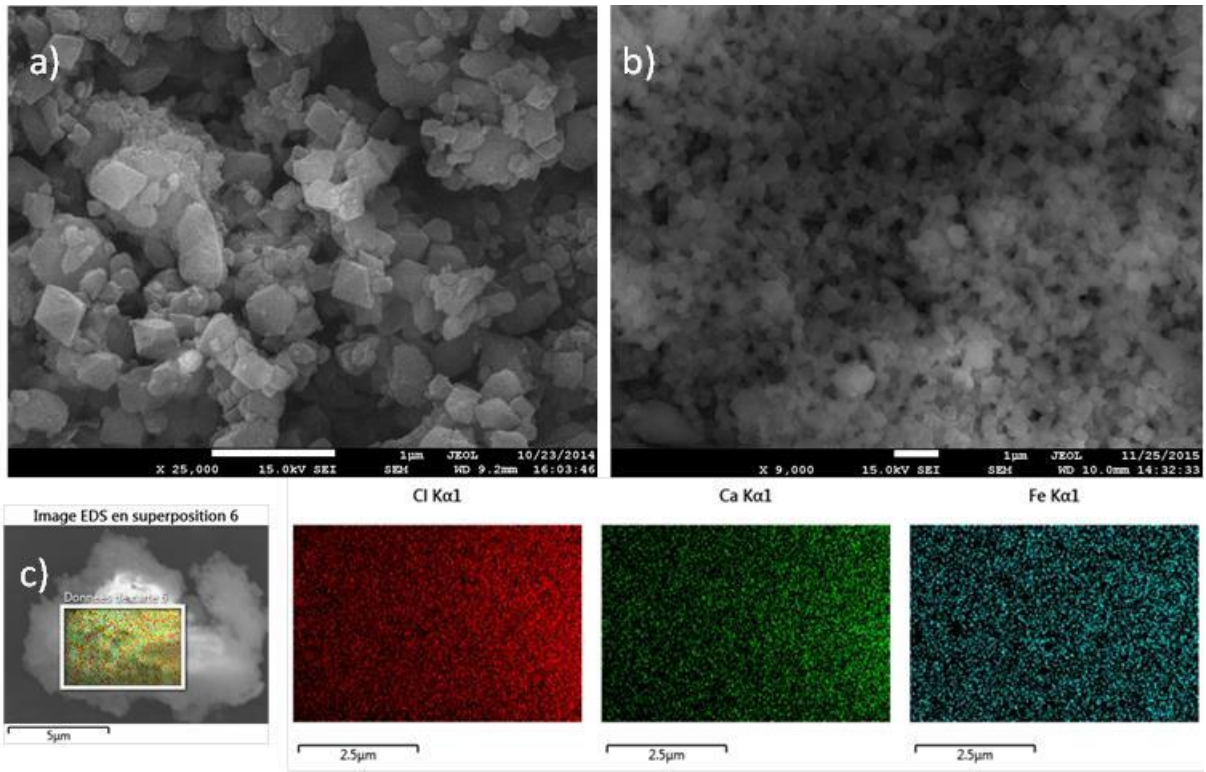

Figure S45. a) SEM of MIL-100(Fe); b) SEM of MIL-100(Fe)/$CaCl_2$ (46%); c) EDS mapping area images for the MIL-100(Fe)/$CaCl_2$ (46%)

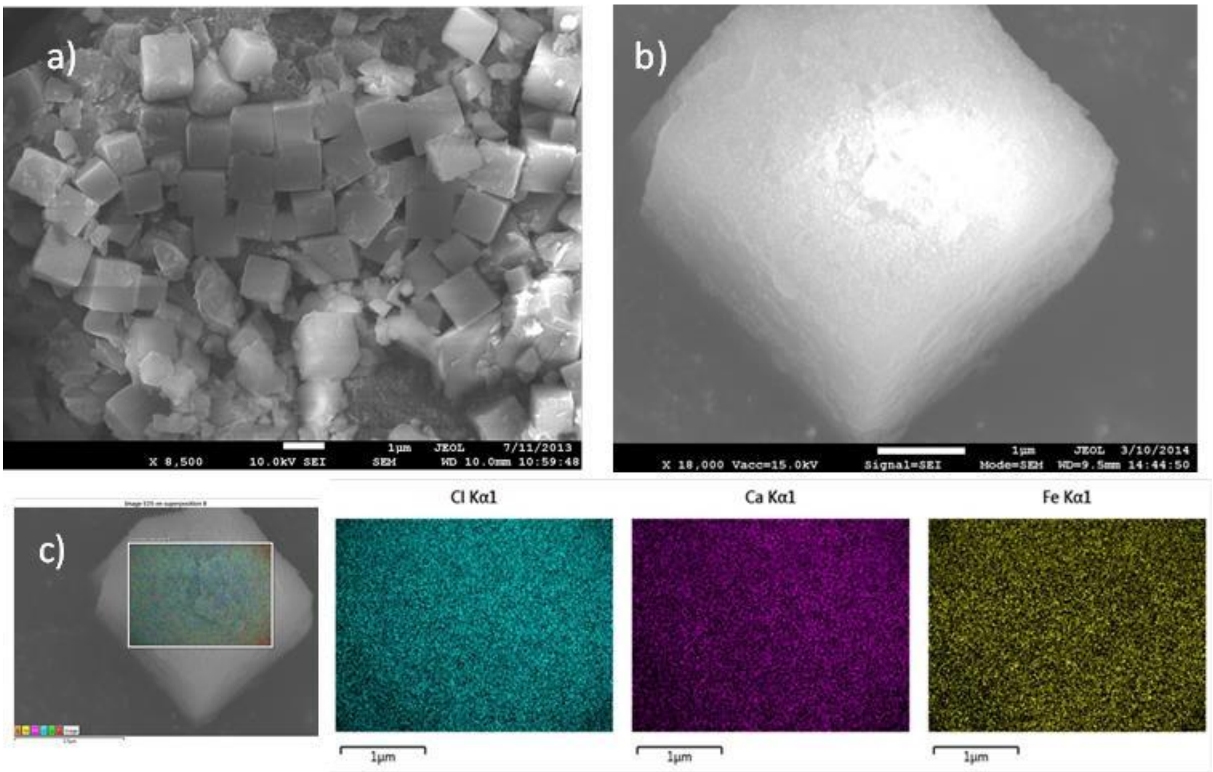

Figure S46. a) SEM of MIL-127(Fe); b) SEM of MIL-127(Fe)/CaCl$_2$ (40%); c) EDS mapping area images for the MIL-127(Fe)/CaCl$_2$ (40%)

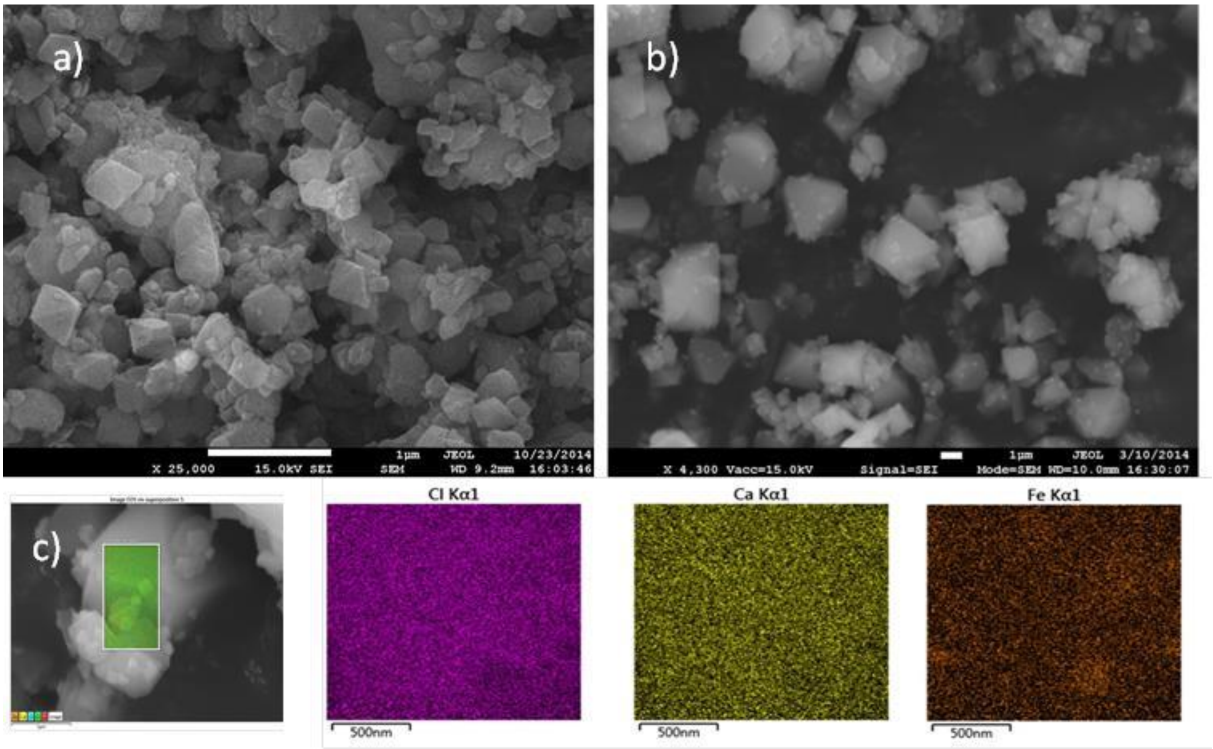

Figure S47. a) SEM of MIL-100(Fe); b) SEM of MIL-100(Fe)/CaCl$_2$ (34%); c) EDS mapping area images for the MIL-100(Fe)/CaCl$_2$ (34%)

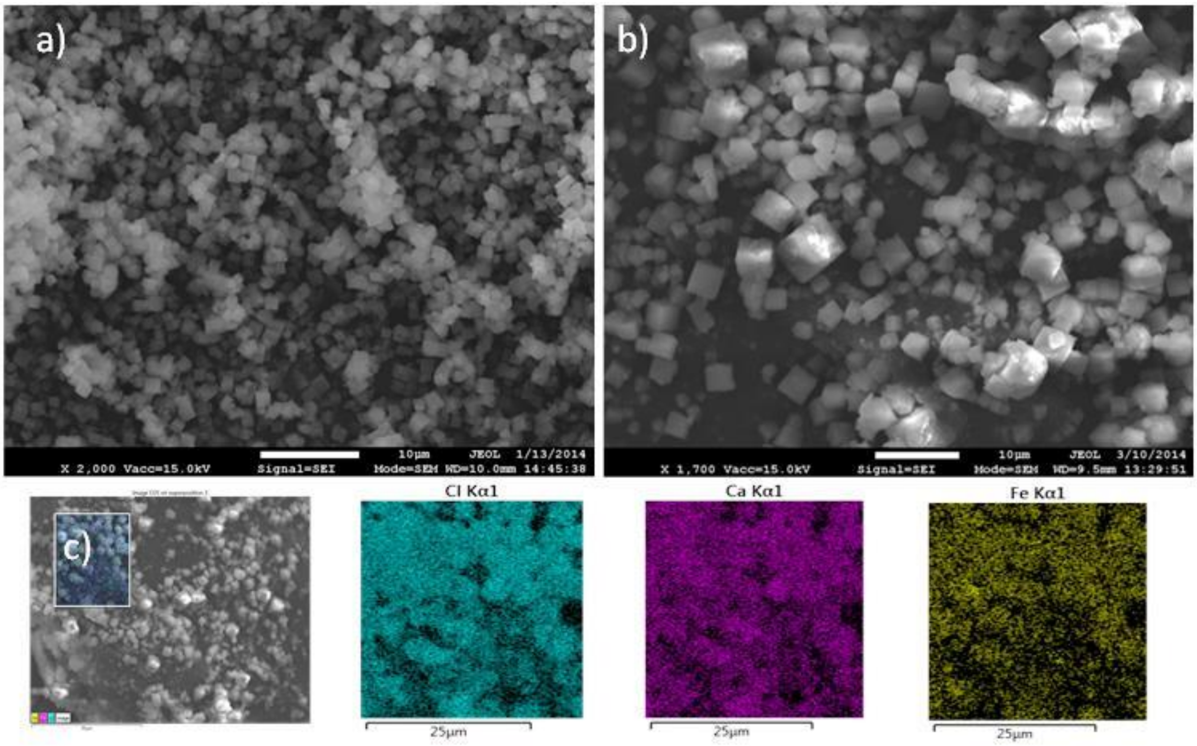

Figure S 48. a) SEM of MIL-127(Fe); b) SEM of MIL-127(Fe)/$CaCl_2$ (31%); c) EDS mapping area images for the MIL-127(Fe)/$CaCl_2$ (31%)

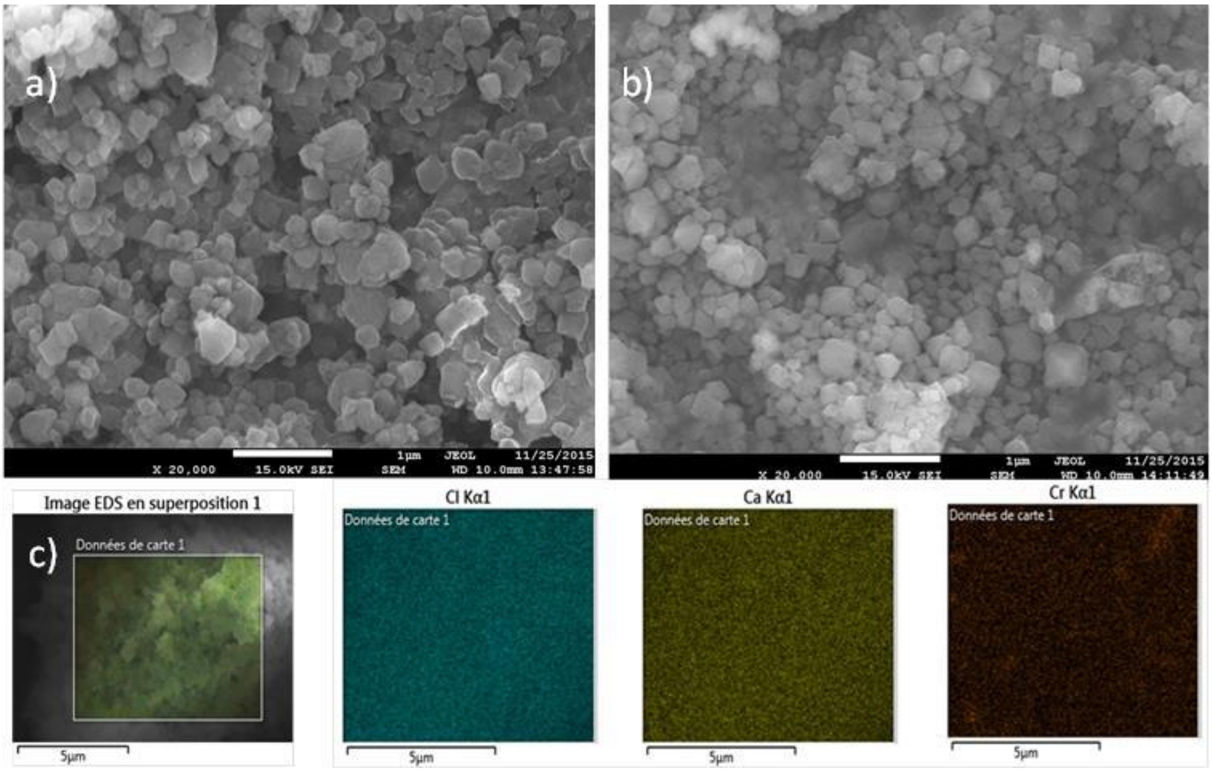

Figure S49. a) SEM of MIL-101(Cr); b) SEM of MIL-101(Cr)/$CaCl_2$ (62%); c) EDS mapping area images for the MIL-101(Cr)/$CaCl_2$ (62%)

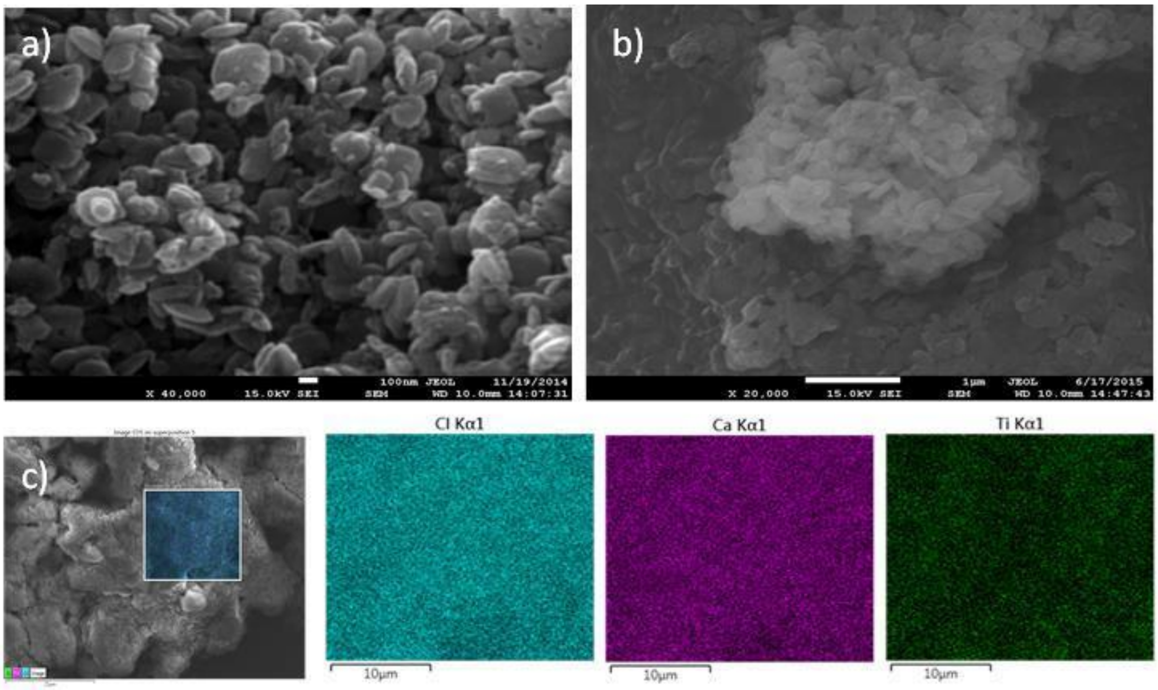

Figure S50. a) SEM of MIL-125(Ti)-NH_2**;** b) SEM of MIL-125(Ti)-NH_2/$CaCl_2$ (45%); c) EDS mapping area images for the MIL-125(Ti)-NH_2/$CaCl_2$ (45%)

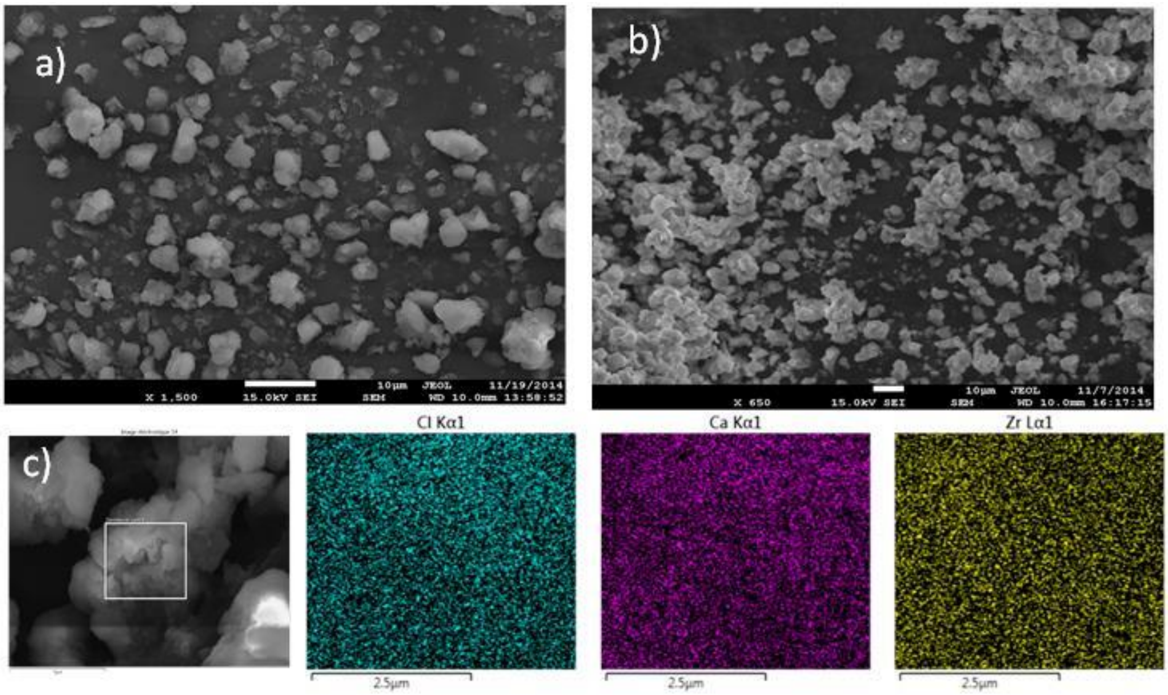

Figure S51. a) SEM of UIO-66(Zr)-NH_2; b) SEM of UIO-66(Zr)-NH_2/$CaCl_2$ (43%); c) EDS mapping area images for the UIO-66(Zr)-NH_2/$CaCl_2$ (43%)

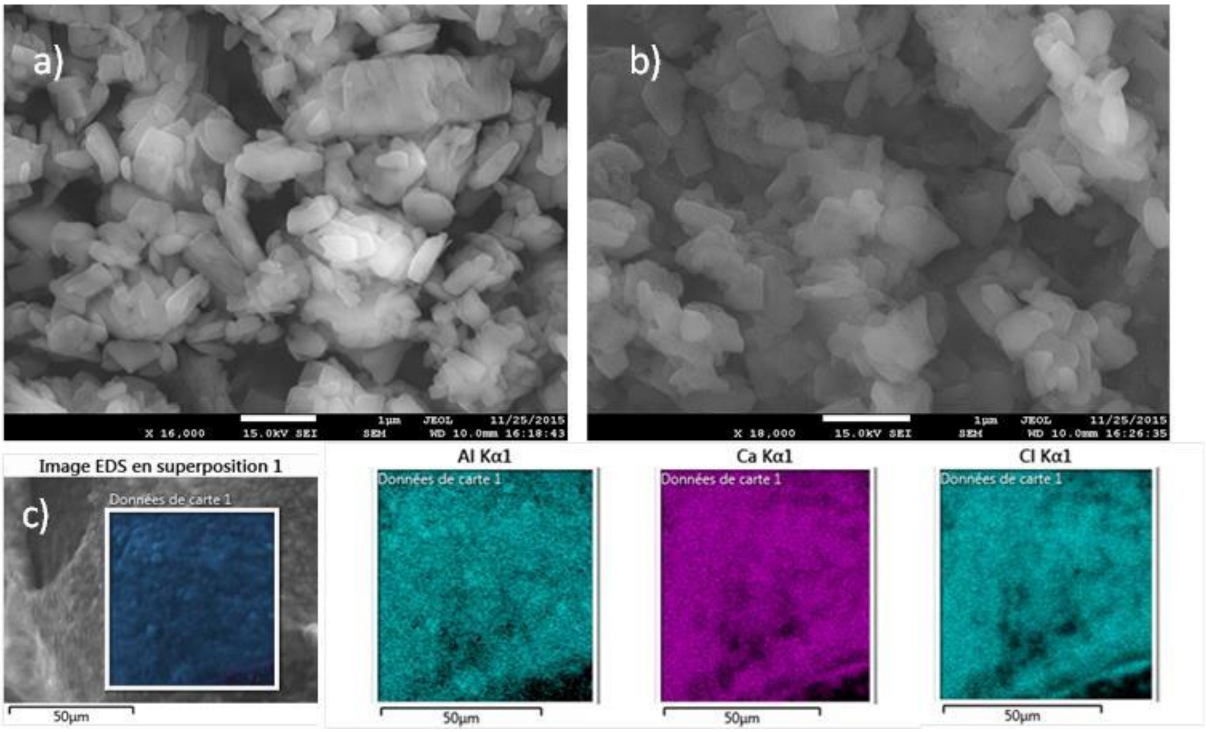

Figure S52. SEM of MIL-160(Al)**;** b) SEM of MIL-160(Al)//$CaCl_2$ (34%); c) EDS mapping area images for the MIL-160(Al)/$CaCl_2$ (34%)

Salt content of composites calculated by thermogravimetry, EDS and elemental analysis

Table S2. Salt content in composites calculated from thermogravimetry, Ca/Me EDS ratio and elemental analysis (based on Ca/Me ratio and based on both Ca/Me and Cl/Me ratio)

Name of composite	ω $CaCl_2$ (TGA) [% wt.]	Ca/Me (EDS)	Ca/Me (el. analysis)	Cl/Ca (el. analysis)	ω $CaCl_2$ (Ca/Me ratio) (EDS) [% wt.]	ω $CaCl_2$ (Ca/Me ratio) (elem. analysis) [% wt.]	ω (Ca + Cl) (Ca/Me and Cl/Me) (elem. analysis) [% wt.]
MIL-100(Fe)/$CaCl_2$ (**46%**)	48	1.7±0.1	1.96	1.54	48±1	50	**46**
MIL-100(Fe)/$CaCl_2$ (**34%**)	36	0.9±0.2	1.17	1.49	33±5	37	**34**
MIL-127(Fe)/$CaCl_2$ (**31%**)	30	1.4±0.2	1.12	1.69	39±3	34	**31**
MIL-127(Fe)/$CaCl_2$ (**40%**)	39	1.8±0.1	1.69	1.59	43±3	42	**40**
UiO-66(Zr)-NH_2/$CaCl_2$ (**43%**)	-	2.0±0.6	2.12	1.82	43±6	44	**43**
MIL-125(Ti)-NH_2/$CaCl_2$ (**45%**)	-	2.3±0.5	1.72	1.70	55±5	48	**45**
MIL-101(Cr)/ $CaCl_2$ (**62%**)	63	2.9±0.2	3.60	1.83	59±2	64	**62**
MIL-160(Al)/$CaCl_2$ (**34%**)	31	1.1±0.3	1.00	1.77	34±23	36	**34**

5. N_2 sorption porosimetry of composites

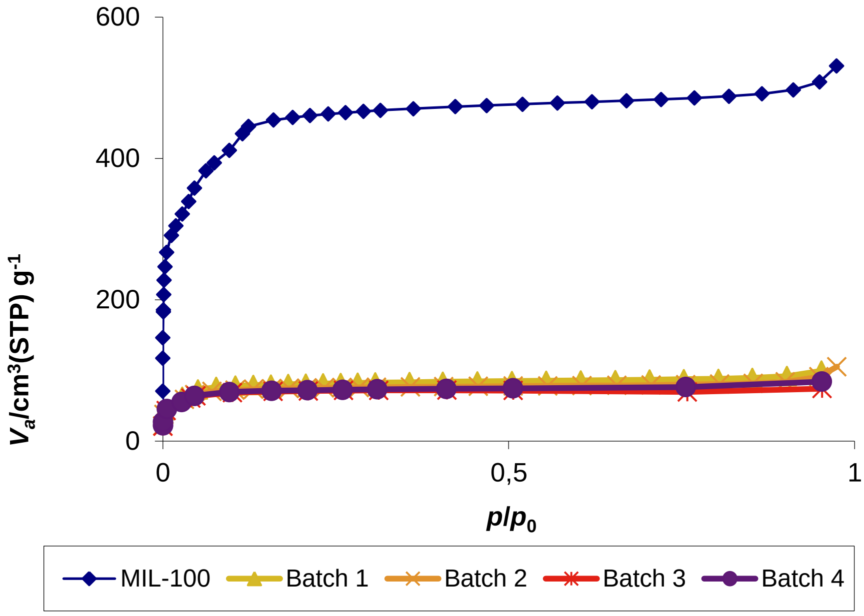

Figure S53. Nitrogen sorption isotherm of MIL-100(Fe) and composite MIL-100(Fe)/$CaCl_2$ (46%) on 4 batches at 77 K. (S_{BET} = 291±13 m^2/g, V_{pore} =0.133±0.016 cm^3/g).

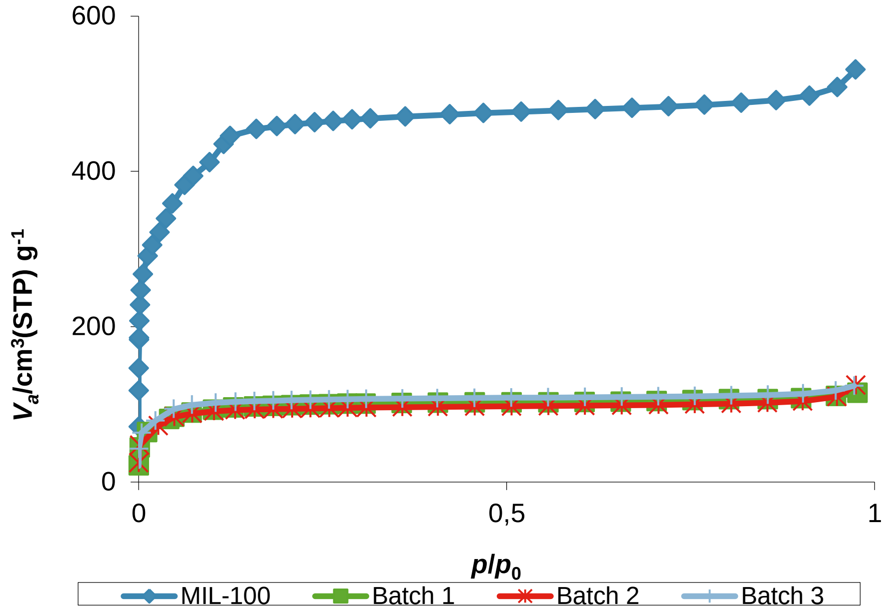

Figure S54. Nitrogen sorption isotherm of MIL-100(Fe) and composite MIL-100(Fe)/$CaCl_2$ (34 %) on 3 batches at 77 K. (S_{BET} = 365±46 m^2/g, V_{pore} =0.188±0.005 cm^3/g).

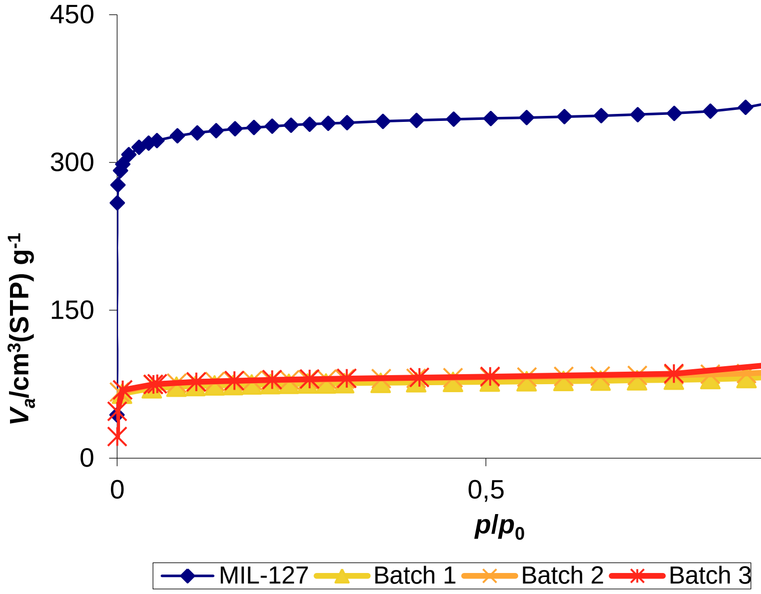

Figure S55. Nitrogen sorption isotherm of MIL-127(Fe) and composite MIL-127(Fe)/$CaCl_2$ (40 %) on 3 batches at 77 K. (S_{BET} = 516±3 m^2/g, V_{pore} =0.223±0.005 cm^3/g).

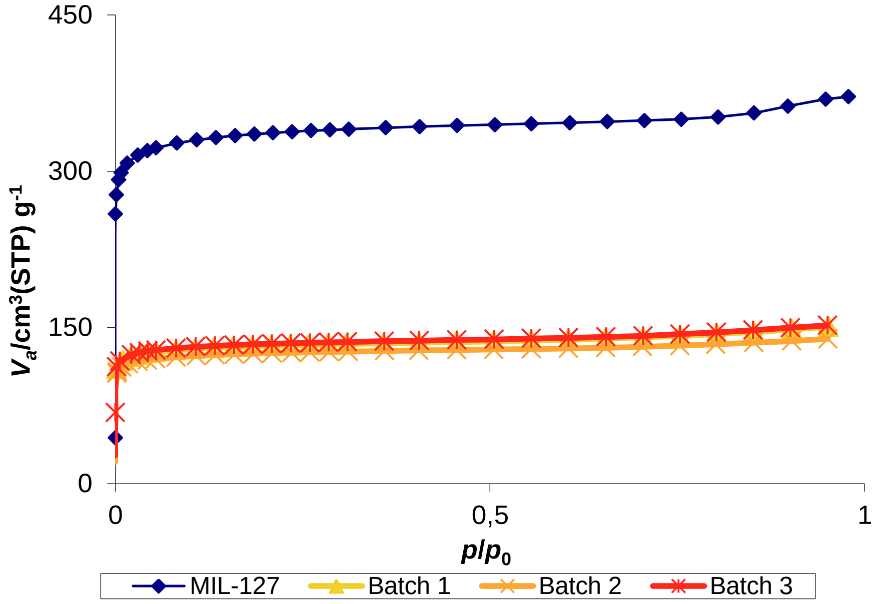

Figure S56. Nitrogen sorption isotherm of MIL-127(Fe) and composite MIL-127(Fe)/$CaCl_2$ (31 %) on 3 batches at 77 K. (S_{BET} = 517±15 m^2/g, V_{pore} =0.228±0.009 cm^3/g).

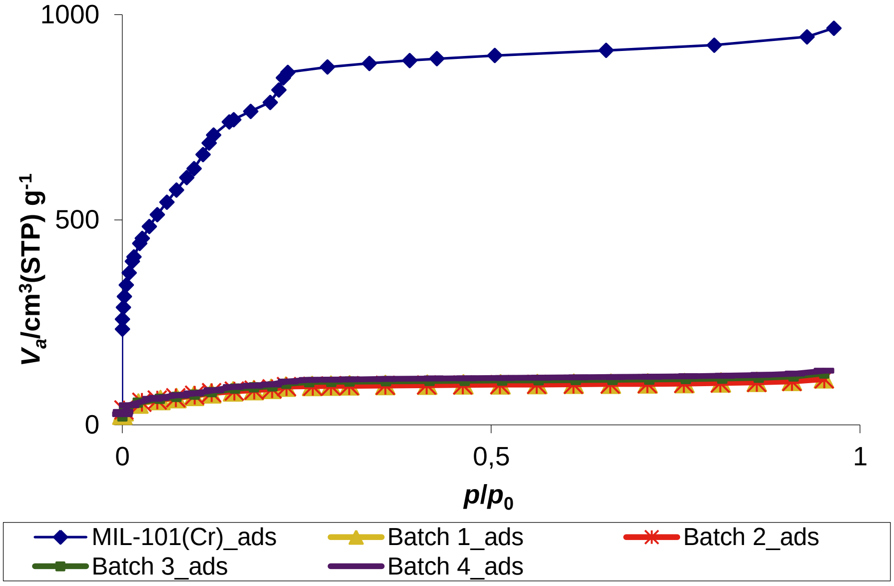

Figure S57. Nitrogen sorption isotherm of MIL-101(Cr) and composite MIL-101(Cr)/$CaCl_2$ (62 %) on 4 batches at 77 K. (S_{BET} = 332±12 m^2/g, V_{pore} =0.19±0.01 cm^3/g).

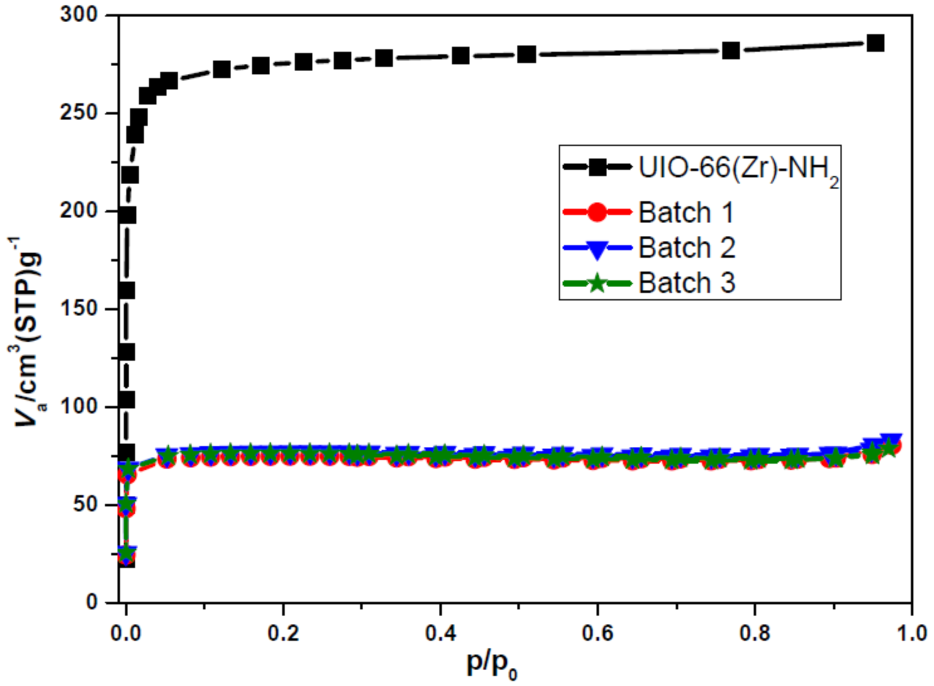

Figure S58. Nitrogen sorption isotherm of UIO-66(Zr)-NH_2 and composite UIO-66(Zr)-NH_2/$CaCl_2$ (43 %) on 3 batches at 77 K. (S_{BET} = 309±10 m^2/g, V_{pore} =0.130±0.004 cm^3/g).

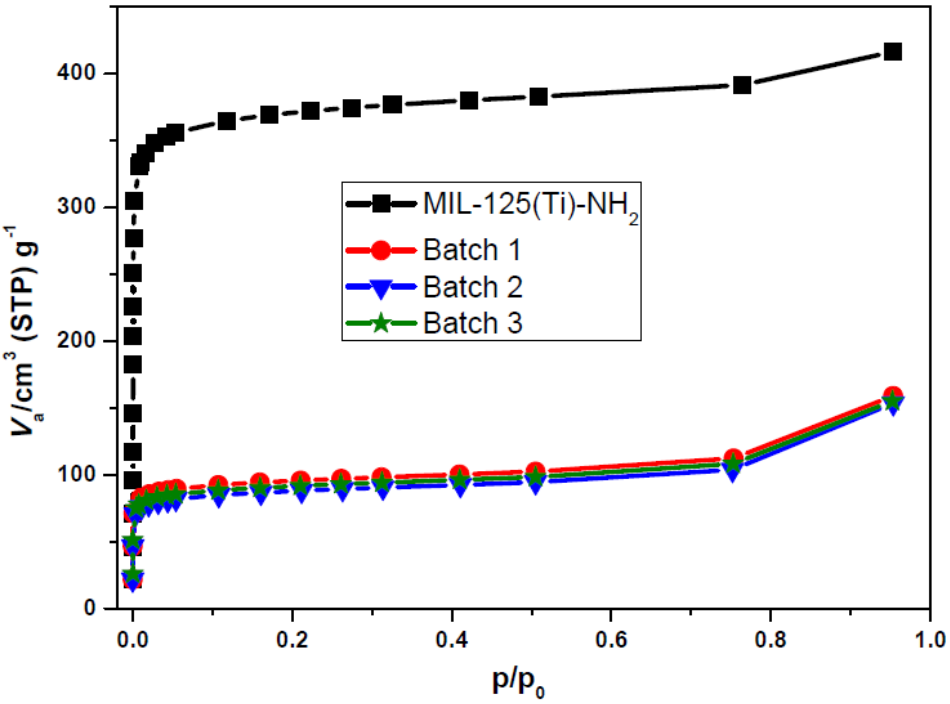

Figure S59. Nitrogen sorption isotherm of MIL-125(Ti)-NH_2 and composite MIL-125(Ti)-$NH_2/CaCl_2$ (45 %) on 3 batches at 77 K. (S_{BET} = 356±13 m^2/g, V_{pore} =0.240±0.004 cm^3/g).

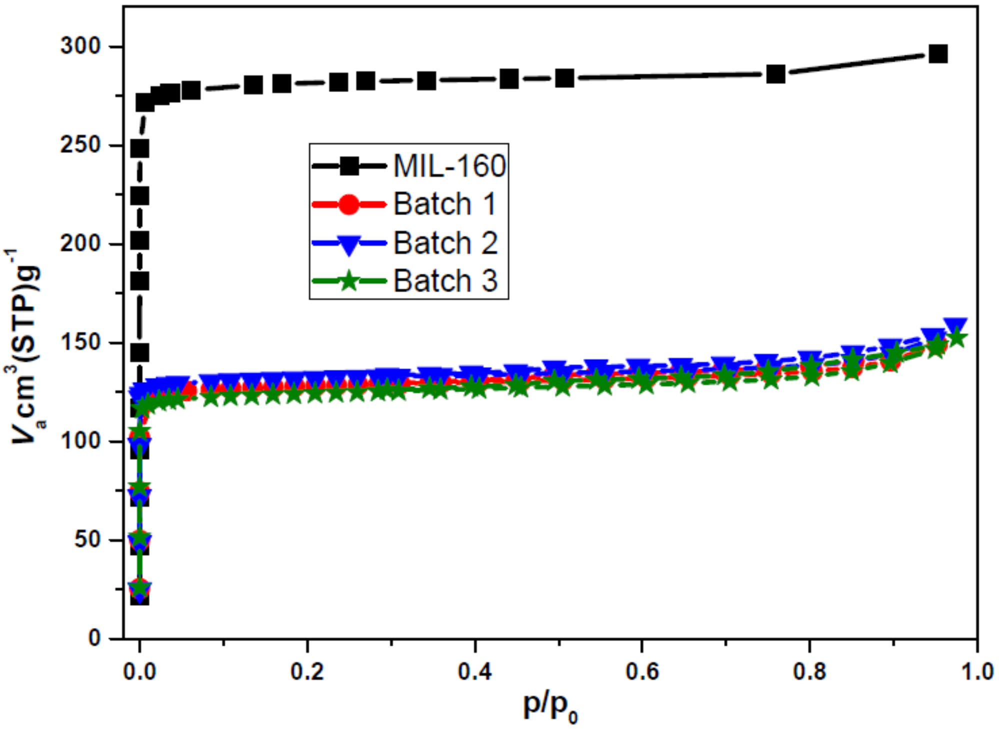

Figure S60. Nitrogen sorption isotherm of MIL-160(Al) and composite MIL-160(Al)/$CaCl_2$ (34 %) on 3 batches at 77 K. (S_{BET} = 523±16 m^2/g, V_{pore} =0.240±0.006 cm^3/g).

6. Water sorption properties of composites. Cycling loading lift

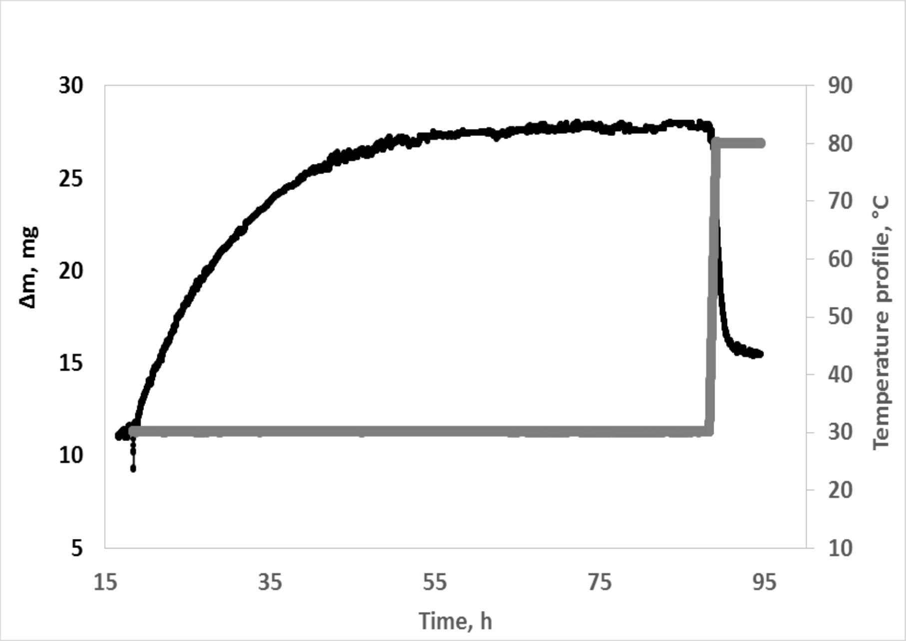

Figure S61. Cycling loading lift (TGA) on 36.92 mg of anhydrous MIL-127(Fe)/CaCl$_2$ (40% wt) composite. Condition of lift: adsorption at 30°C and p=12.5 mbar, desorption at 80°C and p=12.5 mbar.

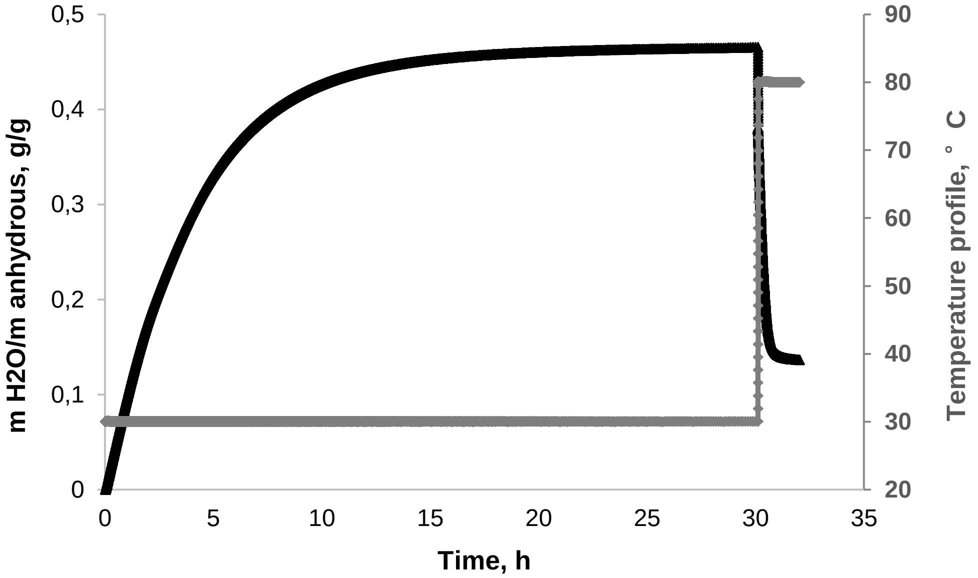

Figure S62. Cycling loading lift (IGASorp) on 28.79 mg of anhydrous MIL-127(Fe)/CaCl$_2$ (31 % wt) composite. Condition of lift: adsorption at 30°C and p=12.5 mbar, desorption at 80°C and p=12.5 mbar.

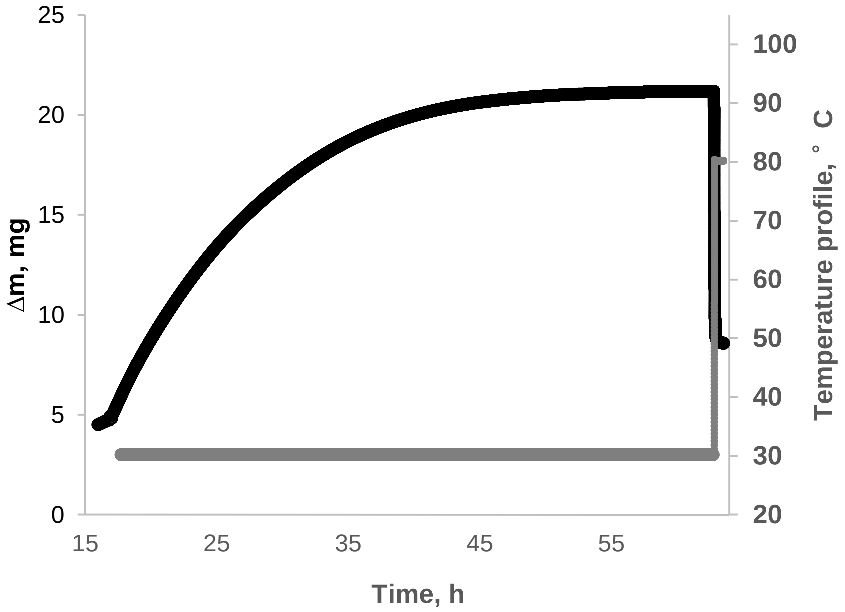

Figure S63. Cycling loading lift (TGA) on 35.87 mg of anhydrous MIL-125(Ti)-NH_2/$CaCl_2$ (45% wt.) composite. Condition of lift: adsorption at 30°C and p=12.5 mbar, desorption at 80°C and p=12.5 mbar.

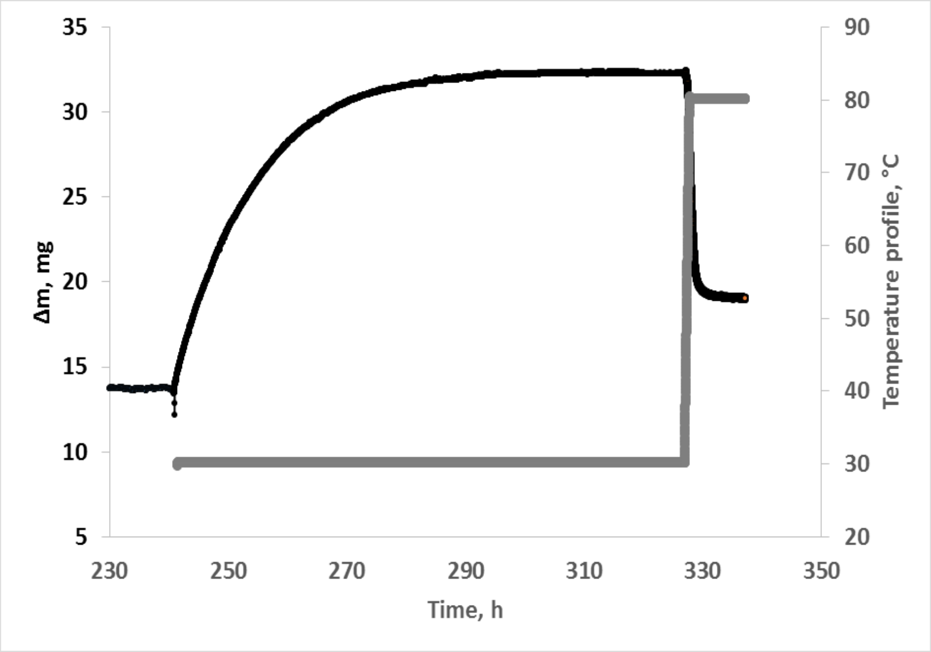

Figure S64. Cycling loading lift (TGA) on 39.05 mg of anhydrous UiO-66(Zr)-NH_2/$CaCl_2$ (43% wt) composite. Condition of lift: adsorption at 30°C and p=12.5 mbar, desorption at 80°C and p=12.5 mbar.

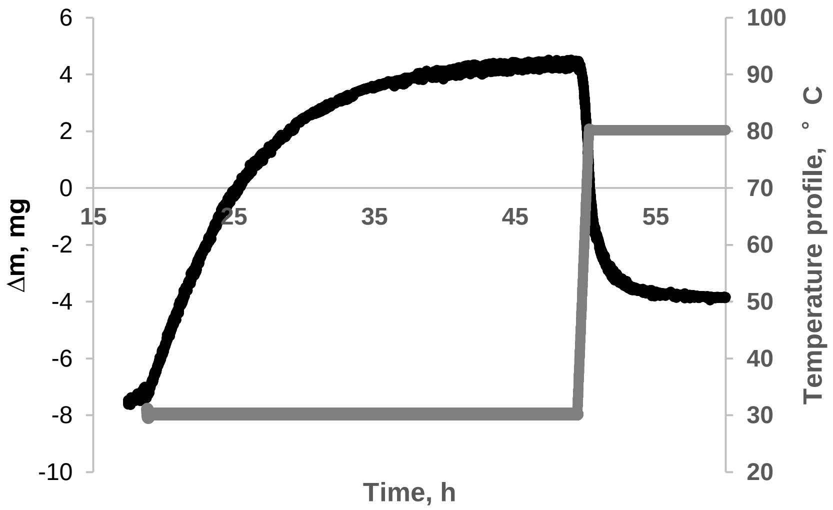

Figure S65. Cycling loading lift (TGA) on 24.79 mg of anhydrous MIL-100(Fe)/$CaCl_2$ (33 % wt.) composite. Condition of lift: adsorption at 30°C and p=12.5 mbar, desorption at 80°C and p=12.5 mbar.

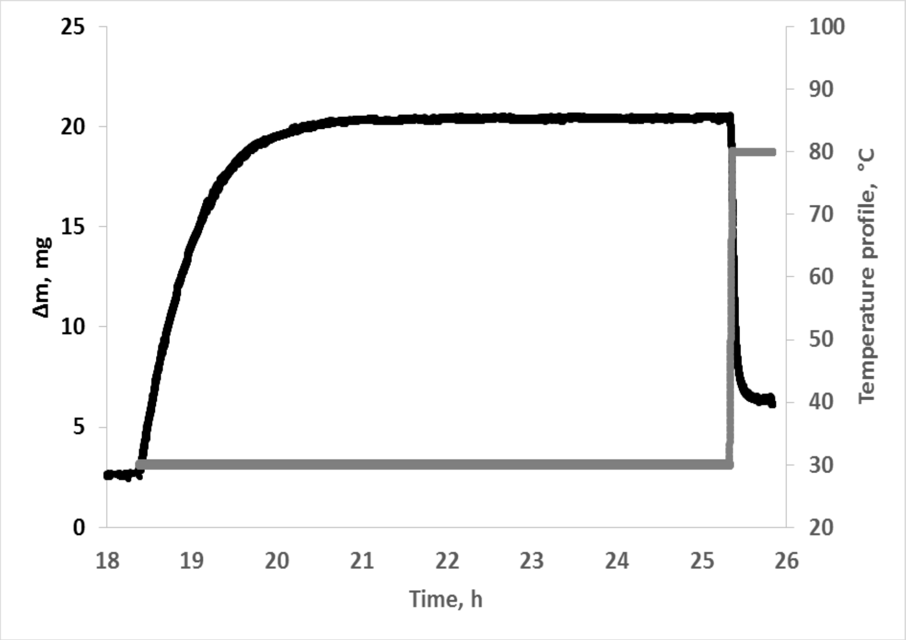

Figure S66. Cycling loading lift (TGA) on 30.60 mg of anhydrous MIL-100(Fe)/$CaCl_2$ (46 % wt) composite. Condition of lift: adsorption at 30°C and p=12.5 mbar, desorption at 80°C and p=12.5 mbar.

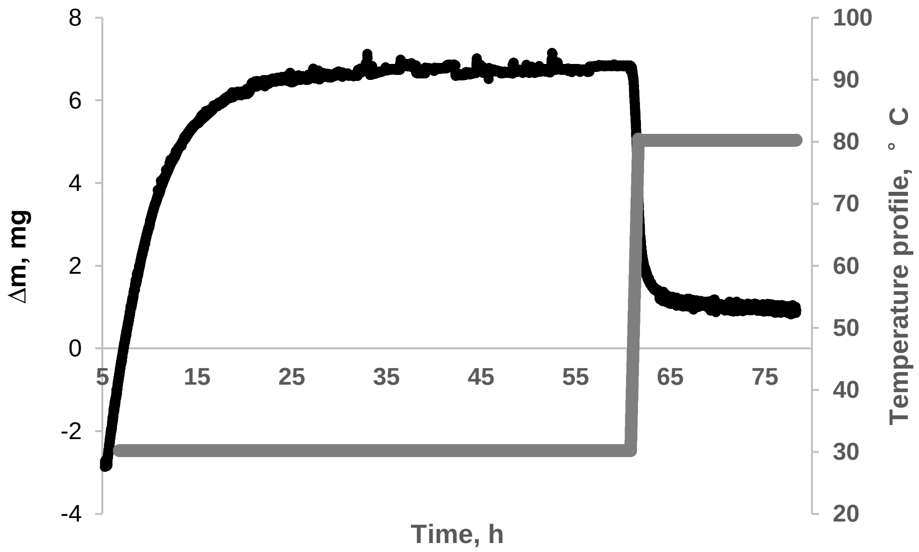

Figure S67. Cycling loading lift (TGA) on 27.70 mg of anhydrous MIL-160(Al)/$CaCl_2$ (34 % wt) composite. Condition of lift: adsorption at 30°C and p=12.5 mbar, desorption at 80°C and p=12.5 mbar.

7. Calculation of energy storage capacity and energy storage density

Energy storage density of material corresponds to stored energy per unit of volume [kWh/m^3]. It is a function of three parameters such as differential heat of adsorption, cycle loading lift and packing density of the material. Energy storage capacity of material corresponds to stored energy per unit of mass [Wh/kg] and depends only on differential heat of adsorption and cycle loading lift of material.

We calculated a theoretical energy storage capacity and energy storage density of second series of composites, considering that a part of the dehydration is due to the chemical reaction of $CaCl_2$ dehydration from hexahydrate to monohydrate and the residual part is due to the physical adsorption on MOF. This calculation requires the heat of hydration and the heat of adsorption in the condition cycling loading lift. According to phase diagram of $CaCl_2$ three reaction of dehydration take place at p=12.5 mbar between 30 and 80°C.

$$CaCl_2 \cdot 6H_2\mathrm{O} = CaCl_2 \cdot 4H_2\mathrm{O} + 2H_2\mathrm{O} \quad \left(\Delta \mathrm{H}_{chem[6\to4]} = 47255 J/mol\right) \tag{1}$$

$$CaCl_2 \cdot 4H_2\mathrm{O} = CaCl_2 \cdot 2H_2\mathrm{O} + 2H_2\mathrm{O} \quad \left(\Delta \mathrm{H}_{chem[4\to2]} = 47850 J/mol\right) \tag{2}$$

$$CaCl_2 \cdot 2H_2\mathrm{O} = CaCl_2 \cdot 1H_2\mathrm{O} + H_2\mathrm{O} \quad \left(\Delta \mathrm{H}_{chem[2\to1]} = 47557 J/mol\right) \tag{3}$$

The heat of adsorption (ΔH_{phys}) of each MOF was estimated according to the condition of cycling loading lift as average integral enthalpy between integral enthalpy corresponding to adsorbed mass and integral enthalpy corresponding to desorbed mass. Thus, energy storage capacity (Q) can be estimated as follow:

$$Q = \Delta m_{chem} \times \Delta H_{chem} + \Delta m_{phys} \times \Delta H_{phys} \tag{4}$$

Here ΔH_{chem} implies enthalpies of above mentioned reaction while Δm_{chem} and Δm_{phys} are exchanged mass corresponding to chemical reaction and physical adsorption, respectively. These exchanged mass can be founded as follow:

$$\Delta m_{chem} = \omega_{chem} \times m_{anhydrous} \tag{5}$$

$$\Delta m_{phys} = \Delta m_{\exp} - \Delta m_{chem} \tag{6}$$

Here $\Delta m_{\exp}$ is total experimental exchanged mass over cycle denoted cycling loading lift.

Energy storage density (E) can be presented as:

$$E = Q \times d \tag{7}$$

where d is packing density of composite material.

We will provide the details of energy storage capacity calculation for second series of composites and energy storage density for composites based on mesoporous MOFs (MIL-100(Fe) and MIL-101(Fe)).

Table S3. Calculated energy storage capacity and energy storage density of second series of composites

Name of composite	ω (Ca + Cl) (Ca/Fe and Cl/Fe) [% wt.]	Δm_{exp} [g/g]	Δm_{chem} [g/g]	ΔH_{phys} [kJ/mol]	Q calculated [Wh/kg]	d [g/cm^3]	E calculated [kWh/m^3]
MIL-127(Fe)/CaCl$_2$ (40%)	40	0.33	0.324	-	243	-	-
MIL-125(Ti)_ NH$_2$/CaCl$_2$ (45%)	45	0.35	0.369	-	254	-	-
UiO-66(Zr)_ NH$_2$/CaCl$_2$ (43%)	43	0.34	0.349	-	248	-	-
MIL-100(Fe)/CaCl$_2$ (46%)	46	0.48	0.39	49.18	357	0.62	222
MIL-101(Cr)/CaCl$_2$ (64%)	62	0.60	0.50	46.45	439	0.64	280

8. Ageing of composites based on MIL-100(Fe) and MIL-101(Cr)

8.1. SEM analysis

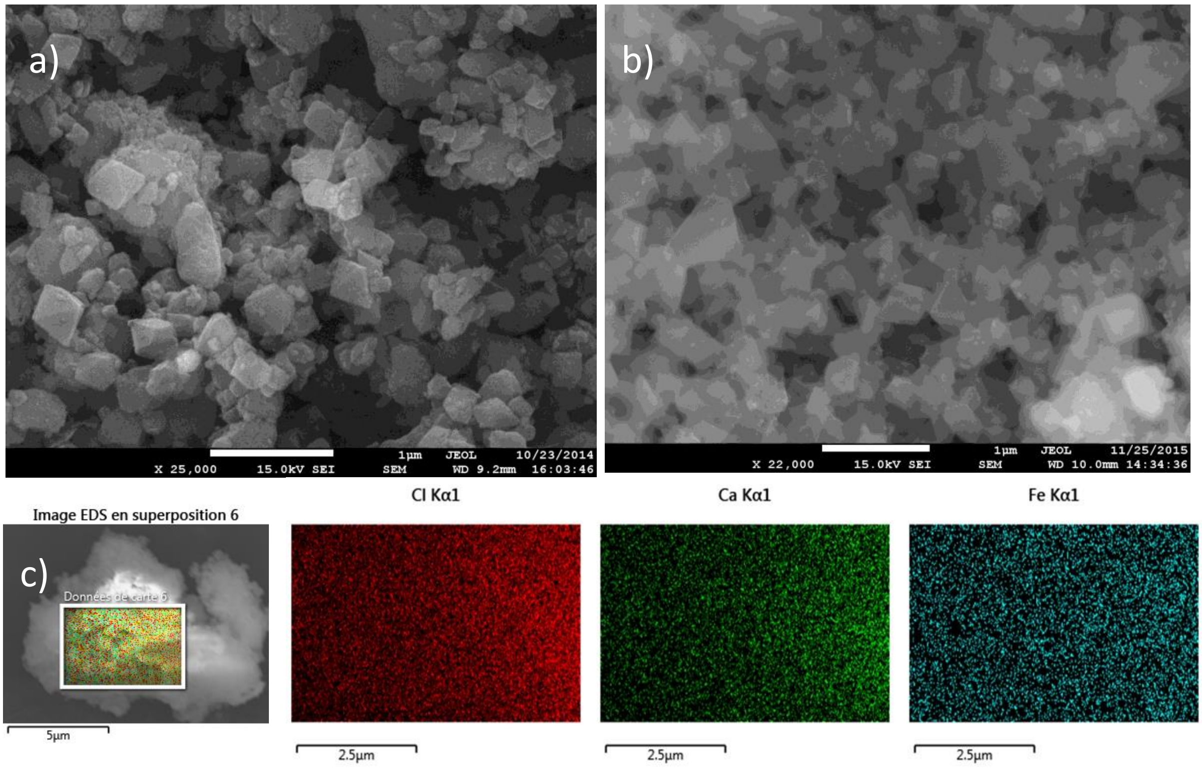

Figure S68. a) SEM of MIL-100(Fe); b) SEM of MIL-100(Fe)/$CaCl_2$ (46%) (1.5 year after synthesis); c) EDS mapping area images for the MIL-100(Fe)/$CaCl_2$ (46%)

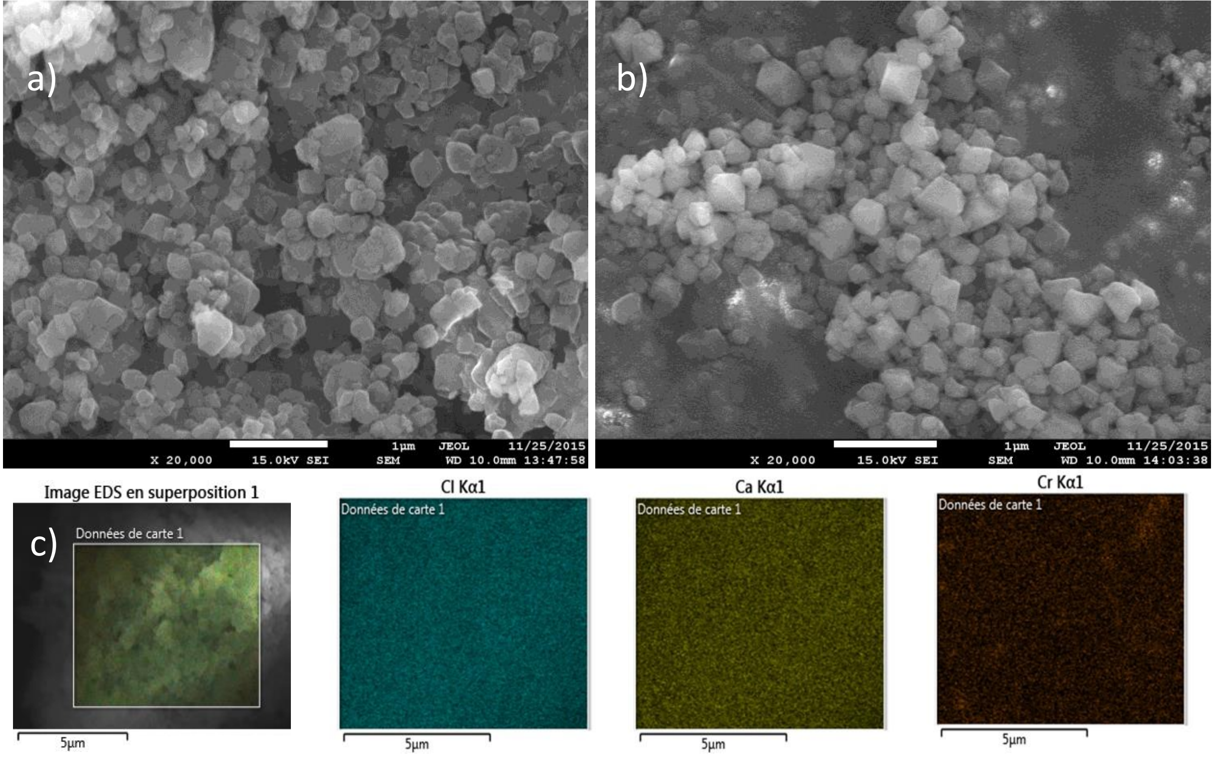

Figure S69. a) SEM of MIL-101(Cr); b) SEM of MIL-101(Cr)/$CaCl_2$ (62%) (0.5 year after synthesis); c) EDS mapping area images for the MIL-101(Cr)/$CaCl_2$ (62%)

8.2. Nitrogen sorption porosimetry

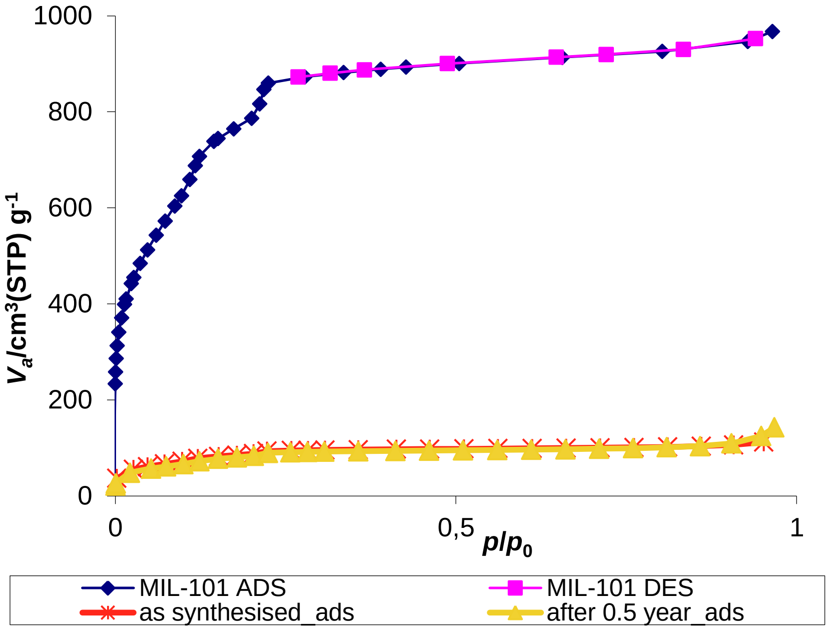

Figure S70. Nitrogen sorption isotherm of MIL-101(Cr) and composite MIL-101(Cr)/$CaCl_2$ (62% wt.) after synthesis (S_{BET} = 323 m^2/g, V_{pore} =0.19 cm^3/g) and after 0.5 years of storing (S_{BET} = 320 m^2/g, V_{pore} =0.22 cm^3/g) at 77 K.

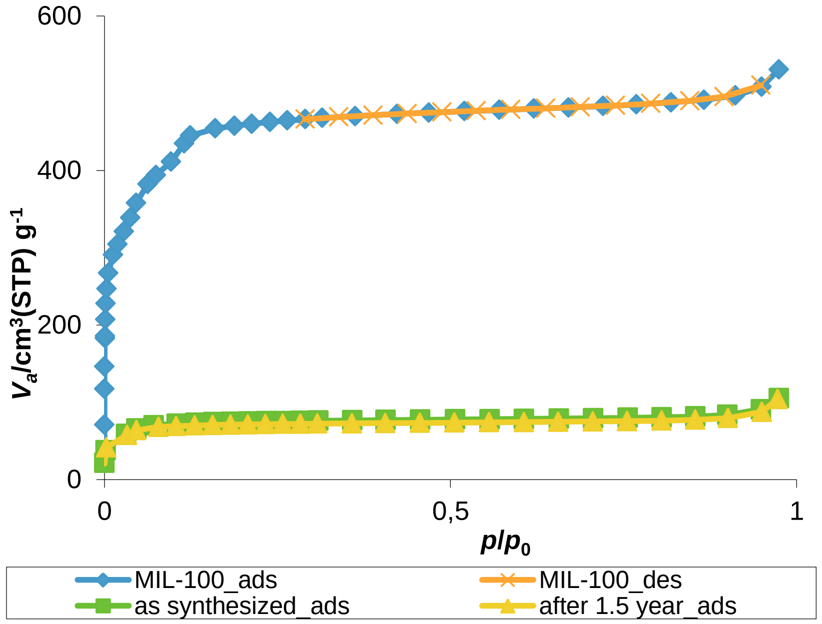

Figure S71. Nitrogen sorption isotherm of MIL-100(Fe) and composite MIL-100(Fe)/$CaCl_2$ (46% wt.) after synthesis (S_{BET} = 278 m^2/g, V_{pore} =0.16 cm^3/g) and after 1.5 years of storing (S_{BET} = 272 m^2/g, V_{pore} =0.16 cm^3/g) at 77 K.

8.3. Thermogravimetric analysis

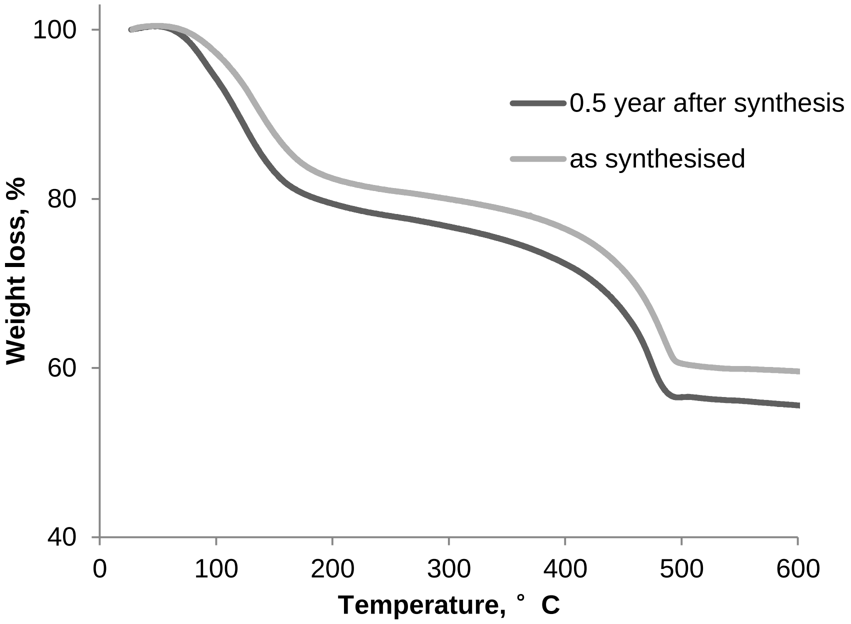

Figure S72. Thermogravimetric analysis profile of MIL-101(Cr)/$CaCl_2$ (62 % wt.) composite under oxygen flow (carrier gas flow rate: 200 ml/min) after synthesis (62 % wt. of $CaCl_2$) and after 0.5 year (60% wt. of $CaCl_2$).

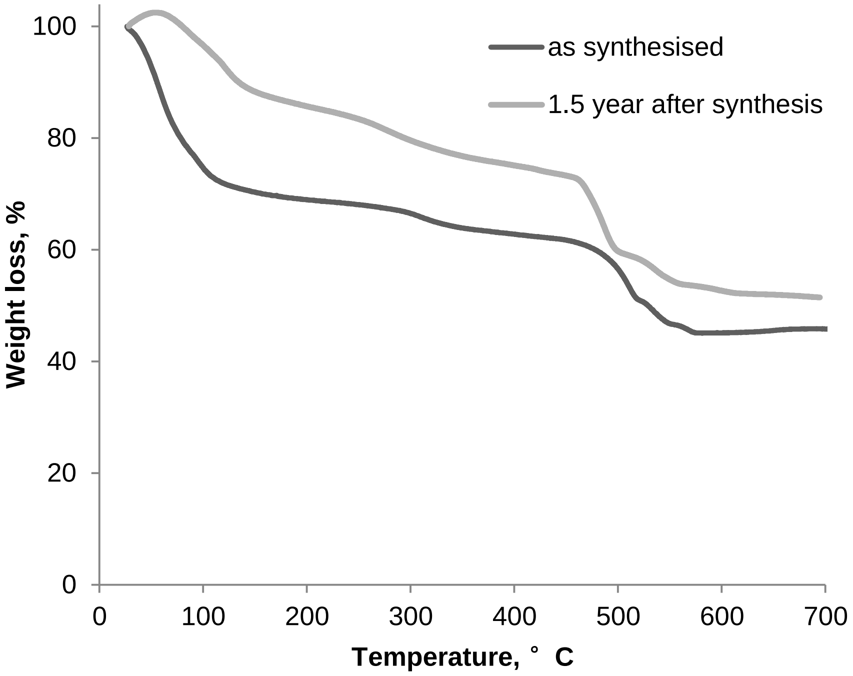

Figure S73. Thermogravimetric analysis profile of MIL-100(Fe)/$CaCl_2$ (46% wt.) composite under oxygen flow (carrier gas flow rate: 200 ml/min) after synthesis (48% wt. of $CaCl_2$) and after 1.5 year (45% wt. of $CaCl_2$).

Supplemental experimental data on salt-MOF composites

Herein, we describe supplemental experimental details that were not included in the article. Firstly, we provide the protocol of MOF synthesis used during experimental work because the conditions of synthesis were optimized for several of them in order to scale-up and/or non-toxic production (in case of MIL-127(Fe), MIL-100(Fe), MIL-101(Cr) and MIL-160(Al)). All the characterizations of MOFs can be found in supporting information of article *'Design of salt-Metal Organic Frameworks composites for heat storage applications'*. Secondly we resume the work concerning salt-MOF composites that can be divided into two parts including 1) development of method for $CaCl_2$-MOF composites synthesis and 2) synthesis of composites based on MOFs and other inorganic salts ($SrBr_2$).

1. Synthesis protocol for MOFs

MIL-100(Fe): optimized protocol

A mixture of $FeCl_3 \cdot 6H_2O$ (0.13 mol, 53.7 g) and trimethyl trimesate (0.09 mol, 18,6 g) dispersed in 140 mL of water was heated for two days at 150 °C using a 400 mL-close vessel reactor. Then, a crystalline orange powder was recovered by filtration, washed with ethanol (140 ml per 1.5 g of solid) for 3 hours, with water (140 mL) for 5 hours and dried under air.

MIL-127(Fe): optimized protocol

5.03 g of NaOH were dissolved in 10 mL of distilled water. 50.8 mmol (18.3 g) of H4-TazBz suspended in 100 mL of propan-2-ol were added, and the resulting mixture was stirred at room temperature. In parallel, 101.9 mmol (28 g) of $FeCl_3$.6H2O were dissolved in 80 mL of propan-2-ol in a flask under reflux. In the last step, both solutions were mixed, and the resulting slurry/solution was mechanically stirred under reflux for 24 hours using a 400 mL-close vessel reactor. A crystalline powder was recovered by filtration, washed with 8 L of distilled water and finally with 8 L of ethanol.

Synthesis of 3,3',5,5'-azobenzenetetracarboxylic acid (H4-TazBz)

In a 3-neck round bottomed flask of 1 L containing 250 mL of distilled water, 19 g of 5-nitroisophthalic acid and then, slowly 50 g of sodium hydroxide NaOH were added followed by heating at 50-60 °C under magnetic stirring during 15 minutes. A pink slurry was formed. 100 g of glucose dissolved in 150 mL of water were slowly added to the previously obtained pink slurry. The solution turned from yellow to orange and then brown. The heating was stopped, and air was bubbled through the solution overnight at room temperature. The mixture was cooled down with an ice-bath in order to increase the amount of precipitate, before recovery of the disodium salt by filtration. The filtrate was then dissolved in 200 mL of distilled water and then this solution was acidified to pH = 1 using 37 % HCl. This yielded a bright orange precipitate, recovered by filtration, washed with ethanol and dried at 70 °C.

MIL-160(Al): optimized protocol

In a round bottom flask (250 ml) containing 75 ml of distilled water were introduced 75 mmol of $Al(OH)(CH_3COO)_2$ (11.71 g) and 75 mmol of 2,5-furandicarboxylic acid (12.16 g). Then, the mixture was stirred under reflux for ca. 24 hrs. The resulting white solid was recovered by filtration, washed with of ethanol and dried in the oven at 100°C to give 13.9 g of dry MIL-160(Al) (yield = 93% and STY = 185 $kg.m^{-3}.day^{-1}$). This procedure was then used to prepare a larger amount of MIL-160(Al) multiplying all amounts by ca. 10 times.

MIL-101(Cr): optimized protocol

MIL-101 was initially prepared from hydrothermal reaction of terephthalic acid (7 mmol, 1.51 g) with $Cr(NO_3)_3$.9H2O (7 mmol, 2.8 g), HF (1.75 mmol), and H_2O (33 mL) at 220°C for 8 h. The resulting green powder was recovered by filtration. To obtain the pure crystals, the as-synthesized chromium terephthalate was further purified by the following two-step processes using hot water (400 mL, T=70°C, 4 hours) and hot ethanol (200 mL, T=60°C, 4 hours). After this first activation treatment this solid was submitted in additional purification procedure with KF (200 mL of 0.03M solution per 1.3 g of preliminary activated solid) solution in order to enhance the accessible pore volume and BET surface area (the BET surface area increase after additional treatment with KF solution was 3700 versus 3200 m^2/g).

MIL-125(Ti)_NH_2: original protocol

2-aminoterephthalic acid (13.75 g, 76 mmol) was added into a mixture of DMF (200 mL) and MeOH (50 mL). The solution was heated up to around 100 ºC until the ligand solid was completely dissolved. Afterwards $Ti(iPrO)_4$ (15 mL, 50 mmol) and distilled water (1 mL) were added rapidly to the hot solution of ligand. The reaction was heated under reflux for 96 hours. After cooled to room temperature, the yellow solid product was collected by filtration, washed with DMF and EtOH. Solvent exchange in MeOH (800 mL) was applied to the crude product for 36 hours at room temperature. The final bright yellow solid of MIL-125(Ti)_NH_2 was collected by filtration and dried at 100 ºC.

UiO-66(Zr)_NH_2: original protocol

To a round bottom flask (100 mL), 2-aminoterephthalic acid (3.62 g, 20.1 mmol) and DMF (50 mL) were added to form a clear solution. Then $ZrCl_4$ (4.66 g, 20 mmol) and HCl (37%, 3.2 mL) were added to the ligand solution. The reaction mixture was heated under reflux with stirring for 24 hours. After cooled down to room temperature, the yellow crude product was filtrated and washed with EtOH, dried at room temperature in air. Then activation of product in MeOH (twice) was applied, leading to the final DMF-free product of UiO-66(Zr)_NH_2.

2. Synthesis of $CaCl_2$-MOF composite

Before choosing the appropriate approach of salt-MOF composite synthesis several experimental conditions were tested. We varied the parameters of synthesis including soaking method, concentration of the inorganic salt solution, the volume of inorganic salt solution used for soaking, soaking time, soaking temperature, cycles of soaking, and drying temperature. The influence of each parameter is given below. Each parameter was studied using one corresponding MOF-matrix and then the results were applied for all studied MOF-matrices. The composites obtained during this study were characterized by thermogravimetric analysis and X-ray analysis, because we aimed to study the influence of different parameters of synthesis on salt content of composite (thermogravimetric analysis) and in the same time control the absence of the salt recrystallized outside of MOF porosity (PXRD). This study allowed us to select the best composites that were fully characterized by means of thermogravimetric analysis, nitrogen sorption porosimetry, PXRD, SEM-EDX and elemental analysis.

The main part of this study was performed on MIL-100(Fe) and MIL-127(Fe). As already mentioned in the article *'Design of salt-Metal Organic Frameworks composites for heat storage applications'* the maximal values of encapsulation capacity for MIL-100(Fe) and MIL-127(Fe) based on theoretical pore volume are 53 and 48% wt. of $CaCl_2$, respectively. However, the real encapsulation capacity of MIL-127(Fe) is even smaller, because $CaCl_2$ could not enter in hydrophilic cages of this MOF with apertures of 3Å.

Soaking method

Two methods of encapsulation were studied. Both of them imply using preliminary dried MOF matrix (3h, 100°C) in one or several encapsulation steps with aqueous solution of $CaCl_2$. In the first method, each encapsulation step was followed by centrifugation and removal of the liquid phase. In this case, the content of encapsulated salt increases very slowly with number of encapsulation steps. It was observed for two MOF-matrices including MIL-100(Fe) and MIL-127(Fe) then controlling the influence of multiple encapsulation steps on final salt content in composite (herein we present the experiments on MIL-127(Fe)).

For the first experiment, our encapsulation steps using $CaCl_2$ solution was applied to MIL-127(Fe) using concentrations (20 wt. %) during 2 hours. The salt content was determined by thermogravimetric analysis (TGA) after 1st, 2nd, 3d, and 4th encapsulation step (Table 1). According to these results, the quantity of incorporated salt does not increase significantly with the number of impregnation steps (the same salt rate in composites MIL-127(Fe)/salt_1-4) (Table 1).

Table 1. Influence of the number of encapsulation step for MIL-127(Fe) based composites

Name	m_{MOF}, [mg]	Concentration of $CaCl_2$ solution [wt. %]	V of $CaCl_2$ solution [ml]	time, [h]	Number of steps	$CaCl_2$ content in the anhydrous composite [wt. %]

MIL-127(Fe)/salt_1	200	20	0.8	2	1	30
MIL-127(Fe)/salt_2	200	20	0.8	2	2	31
MIL-127(Fe)/salt_3	200	20	0.8	2	3	30
MIL-127(Fe)/salt_4	200	20	0.8	2	4	30

The homogeneous distribution of salt in composites prepared by this method was confirmed by SEM-EDS mapping (Figure 1).

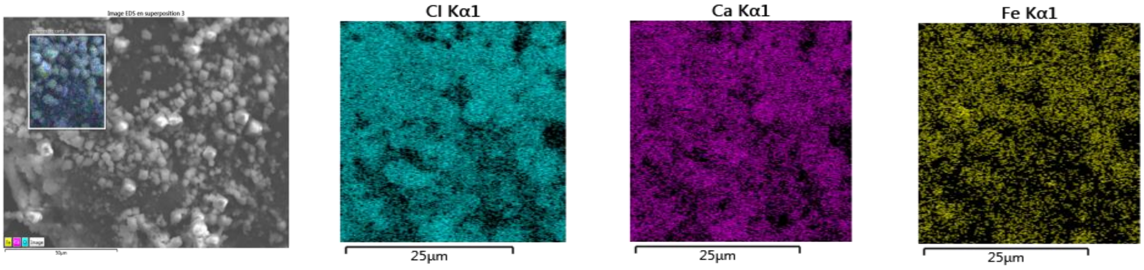

Figure 1. EDS mapping area images of composite MIL-127(Fe)/salt_4

On the contrary, the second method implies drying of composite after each encapsulation step that allows enhancing the salt content during several encapsulation steps resulting in recrystallization of the salt at the surface of MOF. We show, for example, the composite MIL-127(Fe)/salt_5 prepared using second soaking method (Table 2).

Table 2. Preparation of composite MIL-127(Fe)/salt_5

Name	m_{MOF}, [mg]	Concentration of CaCl$_2$ solution [wt. %]	V of CaCl$_2$ solution [ml]	time, [h]	Number of impregnation	CaCl$_2$ content in the anhydrous composite [wt. %]
MIL-127(Fe)/salt_5	250	20	1	0.3	4	70

This method allows a rapid increase of salt content using several encapsulation steps that exceeds the maximum encapsulation capacity of MOF matrix and thus leads to the salt recrystallization at the surface of MOFs particles. This recrystallization is illustrated by PXRD (Figure 2) of the composite MIL-127(Fe)/salt_5.

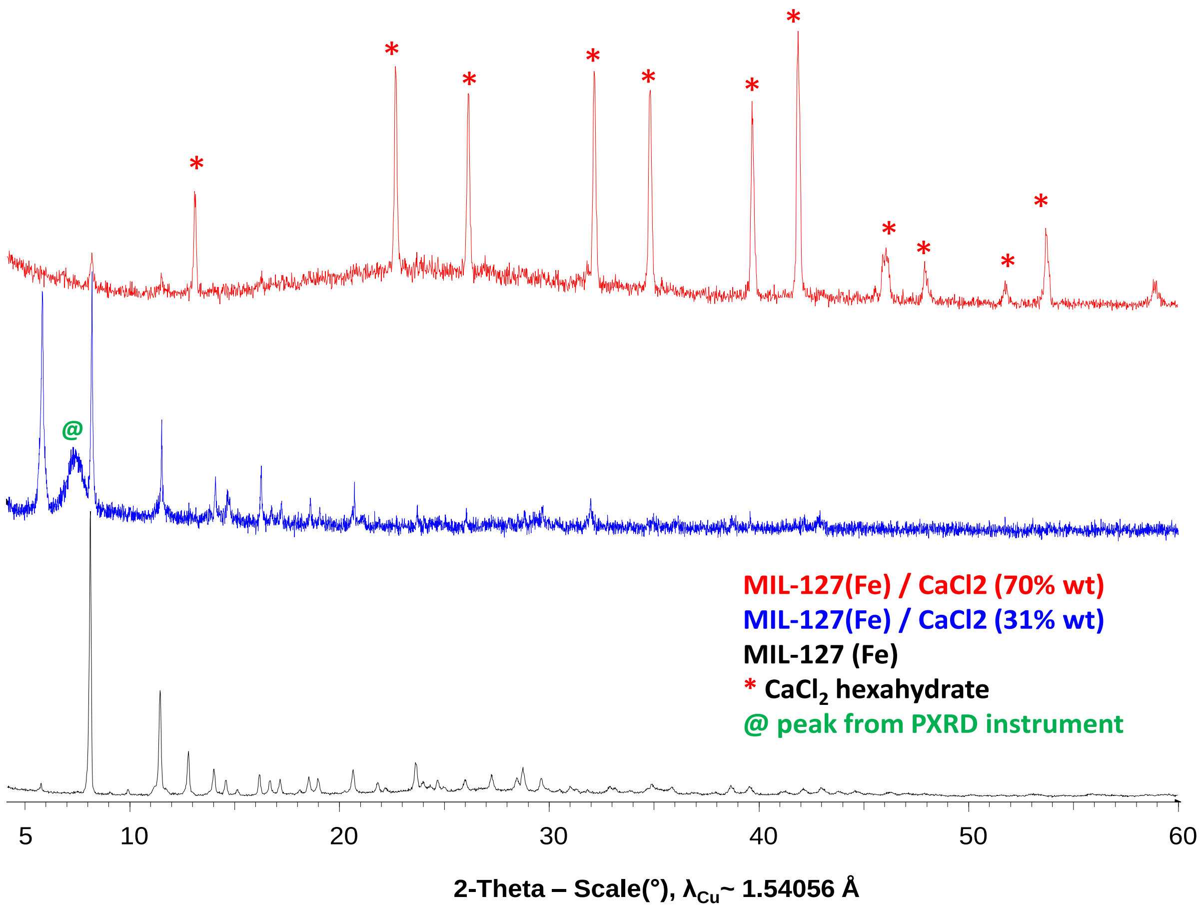

Figure 2. Experimental PXRD patterns of composites of MIL-127(Fe) (in black), MIL-127(Fe)/salt_4 with 31 wt% of salt (in blue) and MIL-127(Fe)/salt_5 with 70 wt% of salt (in red).

In summary, the second soaking method led to fast incorporation of a high salt amount in the porosity of MOFs in comparison with the first method resulting in exceeding of encapsulation capacity of MOF and, thus, salt recrystallization at the surface of MOFs crystals. Therefore, the first method was selected for further preparation of composites using other MOF matrices.

Post-synthesis washing

One of the main objectives in the synthesis of composite is to favor the encapsulation of salt inside the MOF porosity, since the presence of salt at the surface of MOF particle can affect the stability of the composites after multiple adsorption-desorption cycles and lead to a strong decrease of the performance. Post-synthesis rapid washing with H_2O was performed to remove the excess of salt from the surface of MOF particle. In the first experiment, MIL-100(Fe) was used in one encapsulation step using 1 ml of 20-% $CaCl_2$ solution during 0.3 hour followed by rapid washing using Buchner filter. The final $CaCl_2$ amount is given in Table 3.

Table 3. Influence of the post-synthesis washing on the final salt rate in composites

Name	Remark	m_{MOF}, [mg]	time, [h]	Concentration of $CaCl_2$ solution [wt. %]	$CaCl_2$ content in the anhydrous composite [wt. %]
MIL-100(Fe)/salt_1	no washing	250	0.3	20	25
MIL-100(Fe)/salt_2	washing	250	0.3	20	8

Washing after impregnation leads to the removal of the main part of the salt. Post-synthesis rapid washing was also performed using other solvents (EtOH) in order to decrease the solubility of the salt as compared with water solvent. However, it also led to the removal of the main part of the salt and additionally it was difficult to control the final salt rate of composites. Therefore, we selected synthesis without washing for the next preparations of composites.

Temperature and time of soaking

Four different soaking temperatures including room temperature (20 ºC), 40, 50 and 60 ºC were used. The increase of temperature during impregnation process leads primarily to a very high amount of salt in the matrix together with the recrystallization of a significant part of the salt at the surface of MOF particles. Thus, the temperature of soaking was fixed to room temperature.

The increase of soaking time allows enhancing final salt content. For example, the increase of soaking time from 0.3 to 1 hour allows encapsulating 1.5 times more of salt (25 wt% in MIL-100(Fe)/salt_4 versus 37 wt% in MIL-100(Fe)/salt_3).

Name	m_{MOF}, [mg]	Concentration of $CaCl_2$ solution [wt. %]	V of $CaCl_2$ solution [ml]	time, [h]	$CaCl_2$ content in the anhydrous composite [wt. %]
MIL-100(Fe)/salt_3	200	20	0.8	2	37
MIL-100(Fe)/salt_4	200	20	0.8	0.3	25

However, the increase of soaking time above 2 h (4, 12, 24 and 48 hours) did not lead to a significant modification of salt content as compared to 2 hours of soaking. Thus, this soaking time was selected for further synthesis.

Concentration of $CaCl_2$ solution

In order to enhance the salt content in composite using the first soaking method we increased the concentration of salt solution. Since the saturated concentration of $CaCl_2$ in aqueous solution is about 43% in weight percentage, several concentrations lower than 43 wt. %, including 40 wt. %, 35 wt. %, 30 wt. %, 25 wt. %, 20 wt. %, 10 wt. %, and 5 wt. % were applied in the preparation. The highest $CaCl_2$ loading was obtained at 40% concentration of $CaCl_2$ solution. However, concentration of 35% wt. was already sufficient for reaching encapsulation limit for MIL-100(Fe) and MIL-127(Fe) matrices. The concentration below 20% did not lead to important salt content in composites.

The optimal range of concentration was 20-35% resulting in synthesis of two series of composites reported in the article *'Design of salt-Metal Organic Frameworks composites for heat storage applications'*. The control of $CaCl_2$ concentration in solution (20-35%) allows to obtain composites with salt content from 25-50% and 30-48% in case of MIL-100(Fe) and MIL-127(Fe) matrices, respectively (composites are prepared using 0.8 ml of salt solution with soaking time 2h) (Table 4).

Table 4. Influence of the $CaCl_2$ concentration on the Preparation of composites based on MIL-100(Fe) and MIL-127(Fe)

Name	m_{MOF}, [mg]	Concentration of $CaCl_2$ solution [wt. %]	$CaCl_2$ content in the anhydrous composite [wt. %]
MIL-100(Fe)/salt_5	200	25	37
MIL-100(Fe)/salt_6	200	30	42
MIL-100(Fe)/salt_7	200	35	49
MIL-127(Fe)/salt_6	200	20	30
MIL-127(Fe)/salt_7	200	30	38
MIL-127(Fe)/salt_8	200	35	48

From these results, it seems that the $CaCl_2$ concentration of the initial solution is a key parameter that allows tuning the salt content of composites and reaching high salt content closed to the limit of encapsulation capacity (see article *'Design of salt-Metal Organic Frameworks composites for heat storage applications'*) of matrix using only one soaking step (Table 4). This method results in homogeneous distribution of salt in the MOF matrix according to SEM and EDS mapping analyses (see article '*Design of salt-Metal Organic Frameworks composites for heat storage applications*').

Conclusion

In this study we determined the optimal synthesis approach for composites based on MOF and $CaCl_2$. Two series of composites reported in the article '*Design of salt-Metal Organic Frameworks composites for heat storage applications*' were synthesized by following steps:

1) drying the MOF matrix during 3 hours in an oven at 100 °C
2) one step-encapsulation of the $CaCl_2$ in the MOF-matrix using solution of different concentration at room temperature during 2 hour

3) drying of composite at 100°C overnight

3. Synthesis of $SrBr_2$-MOF composites

As mentioned in *Chapter I*, $SrBr_2$ is very promising candidate among inorganic salt owing to its very important energy storage density (630 kWh/m^3). The experimental work aiming at synthesis of $SrBr_2$-MOF composites was initiated. The first results obtained for microporous UiO-66(Zr)_NH_2 and MIL-125(Ti)_NH_2 shows significant recrystallization of the salt outside of MOF matrix even in the case of very diluted initial salt solution. Therefore, we started to prepare composites based on mesoporous MOF, namely MIL-100(Fe). The encapsulation limit of $SrBr_2$ considering density of hexahydrate (adsorption step) for MIL-100(Fe) (theor. pore volume of 1.02 cm^3/g) is ~ 63 wt %.

Prior to encapsulation step, 200 mg of MIL-100(Fe) (S_{BET} = 1818 m^2/g, V_p = 0.815 cm^3/g) was dried during 3 hours in an oven at 100 °C. Then, MIL-100(Fe) was involved in one encapsulation step using 0.8 ml of $SrBr_2$ solution with different concentrations (30, 40, 50 % wt.) during 2 hours (Table 5). The sample was collected following the removal of $SrBr_2$ solution by centrifugation and was completely dried at 100 ºC in an oven for overnight.

Table 5. Composites based on MIL-100(Fe) and $SrBr_2$

Name	Concentration of $SrBr_2$ solution [wt. %]	$SrBr_2$ content in the anhydrous composite [wt. %]	S_{BET} of composite, [m^2/g]	V_{pore} of composite, [cm^3/g]
MIL-100(Fe)/salt_8	30	35	737	0.364
MIL-100(Fe)/salt_9	40	39	577	0.269
MIL-100(Fe)/salt_10	50	45	399	0.199

The content of $SrBr_2$ in these composites is in the range of 35-46% wt. (calculated by thermogravimetric analysis) (Table 5). Powder X-ray diffraction (PXRD) patterns of composites were collected at room temperature. The X-ray diffraction patterns are in good agreement with that of pure MOFs indicating, that the structure of MOFs is preserved in composites, however the strong decrease of relative intensity is clearly evidenced. This phenomenon can be explained by absorption and also by local disorder after incorporation of the salt in mesoporous material. Also PXRD patterns indicate the presents of large amount of salt recrystallized at the surface of MOF in composite MIL-100(Fe)/salt_10 and the presence of smaller amount of the recrystallized salt in composite MIL-100(Fe)/salt_9.

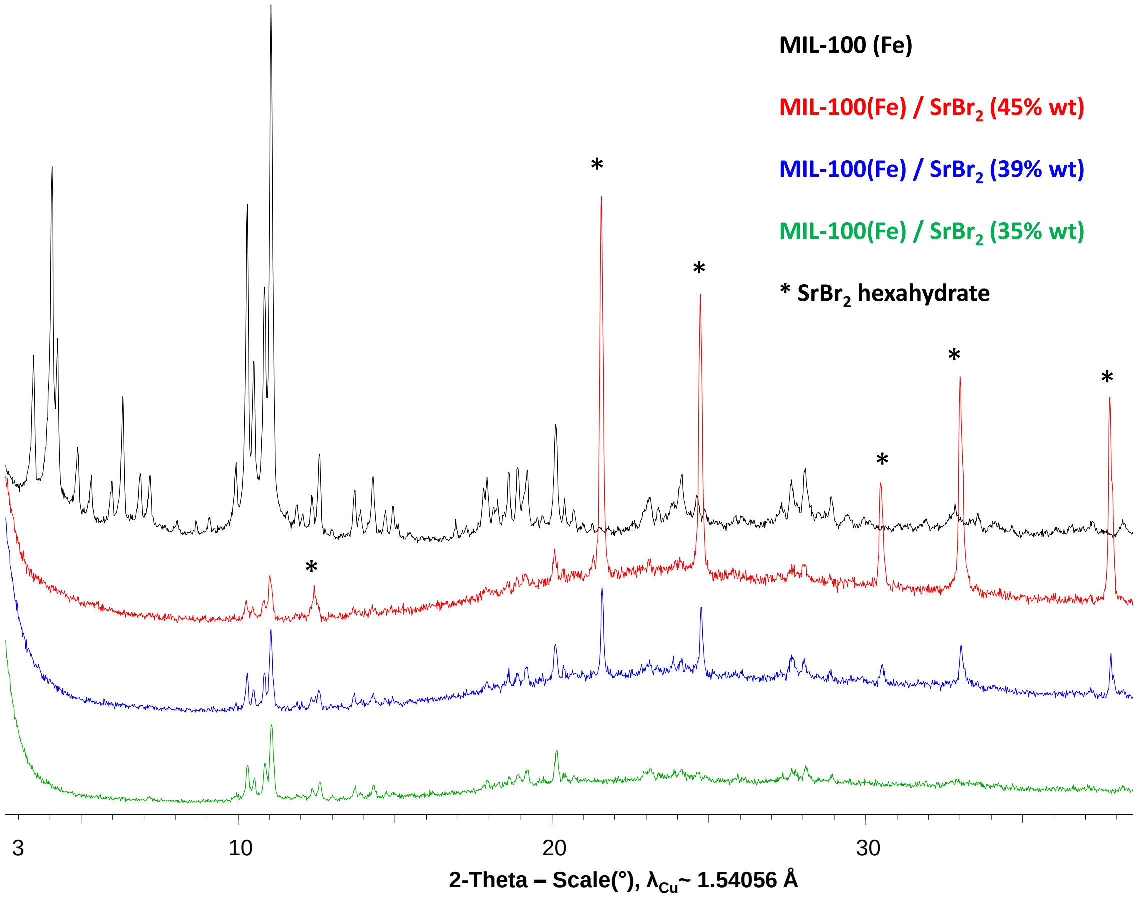

Therefore, the composite MIL-100(Fe)/salt_10 cannot be considered for further water sorption investigation; however the presence of a slight amount of the salt is acceptable if no impact on the stability of composite under numerous adsorption-desorption cycles is evidenced, as observed for the composite MIL-101(Cr)/$CaCl_2$ (62% wt). Indeed, despite a small amount of salt recrystallized at the surface of MIL-101(Cr) particles, only 8% of capacity loss was measured under 10 adsorption-desorption cycles (see article *'Design of salt-Metal Organic Frameworks composites for heat storage applications'*).

Nitrogen sorption porosimetry was also performed for composites based on $SrBr_2$ (Figure 3). The decrease of BET surface area and total pore volume is in agreement with the increase of salt content in the porosity of MIL-100(Fe) (Table 5).

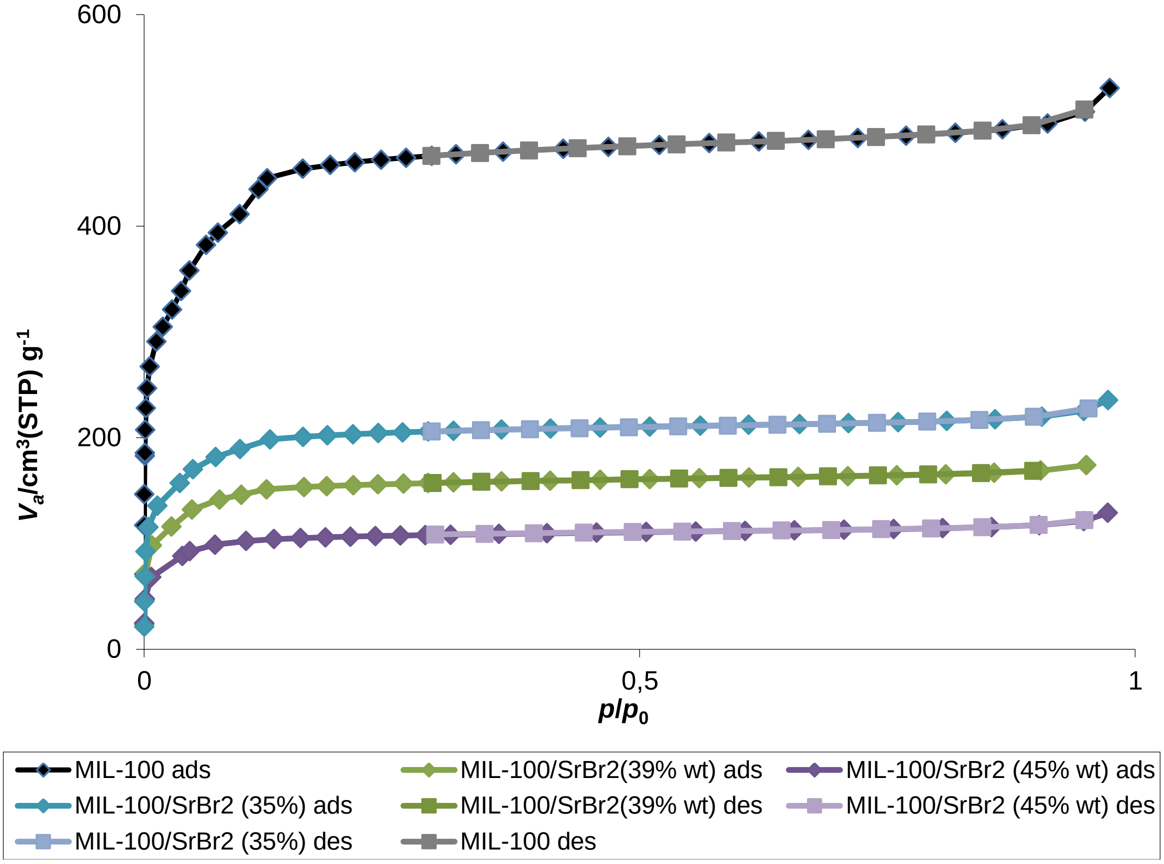

Figure 3. Nitrogen sorption isotherm of MIL-100(Fe) and composite based on $SrBr_2$ and MIL-100(Fe).

The residual pore volume and BET surface area of composite MIL-100(Fe)/salt_8 and MIL-100(Fe)/salt_9 are significantly high that can result in high water sorption capacity of these composites.

The homogeneous distribution of salt in both MIL-100(Fe)/salt_8 and MIL-100(Fe)/salt_9 composites was confirmed by SEM-EDS mapping (Figure 4 and Figure 5, respectively).

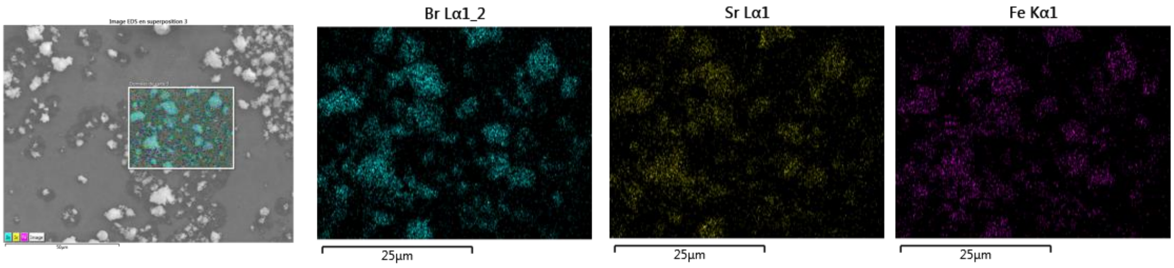

Figure 4. EDS mapping area images of composite MIL-100(Fe)/salt_8

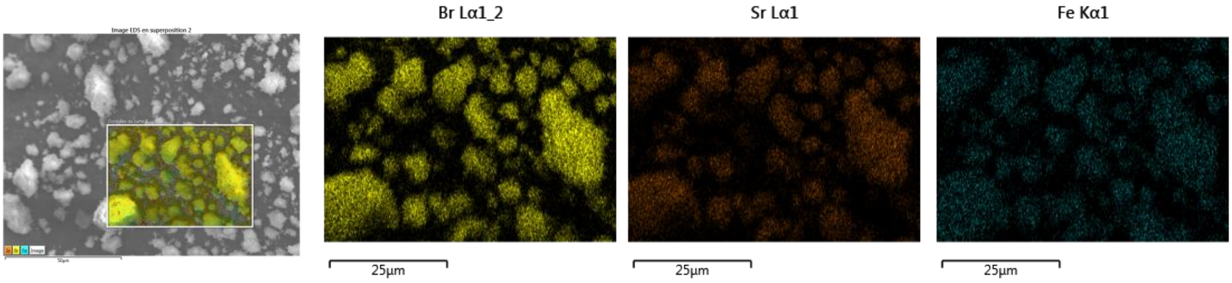

Figure 5. EDS mapping area images of composite MIL-100(Fe)/salt_9

In perspective, the adsorption and cycling loading lift will be measured for these composites in order to investigate their potential for application based on adsorption method.

Chapter IV

Synthesis of the biocompatible and highly stable MIL-127(Fe): from large scale synthesis to particle size control

Chapter IV: Synthesis of the biocompatible and highly stable MIL-127(Fe): from large scale synthesis to particle size control

The work reported in this chapter is described in the format of an article 'Synthesis of the biocompatible and highly stable MIL-127(Fe): from large scale synthesis to particle size control' (DOI: 10.1039/c5ce01864a). It deals with the optimization of the synthesis of MIL-127(Fe) including new synthetic strategies using non-toxic reactants, the control of the crystal size from the micro to the nanoscale, the large-scale production, the investigation of aqueous stability and crystallization kinetic. The author contribution is provided below.

Author contribution

Since MIL-127(Fe), is based on a high valence metal (Fe^{3+}) and an organic linker with four complexing carboxylate groups, it presents a very good aqueous stability.

In the context of my thesis a part of my work was focused on the development of environmentally friendly synthetic route, large-scale production, and preparation of nanoparticles of MIL-127(Fe). The synthesis of microcrystals (28 ± 10 µm) of MIL-127(Fe) in DMF, the study of their water and chemical stability and their kinetics of crystallization were mainly performed by Hubert Chevreau during his PhD.

The first objective of my experimental work deals with the development of new environmentally friendly synthetic strategies of MIL-127(Fe) originally obtained in DMF using hazardous $Fe(ClO_4)_3$ as precursor. Afterwards, the new protocol was applied for their large scale synthesis.

The next objective of this work concerns the control of their particle size at nanoscale. I developed two synthetic routes of MIL-127(Fe) nanoparticles by using microwave-assisted solvothermal method. The first route allows preparing MIL-127_nanoparticles of 214±47 nm with yields of ca. 22% and STY of 165±11 kg.m-3.day-1 during extremely short reaction times (a few minutes). The second route was developed in order to improve the yield and STY. This second synthesis protocol led to higher yields and STY values (31 vs. 22% and 300 vs. 165 $kg.m^{-3}.day^{-1}$, respectively) but produced larger nanoparticles with higher polydispersity in size (i. e. 310±110 nm).

CrystEngComm

Cite this: DOI: 10.1039/c5ce01864a

www.rsc.org/crystengcomm

Synthesis of the biocompatible and highly stable MIL-127(Fe): from large scale synthesis to particle size control

Hubert Chevreau, Anastasia Permyakova, Farid Nouar, Paul Fabry, Carine Livage, Florence Ragon, Alfonso Garcia-Marquez, Thomas Devic, Nathalie Steunou, Christian Serre*, Patricia Horcajada*

Received: ***21st September 2015***, ***Accepted:*** ***1st December 2015***
DOI: 10.1039/c5ce01864a

Controlled-sized crystals, from the nano to the microscale, of the biocompatible and highly stable porous iron(III) 3,3',5,5'-azobenzenetetracarboxylate MIL-127(Fe) MOF have been successfully prepared with very high space-time-yields using different synthetic routes..

Introduction

Metal Organic Frameworks (MOFs) or Porous Coordination Polymers (PCPs), have been extensively studied as a new class of porous solids.[1-3] These crystalline materials are built up from cations and organic polydentate ligands linked by iono-covalent bonds, generating 3D solids with a large structural and chemical diversity,[4] together with an important regular and accessible porosity. Due to these structural properties, MOFs are of great interest for several potential applications such as fluid storage/separation, heat transfer, catalysis[1-3] and, more recently, biomedicine.[5-7] Nevertheless, one of the main drawbacks of MOFs concerns their often low stability towards moisture, an important drawback for applications.[8] Among the strategies reported to overcome the poor water stability of MOFs,[9-12] one of them consists in using water repellent functional groups grafted on the organic moieties either by direct synthesis or by post-synthetic approaches.[13,14] These studies have however revealed a MOF instability attributed to the proximity of the water molecules to the hydrophilic parts of the MOF, *i.e.* M-O or M-N bonds (M= metal) of the inorganic Secondary Building Unit (SBU), leading thus to the material hydrolysis.[8, 9, 11, 12] In addition, the aqueous stability of MOFs is strongly related to the strength of the metal-ligand bond. One way to increase the stability consists of using MOFs based on high valence metals such as tri- (Fe^{3+}, Cr^{3+})[8, 15, 16] or tetra-valent cations (Ti^{4+},Zr^{4+}).[17-22] These have been reported to be less prone to hydrolysis than divalent cations based polycarboxylate MOFs (Zn^{2+}, Cu^{2+}, etc.).[8, 23] Similarly, the nature, basicity and the number of complexing groups seem to strongly impact the chemical stability of MOF.[24] Considering one of the most studied complexing group, *i.e.* carboxylate, the stability of MOFs might also increase with the number of carboxylate functions on the organic linker.

Therefore, a MOF built up from the association of a metal(III) cation and the 3,3',5,5'-azobenzenetetracarboxylate (TazBz) linker such as MIL-127(Fe) or *soc* MOF (Fe, Ga, In) may *a priori* present a good aqueous stability. In addition, the present microporous Fe(III) MIL-127(Fe) or *soc* MOF(Fe) material, originally reported with indium(III) by Eddaoudi *et al*,[25, 26] has shown very interesting features in separation, and catalysis or.[27,28]

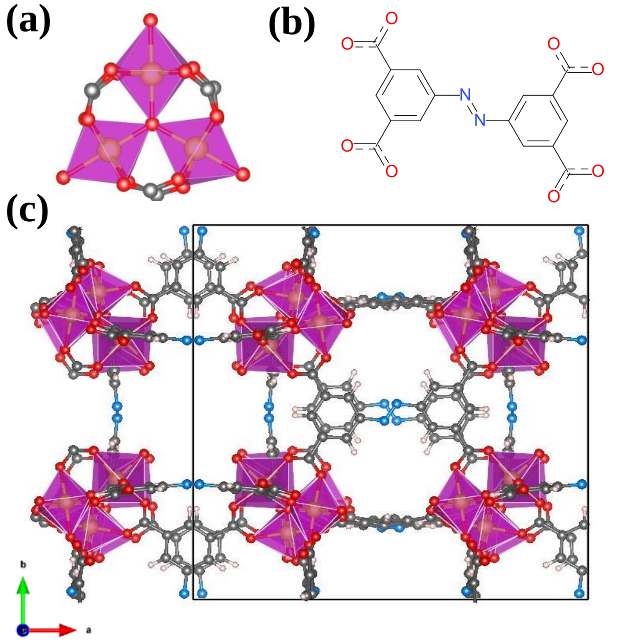

Figure 1: (a) Metal(III) octahedra trimers (b) 3,3',5,5'-azobenzenetetracarboxylic acid (H_4-TazBz) (c) Schematic view of the iron(III) MIL-127 or *soc* MOF (Unit cell in black line). Iron(III) trimers, iron, carbon, oxygen and nitrogen atoms are represented in purple polyhedra, yellow, grey, red and blue, respectively.

This solid is built up from metal(III) octahedra trimers (Figure 1a), sharing one central μ_3-oxo which are linked to six TazBz (Figure 1b) to produce a 3D framework, exhibiting a sodalite (*soc*) topology (Figure 1c) with a noticeable microporosity (S_{BET} ~ 1400 m^2.g^{-1}; V_p ~ 0.7 cm^3.g^{-1}). This structure leads to two types of pores, namely an accessible 1D channel system (~ 6 Å) and cages of *ca.* 10 Å, accessible through very narrow apertures of ~ 3 Å. If the cages are hydrophilic due to the presence of solvent molecules coordinated to the Lewis acid sites, pointing inside the pores, in contrast, the 1D channels exhibit a more hydrophobic character.

MIL-127(Fe) or Fe(III) *soc* MOF analogue, recently reported,[26, 27, 29] has also demonstrated interesting performances in applications such as catalysis, separation and biomolecule (drugs, biologically active gases…) controlled release.[27, 28, 30, 31] Additionally, the low-cost and environmentally friendly nature of the Fe(III) in comparison to In(III), makes the Fe(III) analogue a very promising MOF. However, the previously reported synthetic conditions of the Fe(III) analogue are based on toxic (solvents, reactant) and hardly scalable conditions. Therefore, new synthetic strategies using safer conditions allowing both the control of the crystal size and the large-scale production are prerequisite for future industrial applications.

Herein, we report the controlled-size synthesis, scale-up and full characterization, including a crystallization kinetics study by time-resolved *in situ* energy dispersive X-Ray diffraction (EDXRD), of the iron(III) 3,3',5,5'-azobenzenetetracarboxylate MIL-127(Fe) or Fe *soc* MOF.

Experimental

Synthesis conditions

MIL-127(DMF/HF): 0.33 mmol of iron(III) perchlorate hydrated ($Fe(ClO_4)_3.nH_2O$; 118 mg), 0.33 mmol of 3,3',5,5'-azobenzenetetracarboxylic acid (H_4-TazBz, 119 mg, see supporting (SI) information for the synthesis), 15 mL of dimethylformamide (DMF) and 100 µL of a 5 M hydrofluoric acid solution were introduced in a 23-mL Teflon vessel. The vessel was placed in a metallic Paar bomb and heated at 150°C for 3 days. The obtained brown solid was recovered by centrifugation and washed twice with 10 mL of DMF, then, twice with 20 mL of ethanol and finally, once with 20 mL of distilled water.

MIL-127(DMF): In a round bottom flask containing 500 mL of DMF were introduced 127 mmol of iron(III) chloride hexahydrated ($FeCl_3.6H_2O$; 34.4 g) and 62 mmol of H_4-TazBz (22.2 g). Then, the mixture was stirred under reflux for 16 hrs. The resulting brown solid was recovered by filtration, washed twice with 500 mL of DMF at 50°C, twice with 500 mL of ethanol at 50°C and finally, once with 500 mL of distilled water.

MIL-127(Prop): 5.03 g of NaOH were dissolved in 10 mL of distilled water. 50.8 mmol (18.3 g) of H_4-TazBz suspended in 100 mL of propan-2-ol were added, and the resulting mixture was stirred at room temperature. In parallel, 101.9 mmol (28 g) of $FeCl_3.6H_2O$ were dissolved in 80 mL of propan-2-ol in a flask under reflux. In the last step, both solution were mixed, and the resulting slurry/solution was mechanically stirred under reflux for 24 hours using a 400 mL-close vessel reactor. A crystalline powder was recovered by filtration, washed with 8 L of distilled water and finally with 8 L of ethanol.

MIL-127_NPs1: 0.66 mmol of $FeCl_3.6H_2O$ (178.4 mg) and 0.63 mmol of H_4-TazBz (226 mg) were dissolved under stirring in 20 mL of propan-2-ol. This solution was heated in a microwave oven at 130°C (400 W) for 15 min, with a heating ramp of 55°C *per* min. The obtained solid was cooled down, then recovered by centrifugation (10500 rpm, 15 min) and washed twice with 40 mL of propanol-2-ol, twice with 40 mL of ethanol and finally, with 20 mL of distilled water.

MIL-127_NPs2: 0.9 mmol of $FeCl_3.6H_2O$ (239.5 mg) and 0.6 mmol of H_4-TazBz (222 mg) were dissolved under stirring in a solution of 29 µL of triethylenamine (0.2 mmol) in 20 mL of propan-2-ol. The resulting solution was heated in a microwave oven at 130°C (400 W) for 15 min, with a heating ramp of 55°C *per* min. The obtained solid was cooled down, recovered by centrifugation (10500 rpm, 15 min) and washed twice with 40 mL of propanol-2-ol, twice with 40 mL of ethanol and finally, with 20 mL of distilled water.

All solids were fully characterized by powder X-ray diffraction (PXRD), thermal X-ray Powder diffraction (TXRPD), thermogravimetric analysis (TGA), Fourier transform infrared spectroscopy (FT-IR) and N_2 sorption measurements, and scanning and/or transmission electron microscopy (SEM and TEM). In addition, nanoparticles were also characterized by dynamic light scattering (DLS) and ξ-potential (for further details see SI).

Time resolved *in situ* energy-dispersive *X-ray* diffraction (EDXRD)

Time-resolved *in situ* EDXRD experiments were performed at beam line F3 at light source HASYLAB facility (DESY, Hamburg, Germany). The beam line receives an incident white synchrotron radiation from a bending magnet with an energy within the 8–56 keV range, exhibiting a maximum photon flux at 16 keV. Diffracted radiation was recorded using a fixed angle solid-state germanium detector positioned at around 2.92 ° and data accumulated in 60 s. From EDXRD, the extent of crystallization α was extracted by integration of the most intense (200) Bragg peak (see Figure S17 of SI). Although the second peak corresponding to (022) Bragg reflection can be observed, its rather limited signal/noise ratio precludes any accurate integration. Bragg peak integration was performed using "calf3" (software offered and available for free at beamline F3, private copy by A. Rothkirch/DESY) and "Peak Analyser" contained in the software Origin (OriginLab, Northampton, MA). Solvothermal reactions were performed in sealed borosilicate glass tubes Schott® (H*diam. 100 * 12 mm) with an inner diameter of 9 mm and a volume of 7 mL (for further details see SI).

Water stability

In order to evaluate the water stability of MIL-127, 30 mg of activated MIL-127(DMF) were introduced in a 10 mL round bottom flask containing 3 mL of distilled water (pH = 6.5), followed by stirring at room temperature (RT) or under reflux for 16 h. Similar experiments have been performed in basic media (pH = 8 and 12) by adding NaOH or under acidic conditions (pH = 2) by adding HCl.

Results and discussion

First, the chemical stability of MIL-127 was investigated under severe conditions (boiling water at different pH). Then, the synthesis conditions of MIL-127 were optimized at the laboratory scale in order to achieve a reproducible, environmentally-friendly and scalable production. The synthesis of this solid was optimized at the multigram scale avoiding the use of hazardous

$Fe(ClO_4)_3$, previously used as iron precursor (this solid will be further denoted MIL-127(DMF)). Then, to develop an environmentally friendly synthetic route, compatible with biomedical applications, among others, MIL-127 was successfully prepared using propan-2-ol as solvent (denoted MIL-127(Prop)). A time-resolved *in-situ* EDXRD study of the crystallization of MIL-127(DMF) and MIL-127(Prop) was then performed at the beamline Hasylab (DESY, Hamburg, Germany) in order to get a better understanding of its formation process. Finally, a careful control of the MIL-127 particle size was established, leading either to a 30 microns-sized well-crystallized solid (further denoted MIL-127(DMF/HF)) or homogeneous submicronic particles of *ca.* 300 nm, which paves the way for its use in nanoscience (denoted as MIL-127_NPs).

Chemical stability studies

If XRPD shows a complete amorphization of MIL-127(Fe) under highly basic conditions (pH = 12 at RT), its crystalline structure remains intact under acidic or neutral conditions, even after exposition to boiling water for 16 h at pH ~ 8 (Figure S2). In addition, BET surface areas of MIL-127 after the pH 3 or 8 treatments at RT were *ca.* 1210 or 1320 $m^2.g^{-1}$, respectively (Figure S3). The value dropped to 155 $m^2.g^{-1}$ after the treatment at pH 12, in agreement with the higher degradation rate evidenced by XRPD. Under reflux, the porosity decreases as the pH increases (S_{BET} ~ 1150, 1000, 740 and 450 $m^2.g^{-1}$ at final pHs of 2, 6.5, 8 and 12, respectively; Figure S2). This is probably due to the formation of iron oxides/hydroxides when the pH increases (see Pourbaix diagram).[32] At lower pH, (*i.e.* final pHs of 6.5 and 2), a slight degradation of the framework might take place, as evidenced by the reduction of the BET surface values. The presence of residual Na^+ or Cl^- ions resulting from the addition of NaOH or HCl solutions could also be partially involved in the porosity decrease, as confirmed by energy-dispersive X-ray spectroscopy analysis (EDX; Na/Fe = 0.08 at pH = 12 or Cl/Fe = 0.12 at pH = 3).

Overall, MIL-127 exhibits a rather good stability towards harsh aqueous conditions (boiling water) in comparison to other reported MOFs that rapidly degrade under air moisture.[7,23] For instance, as a tetracarboxylate iron MOF, the MIL-127 exhibits a higher chemical stability than the tricarboxylate iron MIL-100 (degradation of 16% after 60 days *vs.* 44% after 30 days in boiling aqueous solution, respectively).[33]

Solvothermal synthesis of highly crystalline MIL-127.

MIL-127 was successfully obtained as large micrometric cubic crystals of 28 ± 10 µm (number of crystallites *n* = 227) through a solvothermal route in presence of the mineralizing agent HF (MIL-127(DMF/HF); see SI; Figure 2 and Table 1). According to the Lebail refinement of the PXRD patterns, MIL-127(DMF/HF) is isostructural to the indium(III) *soc* MOF (Figures S4 and S5).[25] Although both MOFs present the same cubic space group (P-43n), a slightly shorter cell parameter is obtained for MIL-127 (21.896(3) *vs.* 22.456(1) Å), in agreement with the smaller size of iron(III) cation. TGA (theo. and obs. Fe_2O_3 30.4 *vs.* 28.6 wt%) and elemental analysis (theo: C/Fe = 8.0; N/Fe = 1.0; F/Fe = 0.3 obs: C/Fe = 8.3; N/Fe = 1.2; F/Fe = 0.3) indicate that the chemical composition of the activated solid is in good agreement with the theoretical values based on the structure formula $Fe_3OF(C_{16}N_2O_8H_6)_{1.5}(H_2O)_3.nH_2O$. TXRPD shows that MIL-127(DMF/HF) is thermally stable up to 250°C nder air atmosphere (Figure S6 and S7). In addition, an increase in the Bragg peak intensity observed up to around 100°C can be explained by the desolvation of the solid. It is noteworthy that after activation no significant amount of DMF or non-coordinated ligand (H_4-TazBz) can be detected by FT-IR spectroscopy (Figure S8). The N_2 sorption isotherm, measured at 77 K on the activated solid after outgassing at 200°C overnight, is characteristic of a microporous solid (Figure S9), with a high BET (Brunauer-Emmett-Teller) surface area of *ca.* 1400 $m^2.g^{-1}$ and a pore volume of 0.7 $cm^3.g^{-1}$, in agreement with the porosity of the indium analogue (Table 1).

Scale-up of MIL-127

Despite the very good crystallinity and purity of the obtained MIL-127(DMF/HF), only a low amount (< 100 mg) can be prepared from the solvothermal-HF route after a considerably long reaction time (3 days). In addition, the use of corrosive acids (HF) and the synthesis conditions (*i.e.* autogenous pressure) make this synthetic route inappropriate for a larger scale production. Although a more favorable synthetic route using a round-bottom flask has been previously reported,[27] the use of $Fe(ClO_4)_3.nH_2O$ as the iron precursor, is irrelevant due to its explosive character. Therefore, the synthetic conditions were adapted to a more suitable multigram scale-up of MIL-127 at ambiant pressure and avoiding the use of hazardous reactants. A first route was developed using $FeCl_3.6H_2O$ in DMF, leading to 21 g of activated solid (MIL-127(DMF)) after only 16 h instead of < 100 mg after 3 days. A Lebail refinement of the PXRD pattern of MIL-127(DMF) confirms both the space group and cell parameters of the MIL-127 structure type (Figure S10). Interestingly, in absence of HF during the synthesis, a slight chlorine content was found in the solid (Cl/Fe = 0.1), most of the counterions being OH^- anions. Moreover, the elemental analysis and TGA (Figure S11) of the activated solid is in good agreement with the chemical formula $Fe_3O(OH)_{0.88}Cl_{0.12}(C_{16}N_2O_8H_6)_{1.5}(H_2O)_3.nH_2O$ (theo: C/Fe = 8.0; N/Fe = 1.0; Cl/Fe = 0.04 *vs.* obs: C/Fe = 9.0; N/Fe = 1.0; Cl/Fe = 0.04). The BET surface area, calculated from N_2 isotherms at 77 K, is similar to that the observed for MIL-127(DMF/HF) (~ 1300 *vs.* ~1400 $m^2.g^{-1}$; Figure S13). The SEM images of MIL-127(DMF) (Fig. 1) show quite large and polydisperse cubic shaped microcrystals (2 ± 1 µm; *n* = 194; Table 1).

For an optimal scale-up production, both the yield and the mass of MOF formed *per* volume of the reactor and time ($kg.m^{-3}.day^{-1}$) or space-time-yield (STY) are parameters of prime importance,[34] which has to be the highest as possible. Since both yield and STY values are significantly high (~60% and ~60 $kg.m^{-3}.day^{-1}$; Table 1), this synthesis procedure might be attractive for the MIL-127 mass production.

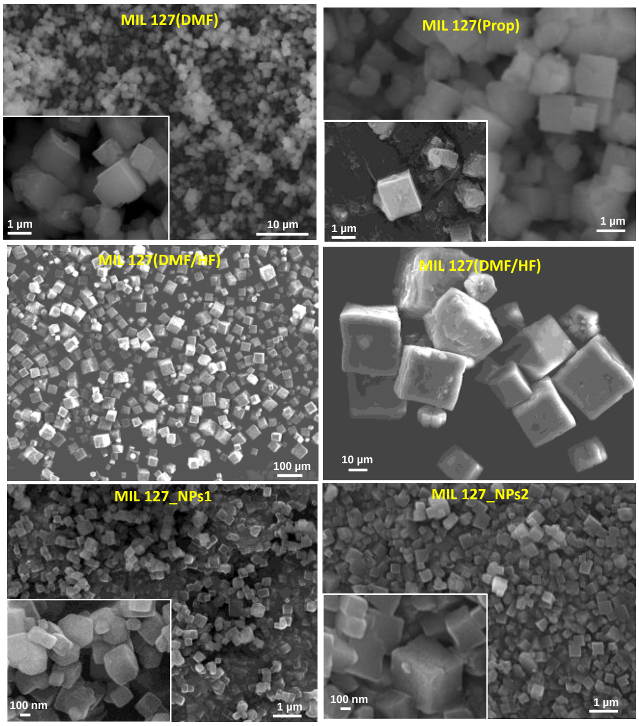

Figure 2: FEG-SEM images of MIL-127(DMF, DMF/HF, Prop) and _NPs1 and _NPs2.

Biocompatible and environmentally friendly MIL-127 synthetic conditions

An important drawback for the above-mentioned low pressure synthesis of MIL-127 concerns the use of the toxic solvent DMF. Thus, we investigated the effect of different solvents using the high-throughput method developed by Stock *et al.*[35] Indeed, this method allows a rapid screening of a large number of reaction conditions but using very small amount of reactants. In particular, the synthesis of MIL-127 was carried out by using 8 polar or non-polar solvents (*i.e.* water, ethanol, methanol, toluene, cyclohexane, cyclohexanol, acetonitrile and propan-2-ol) in presence or not of HCl or NaOH. Only recrystallized linker or amorphous products are obtained when using water or cyclohexanol regardless of the presence of additives (Table S3 and Figure S24). Moreover, except for acetonitrile and propan-2-ol, MIL-127 can be only formed in presence of slightly basic solution. All other conditions led only to amorphous phases or recrystallized H_4-Tazbz. This is probably related with the poor solubility of the ligand in these solvents (<0.2 in water, toluene, cyclohexanol and 0.4, mmol.mL^{-1} in cyclohexane; from experimental solubility tests). Despite a higher solubility in ethanol and methanol (~1.34 and 3.1 mmol.mL^{-1}, respectively), the formation of MIL-127 solid was only detected upon the addition of a base, such as NaOH, which might favor the formation of MIL-127 by enhancing the reactivity of the ligand via its deprotonation. Taking into account the rather good crystallinity of MIL-127 synthesized in propan-2-ol, , this solvent of low toxicity (lethal oral dose 50-LD_{50} (rat) = 5.0 g.kg^{-1})[36] and low cost was selected to allow the optimization of the ecofriendly large-scale synthesis of MIL-127 solid. Note that Eddaoudi *et al.*[29] proposed an alternative synthesis using low-toxic dimethylsulfoxide as solvent (oral LD_{50} (rat) = 14.5 g.kg^{-1}),[37] however requiring the use of other harmful reactant such as tert-butylamine (oral LD50 (rat) = 0.078 g.kg^{-1}).[36]

Table 1. Reactant concentration, yield and STY of the MIL-127s, together with the BET surface areas.

	Size (µm) (PdI)*	[Fe] (mM)	[H_4-TazBz] (mM)	Time (h)	Yield (%)	STY (kg.m^{-3}.day^{-1})	S_{BET} m^2.g^{-1}
MIL-127 (DMF/HF)	28±10$^{\phi}$	22	22	72	26±3	0.5	1400±50
MIL-127 (DMF)	2±1$^{\phi}$	254	124	16	57±4	61±1	1310±60
MIL-127 (Prop)	0.9±0.3$^{\phi}$	500	252	24	86±4	115±3	1350±50
MIL-127 _NPs1	0.25±0.05 (0.1) 0.21±0.05$^{\phi}$	45	31	0.25	22±2	165±11	1360±40
MIL-127 _NPs2	0.40±0.20 (0.3) 0.30±0.11$^{\phi}$	45	31	0.25	31±3	300±15	1390±50

*PdI (polydispersity index)
$^{\phi}$ from FEG-SEM observation

Starting from $FeCl_3 \cdot 6H_2O$, H_4-Tazbz and NaOH, MIL-127(Prop) was successfully obtained as micrometric particles (0.91±0.26 µm (*n* = 125)) by using the cheap and environmentally friendly propan-2-ol at room pressure (P = 1 bar). The high crystallinity and purity of the resulting MIL-127(Prop) sample was confirmed by PXRD, TGA, FT-IR, elemental analysis and N_2 adsorption (Figures S14-S17). In particular, BET surface area is fully consistent with that obtained for the previous MIL-127 solids (~ 1350 m^2.g^{-1}; Table 1). On the whole, both elemental analysis (theo: C/Fe = 8.0; N/Fe = 1 *vs.* obs: C/Fe = 6.5; N/Fe = 0.8; Cl/Fe = 0.1) and TGA (theo. and obs. Fe_2O_3: 30.5 *vs.* 31.2 wt%) (Figure S15) are in agreement with the proposed structure formula $Fe_3O(OH)_{0.66}Cl_{0.33}$ $(C_{16}N_2O_8H_6)_{1.5}(H_2O)_3.nH_2O$.

Despite of a similar obtained yield and a slightly longer reaction time (1 day *vs.* 16 h), the scale-up performed in propan-2-ol solvent (MIL-127(Prop)) exhibits an almost 50% higher STY value than that carried out using DMF (MIL-127(DMF); Table 1). This value is comparable to other reported MOFs, currently commercialized by BASF.[35, 38] This important increase of the STY value is made possible by doubling the concentration of the starting solution. Thus, this safe and environmentally friendly synthetic route represents a promising alternative method for the MIL-127 mass production.

Control over the particle size: towards MIL-127 nanoparticles.

Time resolved *in situ* EDXRD study of the solvothermal crystallization of MIL-127(DMF) and MIL-127(Prop).

Time resolved *in situ* EDXRD experiments were performed on both MIL-127(DMF)and MIL-127(Prop) in order to get insights into the mechanism of the crystallization of MIL-127 and thus, derive general trends of their nucleation and growth processes. As expected, the higher the temperature, the faster the reaction (Figure 3). In both cases, syntheses could be achieved within one hour when higher temperature (T > boiling T) were used. Moreover, according to the 3D crystallization plots (Fig. S18 and

S19), no secondary crystalline phases can be detected, indicating the high purity of MIL-127. In order to gain a better understanding of the reaction process, the surface of the most intense Bragg reflection (002) was integrated (see experimental details in SI) and then, its evolution fitted by applying two different models: *(i)* the model of Avrami-Erofe'ev (AE),[39, 40] one of the most frequently used models for the analysis of hybrid materials crystallization, which was applied through the Sharp and Hancock approach (SH),[41] that consists in a linear regression of the equation (see SI; Figure S20) and *(ii)* the model of Gualtieri,[42] (see SI Figure S22 and S23), recently introduced into the MOF crystallization field, which allows a detailed analysis of the nucleation mechanism and thus is of crucial interest for the synthesis of nanoparticles. The combination of these two models, recently applied to several MOFs including ZIF-8,[43, 44] CAU-1,[45] MOF-14,[46] a lithium thiophene-dicarboxylate,[47] MIL-53,[48] HKUST-1,[49] and more recently by some of us for UiO-66 and analogues,[50, 51] has already provided important information on their crystallization mechanisms. The theory of these models and their application to the particular case of MIL-127(DMF) and (Prop) are provided in SI.

The activation energies E_a of the crystallization reaction of MIL-127(DMF) and (Prop) were extracted from the AE equation combined with the Arrhenius equation. The Ea estimated for MIL-127(DMF) and (Prop) are 102±10 and 92±24 $kJ.mol^{-1}$, respectively (Figure S21) which are among the highest E_a reported so far for MOFs (typically in the range 22 – 136 $kJ.mol^{-1}$).[43-45, 50-52] Further information could be obtained from Avrami exponent *n*, whose value close to 0.6 for MIL-127(DMF) indicates that the growth process is certainly the limiting step of the MIL-127(DMF) crystallization, while those for MIL-127(Prop) between 0.9 and 1.6 indicates a nucleation-limited rate reaction (Table S1). As the AE model does not allow a clear differentiation between the nucleation and growth steps,[53] the model of Gualtieri, introducing a second function related to the nucleation, is generally also applied.[42] It could thus be observed that the nucleation rate constant k_n is significantly higher than the growth rate constant k_g for MIL-127(DMF) but lower for MIL-127(Prop), which is in good agreement with the AE model (Table S2). From the Gualtieri model, one can calculate the nucleation probability P_N during the reaction which shows, in both solvent, a significant overlapping of the nucleation and growth process, indicating a continued formation of nucleation sites late into the rise of crystallites. This is in good agreement with the large polydispersity of the MIL-127 particle size (Table 1 and Figure 3). Nonetheless, at the beginning of the reaction, P_N is higher than 0.5 in DMF but lower than 0.4 in propan-2-ol, showing how the nucleation is enhanced in DMF but rate-limited in propan-2-ol (Figure S22 and S23). This can be explained by the solubility of the linker, which affects the crystallization kinetics, as recently reported.[50, 51] Thus, the TazBz solubility is 8.5 times higher in DMF (6.42 mmol/L) than in propan-2-ol (0.75 mmol/L) at room temperature. Also, it is noteworthy that the constant *b* in the Gualtieri model, which reflects the nature of the nucleation (≤ 15: heterogeneous nucleation, ≥ 20: autocatalytic nucleation)[42] decreases with increasing temperature, suggesting an homogeneous nucleation at low temperature, but an heterogeneous nucleation at high temperature.

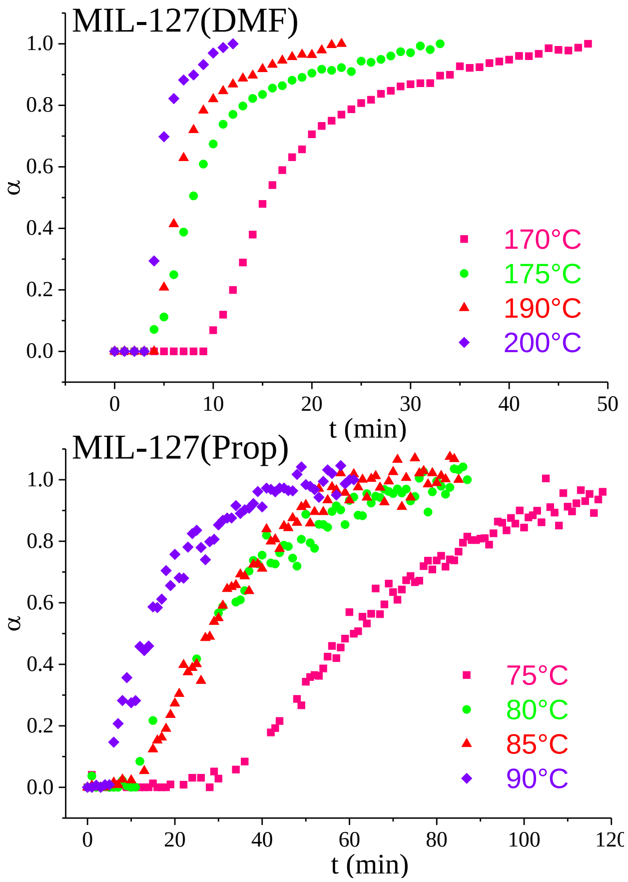

Figure 3: Plots of extent of crystallization (α) against time (t) obtained by integration of the (002) Bragg peak of the MIL-127(DMF) and MIL-127(Prop) synthesized at different temperatures. Crystallization curves were fitted with sigmoidal functions just to have an image of the line progression.

Synthesis of MIL-127_NPs

Crystallization kinetics of the MIL-127 provides valuable information about nucleation and growth, being very useful for the preparation of MIL-127 nanoparticles. Indeed, the absence of any intermediate crystalline phase and the long nucleation step taking place at the early stage of the synthesis are crucial points for the synthesis of monodispersed nanoparticles. The nucleation step could be shortened through a microwave-assisted heating, which is known to produce a large amount of nuclei at very short times.[45] Thus, the fast crystal nucleation kinetics of the microwave-assisted hydro/solvothermal synthesis method, associated with a more homogeneous heating, has been previously applied for the preparation of high yields of non-toxic monodispersed submicron and nanometer-sized iron(III) carboxylate MOFs[50, 51, 54, 55] in very short times (15 min), which is essential when considering its up-scale preparation.[56-58] Thus, considering the extremely short reaction times (few minutes), small and monodispersed MIL-127_NPs (MIL-127_NPs1) of 250±50 nm and polydispersity index of PdI = 0.1, were obtained using the microwave route (see experimental section) together with a yield of *ca.* 22% and a STY of 165±11 $kg.m^{-3}.day^{-1}$. These results are consistent with the SEM-FEG observations, in which small well-faceted cubic nanoparticles of 214±47 nm (*n* = 212; Figure 2 and Table 1) are observed. Note here that Eddaoudi *et al.*[29] reported both micronic particles (~1 µm) and micrometric hollow colloidosomes (~4 and ~15 μm) made up from nanoparticle of the MIL-127(In, Ga) (~300 nm) using an emulsion templating approach, with however no information about the yield.

In an attempt to improve the yield and STY, the nanoparticles were also synthesized in presence of a base (MIL-127_NPs2). Although the addition of the triethylenamine (oral LD$_{50}$ (rat) = 0.46 g.kg^{-1})[59] led to higher yields and STY values (31 *vs*. 22% and 300 *vs*. 165 kg.m^{-3}.day^{-1}, respectively), larger and polydispersed nanoparticles were obtained, as evidenced by both DLS and FEG-SEM measurements (400±200 nm; PdI = 0.3 and 310±110 nm with *n* = 264, respectively; Table 1). This is probably related to the faster kinetics as a consequence of the initial deprotonation of the linker.

PXRD patterns of MIL-127_NPs1 and MIL-127_NPs2 confirm that crystalline particles of MIL-127 have been produced (Figure S25) with, however, a slight peak broadening consistent with the smaller crystal size. Similarly, TGA (Figure S26) and elemental analysis are in good agreement with the structure formula $Fe_3O(OH)_{0.66}Cl_{0.33}(C_{16}N_2O_8H_6)_{1.5}(H_2O)_3.nH_2O$ (theo: C/Fe = 8.0; N/Fe = 1.0 *vs*. obs: C/Fe = 8.0; N/Fe = 1.0; Cl/Fe = 0.1). In addition, both MIL-127_NPs1 and MIL-127_NPs2 possess a BET surface area fully comparable with the bulk material (~ 1400 $m^2.g^{-1}$; Figure S28).

Conclusions

The biocompatible and highly stable iron(III) tetracarboxylate MIL-127(Fe) solid has been successfully prepared through an easily-scalable and environmentally friendly route based on a simple round-bottom flask synthetic approach, which allows achieving important yields and STY, compatible with mass production. In addition, *in situ* EXRPD studies allowed us to gain insights over the crystallization mechanisms in play, paving the way for a control of the particle size from the micro to the nanoscale, leading monodispersed nanoparticles through an efficient and biofriendly microwave-assisted solvothermal method.

Acknowledgments

The research leading to these results has received funding from the European Community's Seventh Framework Program (FP7/2007-2013; n° 228862), UVSQ and CNRS fundings. The authors gratefully acknowledge DESY synchrotron facilities for award of beamtime at F3 beamline HASYLAB, Dr. A. Rothkirch (DESY) for the software support, the Christian-Albrechts-Universität team of Prof. W. Bensch (Kiel, Germany) to lending us the *in situ* furnace device and the group of Prof. N. Stock, especially M. Feyand, for their helpful assistance using the beamline.

Notes and references

[a] *Institut Lavoisier, UMR CNRS 8180, Université de Versailles Saint-Quentin-en-Yvelines, 45 avenue des États-Unis, 78035 Versailles cedex, France Fax: +33 139254452; Tel: +33 139254371; E-mail: patricia.horcajada @uvsq.fr* and *christian.serre@uvsq.fr*

† Electronic Supplementary Information (ESI) available: [details of any supplementary information available should be included here]. See DOI: 10.1039/b000000x/

1 J. R. Long and O. M. Yaghi, *Chem. Soc. Rev.*, 2009, **38**, 1213-1214.

2 H.-C. Zhou, J. R. Long and O. M. Yaghi, *Chem. Rev. (Washington, DC, U. S.)*, 2012, **112**, 673-674.

3 H.-C. J. Zhou and S. Kitagawa, *Chem. Soc. Rev.*, 2015, **43**, 5415-5418.

4 D. J. Tranchemontagne, J. L. Mendoza-Cortes, M. O'Keeffe and O. M. Yaghi, *Chemical Society Reviews*, 2009, **38**, 1257-1283.

5 J. Della Rocca, D. Liu and W. Lin, *Acc. Chem. Res.*, 2011, **44**, 957-968.

6 P. Horcajada, R. Gref, T. Baati, P. K. Allan, G. Maurin, P. Couvreur, G. Férey, R. E. Morris and C. Serre, *Chem. Rev. (Washington, DC, U. S.)*, 2012, **112**, 1232-1268.

7 F. Novio, J. Simmchen, N. Vázquez-Mera, L. Amorín-Ferré and D. Ruiz-Molina, *Coord. Chem. Rev.*, 2013, **257**, 2839-2847.

8 J. J. Low, A. I. Benin, P. Jakubczak, J. F. Abrahamian, S. A. Faheem and R. R. Willis, *J. Am. Chem. Soc.*, 2009, **131**, 15834-15842.

9 J. A. Greathouse and M. D. Allendorf, *J. Am. Chem. Soc.*, 2006, **128**, 10678-10679.

10 Y. Fu, D. Sun, Y. Chen, R. Huang, Z. Ding, X. Fu and Z. Li, *Angew. Chem., Int. Ed.*, 2012, **51**, 3364-3367.

11 P. M. Schoenecker, C. G. Carson, H. Jasuja, C. J. J. Flemming and K. S. Walton, *Ind. Eng. Chem. Res.*, 2012, **51**, 6513-6519.

12 K. Schrock, F. Schroder, M. Heyden, R. A. Fischer and M. Havenith, *Phys. Chem. Chem. Phys.*, 2008, **10**, 4732-4739.

13 J. W. Yoon, Y.-K. Seo, Y. K. Hwang, J.-S. Chang, H. Leclerc, S. Wuttke, P. Bazin, A. Vimont, M. Daturi, E. Bloch, P. L. Llewellyn, C. Serre, P. Horcajada, J.-M. Grenèche, A. E. Rodrigues and G. Férey, *Angew. Chem., Int. Ed.*, 2010, **49**, 5949-5952.

14 J. Lee, O. K. Farha, J. Roberts, K. A. Scheidt, S. T. Nguyen and J. T. Hupp, *Chem. Soc. Rev.*, 2009, **38**, 1450-1459.

15 E. Soubeyrand-Lenoir, C. Vagner, J. W. Yoon, P. Bazin, F. Ragon, Y. K. Hwang, C. Serre, J.-S. Chang and P. L. Llewellyn, *J. Am. Chem. Soc.*, 2012, **134**, 10174-10181.

16 G. Akiyama, R. Matsuda, H. Sato, A. Hori, M. Takata and S. Kitagawa, *Microporous Mesoporous Mater.*, 2012, **157**, 89-93.

17 J. H. Cavka, S. r. Jakobsen, U. Olsbye, N. Guillou, C. Lamberti, S. Bordiga and K. P. Lillerud, *J. Am. Chem. Soc.*, 2008, **130**, 13850-13851.

18 M. Dan-Hardi, C. Serre, T. Frot, L. Rozes, G. Maurin, C. Sanchez and G. Férey, *J. Am. Chem. Soc.*, 2009, **131**, 10857-10859.

19 Y. Fu, D. Sun, Y. Chen, R. Huang, Z. Ding, X. Fu and Z. Li, *Angewandte Chemie International Edition*, 2012, **51**, 3364-3367.

20 V. Guillerm, F. Ragon, M. Dan-Hardi, T. Devic, M. Vishnuvarthan, B. Campo, A. Vimont, G. Clet, Q. Yang, G. Maurin, G. Férey, A. Vittadini, S. Gross and C. Serre, *Angewandte Chemie International Edition*, 2012, **51**, 9267-9271.

21 M. Kandiah, S. Usseglio, S. Svelle, U. Olsbye, K. P. Lillerud and M. Tilset, *J. Mater. Chem.*, 2010, **20**, 9848-9851.

22 C. Zlotea, D. Phanon, M. Mazaj, D. Heurtaux, V. Guillerm, C. Serre, P. Horcajada, T. Devic, E. Magnier, F. Cuevas, G. Ferey, P. L. Llewellyn and M. Latroche, *Dalton Trans.*, 2011, **40**, 4879-4881.

23 T. Devic and C. Serre, *Chem. Soc. Rev.*, 2014, **43**, 6097-6115.

24 N. C. Burtch, H. Jasuja and K. S. Walton, *Chem. Rev. (Washington, DC, U. S.)*, 2014, **114**, 10575-10612.

25 Y. L. Liu, J. F. Eubank, A. J. Cairns, J. Eckert, V. C. Kravtsov, R. Luebke and M. Eddaoudi, *Angew. Chem.-Int. Edit.*, 2007, **46**, 3278-3283.

26 J. Moellmer, E. B. Celer, R. Luebke, A. J. Cairns, R. Staudt, M. Eddaoudi and M. Thommes, *Microporous Mesoporous Mater.*, 2010, **129**, 345-353.

27 A. Dhakshinamoorthy, M. Alvaro, H. Chevreau, P. Horcajada, T. Devic, C. Serre and H. Garcia, *Catalysis Science & Technology*, 2012, **2**, 324-330.

28 J. Moellmer, E. B. Celer, R. Luebke, A. J. Cairns, R. Staudt, M. Eddaoudi and M. Thommes, *Microporous Mesoporous Mater.*, 2009, **129**, 345-353.

29 M. Pang, A. J. Cairns, Y. Liu, Y. Belmabkhout, H. C. Zeng and M. Eddaoudi, *J. Am. Chem. Soc.*, 2013, **135**, 10234-10237.

30 D. Cunha, M. Ben Yahia, S. Hall, S. R. Miller, H. Chevreau, E. Elkaïm, G. Maurin, P. Horcajada and C. Serre, *Chem. Mater.*, 2013, **25**, 2767-2776.

31 J. F. Eubank, P. S. Wheatley, G. Lebars, A. C. McKinlay, H. Leclerc, P. Horcajada, M. Daturi, A. Vimont, R. E. Morris and C. Serre, *APL Materials*, 2014, **2**, 124112.

32 M. Pourbaix, *Atlas of electrochemical equilibria in aqueous solutions*, 1974.

33 *Unpublished results*.

34 G. Gritzner and G. Kreysa, *Pure Appl. Chem.*, 1993, **65**, 1009-1020.

35 N. Stock and S. Biswas, *Chem. Rev. (Washington, DC, U. S.)*, 2012, **112**, 933-969.

36 http://www.sciencelab.com/msds.php?msdsId=9925315.

37 https://www.spectrumchemical.com/MSDS/TCI-D1159.pdf.

38 A. U. Czaja, N. Trukhan and U. Muller, *Chem. Soc. Rev.*, 2009, **38**, 1284-1293.

39 M. J. Avrami, *J. Chem. Phys.*, 1941, **9**, 177.

40 B. V. Erofe'ev, *Compt. Rend. Acad. Sci. USRR*, 1946, **52**, 511.

41 J. D. Hancock and J. H. Sharp, *J. Am. Ceram. Soc.*, 1972, **55**, 74-77.

42 A. F. Gualtieri, *Phys. Chem. Min.*, 2001, **28**, 719.

43 J. Cravillon, C. A. Schroder, H. Bux, A. Rothkirch, J. Caro and M. Wiebcke, *CrystEngComm*, 2012, **14**, 492-498.

44 S. R. Venna, J. B. Jasinski and M. A. Carreon, *J. Am. Chem. Soc.*, **132**, 18030-18033.

45 T. Ahnfeldt and N. Stock, *CrystEngComm*, 2011, **14**, 505-511.

46 F. Millange, R. El Osta, M. E. Medina and R. I. Walton, *CrystEngComm*, 2011, **13**, 103-108.

47 R. El Osta, M. Frigoli, J. Marrot, M. E. Medina, R. I. Walton and F. Millange, *Cryst. Growth Des.*, 2011, **12**, 1531-1537.

48 F. Millange, M. I. Medina, N. Guillou, G. Férey, K. M. Golden and R. I. Walton, *Angew. Chem., Int. Ed.*, 2010, **49**, 763-766.

49 F. Millange, M. Medina, N. Guillou, G. Férey, K. Golden and R. Walton, *Angew. Chem., Int. Ed.*, 2010, **49**, 763-766.

50 F. Ragon, H. Chevreau, T. Devic, C. Serre and P. Horcajada, *Chemistry – A European Journal*, 2015, **21**, 7135-7143.

51 F. Ragon, P. Horcajada, H. Chevreau, Y. K. Hwang, U. H. Lee, S. R. Miller, T. Devic, J.-S. Chang and C. Serre, *Inorg. Chem.*, 2014, **53**, 2491-2500.

52 E. Stavitski, M. Goesten, J. Juan-Alcañiz, A. Martinez-Joaristi, P. Serra-Crespo, A. V. Petukhov, J. Gascon and F. Kapteijn, *Angew. Chem., Int. Ed.*, 2011, **50**, 9624-9628.

53 E. E. Finney and R. G. Finke, *Chem. Mater.*, 2009, **21**, 4692-4705.

54 A. García Márquez, A. Demessence, A. E. Platero-Prats, D. Heurtaux, P. Horcajada, C. Serre, J.-S. Chang, G. Férey, V. A. de la Peña-O'Shea, C. Boissière, D. Grosso and C. Sanchez, *Eur. J. Inorg. Chem.*, 2012, **32**, 5165-5174.

55 P. Horcajada, T. Chalati, C. Serre, B. Gillet, C. Sebrie, T. Baati, J. F. Eubank, D. Heurtaux, P. Clayette, C. Kreuz, J.-S. Chang, Y. K. Hwang, V. Marsaud, P.-N. Bories, L. Cynober, S. Gil, G. Ferey, P. Couvreur and R. Gref, *Nat. Mater.*, 2010, **9**, 172-178.

56 J. Klinowski, F. A. Almeida Paz, P. Silva and J. Rocha, *Dalton Trans.*, 2011, **40**, 321-330.

57 P. Lidström, J. Tierney, B. Wathey and J. Westman, *Tetrahedron*, 2001, **57**, 9225-9283.

58 Z. Ni and R. I. Masel, *J. Am. Chem. Soc.*, 2006, **128**, 12394-12395.

59 C. Serre, C. Mellot-Draznieks, S. Surblé, N. Audebrand, Y. Filinchuk and G. Férey, *Science*, 2007, **315**, 1828-1831.

Supplementary Information (SI)

Synthesis of the biocompatible and highly stable MIL-127(Fe): from large scale synthesis to particle size control

Hubert Chevreau, Anastasia Permyakova, Farid Nouar, Paul Fabry, Carine Livage, Florence Ragon, Alfonso Garcia-Marquez, Thomas Devic, Nathalie Steunou, Christian Serre* and Patricia Horcajada*

Table of Contents

I. Characterization techniques

A small amount of solid was analyzed by a Thermo Nicolet spectrometer (Thermo, USA). The spectrum was recorded from 4000-400 cm^{-1}.

N_2 isotherms were obtained at 77 K using a Belsorp Mini (Bel, Japan). Prior to the analysis, approximately 40-60 mg of activated samples were evacuated for 16 h at 200°C under primary vacuum. BET surface and micropore volume were estimated at a relative pressure lower than 0.25.

Approximately 5-10 mg of the sample were used for the thermogravimetric analysis (TGA). Samples were analyzed under an oxygen flow (20 $mL\cdot min^{-1}$) using a Perkin Elmer Diamond TGA/DTA STA 6000 running from room temperature to 600 °C with a scan rate of 2 $°C\cdot min^{-1}$.

Particle size was monitored by Dynamic Light Scattering (DLS) on a Zetasizer Nano (Malvern Instruments). Samples were prepared by dispersing at 0.1 $mg\cdot mL^{-1}$ of nanoparticles (NPs) at RT in the ethanol by using an ultrasound tip (30% amplitude for 1 min; Digital Sonifer 450, Branson).

Field emission gun scanning electron microspopy (FEG-SEM) images of the crystals were carried out using a microspope JEOL JAMP 9500F.

II. Synthesis of 3,3’,5,5’-azobenzenetetracarboxylic acid[1]

In a 1 L 3-neck round bottomed flask containing 250 mL of distilled water, 19 g of 5-nitroisophthalic acid were added and then, slowly, 50 g of sodium hydroxide NaOH, followed by heating at 50-60 °C under magnetic stirring. A pink slurry was formed.

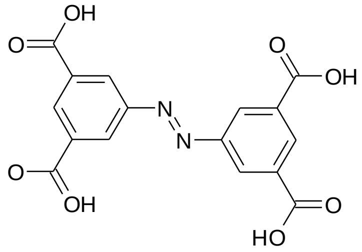

Figure S1: Chemical structure of the 3,3’,5,5’-azobenzenetetracarboxylic acid

100 g of glucose dissolved in 150 mL of water were slowly added to the previously obtained pink slurry. The solution turned from yellow to orange and then brown. The heating was stopped, and air was bubbled through the solution overnight at room temperature. The mixture was cooled down with an ice-bath in order to optimize the amount of precipitate, before recovering the disodium salt by filtration. The filtrate was then redissolved in 200 mL of distilled water and then this solution was acidified to pH = 1 using 37% HCl. This yielded to a bright orange precipitate, recovered by filtration, washed with ethanol and dried at 70°C.

NMR ^1H (d_6-DMSO): 12-13 (broad, 2H), 8.03 (d, J_1 = 8.1 Hz, 4H), 8.03 (d, J_2 = 1.5 Hz, 4H) ; 7.97 (dd, J_1 = 8.1 Hz, J_2 = 1.5 Hz, 4H).
NMR ^{13}C (d_6-DMSO): 166.2, 153.1, 134.1, 132.7, 131.9, 124.0, 122.1.

III. Water stability tests

30 mg of activated MIL-127(DMF) were introduced in a 10 mL round bottom flask containing 3 mL of distilled water (pH = 4.2). The mixture was placed under stirring either at room temperature (RT) or under reflux for 16 h. Stability experiments were performed in basic media (pH = 8 and 12) by adding sodium hydroxide NaOH and in acid media (pH= 2 or 3) by adding hydrochloric acid HCl.

The resulting solids have been characterized by powder X-ray diffraction.

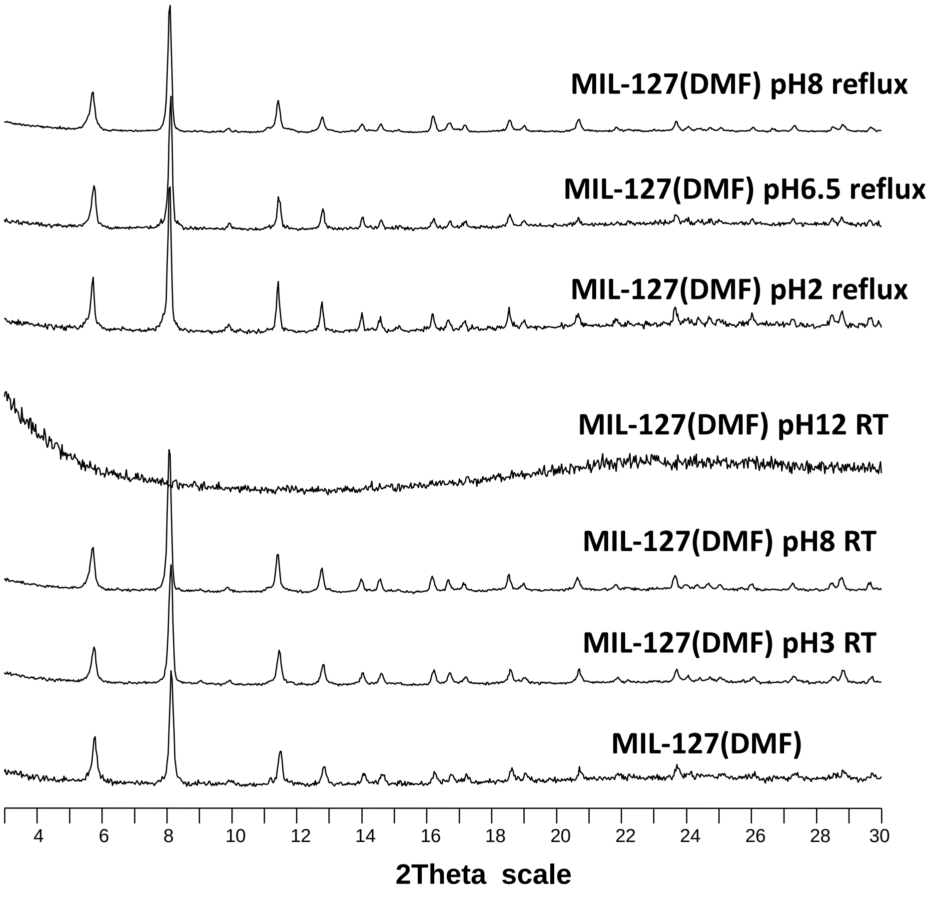

Figure S2: X-ray powder diffraction patterns of MIL-127(DMF) before (black) and after the treatment at RT at pH=2, pH=8 and pH= 12 as well as under reflux pH=2, pH= 6.5 and pH=8.

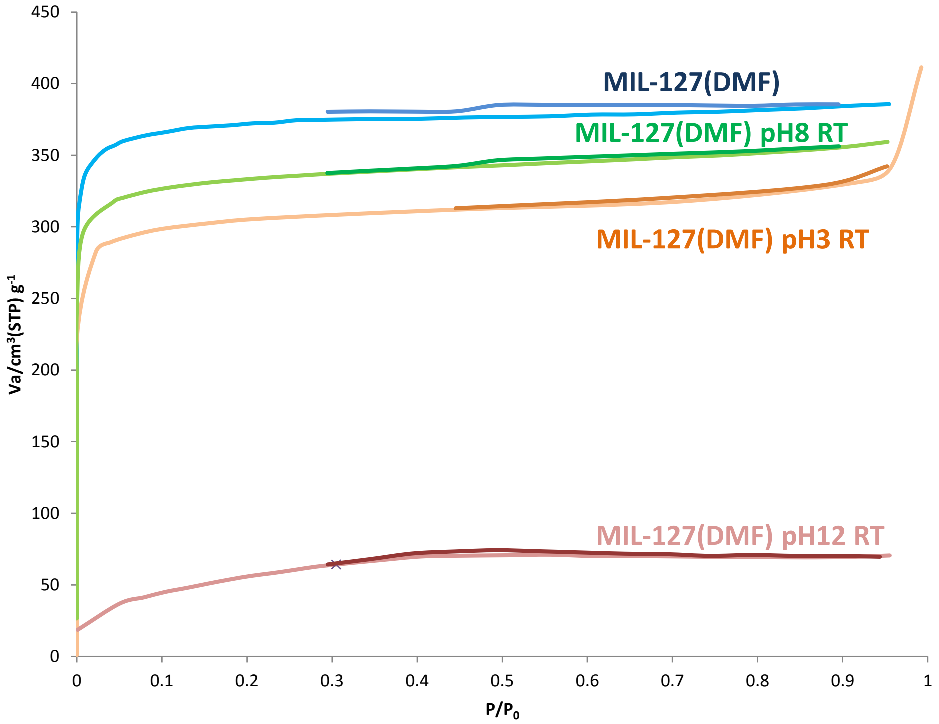

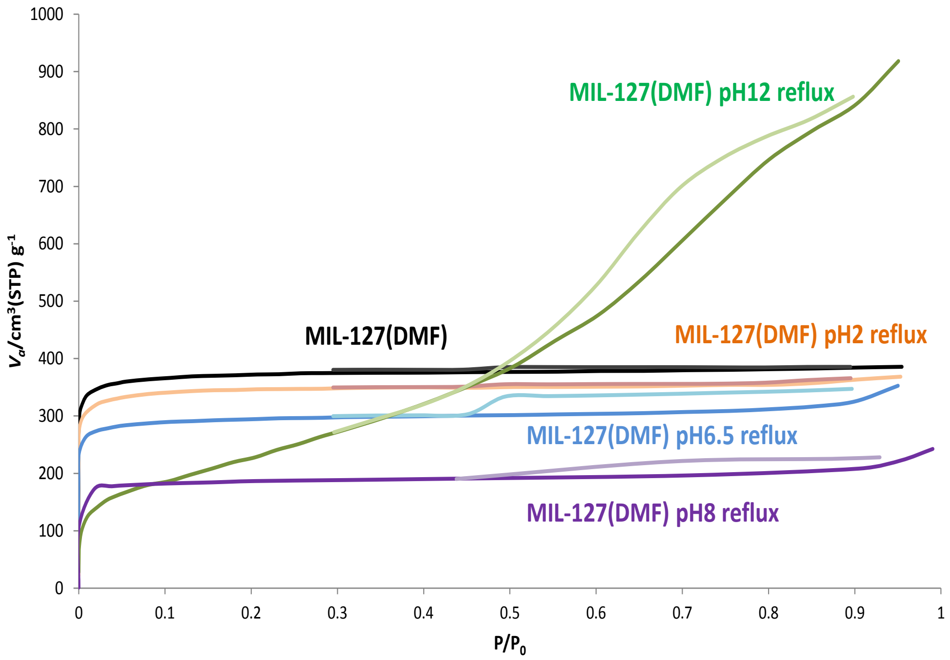

Figure S3: Nitrogen sorption isotherms at 77K of MIL-127(DMF) before (black) and after the treatment at RT (on the top) pH=2, pH= 7, pH=8 and pH= 12 as well as under reflux (on the bottom) pH=2, pH= 7, pH=8 and pH= 12.

IV. Characterization of MIL-127(DMF/HF)

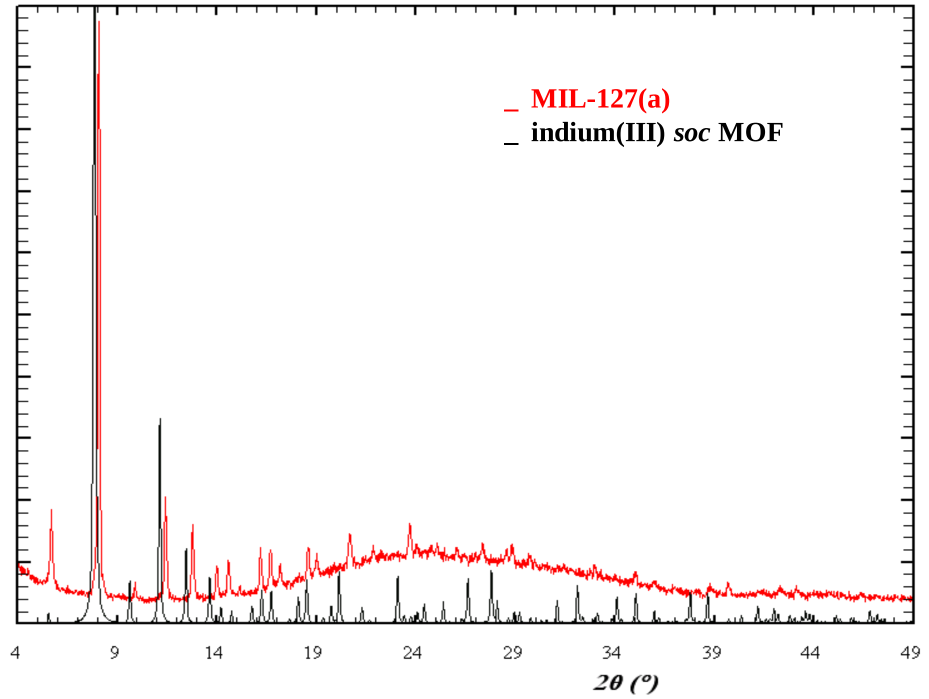

Figure S4: Comparison between the PXRD patterns of the indium(III) *soc* MOF (black line) and MIL-127(DMF/HF) (red line). X-ray powder diffraction (XRPD) patterns were recorded on a Siemens D5000 ($\lambda_{Cu\_\alpha1}$ = 1.54056 Å, $\lambda_{Cu\_\alpha2}$ = 1.54439 Å) at room temperature over the angular range 4-50° 2θ with a step of 0.02°.

PXRD pattern of MIL-127(DMF/HF) was first compared with the simulated XRD pattern of indium(III) *soc* MOF and a strong similarity between them could be observed despite a small shift of XRD peaks of MIL-127(DMF/HF) towards higher 2θ (°) (Figure S4).

In order to confirm the structure of MIL-127(DMF/HF), the X-ray diffraction pattern was indexed on 15 Bragg reflections using Dicvol06, giving a cubic structure with a *a* cell parameter of 21.8527 Å. Then, the cell parameter and space group were refined and determined, respectively, by performing a Lebail refinement on WinPlotR[2] of the FullProf Suite.[3] Thus the structure is cubic with a *a* cell parameter of 21.897(3) Å. The space group P-43n, is identical to that of the indium(III) *soc* MOF (Rp= 4.27, Rwp= 5.45, Chi2= 1.34) (Figure S5).

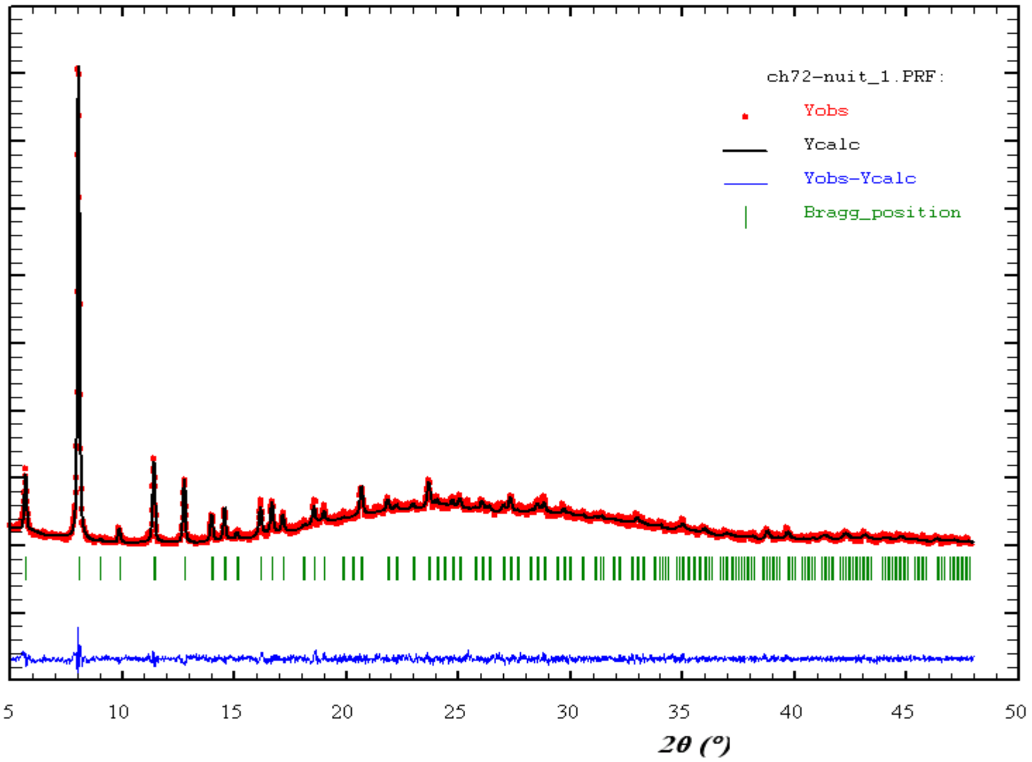

Figure S5: Lebail refinement of MIL-127(DMF/HF) using WinPlotR.[2] Cubic, space group P-43n, a= 21.897(3) Å (Rp= 4.27, Rwp= 5.45, Chi2= 1.34). The PXRD pattern was recorded on a Siemens D5000 ($\lambda_{Cu\_\alpha1}$ = 1.54056 Å, $\lambda_{Cu\_\alpha2}$ = 1.54439 Å) at room temperature over the angular range 5-50 2θ with a step of 0.02°.

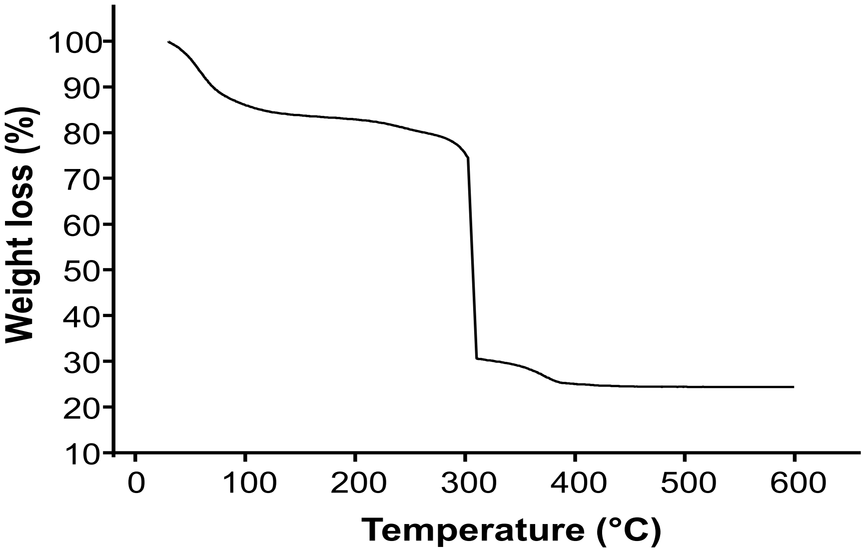

Figure S6: TGA of activated MIL-127(DMF/HF).

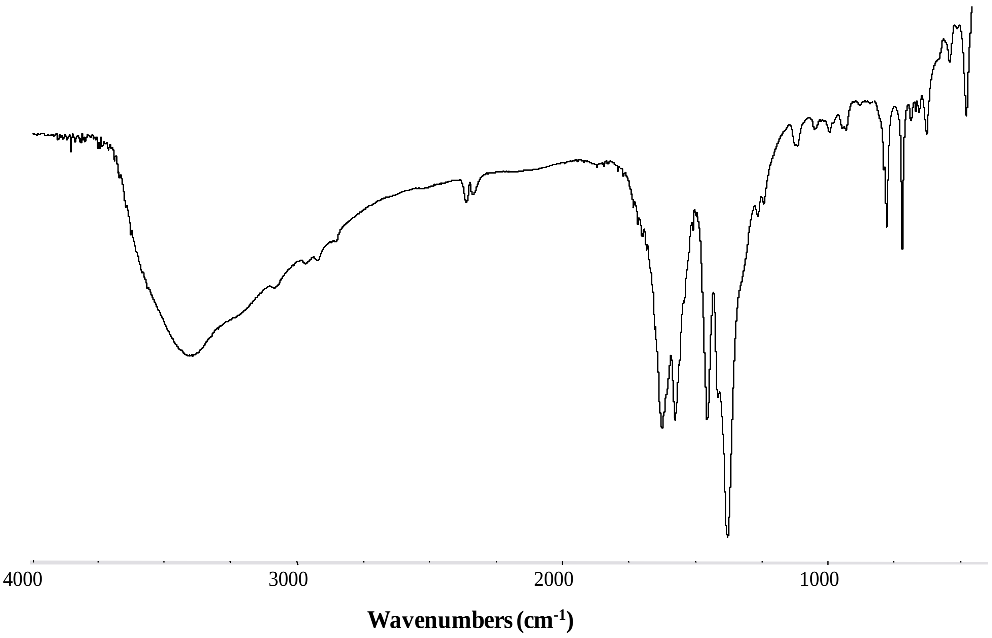

Figure S7: IR spectrum of activated MIL-127(DMF/HF).

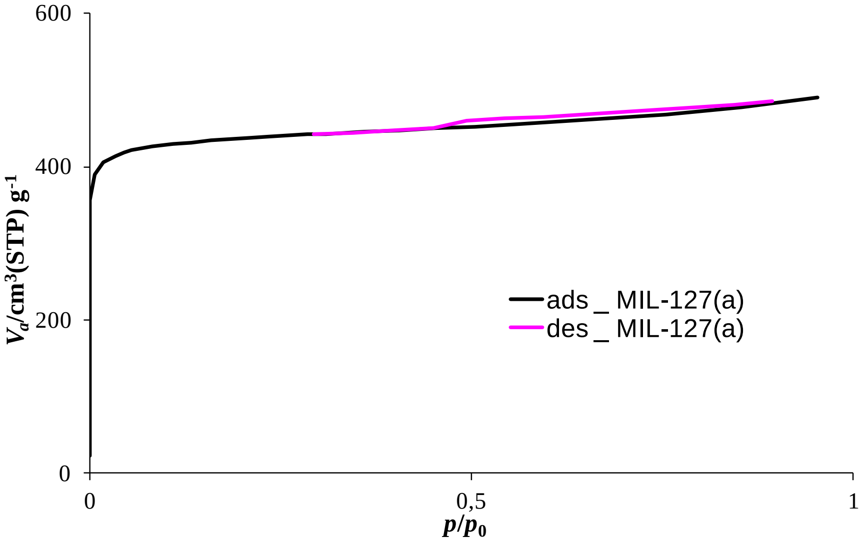

Figure S8: Nitrogen sorption isotherm measurement at 77K of activated MIL-127(DMF/HF). The BET surface area is estimated to 1400 m^2.g^{-1}.

V. Characterization of MIL-127(DMF)

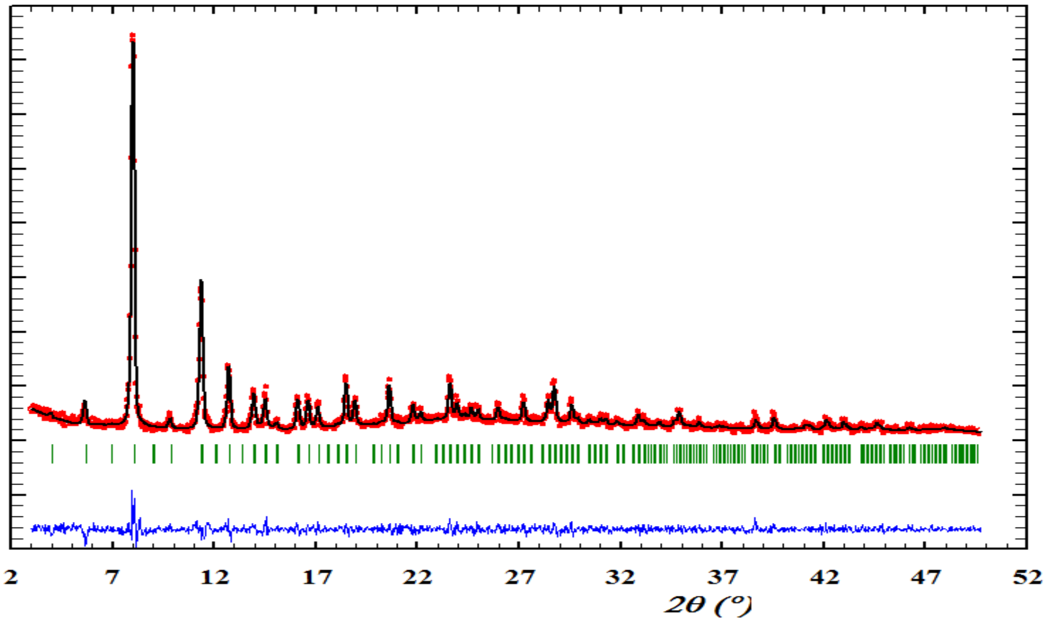

Figure S9: Lebail refinement of MIL-127(DMF) using WinPlotR.[2] Cubic, space group P-43n, a= 21.969(3) Å (Rp= 10.3, Rwp= 13.4, Chi2= 1.39). The PXRD pattern was recorded on a Siemens D5000 ($\lambda_{Cu\_\alpha1}$ = 1.54056 Å, $\lambda_{Cu\_\alpha2}$ = 1.54439 Å) at room temperature over the angular range 2-50 2θ with a step of 0.03°. The Lebail refinement confirms a cubic structure, with a space group P-43n, and a cell parameter a= 21.969(3) Å, as found for MIL-127(DMF/HF).

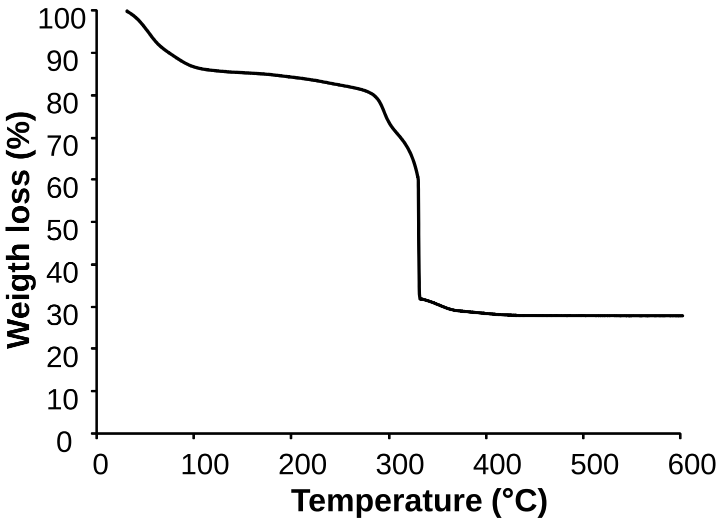

Figure S10: TGA of activated MIL-127(DMF).

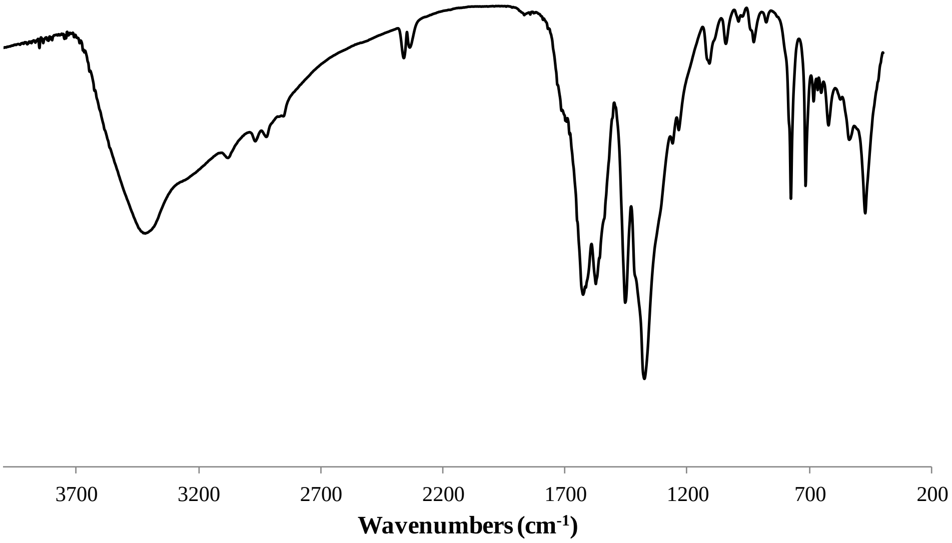

Figure S11: FTIR spectrum of activated MIL-127(DMF).

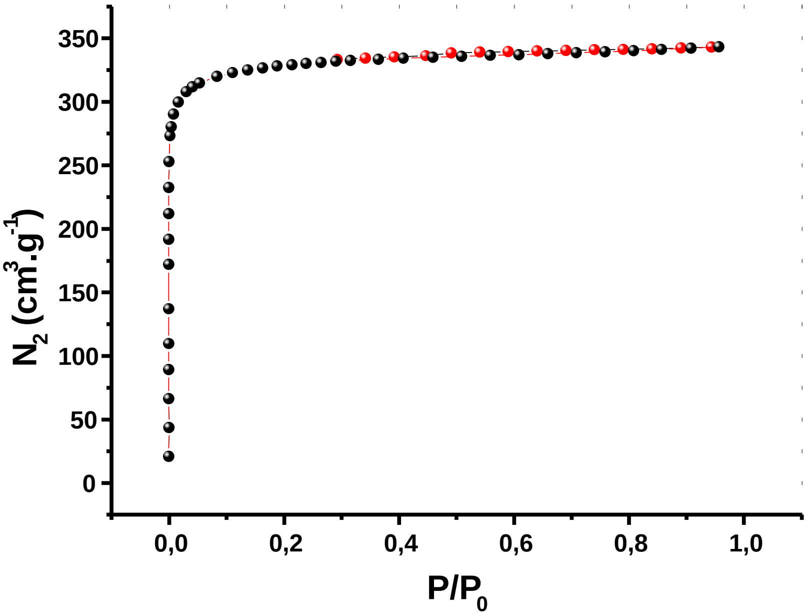

Figure S12: N_2 sorption isotherm at 77K of the activated MIL-127(DMF). The BET surface area is estimated to 1310 m^2.g^{-1}.

VI. Characterization of MIL-127(Prop)

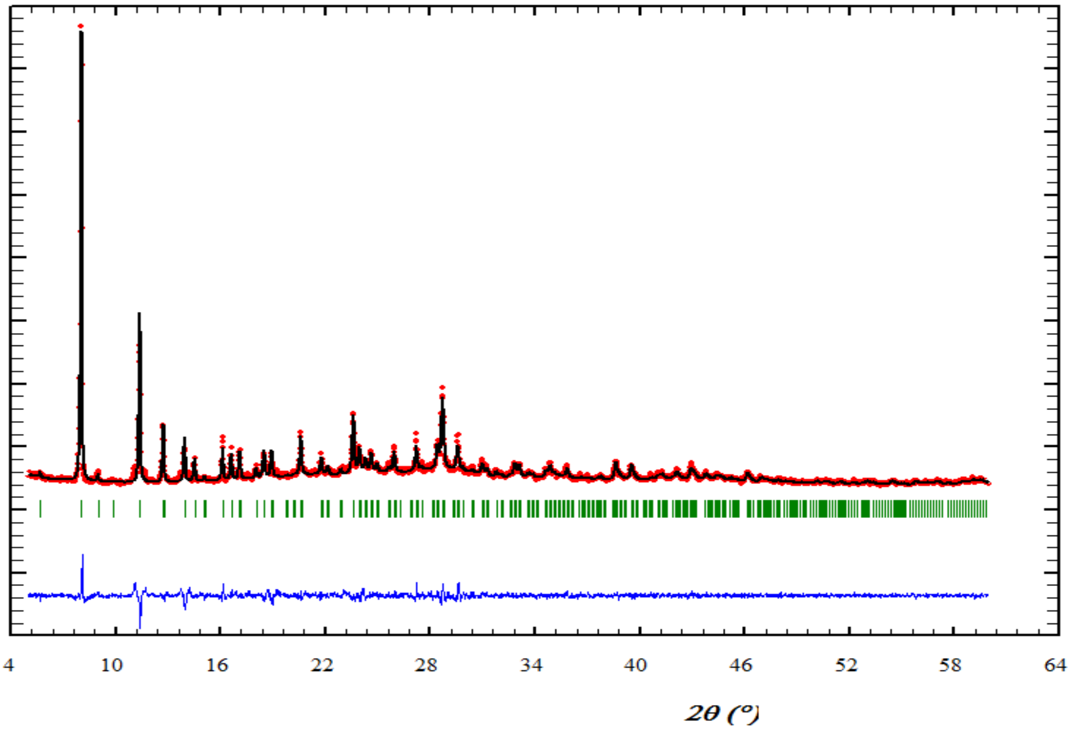

Figure S13: Lebail refinement of MIL-127(Prop) using WinPlotR.[2] Cubic, space group P-43n, a= 21.972(1) Å (Rp= 7.9, Rwp= 10.6, Chi2= 2.21). The PXRD pattern was recorded on a Siemens D5000 ($\lambda_{Cu\_\alpha1}$ = 1.54056 Å, $\lambda_{Cu\_\alpha2}$ = 1.54439 Å) at room temperature over the angular range 4-60° 2θ with a step of 0.02°. The Lebail refinement confirms a cubic structure, with a space group P-43n, and a cell parameter a= 21.972(1) Å, as found for MIL-127(DMF/HF) and MIL-127(DMF).

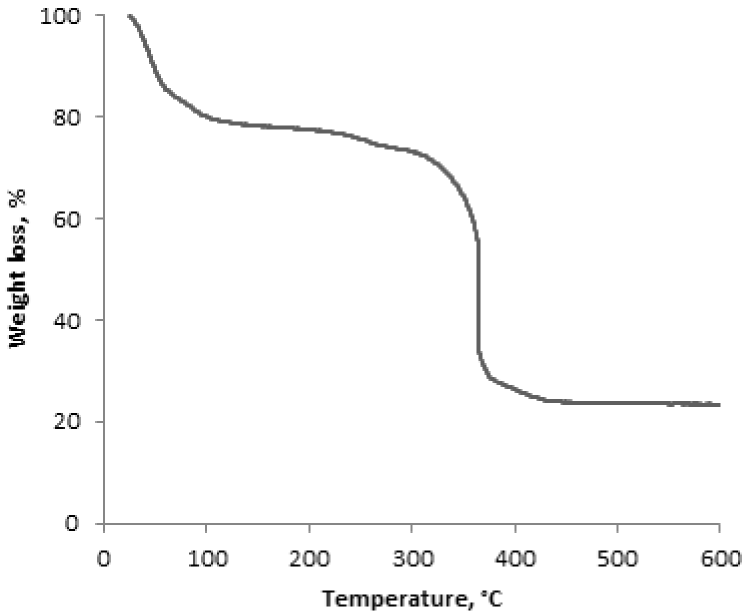

Figure S14: TGA of activated MIL-127(Prop).

.

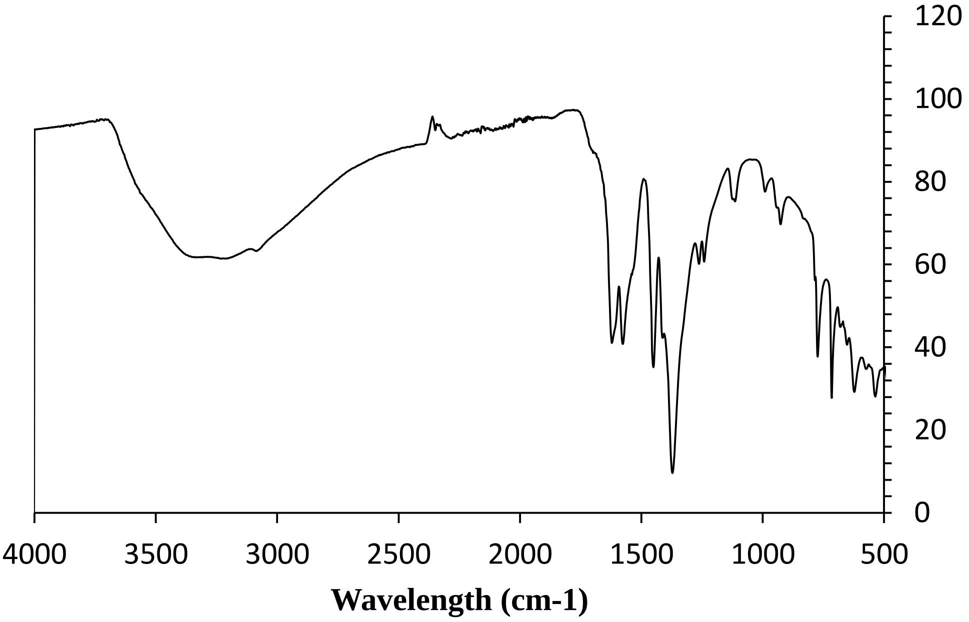

Figure S15: IR spectrum of activated MIL-127(Prop)

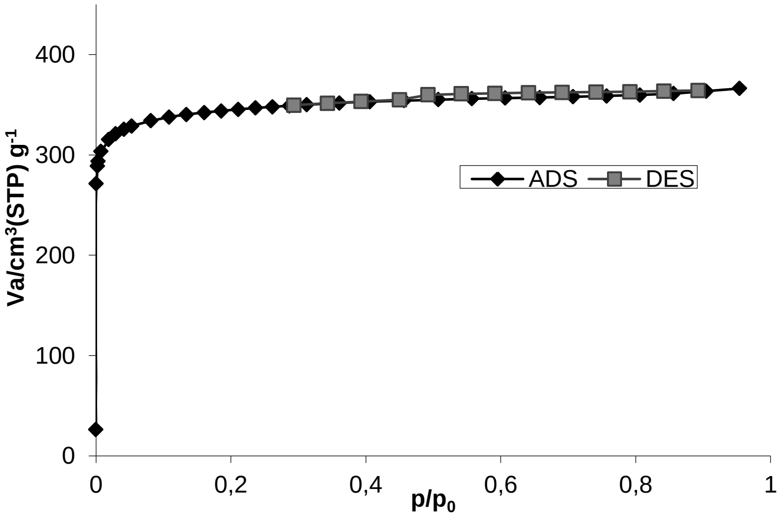

Figure S16: Nitrogen sorption isotherm of MIL-127(Prop) at T = 77 K. BET surface area of 1350 $m^2.g^{-1}$

VII. Time-resolved *in situ* energy-dispersive X-ray diffraction (EDXRD) study of the solvothermal crystallization of MIL-127(DMF) and (Prop)

1. Theory

The d-spacing (Å) of a Bragg peak is calculated from the recorded energy (KeV) as follows:

$$d = \frac{6{,}19921}{E * \sin(\theta)}$$

θ being the incident beam source angle.

Data can be normalized either using the fluorescence or the synchrotron radiation current provided within the recorded instrumental data. As the solid are based on iron, no fluorescence was observed and the second approach applied. The profiles of Bragg peaks were fitted with a Gaussian function, implement in the F3tool software developed by Rotkirch *et al.* (DESY, Hambourg, Germany) and their surface area integrated.

The extent of crystallisation α(t) was obtained as the ratio of the integrated intensities I(t) at the different times to the maximum integrated intensity I*max* at the end of the reaction:

$$\alpha(t) = \frac{I(t)}{Imax}$$

The first approach applied is the Avrami-Erofe'ev (AE) model, which is the most frequently used for the kinetics study of hybrid materials:[4, 5]

$$\alpha(t) = 1 - e^{-(k(t-t_0))^n}$$

Where k is an overall rate constant; t_0 the induction time; n, the Avrami-exponent.

The AE model can used through the approach of Sharp and Hancock, that consists in a linear regression of the AE equation:[6]

$$\ln[-\ln(1-\alpha)] = n\ln(k) + n\ln(t-t_0)$$

The activation energy of the reaction process could thus be determined by calculation of the overal constant k at each temperature and by the use of the Arrhenius equation:

$$k = A\,e^{-E_a/RT}$$

A, the pre-exponential factor; R= 8.314 $J.mol^{-1}.K^{-1}$.

The Gualtieri model consists in a 2-terms function that separates nucleation and growth processes in the following equation, where the first term is related to the nucleation:

$$\alpha(t) = \frac{1}{1+e^{-(t-a)/b}} \quad [1 - e^{-(k_g t)^n}]$$

k_g, the rate constant of the growth; n, the dimension of the growth thus n= 3 (three-dimensional growth) as the crystals are cubic (See SEM-FEG images).

From the Gualtieri model, and more precisely from the a and b parameters, the dimensionless probability of nucleation (a Gaussian function) can be calculated by:

$$P_N = \exp(\frac{-(t-a)^2}{2b^2})$$

a and b, being the position of the peak and the variance of the Gaussian distribution, respectively. The rate constant of nucleation is calculated by:

$$k_n = 1/a$$

2. Experimental

Solvothermal reactions were performed in sealed borosilicate glass tubes Schott® (H*diam. 100 * 12 mm) with an inner diameter of 9 mm and a volume of 7 mL. 0.66 mmol of iron(III) chloride hydrated (180 mg) and 0.33 mmol of H_4-TazBz (118 mg) were dissolved into 2 mL of DMF. The tube was placed under magnetic stirring in an oven preheated to the desired temperature (170, 175, 190 and 200°C) using a circulating oil heater and equipped with a magnetic stirring device.

Bragg peaks integration was performed using “calf3” (software offered and available for free at beamline F3, private copy by A. Rothkirch/DESY).

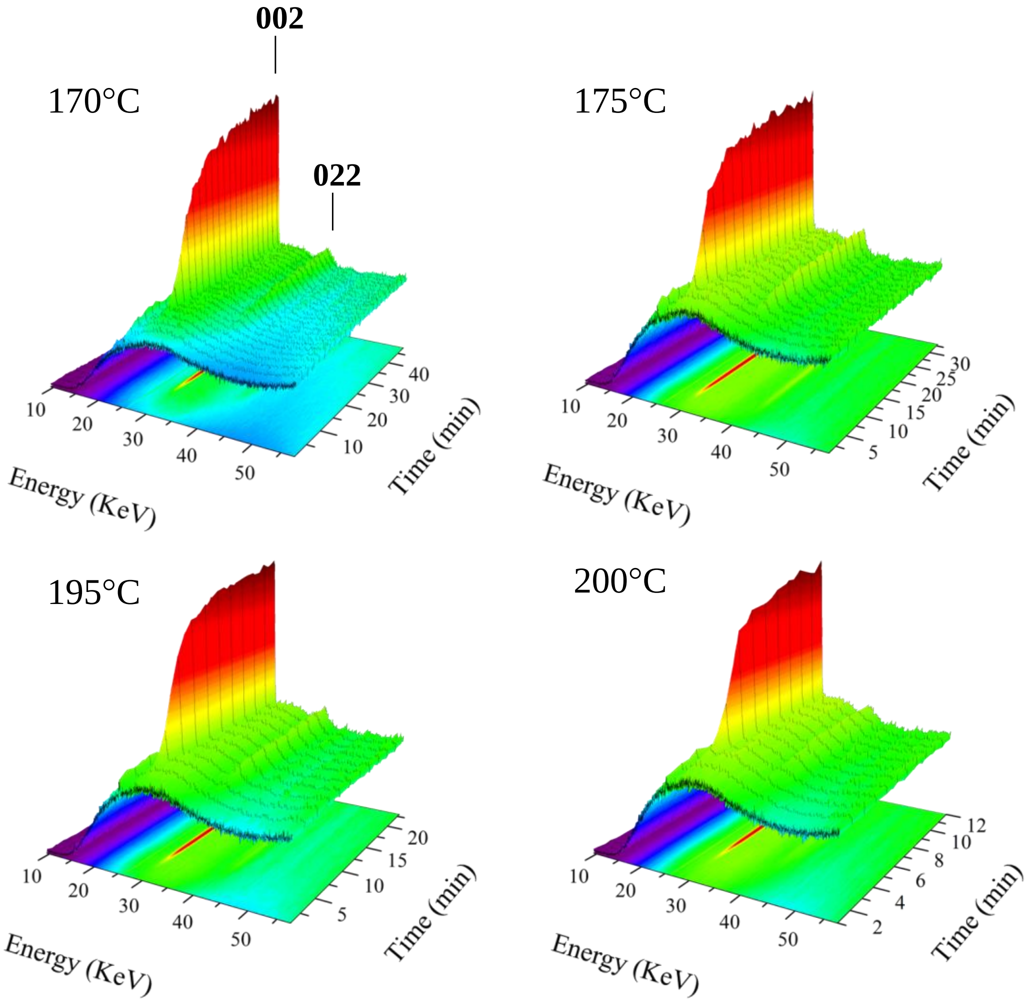

Figure S17: Time resolved in situ EDXRD data measured during the crystallization of MIL-127(DMF) at different temperatures (170, 175, 190 and 200°C).

Figure and S18 show time-resolved EDXRD data recorded at intervals of 60 s during the crystallization of MIL-127(DMF) and MIL-127(Prop), respectively, at four different temperatures. The hkl Bragg reflection (002) of MIL-127(DMF) and MIL-127(Prop), as well as the (022) reflection for MIL-127(DMF), observed after a temperature-dependent induction time t_0 (*i.e.* t_0 decreases with temperature), increase in intensity with time, reaching a maximum intensity at the end of the reaction. The product is presumably a pure MIL-127 as no other crystalline phases can be detected, neither as intermediate phases nor as by-products. After integration of the most intense Bragg reflection (002) and normalization of the integrated intensities to the corresponding synchrotron radiation current and the integrated maximum intensities, the crystallization curves (extent of crystallization α(t) versus time)) (Figure 2 in the main text) can be plotted.

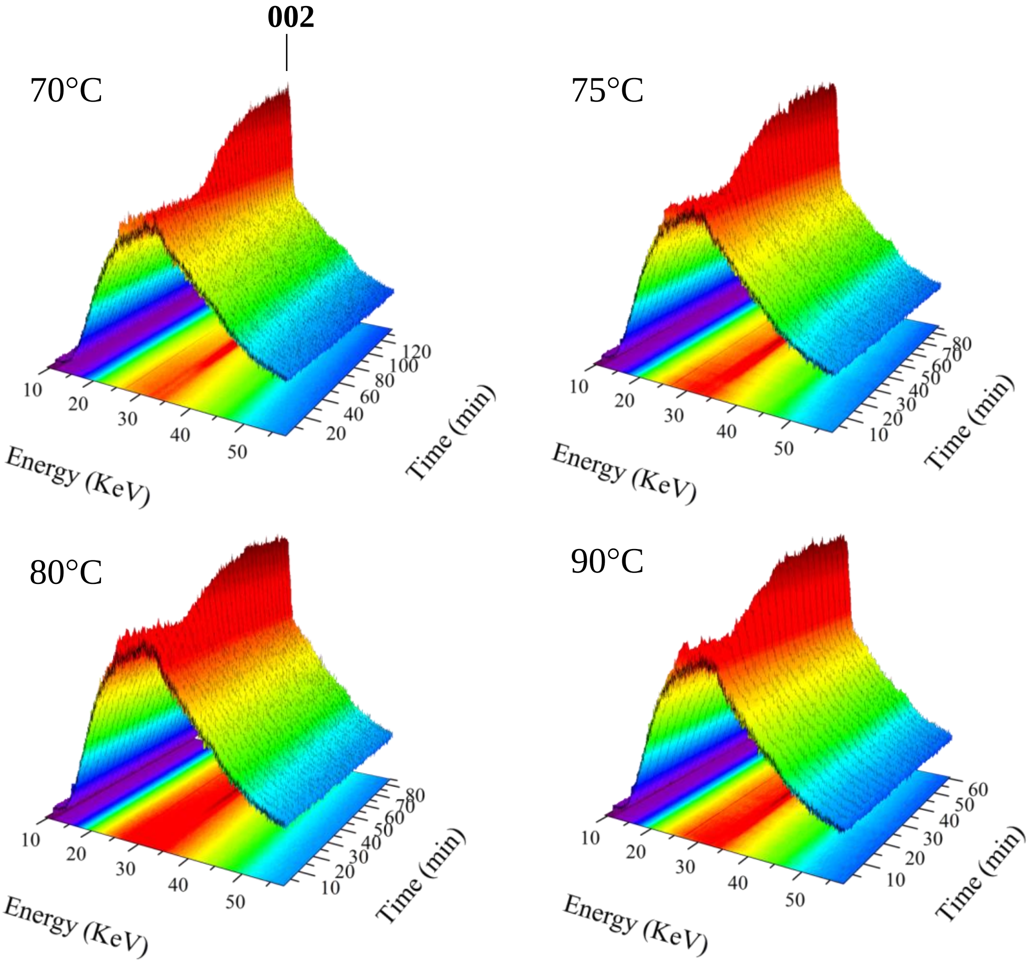

Figure S18: Time resolved in situ EDXRD data measured during the crystallization of MIL-127(Prop) at 75, 80, 85 and 90°C

i. <u>Avrami – Erofe'ev</u>

Then, the curves have been linearized using the Sharp and Hancock approach, allowing the extraction of the Avrami exponent *n* and the rate constant. (Figure S20and Table 1)

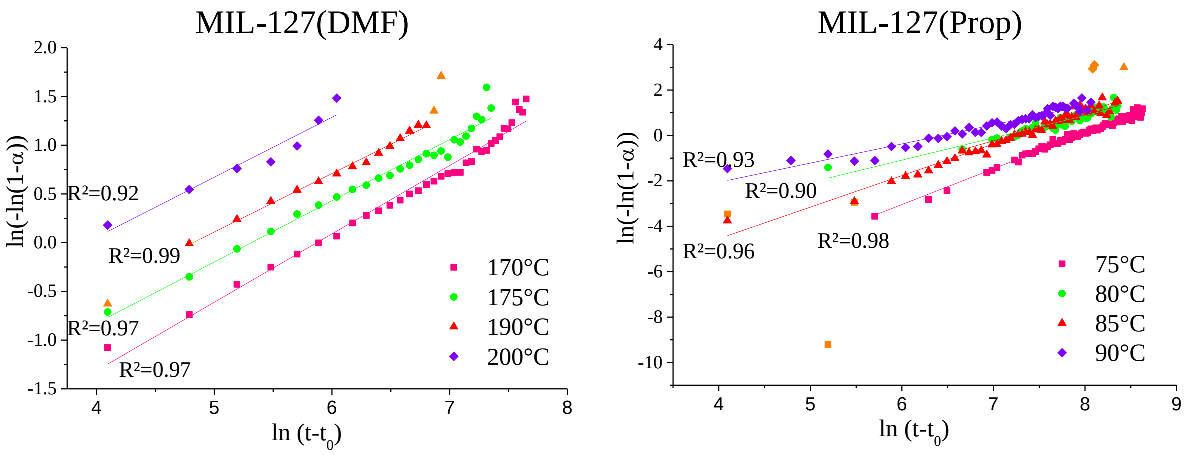

Figure S19: Sharp and Hancock linear regression of the Avrami-Eroféev nucleation-growth crystallization model for MIL-127(DMF) and MIL-127(Prop)

The activation energy Ea for the crystallization of MIL-127(DMF) and MIL-127(Prop) of respectively 102(10) and 92(24) kJ.mol^{-1} can be calculated by using the Arrhenius equation (Figure S209)

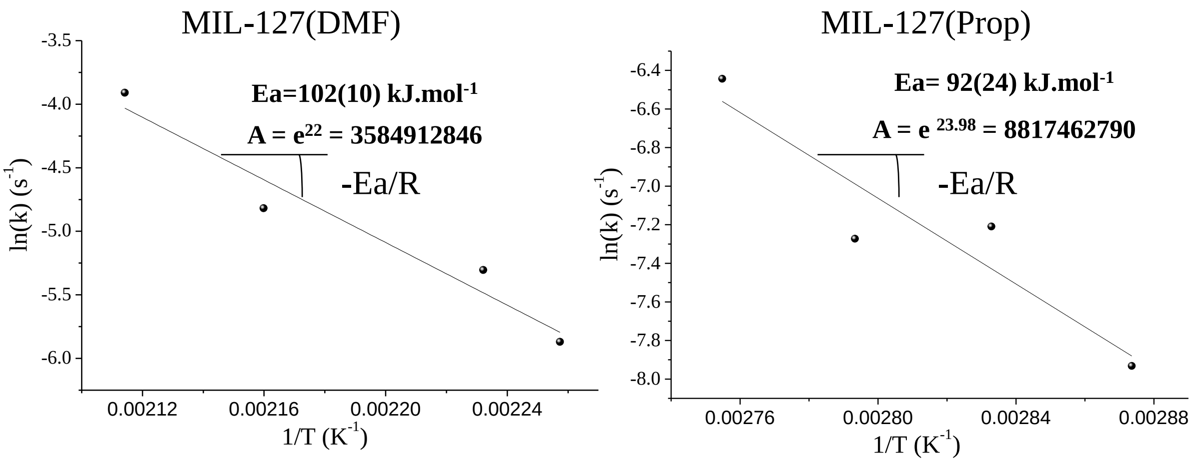

Figure S20: Determination of the Arrhenius activation energies of the synthesis of MIL-127(DMF) and MIL-127(Prop).

For MIL-127(DMF), an Avrami exponent close to 0.6 was obtained, which indicates a diffusion controlled crystal growth mechanism and a high concentration of nucleation sites. Nevertheless, as it will be shown by the use of the Gualtieri model, both nucleation and growth processes occur simultaneously but the crystallization process is kinetically controlled by the growth step.

For MIL-127(Prop), rate constants are significantly higher than those of MIL-127(DMF), which means that the physico-chemical conditions of the MIL-127(Prop) synthesis induces a faster crystallization process compared to that of MIL-127(DMF). A large induction time is observed at 75°C which may be imparted by the low solubility of the ligand at that temperature.

Table S1 : Induction time t_0, overall rate constant k, Avrami exponent n, pre-exponential factor A and activation energy obtained from the Sharp and Hancock fit as a function of the temperature.

Solvent	T (°C)	t_0 (s)	n_{SH}	k_{SH} (s^{-1}).10^{-3}	A (s^{-1})	E_a (kJ.mol^{-1})
MIL-127(DMF)	170	720	0.66	2.82	3.6 10^9	102(10)
	175	360	0.61	4.96		
	190	300	0.6	8.07		
	200	240	0.61	20.05		
MIL-127(Prop)	75	1500	1.6	0.35	8.8 10^9	92(24)
	80	720	1.0	0.81		
	85	540	1.4	0.7		
	90	360	0.9	1.6		

ii. Gualtieri model

Figure S21 and S22 shows the fit of the extent of crystallisation α(t) by the Gualtieri model and the corresponding probability curve of nucleation P_N.

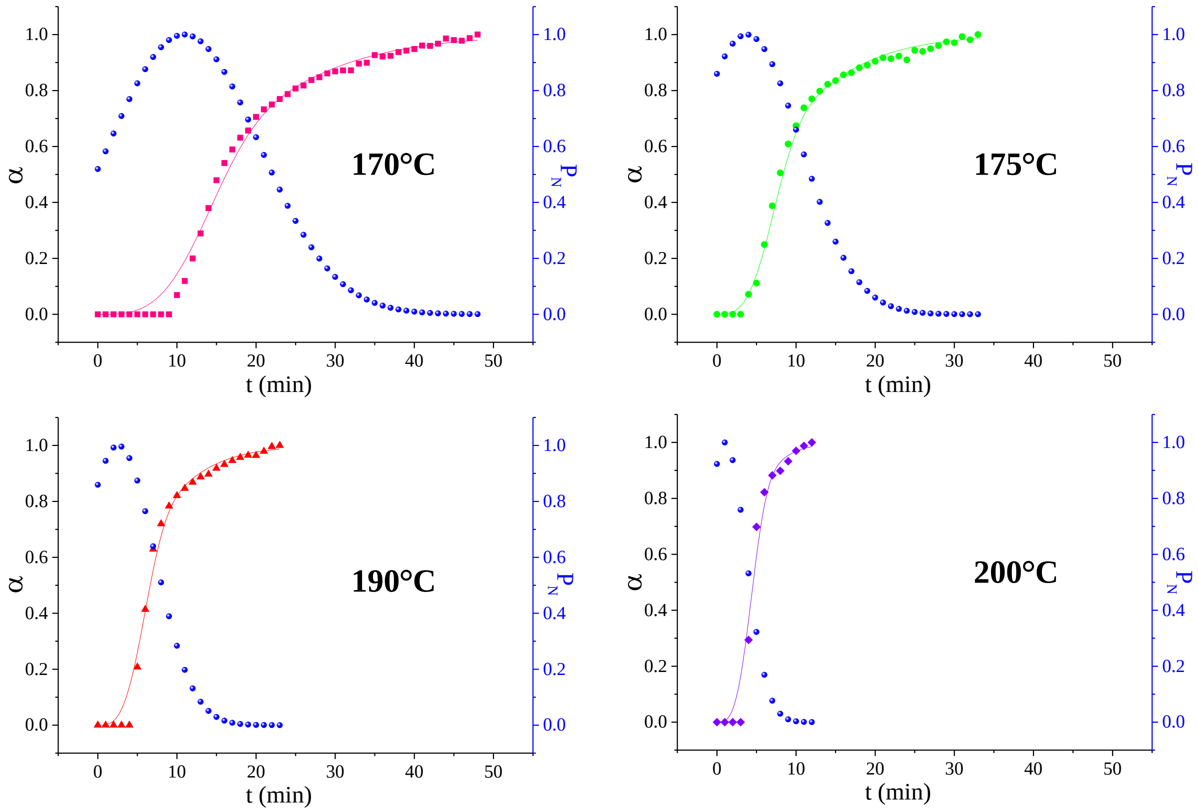

Figure S21: Extent of crystallization of MIL-127(DMF) at 170, 175, 190 and 200°C vs. time (pink squares, green circles, red triangles, violet rhombus, respectively) and corresponding non-linear least-squares fits with the Gualtieri equation (curve) as well as probability curve of nucleation P_N (blue circles).

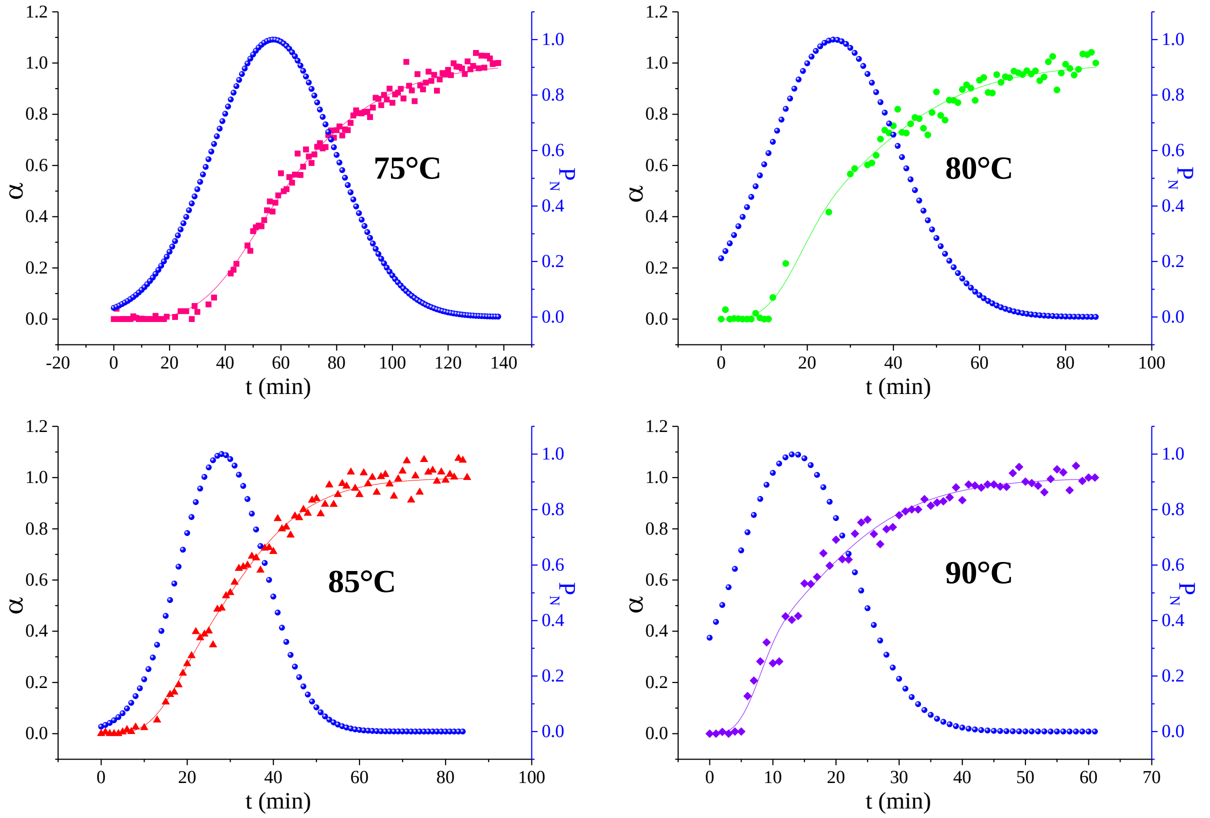

Figure S22: Extent of crystallization of MIL-127(Prop) at 75, 80, 85 and 90°C vs. time (pink squares, green circles, red triangles, violet rhombus, respectively) and corresponding non-linear least-squares fits with the Gualtieri equation (line) as well as the probability curves of nucleation P_N (blue circles).

The activation energies and pre-exponential factor for the nucleation and the growth are extracted from the fits of the extent of crystallization using the Gualtieri equations as shown in Table S2.

Table S2: Kinetic parameters (a, b, k_g and k_n), activation energy Ea and pre-exponential factor A for the nucleation and for the growth using the Gualtieri model.

Solvent	T (°C)	a (min)	b (min)	k_g (s^{-1}).10^{-3}	k_n (s^{-1}).10^{-3}	A_g (s^{-1})	$E_{a,g}$ (kJ.mol^{-1})	A_n (s^{-1})	$E_{a,n}$ (kJ.mol^{-1})
MIL-127(DMF) DMF	170	10.8(9)	9.5(1)	71.1(4)	91.7(4)	2.4 10^5	55(17)	5.3 10^{12}	116(28)
	175	3.7(6)	6.8(4)	133.7(3)	265.7(4)				
	190	2.5(7)	4.6(7)	162.3(5)	388.2(6)				
	200	1.0(5)	2.6(5)	217.4(7)	952.0(6)				
MIL-127(Prop) Propan-2-ol	75	59.0(1)	20.2(3)	24.0(1)	16.9(3)	3.2 10^{14}	106(20)	1.3 10^{12}	92(24)
	80	26.3(2)	14.9(3)	57.0(3)	37.9(4)				
	85	28.1(1)	9.9(1)	63.7(4)	35.5(4)				
	90	13.4(1)	9.1(2)	126.5(8)	74.5(6)				

In agreement with the AE model, it can be observed that k_n is higher than k_g, indicating that the growth step is rate-limiting.

VIII. High throughput tests

In order to investigate the effect of the solvent, several syntheses in different solvents and different pHs have been performed using a high-throughput system of 48 Teflon vessels of 200 µL. 24 of them have been used to perform the synthesis listed in Table S3. Then, the vessels have been introduced in a metallic grid then sealed between 2 metallic blocks with a pressure of 1 bar. Teflon sheets have been used between the vessel and the metallic block in order to improve permeability of the system, then the system has been placed in an oven at 120°C during 24 h.

Table S3: Synthesis conditions of MIL-127 in different solvents.

Nb	Ratio	Metal			TazBz		Solvent		Base/acide		
		Metal	mmol	mg	mmol	mg			quoi	mmol	µL
1	3:1	$FeCl_3$	0.1	27	0.03	11.9	H_2O	200 µl	-	-	-
2	3:1	$FeCl_3$	0.1	27	0.03	11.9	H_2O	200 µl	HCl pur	0.1	8.3
3	3:1	$FeCl_3$	0.1	27	0.03	11.9	H_2O	200 µl	NaOH(5M)	0.1	20
4	3:1	$FeCl_3$	0.1	27	0.03	11.9	Ethanol	200 µl	-	-	-
5	3:1	$FeCl_3$	0.1	27	0.03	11.9	Ethanol	200 µl	HCl pur	0.1	8.3
6	3:1	$FeCl_3$	0.1	27	0.03	11.9	Ethanol	200 µl	NaOH(5M)	0.1	20
7	3:1	$FeCl_3$	0.1	27	0.03	11.9	Methanol	200 µl	-	-	-
8	3:1	$FeCl_3$	0.1	27	0.03	11.9	Methanol	200 µl	HCl pur	0.1	8.3
9	3:1	$FeCl_3$	0.1	27	0.03	11.9	Methanol	200 µl	NaOH(5M)	0.1	20
10	3:1	$FeCl_3$	0.1	27	0.03	11.9	Toluene	200 µl	-	-	-
11	3:1	$FeCl_3$	0.1	27	0.03	11.9	Toluene	200 µl	HCl pur	0.1	8.3
12	3:1	$FeCl_3$	0.1	27	0.03	11.9	Toluene	200 µl	NaOH(5M)	0.1	20
13	3:1	$FeCl_3$	0.1	27	0.03	11.9	cyclohexane	200 µl	-	-	-
14	3:1	$FeCl_3$	0.1	27	0.03	11.9	cyclohexane	200 µl	HCl pur	0.1	8.3
15	3:1	$FeCl_3$	0.1	27	0.03	11.9	cyclohexane	200 µl	NaOH(5M)	0.1	20
16	3:1	$FeCl_3$	0.1	27	0.03	11.9	acetonitrile	200 µl	-	-	-
17	3:1	$FeCl_3$	0.1	27	0.03	11.9	acetonitrile	200 µl	HCl pur	0.1	8.3
18	3:1	$FeCl_3$	0.1	27	0.03	11.9	acetonitrile	200 µl	NaOH(5M)	0.1	20
19	3:1	$FeCl_3$	0.1	27	0.03	11.9	isopropanol	200 µl	-	-	-
20	3:1	$FeCl_3$	0.1	27	0.03	11.9	isopropanol	200 µl	HCl pur	0.1	8.3
21	3:1	$FeCl_3$	0.1	27	0.03	11.9	isopropanol	200 µl	NaOH(5M)	0.1	20
22	3:1	$FeCl_3$	0.1	27	0.03	11.9	cyclohexanol	200 µl	-	-	-
23	3:1	$FeCl_3$	0.1	27	0.03	11.9	cyclohexanol	200 µl	HCl pur	0.1	8.3
24	3:1	$FeCl_3$	0.1	27	0.03	11.9	cyclohexanol	200 µl	NaOH(5M)	0.1	20

Then the 24 vessels have been filtered on a filter block before being characterized by X-ray diffraction. The determination of the compounds is given in figure S23.

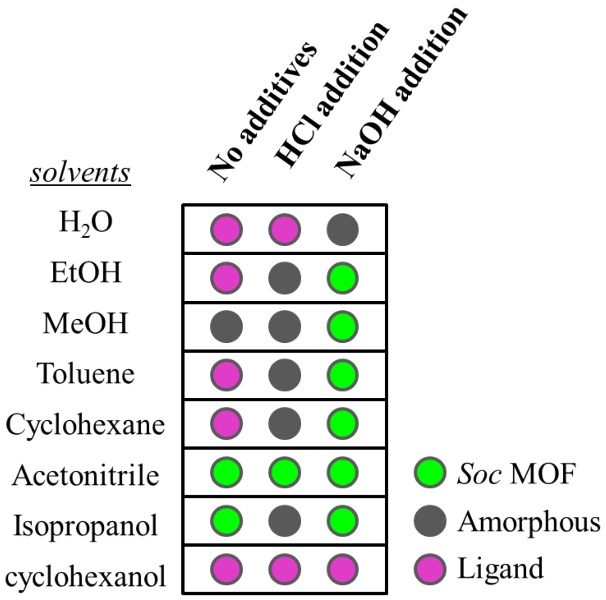

solvents	No additives	HCl addition	NaOH addition
H_2O	🟣	🟣	⚫
EtOH	🟣	⚫	🟢
MeOH	⚫	⚫	🟢
Toluene	🟣	⚫	🟢
Cyclohexane	🟣	⚫	🟢
Acetonitrile	🟢	🟢	🟢
Isopropanol	🟢	⚫	🟢
cyclohexanol	🟣	🟣	🟣

🟢 *Soc* MOF
⚫ Amorphous
🟣 Ligand

Ratio Fe: TazBz 3:1

Figure S23: Results of the X-ray powder diffraction on the 24 syntheses of Table S3.

IX. Characterization of MIL-127 nanoparticles (MIL-127_NPs1 and MIL-127_NPs2)

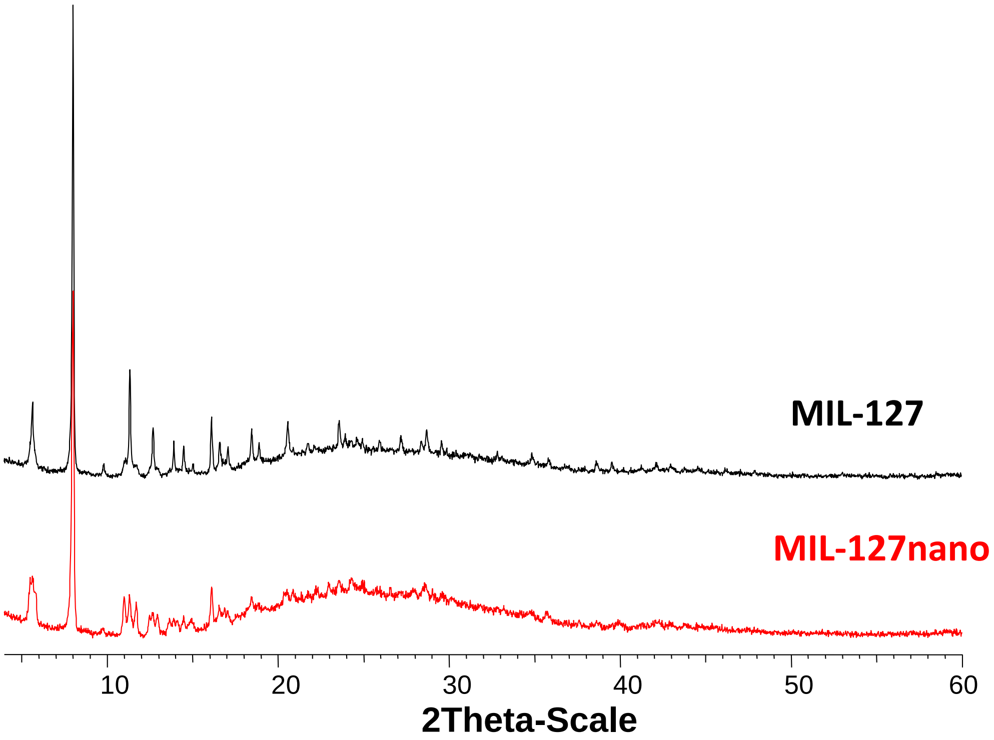

Figure S24: PXRD patterns of MIL-127_NPs1 and MIL-127_NPs2 in comparison with the MIL-127(DMF).

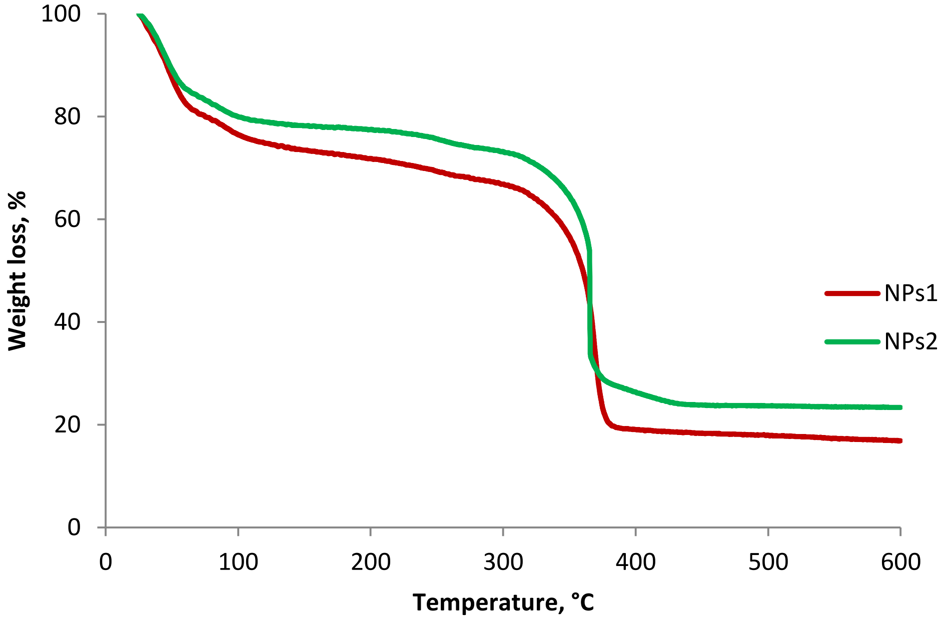

Figure S25: TGA of activated MIL-127_NPs1 and MIL-127_NPs2

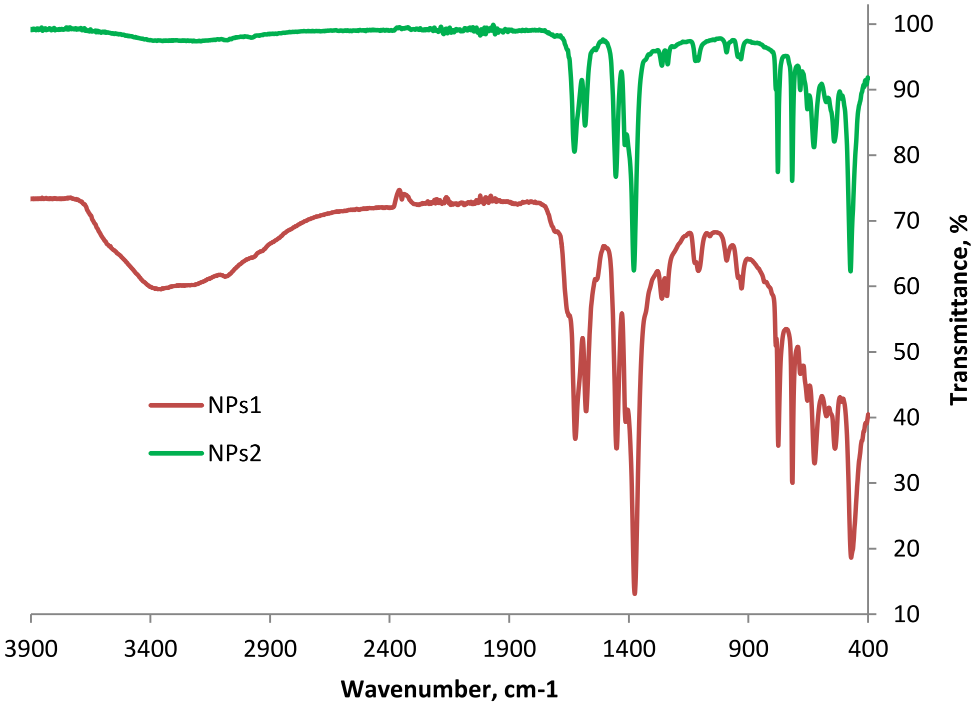

Figure S26: IR spectrum of activated MIL-127_NPs1 and MIL-127_NPs2.

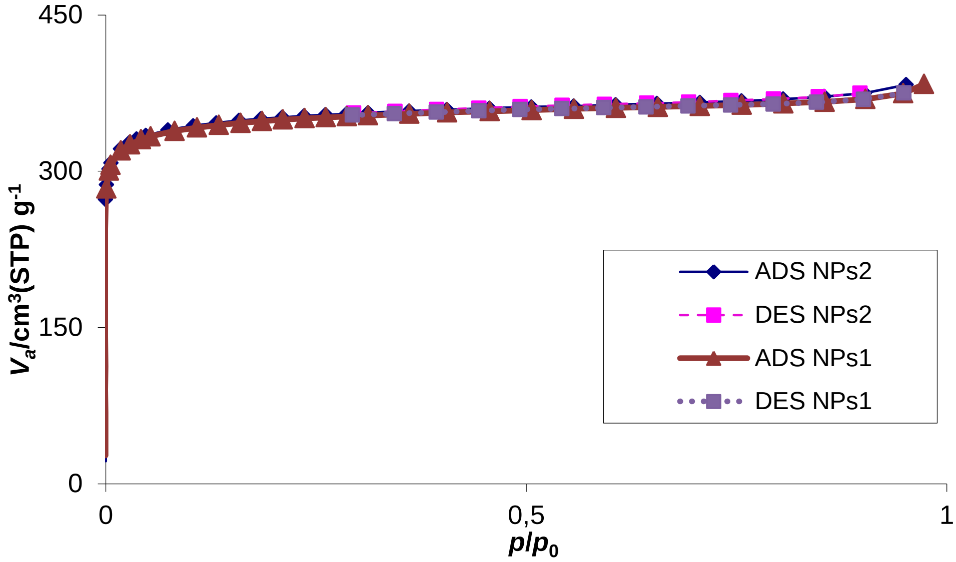

Figure S27: N_2 sorption isotherm at 77 K of activated MIL-127_NP1 and MIL-127_NP2 (previously outgassed at 200°C for 8 h under primary vacuum). BET surface area was 1390 and 1360 $m^2.g^{-1}$, respectively.

References

1 A. Dhakshinamoorthy, M. Alvaro, H. Chevreau, P. Horcajada, T. Devic, C. Serre and H. Garcia, *Catalysis Science & Technology*, 2012, **2**, 324-330.

2 T. Roisnel and J. Rodríguez-Carvajal, *Materials Science Forum, Proceedings of the Seventh European Powder Diffraction Conference (EPDIC 7)*, 2000, 118-123.

3 J. Rodríguez-Carvajal and T. Roisne, *International Union for Crystallography, Newletter N°20 (May-August)*, Summer 1998.

4 M. J. Avrami, *J. Chem. Phys.*, 1941, **9**.

5 B. V. Erofe'ev, *Compt. Rend. Acad. Sci. USRR*, 1946, **52**.

6 J. D. Hancock and J. H. Sharp, *J. Am. Ceram. Soc.*, 1972, **55**, 74-77.

Conclusions and perspectives

Recent advances in the heat reallocation field have shown that Metal Organic Frameworks (MOFs) hold a promising place for such applications. Among the large number of porous materials investigated so far, MOFs have been considered as a new class of sorbents of interest owing to their tunable structural and chemical features and thus, leading to a wide range of sorption behaviours. Their recent success in the field of heat reallocation has been reviewed in *Chapter I*, summarizing the present situation of hydrothermally stable porous MOFs materials which seem appropriate for such applications. These bibliography data allow a selection of the *a priori* best MOF candidates for further experimental work. Besides, *Chapter I* summarizes the advantages and drawbacks of other types of heat reallocation materials.

The concept of MOFs usage for short-term heat transformation systems has already been reported elsewhere. However, at the beginning of this thesis, the potentialities of MOFs for long-terms heat transfer applications had not been studied yet. The first aim of this PhD thesis has then been focused on the evaluation of MOFs for such applications. The water sorption properties of series of stable MOFs selected in *Chapter I* (MIL-101(Cr), MIL-100(Fe), MIL-127(Fe), MIL-160(Al), MIL-125(Ti)_NH_2, and UIO-66(Zr)_NH_2) were studied in the typical conditions of closed energy storage system with a relatively low desorption temperature of 80°C. The comparison of calculated energy storage capacities demonstrated the evidence of an enhanced efficiency for MIL-160(Al), MIL-125(Ti)_NH_2, UIO-66(Zr)_NH_2 and MIL-100(Fe). The hydrophilic microporous MIL-160(Al) was finally selected for further investigation owing to its excellent stability under numerous adsorption-desorption cycles and easy green scalable and cheap synthesis. The shaping of material is required for real application. Thus, an optimization of the large scale synthesis and shaping of the MIL-160(Al) was performed in order to investigate its use for energy storage prototype (open system). The results indicated a very good agreement between energy storage capacities obtained in pilot test and previously calculated values deduced from closed system conditions.

Physical adsorbents are suitable for heat storage application, but the most promising materials are composites based on inorganic porous matrix and hydroscopic salt that provides both sufficient stability and high energy storage capacity. Keeping in mind the requirements for heat storage material formulated in *Chapter I*, the second aim of this PhD thesis has been focused on the development of the novel heat storage materials such as salt-MOF composites. The investigation of the MOF-matrix properties (chemical composition, type of porosity, accessible pore volume, amphiphilic character) on the water sorption characteristic of composites, the evaluation of their energy storage capacity and stability under numerous adsorption-desorption cycles were carried out summarizing their potentialities for heat storage application (*Chapter III*).

It was evidenced that the enhanced pore volume of several MOFs, higher than those of typical inorganic porous materials, allows the encapsulation of larger amounts of salt. To probe how the nature of the MOF matrix may increase the water sorption characteristic of composites by physical adsorption, the cycling loading lift of composites was compared with the one of the corresponding bulk salt. It has been shown, that two parameters allow to significant increase of water sorption capacity: (i) a larger amount of encapsulated salt (related to pore volume of matrix) and a significant residual pore volume of matrix that can contribute through physical adsorption. Noteworthy, when dealing with a strong hydrophilicity of the MOF matrix, a significant decrease of cycling loading lift of the composites is observed due mostly to a less efficient dehydration process of the salt inside the pores. This means that heat reallocation application based on hydrophilic MOFs only shall be considered only when considering pure physical adsorption. Finally, mesoporous amphiphilic MOFs allow a higher loading of salt which completely modifies the shape of adsorption isotherm with a resulting very high energy density together with a good cycling ability for the MIL-100(Fe)-$CaCl_2$ and MIL-101(Cr)-$CaCl_2$ composites. This demonstrates that energy storage composites based on amphiphilic and hydrophobic MOF and salt significantly enlarge the range of possible MOF candidates for energy reallocation purposes.

The last part of experimental results concerns the work on controlled size synthesis and large scale production of the microporous MOF denoted MIL-127(Fe). This MOF is highly water stable and thus, is promising for different applications based on water adsorption method or even in aqueous phase. Thus, an environmentally friendly strategy of synthesis optimization at a large-scale laboratory production has been developed, with a good yield and space-time-yield (STY) of ~60% and ~60 $kg \cdot m^{-3} \cdot day^{-1}$, respectively, which is of interest for real applications including heat reallocation; it also allowed the synthesis at the nanoscale, which is of interest to optimize the packing density.

In terms of perspectives, if water is one possible working fluid for open system energy storage device, however, for closed systems, different working fluids could be considered. One possibility would be to use methanol which possesses a higher saturated vapor pressure compared to water (7.402 kPa versus 1.228 kPa at 10°C, respectively). Thus, as preliminary tests, it allowed to reach the full sorption capacity of amphiphilic MOFs such as MIL-127(Fe) and MIL-100(Fe) at low relative pressure region (below 12.5 mbar), which is impossible in the case of water. It has been shown that MIL-100(Fe)/methanol working pair is a very promising candidate for energy storage in closed system reactor (even for very low desorption temperature of 50°C). It would be interesting to pursue this study. Other working fluids with enhanced saturated vapor pressures could also be investigated for energy reallocation (e.g. butane) that would significantly enlarge the range of possible MOF-candidates (including amphiphilic MOFs and even MOFs with a lower hydrothermal stability).

In the field of MOFs-salts composites, one could assess the performances of new hydrothermally stable MOFs composites with large pore volume and suitable amphiphilic character (amphiphilic or hydrophobic) using for instance other inorganic salts with high energy capacity such as the energy efficient $SrBr_2$. First attempts are reported in Chapter III.

Finally, the optimization of the packing density of composites is another key-issue for increasing the energy density. From this point of view, a control of the particle size of MOFs could be carried out; noteworthy, most of the stable MOFs studied in this thesis have been synthesized as nano or micro-particles. The heat transformation long-term application requires also the use of large quantity of material, and high packing density which can be considered as current limitations for MOFs. If all these robust MOFs can easily be produce at the multi-Kg scale, their packing density has not yet been optimized. This is a very important parameter when considering an energy volumetric density, depends not only on crystallographic density, but also on the particle size and shaping treatment. Thus, one way to improve the packing density of MOFs is to control the particle size (nanoparticles or biomodal particle size) or use an appropriate shaping of the MOF material (e.g. granulation, extrusion, monolith), leading to a strong enhancement of the energy density. Recent progresses in the field of MOFs shaping indicate that such an optimization of the packing density is feasible.

Annex

Résumé de manuscrit

De nos jours, l'évolution rapide des technologies de stockage d'énergie requiert le développement de nouveaux matériaux adsorbants. Le concept de transformation d'énergie basé sur l'adsorption permet de stocker de l'énergie solaire renouvelable sur une courte (heures) ou moyenne (inter saisonnière) période. Les matériaux pour le stockage d'énergie sont le plus souvent des sels inorganiques (chimisorption), des adsorbants physiques ou plus récemment des composites (sel inorganique dans la matrice poreuse).

Ce travail de thèse a pour objectif d'évaluer l'intérêt de matériaux hybrides poreux de type MOFs (Metal Organic Frameworks) pour le stockage d'énergie (i) en tant qu'adsorbants physiques et (ii) comme matrices d'immobilisation de sels inorganiques. Les MOFs sont des solides poreux qui peuvent être décrits par l'association de ligands organiques et de briques inorganiques interagissant par liaisons fortes et définissant une structure cristalline avec une porosité régulière accessible. Les MOFs présentent une grande diversité en termes de composition chimique et de topologie par rapport aux solides poreux inorganiques, ce qui permet de moduler le caractère amphiphile, le volume, la taille et la forme des pores etc. En particulier, le volume poreux de certains MOFs est plus élevé que celui de nombreux adsorbants classiques, ce qui permet de préparer des matériaux présentant une plus grande capacité d'adsorption en eau et un plus grand taux d'encapsulation de sel.

Ce manuscrit est composé de quatre volets principaux: Chapitre I (revu bibliographique) et Chapitre II-IV (résultats expérimentaux).

Le chapitre 1 présente l'état de l'art du stockage d'énergie par voie thermochimique et porte également sur les principaux résultats reportés à ce jour concernant les MOFs dans ce type d'application. La première partie de cette revue résume les différentes technologies de stockage d'énergie (par voie sensible, latent et thermochimique) et se focalise d'une manière détaillée sur le stockage de l'énergie d'origine solaire par réaction thermochimique. Les conditions opératoires des systèmes de stockage (réacteur ouvert ou fermé) sont décrites ainsi que les principales propriétés que doivent présenter les matériaux de stockage d'énergie pour ce type d'application. La deuxième partie de cette revue se focalise sur les propriétés de stockage d'énergie des MOFs. Les MOFs ayant une bonne stabilité hydrothermale, une bonne capacité d'adsorption en eau ainsi qu'une bonne stabilité en cyclage (adsorption-désorption) sont décrits.

Dans le cadre de cette thèse, nous avons étudié une série de MOFs poreux et stables dans l'eau, construits à partir des cations métalliques à haut degré d'oxydation (Fe^{3+}, Al^{3+}, Cr^{3+}, Ti^{4+}, Zr^{4+}) et de ligands polycarboxylates. Nous avons choisi cette série de MOFs en tant qu'adsorbants physiques et comme matrices d'immobilisation de sels pour préparer des composites.

Le chapitre 2 porte sur l'étude de la capacité de stockage d'énergie d'une série de MOFs suivie par la sélection du meilleur candidat pour l'élaboration d'un prototype de stockage. Dans ce chapitre, nous avons comparé les propriétés d'adsorption en eau d'une série de MOFs sélectionnés. Ces résultats ont montré de grandes capacités d'adsorption ainsi que des densités énergétiques relativement élevées pour quelques MOFs les plus hydrophiles. Le MOF le plus performant de cette série (MIL-160(Al)) a été mis à l'échelle, mis en forme et ses propriétés de stockage de chaleur ont été évaluées dans un prototype (réacteur ouvert). Néanmoins, les applications de stockage inter-saisonnier requièrent des matériaux avec une densité énergétique plus élevée par rapport à celle des adsorbants physiques comme par exemple les composites. C'est pour cette raison que nous avons développé des composites à base de MOFs et de sels inorganiques que nous avons décrits au chapitre 3.

Le chapitre 3 se focalise sur le développement des nouveaux matériaux pour le stockage d'énergie, à savoir des composites qui résultent de l'encapsulation de sel inorganiques dans la porosité d'une large gamme de MOFs. Les MOFs sélectionnés permettent d'étudier l'influence de certains paramètres de la matrice (balance amphiphile, volume des pores) sur les propriétés d'adsorption des composites. La synthèse et la caractérisation des nouveaux composites 'sel-MOF' ont été réalisées et leurs capacités de stockage d'énergie évaluées dans les conditions d'utilisation de système de stockage d'énergie. Ces résultats ont montré que les MOFs amphiphiles et hydrophobes avec un volume poreux élevé sont très prometteurs pour le stockage de chaleur.

La capacité de stockage élevée et une bonne stabilité de cyclage (adsorption-desorption) des deux meilleurs composites à base de matrices mésoporeuses (MIL-100(Fe) et MIL-101(Cr)) confirment l'intérêt de ces solides pour ce type d'applications.

Le chapitre 4 se focalise sur l'optimisation de la synthèse d'un polycarboxylate de fer(III) (i. e. MIL-127(Fe)) qui est stable sur le plan hydrothermal et très prometteur pour les applications basées sur l'adsorption d'eau. Nous avons proposé des protocoles de synthèse éco-compatibles qui ont permis d'obtenir des nanoparticules de MIL-127(Fe) avec un rendement correct.